Study of Escaping Electron Dynamics and Applications from High-Power Laser-Plasma Interactions

Dean Richard Rusby

Department of Physics

University of Strathclyde

A thesis submitted for the degree of

Doctor of Philosophy

2017

This thesis is the result of the author's original research. It has been composed by the author and has not been previously submitted for examination which has led to the award of a degree.

Signed: D.

Date: 01/02/18

Abstract

In recent years, high intensity laser-matter interactions ($> 10^{18}$ W/cm^2) have been shown to produce bright, compact sources of many different particles. These include x-rays, neutrons, protons and electrons, which can be used in applications such as x-ray and electron radiography. The potential use of these sources for industrial applications is promising. However, the scalability and tuning of the sources needs to be understood at a fundamental level.

This thesis reports on three aspects of the development and application of these sources; the first two discuss applications of laser-plasma interactions. Firstly, the generation, characterisation and tunability of high-energy x-rays (≈ 200 keV) produced by the hot-electrons generated inside a solid target for the application of x-ray radiography. The characterisation of the x-ray source is conducted using a novel scintillator based absorption spectrometer. This source of x-rays was then used to radiograph a high density test object. Secondly, a novel technique of x-ray backscatter is investigated numerically and demonstrated experimentally for the first time on a laser facility. This uses the high energy electrons generated via wakefield acceleration to probe deeper into materials than traditional backscatter techniques. Finally, an investigation is reported examining the fundamental dynamics of electrons escaping from solid targets under different irradiation conditions. Experimentally, the number of escaping electrons was shown to maximise for certain laser illumination conditions; this was also explored using PIC simulations. The new results discussed in these three sections produce important new understanding of laser-driven x-ray generation and its application to penetrative probing and imaging for possible future industrial applications as well as the understanding of escaping electron dynamics.

Role of the Author

The majority of the analysis and all the simulations in this thesis have been conducted by the author. The author also took part in all the experiments. For more information regarding the role in each publication, please refer to the Publication List.

Chapter 4 The author played a significant role in the planning of the experiment. The scintillator diagnostic was built, set-up and imaged using a camera by the author. The analysis of the scintillator diagnostic, including its development and the simulations of its spectral reponse (see Chapter 3), was solely conducted by the author. The image plate used for the x-ray radiography was scanned by C. D. Armstrong. The images taken on the CsI array were also taken by C. D. Armstrong (Strathclyde & CLF). The joint TAO (Target Area Operators) were L. Wilson and C. Brenner (CLF).

Chapter 5 The author played a significant role in developing the technique that was studied in the experiment. Prior to the experiment the author conducted a programme of Monte Carlo simulations to understand the novel technique being developed. The author also actively participated in the experimental campaign. The results from the experimental campaign were taken and analysed by L. Wilson.

Chapter 6 The author contributed to this experimental campaign, which was fielded by R Dance and R Gray (Strathclyde) and had a significant role in part of it, which was dedicated to the study of escaping fast electron dynamics. The image plate used in the diagnostic to study the escaping electrons was scanned by the author. The response function of the diagnostic and analysis of the data was conducted solely by the author.

Publication List

The author contributed significantly to the papers below, which report on results obtained in the context of this PhD project.

1. **Measurement of the angle, temperature and flux of fast electrons emitted from intense laser-solid interactions.**

   D. R. Rusby, L. A. Wilson, R. J. Gray, R. J. Dance, N. M. H. Butler, D. A. MacLellan, G. G. Scott, V. Bagnoud, B. Zielbauer, P. McKenna, and D. Neely. Journal of Plasma Physics, 81(05):475810505, (2015).

   The author conducted the measurement of electrons emitted from a solid target and characterised the wraparound diagnostic used by running Monte Carlo simulations. The characterisation of the diagnostic is discussed in Chapter 3 and the experimental results in Chpater (6).

2. **Pulsed x-ray imaging of high-density objects using a ten picosecond high-intensity laser driver.**

   D. R. Rusby, C. M. Brenner, C. Armstrong, L. A. Wilson, R. Clarke, A. Alejo, H. Ahmed, N. M. H. Butler, D. Haddock, A. Higginson, A. McClymont, S. R. Mirfayzi, C. Murphy, M. Notley, P. Oliver, R. Allott, C. Hernandez-Gomez, S. Kar, P. McKenna, D. Neely. SPIE Security + Defence, pages 99920E. International Society for Optics and Photonics, (2016).

   The author measured the scaling of the flux of x-rays with incident laser energy. The author also inferred the internal electron temperature by recording the x-ray flux on a novel scintillator spectrometer which is described in Chapter 3. The results of this experimental campaign are discussed in Chapter 5.

3. **Laser-driven x-ray and neutron source development for industrial applications of plasma accelerators.**

   C. M. Brenner, S. R. Mirfayzi, **D. R. Rusby**, C. Armstrong, A. Alejo, L. A. Wilson, R. Clarke, H. Ahmed, N. M. H. Butler, D. Haddock, A. Higginson, A. McClymont, C. Murphy, M. Notley, P. Oliver, R. Allott, C. Hernandez-Gomez, S. Kar, P. McKenna, and D. Neely. Plasma Physics and Controlled Fusion, 58(1):014039, (2016).

   The author characterised the spectra for the radiography section of this publication.

4. **Evaluating laser-driven Bremsstrahlung radiation sources for imaging and analysis of nuclear waste packages.**

   C. P. Jones, C. M. Brenner, C. A. Stitt, C. Armstrong, **D. R. Rusby**, S. R. Mirfayzi, L. A. Wilson, A. Alejo, H. Ahmed, R. Allott, N. M. Butler, R. J. Clarke, D. Haddock, C. Hernandez-Gomez, A. Higginson, C. Murphy, M. Notley, C. Paraskevoulakos, J. Jowsey, P. McKenna, D. Neely, S. Kar, and T. B. Scott. Journal of Hazardous Materials, 318:694-701, (2016).

   X-ray radiography was performed on a sample that is highly applicable to the nuclear industry; the author again charaterised the x-rays used to perform the radiography.

5. **A laser driven pulsed X-ray backscatter technique for enhanced penetrative imaging.**

   R. M. Deas, L. A. Wilson, **D. Rusby**, A. Alejo, R. Allott, P. P. Black, S. E. Black, M. Borghesi, C. M. Brenner, J. Bryant, R. J. Clarke, J. C. Collier, B. Edwards, P. Foster, J. Greenhalgh, C. Hernandez-Gomez, S. Kar, D. Lockley, R. M. Moss, Z. Najmudin, R. Pattathil, D. Symes, M. D. Whittle, J. C. Wood, P. McKenna, and D. Neely. Journal of X-Ray Science and Technology, 23(6):791-797, (2015).

   The author helped evaluate a novel method of x-ray backscatter imaging using an initial beam of wakefield generated electrons. The author also played a key role in the experimental campaign. Further information, including initial models, simulations and further ideas are discussed in Chapter 4.

The author played a supporting role in the research reported in the following publications. Many of these were conducted at the start PhD project in order for the author to gain insights in experimental methods and working with high power laser systems. This includes preparing and operating crucial diagnostics used on the experiments and in the publications; such as Radiochromic-Film stacks and image plate diagnostics.

1. **Annular Fast Electron Transport in Silicon Arising from Low-Temperature Resistivity.**

   D. A. MacLellan, D. C. Carroll, R. J. Gray, N. Booth, M. Burza, M. P. Desjarlais, F. Du, B. Gonzalez-Izquierdo, D. Neely, H. W. Powell, a. P. L. Robinson, **D. R. Rusby**, G. G. Scott, X. H. Yuan, C.-G. Wahlstrom, and P. McKenna. A laser driven pulsed X-ray backscatter technique for enhanced penetrative imaging. Physical Review Letters, 111(9):095001, (2013).

2. **Role of lattice structure and low temperature resistivity in fast-electron beam filamentation in carbon.**

   R. J. Dance, N. M. H. Butler, R. J. Gray, D. A. MacLellan, **D. R. Rusby**, G. G. Scott, B. Zielbauer, V. Bagnoud, H. Xu, A. P. L. Robinson, M. P. Desjarlais, D. Neely, and P. McKenna. Plasma Physics and Controlled Fusion, 58(1):014027, (2015).

3. **Azimuthal asymmetry in collective electron dynamics in relativistically transparent laser-foil interactions.**

   R. J. Gray, D. A. MacLellan, B. Gonzalez-Izquierdo, H. W. Powell, D. C. Carroll, C. D. Murphy, L. C. Stockhausen, **D. R. Rusby**, G. G. Scott, R. Wilson, N. Booth, D. R. Symes, S. J. Hawkes, R. Torres, M. Borghesi, D. Neely, and P. McKenna. New Journal of Physics, 16:0-11, (2014).

4. **Proton acceleration enhanced by a plasma jet in expanding foils undergoing relativistic transparency.**

H. W. Powell, M. King, R. J. Gray, D. A. MacLellan, B. Gonzalez-Izquierdo, L. C. Stockhausen, G. Hicks, N. P. Dover, **D. R. Rusby**, D. C. Carroll, H. Padda, R. Torres, S. Kar, R. J. Clarke, I. O. Musgrave, Z. Najmudin, M. Borghesi, D. Neely, and P. McKenna. New Journal of Physics, 17(10):103033, (2015).

5. **Ion acceleration and plasma jet formation in ultra-thin foils undergoing expansion and relativistic transparency.**

   M. King, R. J. Gray, H. W. Powell, D. A. MacLellan, B. Gonzalez-Izquierdo, L. C. Stockhausen, G. S. Hicks, N. P. Dover, **D. R. Rusby**, D. C. Carroll, H. Padda, R. Torres, S. Kar, R. J. Clarke, I. O. Musgrave, Z. Najmudin, M. Borghesi, D. Neely, and P. McKenna. Nuclear Instruments and Methods in Physics Research, Section A: Accelerators, Spectrometers, Detectors and Associated Equipment, 829:163-166, (2016).

Preface/Acknowledgements

Before I start, I'll have to say that I'm just very grateful to all the people that gave me the opportunity to study my PhD. It has been a pleasure to study and learn everyday. It would be impossible to thank everyone that helped me achieve my goals but I'll definitely give it a go.

Firstly, I thank David for whom this PhD would've been impossible. The one thing I most admire about David is his patience; he will see that I am spending my time on something completely off-topic and will not say anything until I realise it myself. I also admire David's knowledge and work ethic, two qualities that I strive to possess in order to become a better physicist.

I must also thank Paul, who although was not by proximity the face I saw everyday, was a constant source of inspiration. The first contact I had with Paul was when I emailed him regarding a PhD position at 11pm. Within minutes I had a reply. This stuck with me as he had time for someone he had never met and was willing to pass my name onto David which enabled me to begin the PhD.

I want to thank all the members of the Strathclyde group that I've had the opportunity to work with through the years. I would especially like to thank Ross, David, Haydn whom I worked with on the first few experimental campaigns. Their patience and expertise helped greatly and gave me the confidence and ability I now have to work in the lab.

I had already done a placement at the central laser facility before beginning my PhD, so to rejoin the team and work with familiar faces was amazing. Of the CLF staff I would like to thank James, Rob H, Rob C, David C and Margaret whom I worked with as both undergraduate and PhD student and who I hope were happy to see me when I rejoined and happy to see the evolution of me as a scientist. Since rejoining I have had the opportunity of working with many other members of the CLF, and as stated before, there are far too many, but if I've worked with you, thank you.

I could not imagine working with a better team as I currently work. I must thank Graeme, Lucy and Ceri who have had to put up with me talking at them, interrupting them and being a nuisance for 4 years. These 3 have always enable me to see the end goal, the goal of becoming a physicist. I also thank Chris who is the first person I go to with issues.

The other half of our physics team needs thanking. Robbie, Raoul and Holger have always been there to help and answer questions when needed. Special thanks to Alex, who takes time to conduct the doctoral training session that have help me A LOT.

I have also gained some very good friends since my stay in the area. Graeme, Steve, Dan and Lucy; the main persistent members of the infamous quiz team who make Thursday evenings wonderful, thank you. Hopefully we get back to winning ways soon. I must also thank town ultras, climbing friends and TCJB whom make life in Didcot bearable.

I should thank my family. Where would I be without my Mum and Dad always putting up with my phone calls. Always listening to me talk about work and having no idea what I'm talking about. Who also feed me so well on the rare occasion I actually go home. Finally, I'd also like to thank Darren, who is the best brother and inspiration I have ever wished for.

Contents

Abstract ii

Role of the Author iii

Publication List v

Preface/Acknowledgements ix

Contents xi

List of Figures xvii

List of Tables xxvii

List of Symbols xxviii

1 Introduction 1

2 Overview of Underpinning Laser-Solid Interaction Physics 6

2.1 Ionisation from Lasers 6

2.1.1 Multi-Photon Ionisation 7

2.1.2 Barrier Suppression Ionisation 8

2.2 Plasma 10
2.2.1 Plasma Expansion 11
2.2.2 EM waves in Plasmas 12
2.3 Electron interactions with EM waves 15
2.3.1 Single electron interacting with an infinite plane wave . . . 16
2.3.2 Single Electron in a Inhomogeneous Wave 17
2.4 Absorption Mechanisms in Plasmas 18
2.4.1 Collisional Absorption 18
2.4.2 Collisionless Absorption 19
2.4.2.1 Resonance Absorption 19
2.4.2.2 Vacuum Heating 20
2.4.2.3 $\mathbf{J} \times \mathbf{B}$ Heating 21
2.5 Fast Electron Transport 22
2.6 Electron Spectrum 24
2.7 X-ray Production 25
2.7.1 Bremsstrahlung 26
2.7.2 X-ray Attenuation 28
2.8 Summary 30

3 Methodology **32**

3.1 High Power Laser Technology 32

- 3.1.1 Chirped Pulse Amplification (CPA) 33
- 3.1.2 ASE 34
- 3.1.3 Optical Parametric Chirped Pulse Amplification (OPCPA) 35

3.2 Laser Systems 37

- 3.2.1 The Vulcan Laser 37
- 3.2.2 The PHELIX Laser 39
- 3.2.3 The Astra-Gemini Laser 40

3.3 Diagnostics 41

- 3.3.1 Photomultiplier Tubes 41
  - 3.3.1.1 Multi-Channel Plate Photo-Multiplier Tubes . . . 42
- 3.3.2 Ion Diagnostics 42
  - 3.3.2.1 Thomson Parabola 43
  - 3.3.2.2 Radiochromic Film (RCF) 44

3.4 Simulations 47

- 3.4.1 Monte-Carlo Simulations 47
- 3.4.2 Particle In Cell Simulations 49

3.5 Diagnostic Developments 52

- 3.5.1 Cameras 52

3.5.2 Scintillator Based X-ray Spectrometer 53

3.5.2.1 High Energy Design 56

3.5.2.2 High Energy Design - Geant4 Analysis 57

3.5.2.3 Characterisation of Betatron Radiation 62

3.5.3 Image Plate Calibrations 67

3.5.3.1 Sensitivity 69

3.5.3.2 Scan One Recovery/Reconstruction 72

3.5.3.3 Scanning Filters 73

3.5.4 Angular Wrap-Around Stack 74

3.5.4.1 Mono-energetic Electron Absorption Curves . . . 75

3.5.4.2 Mono-energetic X-ray Absorption Curves 77

3.5.4.3 Maxwellian Electron Distribution Absorption . . 78

3.6 Summary 78

4 Diagnosing the Internal Electron Temperature using Bremsstrahlung X-rays 79

4.1 Experimental Method 84

4.2 Experimental Results 88

4.2.1 X-ray Spectra Analysis 92

4.3 Radiography 97

4.4 Summary & Conclusions 101

5 Penetrative Imaging using Backscattered X-rays Produced by Wakefield Accelerated Electrons 103

5.1 Modelling 107
    5.1.1 GEANT4 Modelling 111
5.2 Experimental Methods 119
5.3 Further Work 121
5.4 Conclusions 128

6 Escaping Electron Dynamics as a Function of Laser Pulse Duration and Focal Spot Size 130

6.1 Escaping Electrons as a Function of Laser Focal Spot Size 131
    6.1.1 Experimental Method 133
    6.1.2 Experimental Results 134
    6.1.3 Numerical Simulations 139
        6.1.3.1 PIC - Method 139
        6.1.3.2 PIC - Results 142
    6.1.4 Temperature Extraction 150
    6.1.5 Escaping Electron Dynamics 156
6.2 Escaping Electrons as a Function of Pulse Duration 161
    6.2.1 Experimental Method 162
    6.2.2 Experimental Results 162

6.2.3 Modelling 166

6.2.3.1 TNSA Modelling 166

6.2.3.2 Modelling of the Escaping Electrons 171

6.3 Conclusions and Future Work 174

7 Summary & Conclusions 178

7.1 Diagnosing the Internal Electron Temperature using Bremsstrahlung X-rays 178

7.2 Penetrative Imaging using Backscattered X-rays Produced by Wakefield Accelerated Electrons 179

7.3 Escaping Electron Dynamics as a Function of Laser Pulse Duration and Focal Spot Size 180

7.4 Further Work 182

A Appendix 184

A.1 Gaussian Filter 184

References 186

List of Figures

2.1 Basic schematic of Multi-Photon Ionisation (MPI) and Barrier Suppression Ionisation (BSI). 9

2.2 A schematic of the absorption mechanisms. 22

2.3 An example of the electron distributions that are produced from laser solid interactions. 24

2.4 Basic schematic of an electron accelerating around a positively charged atom. 26

2.5 Ratios of each attenuation process to the total attenuation for a) Carbon and b) Tantalum. 29

3.1 A basic schematic of Chirped Pulse Amplification (CPA) 33

3.2 The history of the maximum achievable focused laser intensity since 1960 34

3.3 A simple temporal schematic of a high power laser pulse with ASE present 35

3.4 Basic schematic of the Optical Parametric Amplification process. . 36

3.5 An overview layout of the Vulcan Laser. 38

3.6 Basic Schematic of a photomultiplier tube. 41

3.7 Schematic of a MCP-PMT. 42

3.8 Basic schematic of a Thomson parabola. 44

3.9 Example of an output from SRIM for an RCF stack with HDV2 film in-between layers of aluminium filtering. 46

3.10 The total x-ray energy emitted from a solid target for different input electron numbers. 49

3.11 Linearity and dynamic ranges of the selection of cameras at the Central Laser Facility. 53

3.12 Basic schematic of the scintillator based absorption spectrometer. 55

3.13 Attenuation curves for a) carbon and b) bismuth. 55

3.14 Attenuation curves provided by NIST XCOM for two scintillator materials; BGO and BC422q. 57

3.15 Response curve generated from energy deposited in each scintillator layer using GEANT4 59

3.16 Visual output of electrons inside the scintillator layers for 10^4 2 MeV incident photons. 59

3.17 Spectra of x-rays entering different layers of scintillators. 60

3.18 The average counts measured on a) the BC422q and b) BGO for three different incident laser intensities. 61

3.19 Fractional absorption as a function of energy for the scintillator based spectrometer designed for detecting betatrons x-rays. 63

3.20 Normalised output of scintillators for different critical energy betatron spectra. 63

3.21 The basic experimental layout for creating betatron x-rays. 64

3.22 The signal recorded on the first layer of EJ208 as a function of gas cell pressure. 65

3.23 The normalised signal from a shot at 100 mBar plotted with the expected output of the scintillator array for many critical energies. 66

3.24 Decay curves with the labelled scan 70

3.25 Decay curves of two scanners for the same area with ratios 70

3.26 The PSL per particle for image plate for a number of different particles. 71

3.27 a) The signal at scan 1 against signals at different scans and b) the gradients of each plotted against scan number. 72

3.28 Example of the wraparound diagnostic installed on laser-solid experiment with a copper target in the middle. 74

3.29 Arrangement of Image Plate between Fe filters used in wrap around stack with two variations. 74

3.30 SRIM calculations for design A and B of the wraparound diagnostic 76

3.31 Fractional absorption of the image plates at different mono-energetic electron energies. 76

3.32 Fractional absorbed energy for different mono-energetic x-rays. . . 77

3.33 Fractional absorbed energy for different electron Maxwellian distributions. 77

4.1 A collection of electron temperatures from laser solid experiments recorded using electron and x-rays spectrometers with scaling laws. 81

4.2 Schematic of the experimental setup in Target Area West. 85

4.3 Scintillator Diagnostic with example of output. 85

4.4 Absorption of the CsI(Tl) array and image plate used for radiography. 87

4.5 The average counts on the layers of scintillator as a function of incident laser energy. 88

4.6 The modelled x-ray flux from GEANT4 as a function of the incident laser energy. 89

4.7 The average counts from the first two layers of the scintillator array as a function of atomic number of the target. 91

4.8 Fractional absorption of the BGO layers in the scintillator array with the addition of the Al port. 92

4.9 a) The x-ray spectra from GEANT4 simulations for a distribution of 1 MeV electrons incident onto three different 1 mm targets. . . 93

4.10 The refluxing/recirculation of the electrons inside the target cause a modification to the x-ray spectra as shown in a) with the output of the diagnostic shown in b). 94

4.11 The simulated output of the diagnostic for a number of different electron temperatures through an 1 mm Aluminium target 95

4.12 A histogram of the extracted temperature of a shot with the uncertainties randomly added to the data. 96

4.13 The temperatures extracted from the new results presented in this thesis plotted with the temperatures from the literature. 97

4.14 Calculated x-rays transmission of the steel cylinder. 98

4.15 Outputs of both detectors used for radiography and a lineout of the data. 98

4.16 Radiograph of steel spheres of varying sizes (submillimetre to 2 millimetre) embedded in concrete recorded on an image plate from a full energy. 99

4.17 Three shots taken on 100 μm thick Ta with varying laser energy to radiograph steel spheres of varying sizes in-bedded in concrete recorded on the CsI array. 100

4.18 Lineouts of the steel spheres 100

5.1 a) The angular emission of x-rays for energies ranging from 10-500 keV given by the Klien-Nishina Formula. b) the self-normalised probability that the attenuation is caused by Compton scatter for three different materials. 105

5.2 The stopping power of electrons in SiO_2 taken from the ESTAR NIST database. 108

5.3 The average energy of the electrons and x-rays as a function of depth. 109

5.4 The normalised backscatter x-rays as a function of depth. 110

5.5 Schematic of the GEANT4 setup used to model the forward electron, forward x-rays and the returning backscattered x-rays. . . . 111

5.6 A comparison between the model and GEANT4 simulation for the electron energy, forward x-ray energy, total backscatter and backscatter per unit length x-rays. 113

5.7 Typical backscattered x-ray spectrum from SiO_2. 114

5.8 Normalised backscatter signal for a number of different incident electron energies. 114

5.9 Demonstration of temporally resolving distances between objects using a short pulse of electrons. 115

5.10 Spatial profile of an electron beam propagating 10 m in Air for a) 250 MeV, b) 500 MeV and c) 1 GeV electrons. 116

5.11 The FWHM of the scattered electron beams with energies from 100 MeV to 1 GeV recorded at 1, 10, 50 and 100 m. 117

5.12 The remaining fraction of the a) electrons and b) the produced x-rays for different incident electron energy as a function of depth. 118

5.13 The survival fraction of 50, 100 and 250 keV x-rays as energy as a function of distance in air. 118

5.14 The schematic of the x-ray backscatter experiment that took place on the Astra-Gemini laser system. 120

5.15 The 40 shot average output from the MCP-PMT showing the voltage peaks that correspond to backscattered x-rays returning from different objects. 121

5.16 a) Arrangement of objects with b) 2D x-ray backscatter image. . . 122

5.17 Spectral simulation of the backscattered x-rays from an object between two Al plates. 123

5.18 a) Cross sections of carbon, copper and tantalum for X-ray/Gamma induced nuclear reactions. b) The relationship between the atomic number and the peak cross section. 124

5.19 Pair production attenuation cross section for 10 MeV x-rays as a function of atomic number 126

5.20 The number of 511 keV x-rays and neutrons produced plotted against density a) and atomic number b). 127

5.21 The temporal detection of neutrons from a 10 mm tungsten cube behind 50 mm of concrete. 127

6.1 Top down schematic of the experimental setup conducted at the PHELIX laser. 133

6.2 Originally scanned image plate from an in-focus shot onto 100 μm thick Cu. 134

6.3 The remapped image with the target normal and laser axis marked on and with the corresponding polar plot of the data. The laser axis is marked on the polar plot with a dotted line. 135

6.4 Polar plots of the escaping electrons recorded on the wraparound diagnostic for a number of different laser foci. 136

6.5 Integrated and peaks counts taken from the wraparound diagnostic as a function of incident laser intensity. 137

6.6 The reflectivity measurements at the 1 and 2ω which have been normalised. 138

6.7 Estimated pre-plasma using the measured shadow from Wagner *et al* and the modelling conducted by McKenna and Carroll *et al*. . . 141

6.8 EPOCH simulations of the intensity of the laser as it interacts with the target. 143

6.9 Plot of the intensity and density from the simulations conducted at different defocuses. 144

6.10 The ratio of the modified density to the original density. 145

6.11 Temporal evolution of the forward propagating hot electron population inside the target a) and outside the target b). 145

6.12 The electron spectra from all the simulations at a single time; 0.75 ps for the internal and 0.9 ps for the external electrons. 147

6.13 The simulated output of the wraparound diagnostic using the simulated electron spectra from EPOCH. 148

6.14 Intensity of the laser from 3 simulation with different focus positions incident onto a target without a long pre-plasma. 149

6.15 The a) internal and b) escaping electron distributions for the shorter pre-plasma simulation. 149

6.16 The output of the wraparound diagnostic with the input of the electron spectra from simulation with no long pre-plasma. 150

6.17 The escaping electron distribution from an infocus and 200 μm defocus shot with 3 different forms of electron distribution: Boltzmann, Maxwellian, and Maxwell-Jüttner. 151

6.18 The normalised output of the wraparound when the response function is multiplied by different Boltzmann electron temperature distribution. 151

6.19 The PSL extracted from the peak of the angular distribution for all foci. 152

6.20 The r-squared values calculated from comparison between the experimental data and the different estimations for the percentage of escaping electrons. 154

6.21 The experimentally measured temperatures from the wraparound diagnostic. 155

6.22 The temporal evolution of the electric fields on the rear surface of the target. 157

6.23 A lineout of the electric field in X (the spatial dimension perpendicular to the target surface) on the rear surface of the target at the peak. 158

6.24 Escaping electron distributions from inside and outside the target. 159

6.25 Fitted temperatures for the internal and escaping electron distributions 159

6.26 Fitted temperature for the internal forward and refluxed electrons. 160

6.27 Layout of the RCF stack used on the experiment conducted in TAP.163

6.28 The first two layers of the wraparound diagnostic plotted alongside the corresponding polar plots. 164

6.29 The integrated PSL and integrated dose as a function of laser pulse duration. 165

6.30 The peak electron signal as a function of intensity for different pulse durations. 165

6.31 The integrated proton dose from the RCF layers plotted against the RCF layer energy threshold. 166

6.32 The temperature extracted from the wraparound diagnostic and RCF stack for the electrons and proton respectively. 167

6.33 The maximum proton energy models plotted as a function of pulse length with the experimental data. 170

6.34 Temporal plot of a laser created in the capacitor model 172

6.35 Electron energy evolution and spectra from capacitor model . . . 172

6.36 The modelled total escaping electron numbers compared to the integrated unit incident laser energy from the experiment 173

6.37 The fraction of escaping electrons from the capacitor model as a function of pulse duration. 174

A.1 Example of the Gaussian filter applied to each layer of IP to remove blemishes and scratches. 185

List of Tables

3.1 A summary of the deliverable laser parameters for each laser system discussed 40

3.2 Neutron coherent and incoherent scattering cross sections for elements in the scintillator array. The element with the highest total cross section is hydrogen. 62

3.3 The different types of Image Plate that are commonly used in diagnostic and information on the compositions. 68

6.1 The outputs from EPOCH that have been split into different categories to aid analysis. 142

6.2 A table of the temperatures extracted from the best fits for electron escaping fractions from 5-15% for the infocus data. 153

List of Symbols

a_B	Bohr radius
E_s	electrostatic force between electron and nucleus
$\hbar$	Planck's constant over 2 π
ϵ_0	permittivity of free space
e	fundamental charge
π	ratio of circumference to diameter
m_e	rest mass of electron
$\mathbf{E}$	electric field
c	speed of light in a vacuum
I	intensity
ω	angular frequency
λ	wavelength
E_{ion}	ion electrostatic potential
ω_L	laser angular frequency
λ_D	Debye length
Λ	plasma parameter
n_e	electron number density
T_e	electron temperature
T_i	ion temperature
c_0	ion sound speed
m_i	rest mass of ion
τ_L	laser pulse duration
k_b	Boltzmann's constant
ρ	charge density
μ_0	permeability of free space
k	wave vector
ω_p	plasma frequency
γ	Lorentz factor
n_c	critical density
δ	skin depth
η	refractive index
P_{crit}	critical self-focusing power
v_q	quiver velocity
$\mathbf{p}$	momentum
$\mathbf{B}$	magnetic field

v	velocity
a_0	normalised vector potential
S	Poynting vector
v_{drift}	electron drift velocity
$\mathbf{F}_{pond}$	ponderomotive force
U_p	ponderomotive potential
v_{ei}	electron-ion collision frequency
f_{abs}	absorption fraction
l_{ss}	scale length
ξ	Denisov function
v_{osc}	electron oscillation velocity
J_A	Alfven current
p	momentum
j_{fast}	fast electron current
j_{return}	return electron current
η_e	resistivity target to electrons
N_f	number of fast electrons
K_2	Bessel function of the second kind
P_B	Larmor equation
b	impact parameter
Z	atomic number
W_B^c	emissivity of bremsstrahlung
σ_{photo}	photoelectric attenuation coefficient
E_γ	energy of x-ray
σ_{total}	total attenuation coefficient
T_γ	transmission of x-rays, Beer-Lambert law
$d_{B,y}$	deflection from magnetic field in y
$d_{E,z}$	deflection from electric field in z
v_i	velocity of ions
f_{VFP}	Vlasov-Fokker-Planck distribution function
$C(f)$	collisional term in VFP equation
I_B	intensity of betatron x-rays
θ_B	angle of emission of betatron
E_c	betatron critical energy
$K_{1/3}, K_{2/3}$	modified Bessel function
$T_{hot,Beg}$	hot electron temperature scaling from Beg *et al*
$T_{hot,Wilks}$	hot electron temperature scaling from Wilks *et al*
$T_{hot,Haines}$	hot electron temperature scaling from Haines *et al*

λ_μ	wavelength of laser in microns
I_{18}	laser intensity in unit of 10^{18} W/cm^2
α	fine structure constant
r_c	coulomb radius
φ	laser phase front
R_r	Rayleigh range
R_C	radius of curvature
τ_{acc}	ion acceleration time
$\tau_{expansion}$	sheath expansion time
u_e	average electorn velocity
$q_{esc\,e^-}$	escaping electron charge

Chapter 1

Introduction

The study of laser interactions with all forms of matter is almost as old as the laser itself. The word laser itself is an acronym for light amplification by stimulated emission of radiation. Consider a set of atomic energy levels; the lowest level contains the electrons in their unexcited ground state. These electrons can be promoted to an upper energy level through some excitation process. These electrons can then fall from this energy level to one that is above the ground state but is 'meta-stable'; this means that the decay lifetime is relatively long compared to the other decay processes. If a photon passes sufficiently close by the atom with similar energy to the difference between the metastable state and another energy level, the electron can be forced to decay. As the electron decays, it will emit a photon that matches the energy and phase of the one that passed it by. This is known as stimulated emission. When more electrons inhabit the metastable state than the energy level below, which is known as population inversion, amplification can occur.

The first optical laser was created in 1960 by Maiman [1], and as early as the mid 1960's accelerated ions were measurable from interactions with achievable intensities of approximately 10^{10} W/cm^2. The principle of accelerating particles is a major area of research in laser-plasma physics and has been constantly developing since.

One of the major developments in the application of laser technology was in 1972. At this time, scientists were developing methods to miniaturise fusion reactions; Nuckolls *et al* [2] proposed that intense laser beams could be used to uniformly compress a sphere such that fusion would occur. Fusion is the process where two nuclei are close enough together that the short range, attractive nuclear forces overcomes the electrostatic repulsion and the two atoms fuse to become a heavier element.

For lighter elements, the binding energy of the heavier combined nucleus is smaller than the binding energy of the two separate atoms. The difference in the rest mass energies is converted into energy; the amount of which is dictated by Einstein's equation $E = mc^2$. This process occurs naturally at the centre of our sun through the proton-proton chain reaction. Reproduction of this method in the laboratory would be nearly impossible due to the time-scales required for a number of the processes to occur, as such, fusion in the laboratory takes a slightly different route. The fuel in the laboratory case is typically made of a mix of deuterium and tritium as the cross-section of this reaction is more favourable than any other combinations of isotopes/elements.

The technique of using laser beams to directly or indirectly cause the compression of a fuel to induce a fusion reaction is known as inertial confinement fusion (ICF). A simple criterion for fusion ignition (more energy out than in) can be found by considering the confinement time of the fuel and the time for a fusion reaction to occur; this leads to $\rho R > 3$ g/cm^2, which is the relationship between the density and radius of the fuel; this is known as the Lawson criterion. The density of a cryogenic deuterium-tritium fuel is relatively small (>0.5 g/cm^3); to satisfy the criterion would require a large amount of fuel (in the region of kilograms). This would lead to a reaction yielding approximately that of a large nuclear explosion, which is impractical as a fusion power source. To reduce the total fuel and to still meet the ρR criteria, the density of the fuel must be higher; this is why the fuel requires compression.

It is proposed that the necessary compression can be achieved by heating the outside of a spherical fuel pellet, either directly by the laser or indirectly from x-rays, such that the outward expansion of the outer layer causes a rocket-like inward thrust towards the centre of the fuel.

The National Ignition Facility (NIF) [3] was commissioned in 2008 and is currently researching indirect heating through x-rays to compress a pellet of DT fuel. One of the problems that many researchers have highlighted is that the uniform compression of fuel is difficult to achieve due to the hydrodynamic plasma instabilities that arise. This has led to alternative ideas such as fast ignition which proposes that similar compression is conducted as discussed above, but the ignition of the fuel is caused by energy being delivered into a so-called hotspot by a secondary source. There are many choices for the secondary source such as electrons [4, 5] or protons/ions [6] created from short-pulse, high-intensity lasers.

There are many other applications that are also gaining traction in the community. For example, electrons oscillating in the wake of a laser propagating through a plasma can create bright sources of betatron x-rays [7]. The spectrum of these x-rays currently peak between 1-30 keV, making them ideal for radiography of medical samples [8]. The coherence of the betatron x-rays also allows for phase contrast radiography to be performed on soft tissues that can increase the quality of images [9].

The production of much higher energy x-ray radiation is also possible from laser interactions with high-density solid targets. The multi-mega-Ampere and multi-MeV electron beam produces bremsstrahlung as it interacts with the atoms of the target.

The x-rays generated are highly energetic with energy from a few keV to many MeVs; as a result they can penetrate through materials to provide radiographs of large and high density objects. Additionally, x-rays are produced from a small point-like source which allows the images to be magnified to a large field of view and also leads to a source-size and spatial resolution of $\approx$100 μm [10, 11]. Finally, and one of the most important characteristics, the pulse duration of x-rays generated is similar to that of the initial laser (which can vary from several picoseconds to tens of femtoseconds), which leads to an incredibly short x-ray pulse capable of taking freeze-frame images of processes that occur in a billionth of a second. This is much shorter than conventional techniques ($\approx$ 100 ps). This leads to a short, small and penetrating x-ray source.

Conventional, competitive high-energy imaging technology exists in the form of linear accelerators. However, this technology will compromise one of the previously mentioned parameters to achieve the other two. For example, to perform penetrating x-ray radiography will lead to a long exposure time, sacrificing temporal and often spatial resolution simultaneously. Lower energy imaging technology, such as those present in modern airport security scanner, currently poccess the high resolution and object identification through 2-colour x-ray imaging. Lasers have aided in the security industry through the application of Spatially Offset Ramen Spectroscopy (SORS), however, scanning large objects using a laser driven x-ray source is another potential avenue of application to be investiagted.

The production of highly energetic x-rays from laser-solid interactions has been conducted numerous times [10, 11, 12, 13]. However, the tunability and full potential of the applications still needs to researched.

On a single shot basis the above applications compare well to conventional techniques, although the average flux of x-rays/photons is often much lower due to the repetition rate of current laser technology and associated targetry technology. Many current high-power systems, as described in Chapter 3, may take one shot approximately every 10-60 minutes depending on the experimental setup. However, new laser systems are being built that not only possess higher peak irradiance but also faster repetition rates [14, 15, 16]. Such systems will be essential in enabling laser driven sources to be relevant and competitive within industrial and security imaging sectors.

This thesis reports on investigations of two possible applications of high-intensity laser interactions: x-ray radiography of dense objects (Chapter 4), and penetrative x-ray backscatter from a high flux electron beam (Chapter 5). Both of these have experimental results which demonstrate their viability. Also I discusses the measurement of the internal and external electron temperature (Chapter 4 and 6), the understanding of which will aid in the development of hard x-ray radiography. At the beginning of each results chapter (4-6) I give a brief review of the current progress of the physics and also discuss the relevance of the research conducted.

Chapter 2

Overview of Underpinning Laser-Solid Interaction Physics

The processes involved in laser-solid interactions cross many branches of physics; including nuclear, quantum, electromagnetic and plasma. This chapter provides an overview of the underpinning physics; from the ionisation of the atoms, to the mechanisms that generate the hot electrons which propagate into the target, and the production of the subsequent x-ray radiation.

2.1 Ionisation from Lasers

To accelerate electrons, they must firstly be freed from their atom. The simplest method of considering ionisation of an atom due to an incident laser pulse is to first examine a hydrogen atom and the basic Bohr model. The Bohr radius is given as,

$$a_B = \frac{4\pi\epsilon_0\hbar^2}{m_e e^2} = 5.3 \times 10^{-11}\,\mathrm{m} \tag{2.1}$$

where $\hbar$ is Planck's constant divided by 2π, m_e is the mass of an electron and e is the charge of an electron. The electric field, E_s, between the electron and the nucleus is,

$$E_s = \frac{e}{4\pi\epsilon_0 a_B^2} = 5.15 \times 10^9 \text{ V/m} \tag{2.2}$$

For a laser to ionise the atom in this model, the electric field must be equal to the one calculated above. The intensity required for a such a laser is given by,

$$I = \frac{\epsilon_0 c \mathbf{E}^2}{2} = 3.51 \times 10^{16} \text{ W/cm}^2 \tag{2.3}$$

This sets a basic intensity limit to ionise a hydrogen atom, often referred to as the atomic unit of intensity, which is quite high. However, ionisation is observed at lower intensities; generated by the processes described below.

2.1.1 Multi-Photon Ionisation

As the optical laser intensity is increased, ionisation can initially occur in a process known as Multi-Photon Ionisation (MPI) [17]. Normally, when considering photoelectric ionisation, a photon with energy $\hbar\omega$ exchanges all its energy with an electron. If this energy is greater than the threshold energy for ionisation (E_{ion}) the electron escapes and the atom is ionised. If the energy is below the threshold, the electron does not escape and photons are re-emitted. In the latter case, the electron has a relaxation time, which is the time between receiving the energy from the photon and then re-emitting. This time is incredibly short, however, if another photon is absorbed by this electron during this time the electron can gain additional energy. If the absorbed energy from multiple photons is greater than E_{ion} the electron can escape. This process is known as Multi-Photon Ionisation. If the electron absorbs more photons than required to escape the atom, the electron will have some energy that is a multiple of the energy of the absorbed photons minus the ionisation potential. This is known as Above-Threshold Ionisation [18, 19].

The final kinetic energy of the electron, E_f, can be written as,

$$E_f = (n + s)\,\hbar w - E_{ion} \tag{2.4}$$

where n is the required number of laser photons absorbed for the ionisation to occur, s is the excess photons that may be also absorbed and E_{ion} is the ionisation threshold energy of the associated ion. This allows for a number of lower energy photons to ionise an atom, as shown in Figure 2.1 a); allowing the threshold for this process to be lower than the previously discussed ionisation when considering the Bohr Radius.

Once an electron is ionised, this electron is openly exposed to the electric field of the laser and will oscillate back and forth. This electron will collide with the un-ionised ions/electrons around it, causing more particles to be ionised. This will sequentially cause more and more particles to become ionised. This is a cascade ionisation process, which can become the main ionisation process once the electron is freed by a process such as multi-photon ionisation or one of the other method discussed in the following section.

2.1.2 Barrier Suppression Ionisation

Another process which can ionise an atom occurs at higher intensities. Consider a simplified case of an electron trapped in a 1D electric potential, $V(x)$, of the nucleus under the influence of the laser field, which can be described by the following,

$$V(x) = -\frac{Ze^2}{x} - e\mathbf{E}x \tag{2.5}$$

where E is the electric field from the laser and Z is the atomic number of the atom. This can lead to two situations arising. Firstly, the potential well that traps the electron can be altered such that the electron could tunnel through the potential barrier; this is known as tunnel ionisation. If the field of the laser is

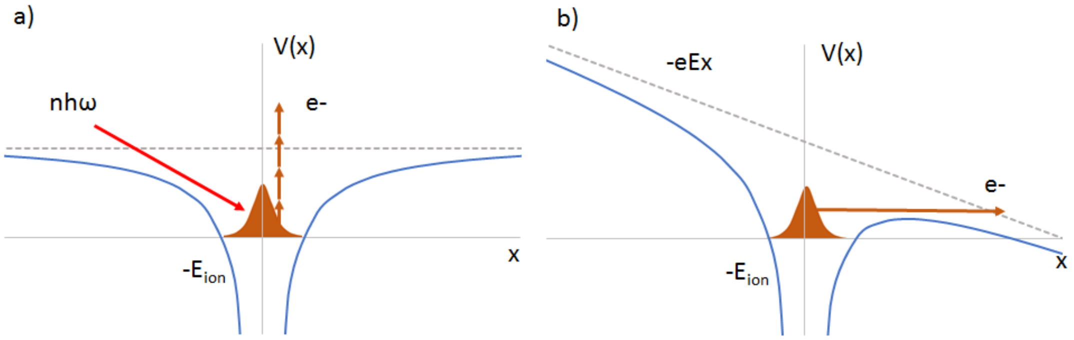

Figure 2.1: a) Multi-Photon Ionisation (MPI). Multiple photons are absorbed to ionise the electron from the potential well. b) Barrier Suppression Ionisation (BSI). The potential well is altered by the electric field of the laser; this allows for the electron to escape over the barrier. If the barrier is still present, the electron can tunnel through which is known as tunnelling ionisation.

high enough, the barrier could be suppressed such that the electron is allowed to freely escape. This is known as barrier suppression ionisation. The alteration of the field potential is shown in Figure 2.1 b).

The amount by which the barrier suppression or multi-photon/above-threshold ionisation dominates the ionisation processes is given by the Keldysh Parameter [20], which is expressed as,

$$\gamma_k = \omega_L \sqrt{\frac{2E_{ion}}{I_L}} \tag{2.6}$$

where I_L is the intensity of the laser, ω_L is the angular frequency of the laser. If γ_k is greater than one, then multi-photon ionisation dominates the ionisation processes, whereas if γ_k is less than 1, barrier suppression is dominant (obviously ignoring the case where a single photon has sufficient energy to release an electron). If a significant portion of atoms are ionised this can form a plasma, which is described in the following section.

2.2 Plasma

Unlike traditional states of matter, an ideal plasma consists of free charged particles. These free particles influence one another in such a way that the plasma can be described as having collective behaviour. A physical parameter that arises when there are many freely moving charges in a system is the Debye Length, λ_D, which is the characteristic length by which the electric potential of a charge falls off by $1/e$ due to the damping/screening from nearby charges. This potential is described as,

$$\varphi\left(x\right) = \varphi_0 \text{exp}\left(-\frac{x}{\lambda_D}\right) \tag{2.7}$$

where the Debye length is,

$$\lambda_D = \sqrt{\frac{\epsilon_0 k_B T_e}{n_e e^2}} \tag{2.8}$$

where $k_B T_e$ is the temperature of the electron distribution and n_e is the number density of the electrons. Normally the electric potential is dependent on the inverse of the distance from the charge, however for a plasma there is an additionally term that falls exponentially.

A plasma can be described using the Plasma Parameter, Λ, and is given as,

$$\Lambda = 4\pi n_e \lambda_D^3 \tag{2.9}$$

This equation essentially determines the electron number within a sphere with the radius of a Debye length, also known as a Debye sphere. When the Plasma Parameter is much greater than 1, $\Lambda >> 1$, this is known as an ideal plasma. The plasma is termed as having collective behaviour as the collective electrostatic collisions are dominant compared to the single particle collisions.

A plasma can also be described as either weakly or strongly coupled; this is determined by considering the potential and kinetic energy of the plasma. The potential energy is the result of the electrostatic interactions whereas the kinetic energy can be approximated as the average energy/temperature of the plasma. This is given as,

$$\frac{P.E.}{K.E.} \approx \frac{e^2 {n_e}^{-1/3}}{T_e} \tag{2.10}$$

If the plasma is sparsely populated and/or has a high temperature, then it can be described as weakly coupled.

In nature there are many forms of plasma, such as the interstellar medium, solar winds and the chromosphere of the sun.

2.2.1 Plasma Expansion

Often, in laser-solid interactions, a plasma is formed on the front side of the solid which is initiated by the intensity pedestal prior to the main laser pulse, the generation of which will be discussed in Chapter 3. The interaction between the laser and the so-called 'pre-plasma' will be examined in the next sections, but first the expansion of this plasma will be described. As a plasma expands into the vacuum away from the target with a constant temperature, the density gradient is usually a falling exponential, which can be described as,

$$n_e\left(x\right) = n_o e^{-x/L} \tag{2.11}$$

where n_0 is the solid number density ($\approx 10^{21}$ cm^{-3}) and L is the so-called 'scale length' which can be estimated as,

$$L \approx c_0 \tau_L \tag{2.12}$$

where τ_L is the duration of the pulse or the expansion time. c_0 is the ion sound speed which is given as,

$$c_o = \sqrt{\frac{k_B\left(ZT_e + T_i\right)}{m_i}} \tag{2.13}$$

Understanding the role of the preplasma is important because the peak of the laser pulse often propagates through such a density gradient. Due to this, the interaction between an electro-magnetic wave and a plasma will be described in the following section.

2.2.2 EM waves in Plasmas

The propagation of electromagnetic waves is described using the Maxwell equations,

$$\nabla \cdot \mathbf{E} = -\frac{\rho}{\epsilon_0} \tag{2.14}$$

$$\nabla \cdot \mathbf{B} = 0 \tag{2.15}$$

$$\nabla \times \mathbf{E} = -\frac{\partial \mathbf{B}}{\partial t} \tag{2.16}$$

$$\nabla \times \mathbf{B} = \mu_0 \mathbf{J} + \frac{1}{c^2}\frac{\partial \mathbf{E}}{\partial t} \tag{2.17}$$

where **E** and **B** are the electric and magnetic fields, ρ and **J** are the charge and current density, and ϵ_0 and μ_0 are the permittivity and permeability of free space respectively.

As stated previously, the plasma is made up of freely moving charged particles. Typically, this is split into two species, the ions and the electrons. As the mass of the electrons is much lower than that of the ions, they will move more easily under the influence of external forces, such as those produced by a short laser pulse. It is therefore convenient to consider that the ions are quasi-stationary. As the electromagnetic wave travels through a plasma the fields will act on the electrons. This will feedback onto the propagating electro-magnetic wave altering the dispersion relation. Firstly, to calculate the dispersion relation we must obtain the general wave equation. If we take the curl of Faraday's Law (Eq. 2.16) we find,

$$\nabla \times (\nabla \times \mathbf{E}) = -\frac{\partial}{\partial t} (\nabla \times \mathbf{B}) \tag{2.18}$$

Substituting equation 2.17 into equation 2.18 and using the vector identity $\nabla \times (\nabla \times \mathbf{A}) = \nabla (\nabla \cdot \mathbf{A}) - \nabla^2 \mathbf{A}$, we find,

$$\nabla^2 \mathbf{E} = \frac{1}{c^2} \frac{\partial^2 \mathbf{E}}{\partial t^2} + \mu_0 \frac{\partial \mathbf{J}}{\partial t} \tag{2.19}$$

The general solution for the electric field, $\mathbf{E}$, from equation 2.19 is,

$$\mathbf{E} = E_0 e_x \exp \left[i \left(kx - \omega_L t \right) \right] \tag{2.20}$$

where k is the wave-vector and ω_L is angular frequency of the laser. Substituting equation 2.20 into equation 2.19 and assuming $\mathbf{J} = -en_e(dr/dt)$, we can solve each term separately,

$$\nabla^2 \mathbf{E} = \nabla^2 \left(E_0 e_x e^{i(kx - \omega t)} \right) = -k^2 \mathbf{E} \tag{2.21}$$

$$\frac{\partial^2 \mathbf{E}}{\partial t^2} = \frac{\partial^2}{\partial t^2} \left(E_0 e_x e^{i(kx - \omega t)} \right) = -\omega^2 \mathbf{E} \tag{2.22}$$

$$\frac{\partial \mathbf{J}}{\partial t} = \frac{\partial}{\partial t} \left(-en_e \frac{\partial r}{\partial t} \right) = -en_e \frac{\partial^2 r}{\partial t^2} = \frac{e^2 n_e \mathbf{E}}{m_e} \tag{2.23}$$

Substituting equations 2.21, 2.22 and 2.23 into equation 2.19 and dividing by $\mathbf{E}$ we find the dispersion relation for EM waves in a plasma,

$$\omega^2 - \frac{e^2 n_e \mu_0 c^2}{m_e} = \omega^2 - \omega_p^2 = k^2 c^2 \tag{2.24}$$

The difference between the dispersion relation of a plasma and the vacuum is the plasma frequency, ω_p; the natural frequency at which the plasma oscillates which is given as,

$$\omega_p = \sqrt{\frac{n_e e^2}{\gamma m_e \epsilon_0}} \tag{2.25}$$

where γ is the relativistic correction applied to the mass of the electron m_e and is given as $\gamma = 1/\sqrt{1-(v^2/c^2)}$, where v is the velocity of the particle. The plasma frequency only varies with the electron number density n_e. Therefore, a so-called critical density, n_c, can be defined at which the plasma frequency, ω_p, and laser frequency, ω_L, are equal; at which the wavevector k must equal zero and therefore the laser can no longer propagate. Rearranging equation 2.25, the critical density can be shown to be,

$$n_c = \frac{\epsilon_0 \gamma m_e \omega_L^2}{e^2} \tag{2.26}$$

If the number density of electrons in the plasma is less than the critical density then the plasma is described as underdense, whereas if it is above it is overdense.

If electrons oscillating in an intense laser field are moving relativistically, then the gamma/Lorentz factor can effectively increase the mass of the electron which increases the critical density. This allows the laser to propagate further and to higher densities. This process is known as relativistically induced transparency. This can have interesting effects such as making a thin solid material become transparent, enabling the laser to propagate further into the target which can affect the accelerated particles [21].

The laser is actually able to penetrate slightly beyond the relativistic critical surface. The wave-vector for the laser at this point is imaginary and the spatial dependence is an exponential decay. The gradient of the exponent by which the laser penetrates is known as the collisionless skin depth, δ. It is defined as,

$$e^{ikx} = e^{-|k|x} = e^{-x/\delta}, \delta = |k|^{-1} = \frac{c}{\left(\omega_p^2 - \omega^2\right)^{1/2}} \tag{2.27}$$

The refractive index of a plasma is dependent on the frequency of the laser and the plasma frequency; therefore it is also dependent on the electron number density. The refractive index can be approximated as,

$$\eta \approx \sqrt{1 - \left(\frac{\omega_p}{\omega_L}\right)^2} = \sqrt{1 - \left(\frac{n_e}{n_c}\right)^2} \tag{2.28}$$

The intensity of a focused laser beam is typically higher in the middle. The plasma frequency, ω_L, is altered by the Lorentz factor, γ, which has a larger effect at the centre. This affects the refractive index in equation 2.28, causing the plasma to act as a focusing lens as the centre of the beam now has a high refractive index. This causes the beam to focus, an effect known as relativistic self-focusing.

The beam can also self-focus due to the Ponderomotive expulsion of electrons from the most intense region of the beam (see Section 2.3.2). There is an expression for the power that determines whether the laser beam will self-focus through this process known as the critical power, P_{crit}; which is given as,

$$P_{crit} \cong 17.5\left(\frac{\omega}{\omega_p}\right)^2 \mathrm{GW} \tag{2.29}$$

This expression is developed both numerically and experimentally [22]. Self-focusing can allow the laser to reach higher intensities due to a reduction in the spot size.

2.3 Electron interactions with EM waves

As stated in the previous section, electrons will experience a force from the laser field whereas the ions can be assumed to be quasi-stationary on the timescale of the oscillating field. Therefore, we only consider the interaction between the electrons and the electromagnetic wave with a quasi-static ion background.

In most experimental situations we have a finite pulse with a spatial and temporal variation in intensity. However, for the ease of introduction, an infinite plane laser wave interacting with a single electron shall be considered initially.

2.3.1 Single electron interacting with an infinite plane wave

The electron in an electromagnetic field will experience a force that is described by the Lorentz force,

$$\mathbf{F} = \frac{d\mathbf{p}}{dt} = q\left(\mathbf{E} + v \times \mathbf{B}\right) \tag{2.30}$$

where v is the velocity of the electron and $\mathbf{p}$ is the momentum which is given by,

$$\mathbf{p} = \gamma m_e v \tag{2.31}$$

In the non-relativistic case, the magnetic field is a factor of c less than the electric field, therefore it can be neglected. In this case the quiver velocity, v_q, of the electron in the electric field can be shown to be,

$$\frac{\partial v}{\partial t} = \frac{e\mathbf{E}}{m}, \mathbf{E} = E_0 \mathrm{cos} \omega_L t \tag{2.32}$$

$$v_q = \frac{eE_0}{m\omega_L} \mathrm{sin} \omega_L t = a_0 c \mathrm{sin} \omega_L t \tag{2.33}$$

where a_0 is the normalised vector potential which is the ratio of the classical and relativistic momenta. There exists an intensity threshold where the velocity of the electron becomes relativistic when oscillating in the laser field; this occurs when a_0 is greater than 1. For linearly polarised light, can be rearranged as,

$$a_0 \equiv \frac{eE_0}{m\omega_L c} \cong 0.85 \left(\frac{I_L \lambda^2}{1.37 \times 10^{18} \mathrm{Wcm}^{-2} \mu\mathrm{m}^2} \right)^{1/2} \tag{2.34}$$

This shows that for intensities greater than $\approx 1.6 \times 10^{18}$ W/cm^{-2} and a laser wavelength of 1 μm, the velocity of the electron can be considered relativistic.

The electron motion is initially in the direction of the electric field which is perpendicular to the magnetic field. At a certain point the magnetic field can no longer be neglected, this occurs when $a_0 > 1$. The magnetic field term, $v \times B$, in equation 2.30 determines that the electrons experience a force in the laser direction. This drift velocity, v_{drift}, can be calculated by inserting the quiver velocity of the electron from equation 2.33 into equation 2.30, only considering the $v \times \mathbf{B}$ term and using the fact that $\mathbf{B} = E_0 \cos(\omega_L t)$,

$$v_{drift} = \frac{e^2}{4m_e^2 \omega_L c} c^2 \cos(2w_L t) = \frac{a_0^2}{4} c \cos(2\omega_L t) \tag{2.35}$$

This shows that for a laser that enables relativistic electron quiver velocities, there is a fundamental drift of the electrons in the direction of the laser. Also note, this occurs twice per laser cycle and always points in the direction of the laser as the cross product of the current density from the electric field and the magnetic field is always pointing in the laser direction.

2.3.2 Single Electron in a Inhomogeneous Wave

As stated before, the assumption of an infinite plane wave was a simplification of the laser interaction with an electron. In reality, the laser has a finite temporal and a spatial intensity profile.

If the laser is focused, the electron can experience an electric field that is large enough to oscillate it such that at different positions during the oscillation, it will experience a different laser intensity. In this case, the restoring force from the lower intensity regions is not enough to return the electron to the higher intensity regions. This process will result in the electron gaining net momentum, taking it away from the higher intensity regions every laser cycle. This is known as the Ponderomotive force. This force, $\mathbf{F}_{pond}$, can be shown to be, in the classical case, the negative average gradient of the ponderomotive potential given by Gibbon [23] as,

$$\mathbf{F}_{pond} = -\nabla\Phi_{pond} = -\frac{e^2}{4m_e \omega_L^2} \nabla \mathbf{E}^2 \tag{2.36}$$

In the relativistic case we have,

$$\mathbf{F}_{pond} = -m_e c^2 \nabla \gamma \tag{2.37}$$

The kinetic energy gain from the ponderomotive force in a linearly polarised laser cycle for the relativistic case can be shown to be,

$$U_p = m_e c^2 \left(\gamma - 1\right) \tag{2.38}$$

This essentially can be considered as an effective temperature of the electron accelerated by this mechanism [24]. This is an example of an absorption mechanism for a single electron. There exist multiple absorption mechanisms that can occur in plasma which are described in the next section.

2.4 Absorption Mechanisms in Plasmas

Absorption mechanisms refer to the energy transfer from the laser to the plasma/electrons. For plasmas there are a few mechanisms for this energy transfer to occur. These are typically split into two categories; collisional and collisionless absorption.

2.4.1 Collisional Absorption

Collisional Absorption, often called Inverse Bremsstrahlung, occurs when an electron in a plasma is oscillating in a relatively low intensity laser field; approximately 10^{12-15} W/cm^2.

As the laser field oscillates the electron at the quiver velocity, the electron temporally gains kinetic energy from the laser field. During this oscillation, the electron has the possibility of having a collision with an ion that is present in the plasma.

This transfers energy from the laser to the ions in the plasma via the electrons. This occurs on average at the electron ion collision frequency,

$$\nu_{ei}\left(n_c\right) \propto \frac{n_c Z^*}{T_e^{3/2}} \tag{2.39}$$

where Z^* is the effective charge of the ionised atom. The fraction of absorbed energy [24] by the plasma over a scale length L is given as,

$$f_{abs} = 1 - \exp\left(\frac{32}{15}\frac{\nu_{ei}\left(n_c\right)}{c}L\right) \tag{2.40}$$

The absorption is maximised for plasmas with long scale lengths, high atomic number and low temperature. From equation 2.39, it is apparent that the collision frequency will decrease as the temperature of the electron increases; this means that for higher intensities the absorption from this mechanism will decrease.

2.4.2 Collisionless Absorption

There are a number of collisionless absorption mechanisms; each of the relevant ones shall be discussed in the following section.

2.4.2.1 Resonance Absorption

Consider a laser incident on to a solid target at an angle θ_i with some non-uniform plasma density with polarisation in the same plane as the angle (from here on this is known as p-polarisation). As the laser propagates into the plasma with a wave vector $k = ((\omega_L/c)\mathrm{sin}\theta_i, k_y, 0)$, it experiences an increasing electron density, which can be described as $\nabla n_e = (\delta n_e/\delta x, 0, 0)$. A basic schematic of the main absorption mechanisms is shown in Figure 2.2. The dispersion relation from equation 2.24 is modified to become,

$$\omega_L^2\left(1 - \sin^2\theta_i\right) = \omega_p^2 + c^2 k_y^2 \tag{2.41}$$

The wave-vector, k_y, changes as density increases; when $k_y = 0$ the beam is reflected at $n_e = n_c \cos^2 \theta_i$, note this occurs before the critical density. For the case of a p-polarised laser, the electric field can tunnel to the critical density. At the critical density the frequency of the laser and the plasma are matched, which allows the laser to resonantly drive a plasma wave. The electric field decays exponentially past the critical density yielding a weak restoring force on the electrons; this leads to the plasma wave breaking and electrons passing into the target with high energies.

The absorbed energy/fraction from resonance absorption is described using the Denisov function [25], ξ which is given as,

$$\xi = (kL)^{1/3}\mathrm{sin}\theta_i \tag{2.42}$$

which relates to the fraction of absorbed energy, f_{abs}, as,

$$f_{abs} \propto \xi\mathrm{exp}\left(-\frac{2}{3}\xi^3\right) \tag{2.43}$$

The angle of incidence, θ_i, and scale length, L, will affect the absorption from this mechanism. This is because an initial scale length or pre-plasma must be present for the mechanism to occur, where typically the scale length is greater than the laser wavelength, $L > \lambda_L$. Secondly, the angle dictates how close the laser reaches the critical density.

2.4.2.2 Vacuum Heating

Vacuum heating is a similar mechanism to resonance absorption, however in this instance the scale length of the pre-plasma is shorter than the amplitude of the electron oscillation. This process was first proposed by Brunel [26] and observed in PIC codes by Gibbon and Bell [27]. The electric field of a p-polarised laser can pull the electrons into the vacuum on one half cycle, and on the second half, the electric field accelerates the electrons into the target. The laser must be p-polarised so that the electric field is acting perpendicular to the target surface. In this picture, the electrons do not experience a restoring force equal to the acceleration as they pass the critical surface, yielding a net energy exchange to the electrons.

2.4.2.3 J × B Heating

In section 2.3.1 it was shown that the electron quiver velocity becomes relativistic above intensities of 10^{18} W/cm^2 for a laser wavelength of 1 μm. At these intensities, the magnetic field becomes relevant and results in a force that causes the electrons to move in the direction the laser, as shown in equation 2.35. If these electrons move past the critical density whilst moving at this velocity they gain net energy from the laser. The laser also acts on the electrons via the Ponderomotive force as described in section 2.3.2. The combination of these two effect are described by Kruer and Estabrook [28] who obtain a total force given as,

$$\mathbf{F} = -\frac{m}{4}\nabla v_q^2 \left(1 - \cos 2\omega_L t\right) \tag{2.44}$$

Note that this does not depend on the direction of oscillation relative to a density gradient unlike the previous mechanisms discussed; this means that there is no difference between an s-polarised or p-polarised laser pulse.

The $\mathbf{J} \times \mathbf{B}$ mechanism also differs from the resonance and vacuum heating absorption mechanisms as the electrons are accelerated along the direction of laser propagation, often refered to as the laser axis, rather than normal to the critical density.

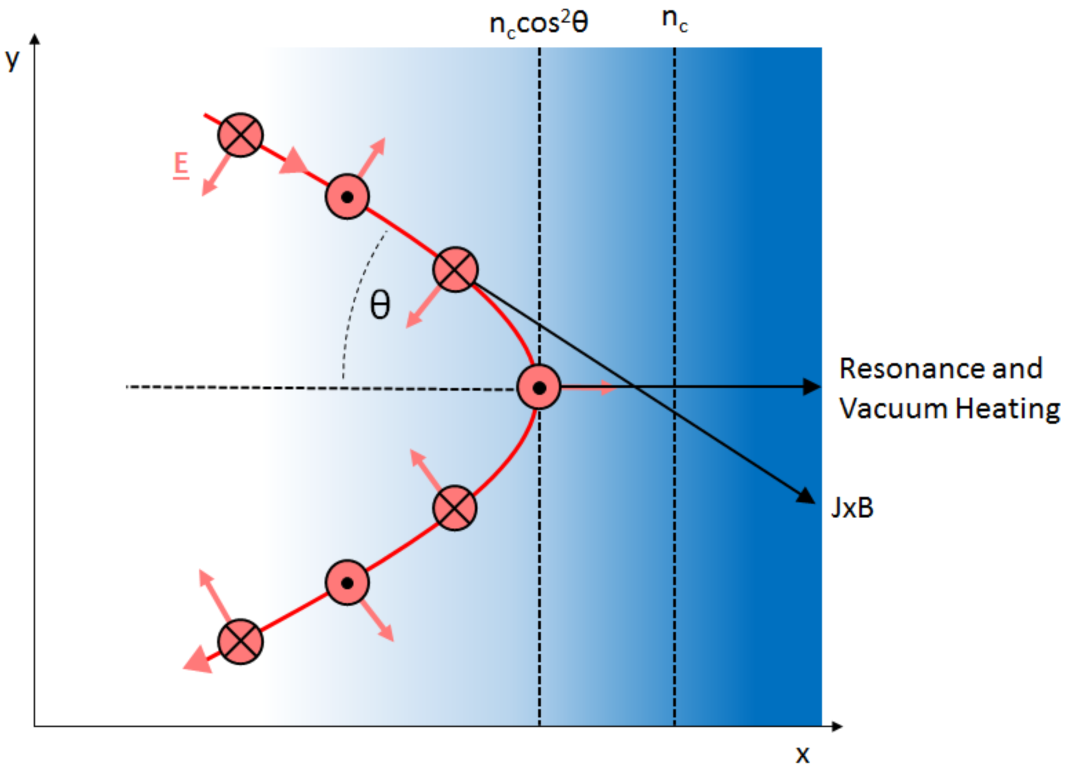

Figure 2.2: A schematic of the absorption mechanisms described in the text with the relevant angle of accelerated hot electrons relative the incident laser. The circles along the beam represent illustrate the polarisation of the laser (in this case a p-polarised laser) and the directions of the electric and magnet fields.

2.5 Fast Electron Transport

The previous sections highlighted how the laser transfers energy to the electrons through a number of mechanisms. Once the electrons pass the critical surface, they are no longer within reach of the laser field and are thus injected into the target. The population of electrons injected can possess peak currents of many mega-amperes. The current of electrons inside the target exceeds the Alfven limit [29, 30], j_A, a limit which predicts that if the current is too high the self-induced magnetic field will start to break-down the electron beam by turning the electrons back against the direction of the beam propagation. The size of this current can be estimated using the following,

$$\mathbf{j}_A = \frac{4\pi}{e\mu_0}\mathbf{p} \tag{2.45}$$

where p is the momentum of the electrons. Assuming a 1 MeV electron beam that is infinitely wide, the current limit from equation 2.45 is approximately 47.5 kA. Additional effects must be occurring to overcome the Alfven limit to enable the fast electron population to propagate within the target.

A return current of electrons is drawn from the background plasma to neutralise the fast electron current. This is a localised current that is drawn in the opposite direction to the main electron current. This can be described simply as,

$$\mathbf{j}_{fast} + \mathbf{j}_{return} \approx 0 \tag{2.46}$$

The return current, j_{return}, contains significantly more electrons and is cooler than the hot electron current, j_{fast}.

If the return current does not exactly equal the forward propagating fast electron current, magnetic fields can form. This magnetic field can be calculated from Maxwell's Equations,

$$\mathbf{E} = \eta_e \mathbf{j}_{return} \tag{2.47}$$

$$\frac{\partial \mathbf{B}}{\partial t} = -\nabla \times \mathbf{E} = -\nabla \times (\eta_e \mathbf{j}_{return}) \tag{2.48}$$

$$\nabla \times \mathbf{B} = \mu_0(\mathbf{j}_{fast} + \mathbf{j}_{return}) \tag{2.49}$$

where η_e is the resistivity of the plasma/target. This shows that a magnetic field can be generated when $\mathbf{j}_{return} \neq \mathbf{j}_{fast}$. The resulting magnetic field can lead to a pinching of the of electron beam as it travels through the target.

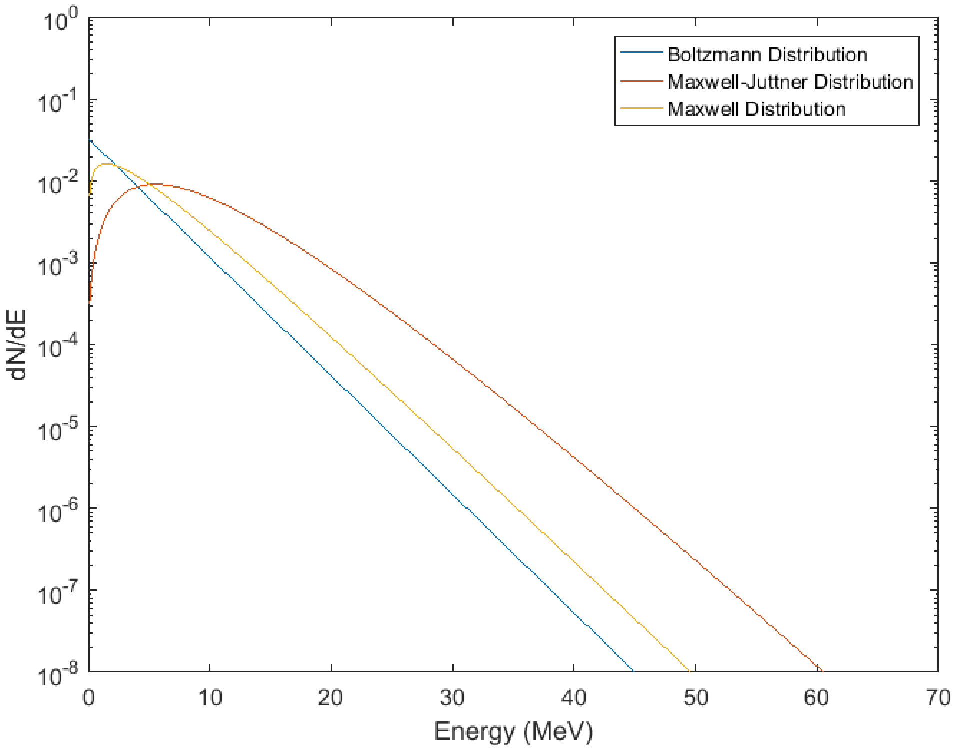

Figure 2.3: An example of the electron distributions that are produced from laser solid interactions. The temperature in the above graph is 3 MeV for all the example distributions.

2.6 Electron Spectrum

The result of the absorption mechanisms discussed in section 2.4 is a population of electrons that have gained significant energy from the laser and are now travelling through the target. The energy given to the electrons depends on many different factors, for example, what part of the laser cycle accelerates the electrons or where in the plasma they experience the laser field. Bezzerides *et al* [31] shows that from resonance absorption, the time averaged randomness leads to a Maxwellian type electron energy distribution. A Maxwellian distribution with a single temperature can be described as,

$$f\left(E_f\right) = N_f\sqrt{\frac{4E_f}{\pi(k_BT_f)^3}}\exp\left(-\frac{E_f}{k_BT_f}\right) \tag{2.50}$$

where E_f is the energy of the fast electrons, T_f is the temperature of the fast electrons and N_f is the total number of fast electrons. For laser intensities greater than 10^{18} Wcm^{-2} the energy spectrum is given by the relativistically modified Maxwell-Jüttner distribution,

$$f(\gamma) = \frac{N_f \gamma^2 \beta}{\alpha K_2 (1/\alpha)} \exp\left(-\frac{\gamma}{\alpha}\right) \tag{2.51}$$

where $\alpha = k_B T_f / m_e c^2$, $\beta = v/c$, $\gamma = 1/\sqrt{1-\beta^2}$ and K_2 is a Bessel function of the second kind. An example of the distributions are shown in Figure 2.3 as well as a Boltzmann distribution for a temperature of 3 MeV. Also note that the area under each of the distributions is normalised to 1 to ensure each represent the same number of electrons.

The number of accelerated hot electrons, N_f, depends on the temperature of the electrons and the amount of laser energy absorbed. The absorption of the laser is often measured using a scatter screen that captures the reflected laser energy or through x-ray measurements. A review paper by Davies collected all the relevant data available in the field. The absorption can reach as high as 80% for some laser conditions. A fit to the data by Davies [32] is given as,

$$f_{abs} = \left(\frac{I\lambda^2}{4.3 \times 10^{21}\mathrm{Wcm}^{-2}\mu\mathrm{m}^2}\right)^{0.2661} \tag{2.52}$$

The temperature of the fast electrons, T_f, is related to the incident intensity and wavelength of the laser. This is often described using so-called scaling laws [24, 33, 34] which will be discussed in more detail in Chapter 4.

2.7 X-ray Production

X-ray radiation from atomic processes during laser plasma interactions can be generated in three ways: free-free, free-bound and bound-bound emission. The

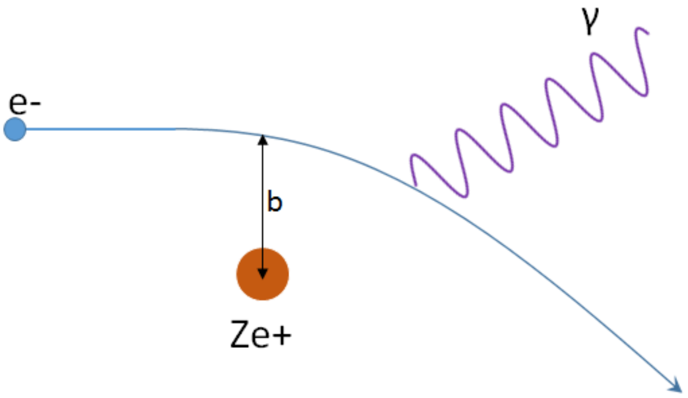

Figure 2.4: Basic schematic of an electron accelerating around a positively charged atom.

first mechanism, free-free, occurs when free electrons interact with heavier ions and emit x-rays known as bremsstrahlung. If a free electron recombines with an atom an x-ray can be emitted, this is the second mechanism free-bound. The final mechanism produces line emission from transitions between discrete energy levels in the atom.

The production of bremsstrahlung will be discussed in this section as is it the most relevant to the research described in this thesis.

2.7.1 Bremsstrahlung

The word Bremsstrahlung comes from German meaning ‘braking radiation’ which aptly describes the process by which the x-rays are created. An electron passing by an ion of charge Ze will experience an attraction. This attraction will cause the electron to accelerate towards the ion displacing its path, as shown in the basic schematic in Figure 2.4. Accelerating charges produce radiation; to conserve energy the electron will lose some energy, hence the term ‘breaking radiation’. The power emitted by a single oscillating/accelerating particle is given by the

Larmor Equation,

$$P_B = \frac{2}{3}\frac{e^2 a^2}{4\pi\epsilon_0 c^3} \tag{2.53}$$

where a is the acceleration which can be described using Coulombs law,

$$F = ma = -\frac{Ze^2}{4\pi\epsilon_0 x^2} \tag{2.54}$$

and x, for bremsstrahlung, is the distance between the electron and ion. From Figure 2.4, the closest distance between the electron and ion is known as the impact parameter, b. It can be approximated that $x \sim b$. Note that as electrons are the lightest particles in this interaction, they will experience the largest acceleration and therefore emit the most power. The interaction will be very short, where the time, Δt, can be approximated as $2b/v$, where v is the velocity.

The total emitted energy in a single collision can be calculated by substituting equation 2.54 into 2.53 and multiplying by Δt,

$$P_B \Delta t = \Delta E = \frac{2}{3}\frac{e^2}{c^3}\left(\frac{Ze^2}{mx^2}\right)^2 \frac{2b}{v} = \frac{4}{3}\frac{Z^2 e^6}{c^3 m^2}\frac{1}{b^3 v} \tag{2.55}$$

For a beam of electrons, there are a number of impact parameters db. The number of electron collisions per ion per unit time can be expressed as $n_e v 2\pi b db$. The power radiated is therefore,

$$W = n_e v \int \Delta E 2\pi b db \approx \frac{4}{3}\frac{Z^2 e^6}{m^2 c^3} 2\pi n_e \int_{b_{min}}^{b_{max}} \frac{db}{b^2} \tag{2.56}$$

where b_{max} and b_{min} are the maximum and minimum impact parameters. Here, b_{max} can be expressed as the Debye length and b_{min} as the De Broglie wavelength [35], and therefore $b_{min} \ll b_{max}$. The integration yeilds,

$$W \approx \frac{16\pi^2}{3}\frac{e^6}{mhc^3} Z^2 n_i v \tag{2.57}$$

The energy spectra of the electron has already been described as Maxwellian.

Considering a Maxwellian temperature distribution of velocities given by,

$$f_e = n_e \left(\frac{m}{2\pi k_B T_e} \right)^{3/2} \exp\left(-\frac{mv^2}{2k_B Te} \right) \tag{2.58}$$

Integrating over the entire electron distribution [35] we find,

$$W_B^v \approx \frac{32\pi}{3} \left(\frac{2\pi}{3k_B T_e m_e} \right)^{1/2} \frac{Ze^6 n_e^2}{m_e c^3} \exp\left(-\frac{h\upsilon}{k_B T_e} \right) \tag{2.59}$$

$$W_B^v \cong 6.8 \times 10^{-52} Z n_e^2 T_e^{1/2} \exp\left(-\frac{h\upsilon}{k_B T_e} \right) \mathrm{Wm^{-3}Hz^{-1}} \tag{2.60}$$

The shape of the x-ray spectrum is dependent on the temperature of the hot electrons. The lower end of the spectrum can be readily absorbed by the material producing it. The main processes of attenuation are discussed in the following section.

2.7.2 X-ray Attenuation

The attenuation of x-rays can occur through a number of different processes. These processes can be split into three different regions where a particular process is dominant.

For the low energy x-ray the dominant process is the photoelectric effect. This is the entire absorption of the photon energy which is transferred to an electron. This is more likely to occur in materials with high atomic numbers and to the electrons most tightly bound to the atoms. The photoelectric mass attenuation coefficient, σ_{photo}, is approximately given by,

$$\sigma_{photo} \propto Z^n {E_\gamma}^3 \tag{2.61}$$

where n is a constant that varies between 4 and 4.8 depending on the material [36] and E_γ is the energy of the x-ray. The energy at which this dominates depends

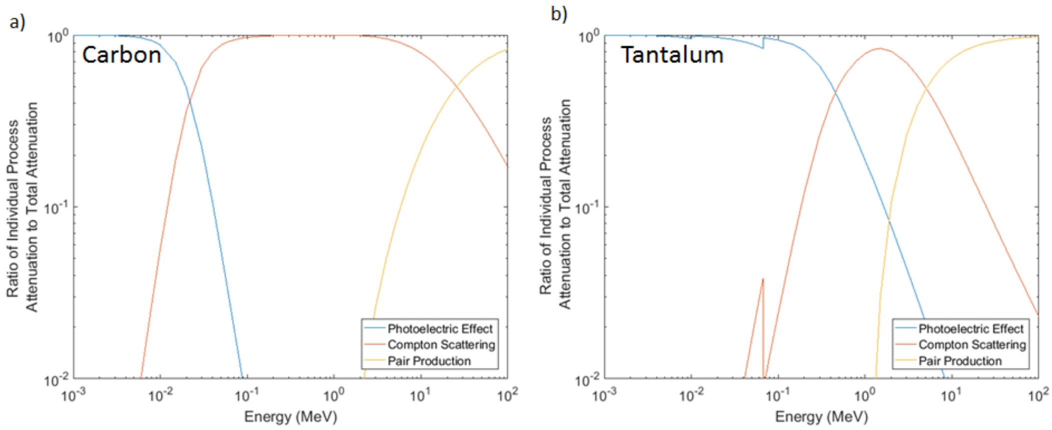

Figure 2.5: Ratios of each attenuation process to the total attenuation for a) Carbon and b) Tantalum. The differences between the two are mainly due to the changes in atomic number. The photoelectric effect is dominant to much higher energies and pair production becomes dominant for lower energies for the higher atomic number material.

on the atomic number of the material; for materials with higher atomic numbers the photoelectric effect will be dominant at higher energies compared to materials with lower atomic numbers.

The second energy region is dominated by Compton scattering, also known as incoherent scattering. This process occurs between the outer-most electrons and the x-rays, where the x-ray transfer parts of its energy to the electron and then scatters. The angle of deflection is dependent on the energy transferred in the collision. This will be discussed in more detail in Chapter 5.

At the highest energies, pair production can occur. This is the process where the x-ray can become a pair of particles with a net charge of zero. At two times the electron rest mass (1.022 MeV) the x-ray photon can become an electron-positron pair. If the x-ray possesses energies greater than 211.3 MeV it can produce a muon pair. The angle at which these particles are emitted depends on the initial energy of the x-ray due to the conservation of momentum/energy.

The regions in which each of these processes are dominant, as expected by the dependence on atomic number, vary for different materials. The extent of which is shown in Figure 2.5 which plots the calculated ratios of the attenuation due to each process to the total attenuation. The two materials here, carbon and tantalum, represent a low and high atomic number material. It is clear that for the high atomic number, the photoelectric effect is dominant to much higher energies compared to the low atomic number. Also the pair production process becomes dominant earlier for the high atomic number material. The cross-section for Compton scatter varies slightly for different materials, and as such, dominants for a larger region for the low atomic number material.

X-rays can also excite the nucleus; this is known as a photonuclear reaction. This can cause a neutron to be released through a (γ,n) reaction. Typically the cross section for such an interaction is on the order of hundreds of millibarns (10^{-29} m^2); compared to the other effects mentioned above (approximately 10 barns at 1 MeV for Cu), this has negligible attenuation. However, there will be neutrons created through this process during laser-solid interactions.

The transmission T_γ of a material for x-rays is given by the Beer-Lambert law,

$$T_\gamma = e^{-\sigma_{total} l \rho} \tag{2.62}$$

where σ_{total} is the total mass attenuation coefficient, l is the length/depth of the material and ρ is the density of the material. The form of this equation shows that the transmission falls exponentially as a function of distance. It also shows that for denser materials the transmission will be lower.

2.8 Summary

The aim of this chapter was to summarise the basics of laser-plasma interactions. Initially, the ionisation of atoms due to optical light at high intensities is described. When the laser is incident onto a solid target, this can lead to the formation of a plasma on the front surface which expands into the vacuum. The interaction between the laser and the front surface plasma results in the acceleration of electron to high energies through a number of absorption mechanisms. The injected electron beam has a current of multi-mega-Ampere with temperatures up to mega-electron-volts.

As the electrons pass through the target, they will interact with the target atoms generating x-rays through bremsstrahlung. These x-rays will have a spectrum that depends on the temperature of the injected electron beam.

The following chapter discusses the laser systems and diagnostics used to study such interactions.

Chapter 3

Methodology

This chapter reviews the techniques and developments used to conduct the research discussed in later chapters in the thesis. This will include an overview of high-power/intensity lasers as well as details of the laser systems used to conduct the research. Additionally, the numerical simulations which aid in the understanding of experimental results as well as diagnostic developments conducted by the author are reviewed.

3.1 High Power Laser Technology

Since the invention of the laser over 50 years ago, developments have been made in many aspects of laser technology, for example the developments of Q-switching to allow for short-pulsed lasers or the development of more advanced gain media. As the peak laser intensity increased, this opened the door for further exploration in the field of laser plasma physics. The technique of Chirped Pulse Amplification (CPA) [37] stands out as probably one of the most important evolutionary steps in the field of high peak power laser systems.

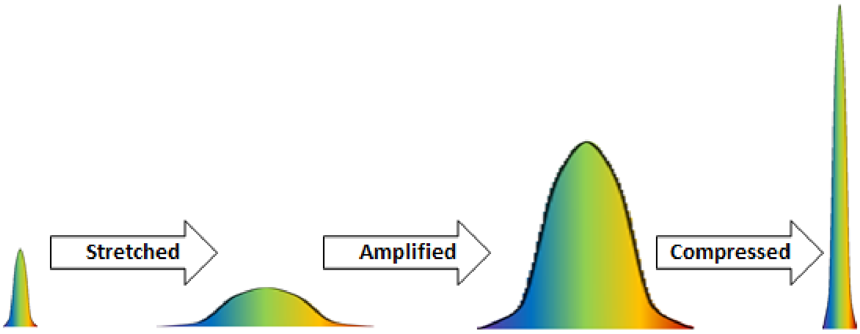

Figure 3.1: A basic schematic of Chirped Pulse Amplification (CPA). The laser is stretched to reduce the intensity to prevent damage to optics. The beam is safely amplified and then compressed, increasing the intensity.

3.1.1 Chirped Pulse Amplification (CPA)

Chirped Pulse Amplification uses the method of stretching the pulse prior to amplification to reduce the fluence of the beam. The reduction of the fluence helps to prevent the laser from damaging optics and gain media in the laser chain which is one of the main challenges for highest peak intensity laser systems. Lowering the intensity directly reduces the effect of the non-linear refractive index distorting the beam wavefront, which causes self-focusing of the laser and can also lead to damage of the gain medium and other optics.

CPA traditionally uses a pair of gratings to introduce a positive dispersion, meaning that the shorter-wavelengths take longer to pass through the setup compared to the longer-wavelengths. The device that does this is known as a stretcher. This path difference stretches the pulse in time which therefore reduces the intensity, allowing the pulse to be amplified without incurring significant non-linear effects. After the amplification process is complete, a negative dispersion is applied in the compressor to reverse the effect of the positive dispersion and compress the pulse. A basic schematic of the CPA technique is shown in Figure 3.1. Figure 3.2 shows a history of the peak achievable intensity; a massive increase occurred a few years after the first optical CPA technique was demonstrated, which opened up areas of physics that were previously unavailable.

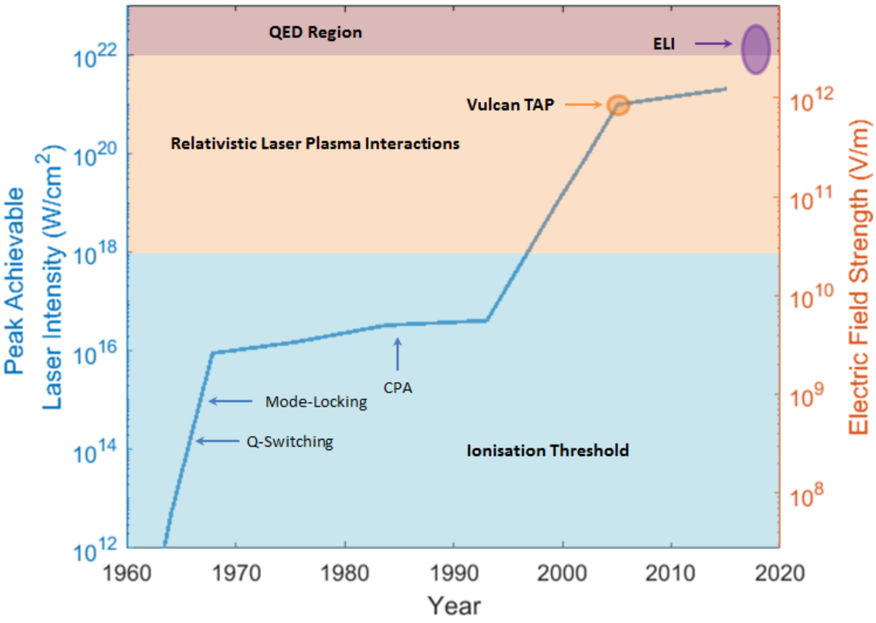

Figure 3.2: The history of the maximum achievable focused laser intensity since 1960 (adapted from Gray [38]). The regions highlight the areas of physics available for a laser with a wavelength of 1 μm. The construction of new laser systems promises to deliver higher peak intensities in the future [15].

3.1.2 ASE

An intense main pulse is readily achieved using CPA and other such amplification techniques. However, due mainly to spontaneous emission from the gain medium, an unwanted lower intensity pedestal of the laser is also amplified, which is known as amplified spontaneous emission (ASE).

When a gain medium is pumped, the excited atoms are held in a long life-time energy level (also known as a meta-stable state) before the main pulse stimulates them and amplification can occur. However, excited atoms can spontaneously decay from this energy level before the main pulse arrives. This process is inherently random and emits photons in 4π Steradians. If this spontaneous emission emits at an angle that allows it to propagate along the remaining laser chain it will be amplified along with the main pulse. This causes a pedestal either side of the main pulse where the leading edge can arrive up to nanoseconds before.

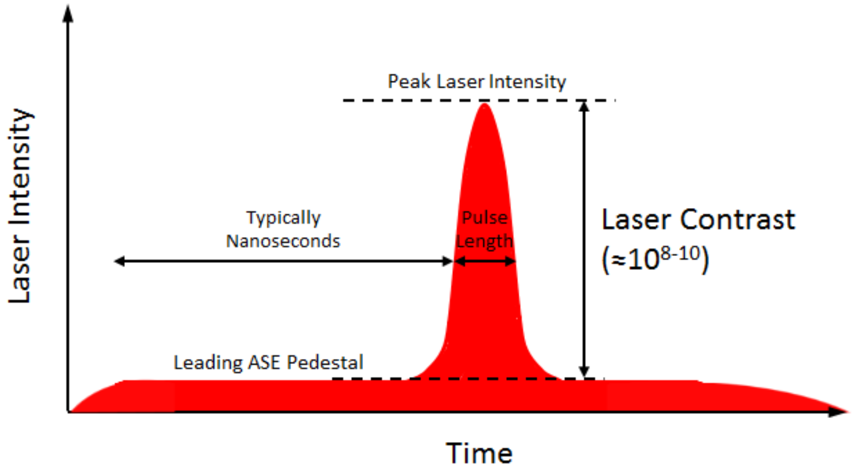

Figure 3.3: A simple temporal schematic of a high power laser pulse with ASE present, which can arrive nanoseconds before the main pulse. The laser contrast is the intensity ratio between the peak of the laser and the intensity of the ASE.

Figure 3.3 shows a temporal schematic of the a high powered laser pulse with a leading ASE pedestal. The ratio between the intensity of the main pulse and the pedestal is known as the intensity contrast of the laser. For modern laser systems this contrast can vary between 10^{6-10} [39, 40]. If the peak laser intensity is 10^{20} W/cm^2 with a contrast of 10^8, then the ASE pedestal has an intensity of 10^{12} W/cm^2 which is intense enough to ionise the surface of solid targets, see Chapter 2. This ionisation causes plasma to expand from the front of the target which can change the nature of the interaction, often creating conditions where instabilities can grow such that they cause unpredictable absorption and electron beam pointing due to filamentation [41] or magnetic field growth [42].

3.1.3 Optical Parametric Chirped Pulse Amplification (OPCPA)

Optical Parametric Chirped Pulse Amplification (OPCPA) is similar to CPA as it uses a stretcher to reduce the intensity of the beam prior to amplification before the beam is finally compressed to a short pulse length. The difference in this technique is in the method used to amplify the laser which is known

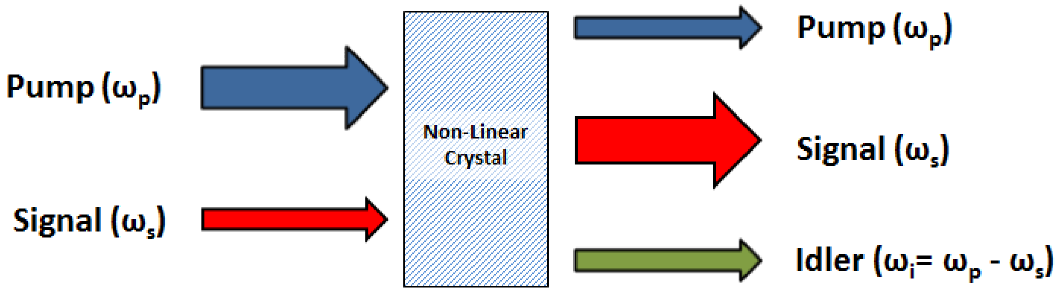

Figure 3.4: Basic schematic of the Optical Parametric Amplification process. The non-linear crystal is used to amplify the signal pulse using the pump pulse. In this process, an idler beam is produced whose frequency is the difference between the frequency of the pump and signal pulses.

as Optical Parametric Amplification (OPA). This technique uses a non-linear crystal and a pump pulse, which has a higher energy and frequency than the main pulse. The pump and main pulse are incident onto the non-linear crystal which parametrically creates a third pulse called the idler. During this process, the pump exchanges energy to both the idler and the main pulse.

There are many advantages to using OPCPA. Firstly, there is no direct interaction between the photons and the non-linear crystal which means there are no dissipative loses into the crystal; ideally this means that thermal effects can be effectively ignored. This potentially allows OPA systems to operate at higher repetition rates. Also, the amplification process only occurs whilst the pump beam is present; if the system is well timed this can effectively lead to a reduction of ASE/fluorescence, increasing the contrast of the laser. The amount of gain provided is also larger per unit volume than traditional techniques. Finally, and probably the most important advantage in terms of reaching the highest peak intensities, is the ability to amplify a number of wavelengths simultaneously whereas for many standalone laser materials only a narrow range of wavelength can be amplified. The minimum pulse length achievable from a pair of gratings is inversely proportional to the bandwidth of the laser chain (i.e. the width that the laser is spectrally); this is known and the bandwidth limit. As OPA systems can have a large bandwidth, it is possible to achieve significant compression to short pulse durations, which leads to high peak intensities.

3.2 Laser Systems

Much of the cutting edge research, especially in the most intense regimes (10^{18-22} W/cm^2), requires increasingly complex systems. This often leads to national/international scale facilities [3, 15, 43, 44, 45] being built to accommodate the high-power laser community; however, more recently university scale systems are becoming more widespread [46, 47, 48].

Current high power laser facilities require scientists and engineers with a wide range of knowledge to meet the numerous challenges encountered high-power laser experiments. The development of novel target fabrication techniques ([49], Chapter 17) is required to create a variety of technically demanding targets. Scientific expertise is required in radiation shielding and safety [50] due to the creation of numerous types of highly energetic particles. Additional shielding is also required due to the presence of large Electro-Magnetic Pulses (EMP) [51, 52]. These are just some examples of the combination of challenges that must be overcome to conduct such experiments.

The experimental work in this thesis has taken place at a number of laser facilities that all have different laser parameters. The aim of this section is to give a brief overview of these facilities, their characteristics and the methods that are used to create some of the most intense laser pulses in the world and the delivered parameters such as energy, wavelength and pulse-duration.

3.2.1 The Vulcan Laser

The Vulcan laser system is based at the Central Laser Facility (CLF)[53]. The main amplification stages of the Vulcan laser uses Nd:YAG which is primarily a

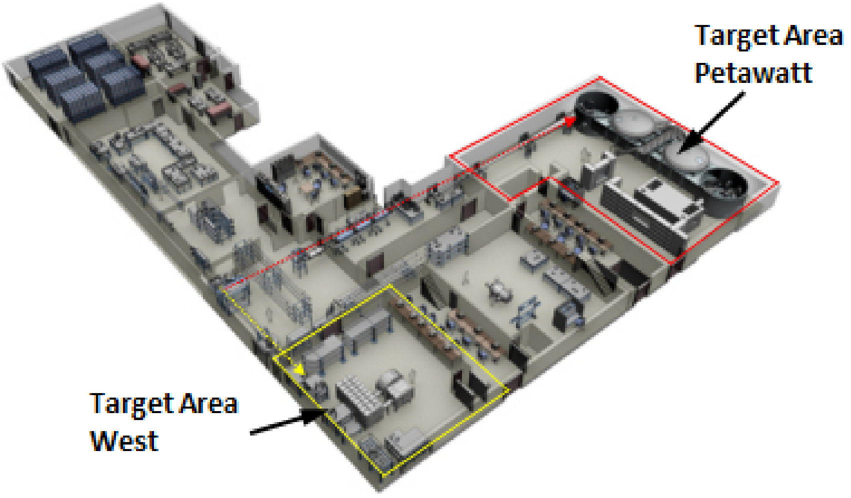

Figure 3.5: An overview layout of the Vulcan Laser. Target Area Petawatt (TAP) and Target Area West (TAW) are highlighted in red and yellow respectively. The dotted lines represent the place where the beam lines between TAP and TAW separate. Prior to this the two beams follow the same path.

4-level gain medium that emits at 1.054 μm and is pumped using flash lamps. Initially, an oscillator feeds a stretcher with 120 fs pulses that are stretched to 4.5 ns. The oscillator uses Ti:Sapphire, as it is able to generate a large bandwidth of frequencies, giving it potential to be compressed to very short pulse lengths. The pulse is then sent to a pre-amplifier that uses OPCPA to deliver pulses of approximately 10 mJ.

The beam is then directed into the main amplification stages, where the energy is increased to 85 J in a beam of diameter 150 mm, before being sent into the final amplification stage that increases the energy to 650 J. Through both of the main amplifier stages, adaptive optics are used to ensure that the wave-front quality remains optimum to keep the focal spot quality high. The beam is also spatially filtered using pinholes, which are usually 10-20 times the diffraction limit. This smooths the beam by eliminating the high frequency components. The exit beam is spatially expanded to 600 mm and finally directed into Target Area Petawatt (TAP) where it is compressed using two 940 mm diameter gratings to 0.7-1 ps. After this process, the laser energy is $\approx$450 J. The laser is focused using an F/3 off-axis parabola to a spot of diameter of $\approx$5 μm. This yields an intensity of

10^{20-21} W/cm^2.

Vulcan has a second operational target area; Target Area West (TAW) [54]. TAW has two main high-power beam lines, 10 ps and 1 ps after compression. The energy delivered into the area is ≈150 J. The two laser pulses are focused using an F/3 off-axis parabola to a focal spot diameter of ≈9 μm. The peak intensity is 10^{19} W/cm^2.

3.2.2 The PHELIX Laser

The PHELIX laser is based at GSI in Darmstadt [55]. The front-end of the laser consists of a commercially available femtosecond oscillator that delivers a 4 nJ, 100 fs pulse, of wavelength 1 μm at 76 MHz. The pulse is stretched to a length of 2.4 ns and amplified using two regenerative amplifiers, made from Ti:Sapphire operating at the repetition rate of 10 Hz. They have an approximate output of 30 mJ. A pre-amplifier further amplifies the pulse using 2 × 19 mm and 1 × 45 mm diameter flash-lamped-pumped Nd:glass rods. The beam is then expanded to 70 mm to keep it below the damage threshold.

The main section of the laser chain is made up of 5 Nd:glass amplifiers; the laser pulse transverses this amplifier section twice. After this point the beams have a diameter of 28 cm, and an approximate total energy of 200 J. The beam is then spatially filtered before being sent into the compressor and the pulse length is reduced to ≈ 0.7 ps. The beam post-compressor contains 75% of the energy, it is then focused by an F/1.5 off-axis parabola to a ≈4 μm focal spot. The peak intensity is 10^{20-21} W/cm^2.

3.2.3 The Astra-Gemini Laser

The Astra-Gemini laser system [56] is based entirely around energy amplification in Ti:Sapphire rather than the Nd:glass. The central wavelength of the light is 800 nm. The three early amplifier-stages deliver approximately 1 J in 35-50 fs to the target area with a rep-rate of 1 Hz. The final stage splits the laser into two; each beam line uses a Ti:Sapphire crystal that is pumped using a Nd:glass based laser that has been frequency doubled to green. These lasers deliver 26 J of laser pump energy to each of the final amplifier, increasing the final laser energy to approximately 20 J. The final pump lasers are capable of firing once every 20 s which limits the repetition-rate of the entire system. The beam is compressed to sub-50 fs before entering the target area. This process is identical for two beams that each deliver 15-20 J laser pulses capable of firing simultaneously.

Both solid target and wakefield based experiments are conducted in the Astra-Gemini target area. In this thesis, the Astra Gemini target area was utilised for laser wakefield acceleration and as such, the focusing optic can either be a long F/20 or F/40, giving a focal spot of 25-35 μm. The final energy in the pulse is much lower than that of Vulcan or PHELIX, however, the shorter achievable pulse length is still able to yield intensities of 10^{19} W/cm^2.

The parameters of the lasers discussed are shown in Table 3.1. Although the laser systems and deliverable parameters have been briefly introduced here, when each laser is applied, the parameters used for each specific experiment will be reiterated.

Laser System	Laser Energy (J)	Wave Length (μm)	Pulse Length (ps)	Focusing Optic	Time Between Shots	Intensity (W/cm^2)
Vulcan (TAP) [53]	600	1.054	0.7	F/3	30 min	10^{20-21}
Vulcan (TAW) [54]	100	1.054	0.7 and 10	F/3	30 min	10^{18-19}
PHELIX [55]	200	1.054	0.6	F/1.5	90 min	10^{20-21}
Astra Gemini [56]	20	0.8	0.040	F/20 or F/40	20 sec	10^{19}

Table 3.1: A summary of the deliverable laser parameters for each laser system discussed

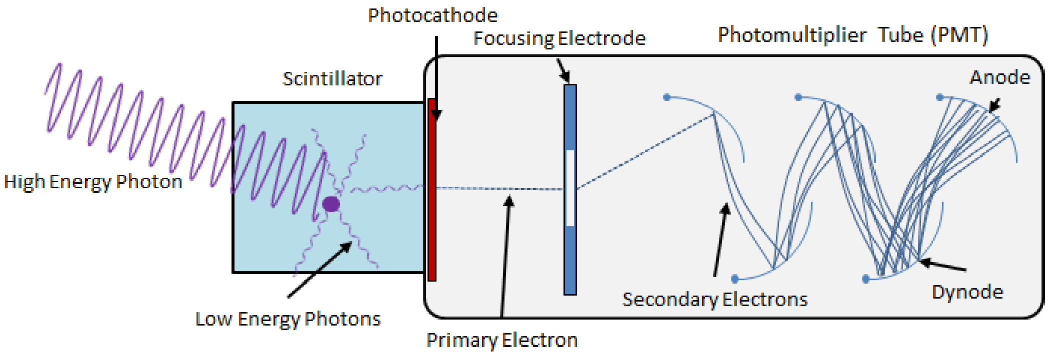

Figure 3.6: Basic Schematic of a photomultiplier tube. A high energy x-ray interacts with the scintillator, creating lower energy photons that convert to electrons in the photocathode. The electron is focused and then strikes the dynode which produces more lower energy electrons; these then accelerate towards the next dynode. The signal is recorded by the anode at the end of the chain.

3.3 Diagnostics

3.3.1 Photomultiplier Tubes

Photomultiplier Tubes (PMTs) are devices capable of detecting high energy particles, typically through secondary optical photon detection. Their basic operation depends on two physical principles; the photoelectric effect and secondary emission. The photoelectric effect occurs on the photocathode at the front of the PMT, as shown in Figure 3.6. The electrons from the cathode are focused towards the first dynode using a focusing electrode. Each dynode is held at a higher voltage (≈100 V) than the previous one. Initially, electrons strike the first dynode producing more low energy electrons which are accelerated towards the second; this process is repeated down a chain of dynodes. At the end the electrons strike an anode that results in a large detectable signal. PMTs, when used for high energy particle detection, are often placed behind a scintillator and used to detect the secondary photons from the ionising radiation.

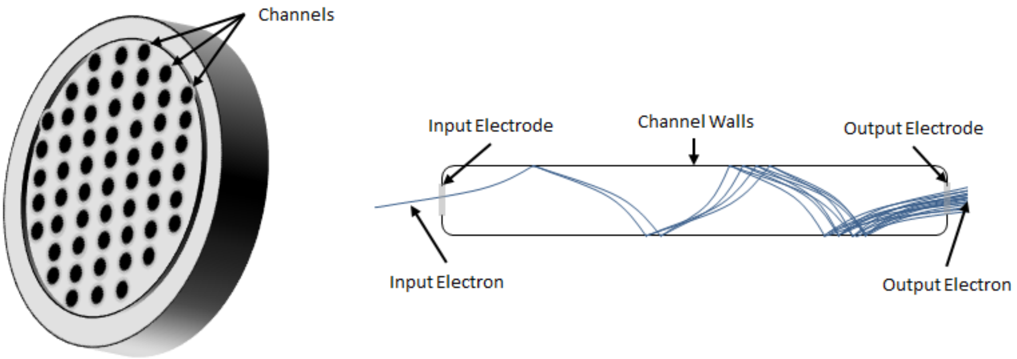

Figure 3.7: A multi-channel plate photomultiplier tube utilises many channels to amplify the electron numbers. The channel has a potential along it and acts similarly to the plates in a PMT.

3.3.1.1 Multi-Channel Plate Photo-Multiplier Tubes

To achieve better temporal resolution, Multi-Channel Plate Photo-Multiplier Tubes (MCP-PMT) can be deployed. The operation of the MCP-PMT is similar to a PMT, however, it consists of many channels that are capable of amplifying electron numbers, as shown in Figure 3.7. This method allows for a compact design that also achieve high-gain and temporal resolution. Current models of MCP-PMTs can achieve temporal resolution on the order of 1/6 nanoseconds.

3.3.2 Ion Diagnostics

The measurement of the ion and proton beams from a laser-plasma interaction is one of the primary diagnostic tools used in understanding the fields present at the rear of the target. These diagnostics complement others discussed later that measure different particles to give a more extensive picture of the entire interaction.

The two diagnostics used to characterise the protons/ions in this thesis are described in this section, the Thomson Parabola spectrometer and the RCF stack.

3.3.2.1 Thomson Parabola

To provide high resolution for spectral analysis of ion/proton beams, a Thomson Parabola can be used [57, 58, 59]. The typical design of a Thomson parabola consists of a magnetic field and electric field that are used to separate ions with different charge to mass ratios, q/m, and velocities. A schematic of the Thomson parabola used in later experiments is shown in Figure 3.8.

Firstly, a pair of magnets are used to deflect particles before an electric field is applied using a pair of charged plates. The deflection from each of these can be calculated from the Lorentz Force, $\mathbf{F} = q(\mathbf{E}+\mathbf{v}\times\mathbf{B})$. The electric field deflection is perpendicular to the deflection from the magnetic fields. The displacement from each plate, $d_{B,y}$ and $d_{E,z}$, for magnetic (B_z) and electric fields (E_z) can be expressed as,

$$d_{B,y} = \frac{q}{m} B_z \frac{L_B^2}{v_x} \tag{3.1}$$

$$d_{E,z} = \frac{q}{m} E_z \frac{L_E^2}{v_x^2} \tag{3.2}$$

where v_x is the x component of the velocity of the ion as it passes through the fields, and L_B and L_E are the lateral lengths of the physcial area where the electric and magnet fields occupy respectively. The ions with the same charge to mass ratio will be deflected such that they follow the same dispersion due to the sum of these two deflecting fields. As slower ions spend longer in each field, the deflection they experience will be greater than higher energy ions/protons that experience the fields for a shorter time.

As shown on the schematic in Figure 3.8, the Thomson parabola requires a pinhole on the front to reduce the beam size. Smaller pinholes lead to better energy resolution but lower flux. The requirement of a pinhole makes the alignment of the Thomson parabola crucial and limits the viewing angle of the diagnostic to a small solid angle. Normally during experiments, a number of Thomson parabolas

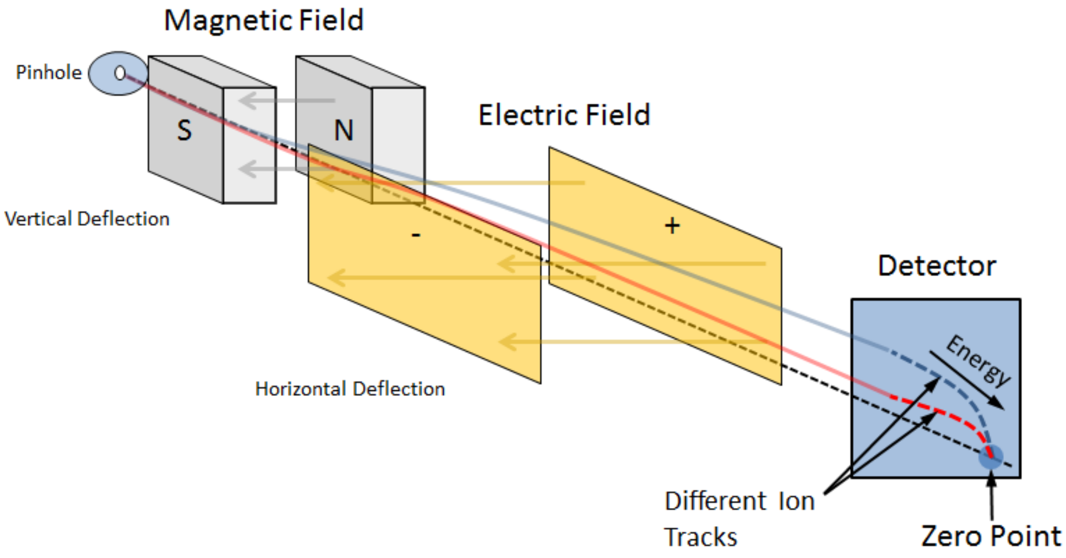

Figure 3.8: Basic schematic of a Thomson parabola. The magnetic field induces a vertical force perpendicular to the magnetic field lines whereas the electric field induces a horizontal force parallel to the electric field lines. Further details of the specific Thomson Parabola used in this thesis can be found in Gwynne *et al* [57]

are deployed simultaneously to provide ion/proton spectra at different angles.

3.3.2.2 Radiochromic Film (RCF)

Radiochromic film (RCF) stacks can be used to provide the spatial and spectral characteristics of the accelerated ion beam. The film contains an active layer that reacts when exposed to ionising radiation. This leads to a darkening of the film that is related to the dose deposited in the active layer. An exposed RCF is scanned using a flat-bed scanner where the data is digitised into 16 bit Red, Green and Blue (RGB) channels. Each colour has a different opacity relationship as a function of dose deposited in the active layer. Where each channel is most sensitive (when there is the largest change in dose), that channel is used to diagnose the dose.

There are many different types of RCF film. However, only HDV2 was used in this thesis. HDV2 consists of two layers: an 8 μm active layer and a 97μm supporting substrate at the rear that is transparent.

Protons and other ions have a well understood deposition curves in materials. This is described using the Bethe-Bloch relationship,

$$\frac{dE}{dx} = \frac{4\pi e^4}{m_i v_i^2(x)} q^2 Z_{targ} \ln\left(\frac{m_i v_i^3(x)}{q e^2 \omega_e}\right) \tag{3.3}$$

where Z_{targ} is the atomic number of the target/material that the proton/ion is propagating through and ω_e is the electron orbital frequency about the ion. The stopping is initially continuous, however as the ion/proton loses energy the velocity will drop which will lead to greater energy loss. This effect leads to the proton rapidly losing lots of energy and then suddenly stopping. This effect results in what is known as a Bragg peak and is a characteristic feature of proton/ion stopping in materials.

To utilise this property of ion/proton stopping, RCF is layered in an array with filter material between each layer. The layers of RCF then are effectively only sensitive to protons above a threshold energy. This allows for easy extraction of the maximum proton energy using an RCF stack [60]. The RCF stack is usually sufficiently large to record the angular profile of the emitted protons.

To accurately calculate the energies in an RCF stack, SRIM [61] (Stopping Ranges In Matter), a Monte Carlo based code, is used to model the penetration of ions/protons and then find the energies which the Bragg peak falls in the active layer of the RCF. An example of a stack design is shown in Figure 3.9 with the Bragg peaks modelled using SRIM to find the threshold energies.

To enable an RCF stack to be used in conjunction with a Thompson Parabola, which requires a clean a line of sight to the target, modifications must be made to the RCF stack. This can be achieved by using two smaller RCF stacks with a gap in the middle or a stack with a hole in the middle. Using both techniques at the same time to measure the proton spectra and beam profile is advantageous

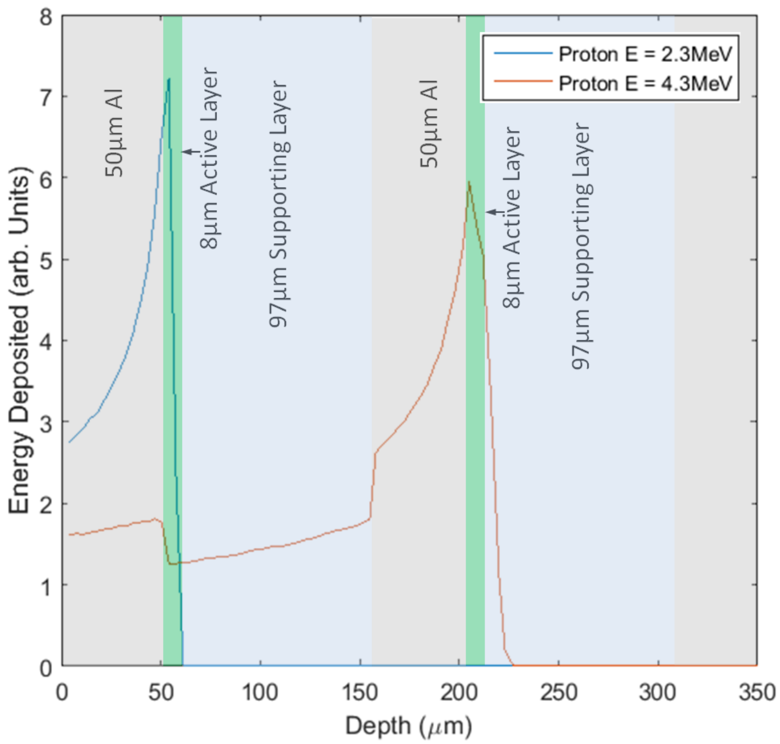

Figure 3.9: Example of an output from SRIM for an RCF stack with HDV2 film in-between layers of aluminium filtering. The two energies shown have Bragg peaks that fall inside the active layer; this technique is used to build the response function of stacks with many layers.

when attempting to measure its properties.

To deconvolve the proton spectra SRIM can be used to produce a response curve for each layer of the RCF stack. From here there are two methods to deconvolve the spectrum. Firstly, a simple thermal spectrum can be assumed and fitted to the data. This method is quick however but lacks the ability to resolve spectral features. The second method also requires a response function for each layer of the RCF stack. The process of deconvolution first calculates the energy deposited on the final layer of the RCF stack that has visible signal. The energy of the protons that reach this layer is known as well as the energy that these protons deposit in the layers before; this energy is then subtracted from the earlier layers. This is then repeated for the second last layer, and so on. To achieve accurate results using this method a good response function must be acquired and the RCF must have adequate spectral resolution which requires more layers of RCF in the stack.

3.4 Simulations

The act of making measurements is only half the task; the key is explaining the results and understanding the underlying physics otherwise the measurements are meaningless. However, explaining the processes of sub-picosecond interactions of trillions of particles using what are often time integrated diagnostics is difficult. Analytical models can be used to help in the understanding of some problems. However, the number of parameters to consider are often large; this can make accurate analytical solutions different to obtain. The alternative method is numerical modelling/simulations. Two distinct methods of numerical modelling, each with its own merits and operational limitation, are discussed in the following section.

3.4.1 Monte-Carlo Simulations

Monte Carlo methods use a random sampling of a system, repeating until the average statistical behaviour of the system can be approximated. The benefits of using multiple particles to gain statistical results is ideal for many areas of physics; particularly for particle physics.

GEANT4 is a Monte Carlo based toolkit that is capable of simulating a wide range of different physical models as well as comprehensive geometry and tracking methods [62]. GEANT4 was developed as an object-oriented simulation program by CERN and many other collaborators. The first release of GEANT4 came in 1998 and is now used by a wide range of scientists around the world.

At the beginning of a typical GEANT4 simulation a particle is created with a given energy, direction and location and allowed to propagate into the system/

geometry. The particle is assigned a random number which will differentiate it from other initial particles and therefore determine its unique interactions with the system through various physical process. The physical interactions that the particle will undergo are determined by the transport data of the particular material that it is travelling through. This data is usually created using extensive theoretical and experimental models. The initial particle may create secondary or tertiary particles or radiation during its path, these are all simulated in turn. Once all the kinetic energy in the system is equal to zero, including the all daughter/secondary particles, a new particle is created with a different random number and the process is repeated.

The Monte Carlo method has limitations. The single particle nature of Monte Carlo based simulations neglect how each particle interacts with one another. It is therefore better at examining situations where collective effects can be ignored such as particle interactions with bulk materials. In GEANT4, these include electron transport effect, such as those discussed in 2.5, or high temperature opacity of solid targets.

GEANT4 has the capability of simulating many different physical interactions ranging from hadronic, electromagnetic processes [63, 64, 65] or neutron transport [62]. It comes with a complete set of electromagnetic models that are capable of operating in many different energy regions. GEANT4 will be used throughout this thesis for a variety of problems such as creating x-ray spectra from electrons travelling through solid targets, measuring particle absorption and calculating electron stopping ranges in number of different materials.

As stated earlier, Monte Carlo simulations require repetition before the statistical nature of the system being analysed to converge. To test the number of times the particle needs to be input (in GEANT4 this is known as an event), a simple simulation was conducted.

The simulation was setup similar to the investigations conducted in Chapter 4

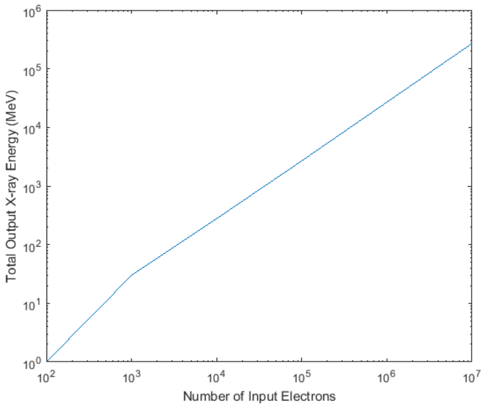

Figure 3.10: The total x-ray energy emitted from a solid target for different input electron numbers. The simulation begins to converge above 10^3 input particles.

with an electron spectra incident onto a solid target of copper. The simulation was conducted multiple times with different input particle numbers. The total x-rays emitted from the rear of this target as a function of input electron number is shown in Figure 3.10; this shows that the energy of the x-rays converge above 10^3 events. Most simulations in this thesis, although pocessing different geometries, will be conducted with more many more orders of magnitude events as Monte Carlo simulations are fairly inexpensive computationally. .

3.4.2 Particle In Cell Simulations

Particle In Cell (PIC) codes are designed to solve the dynamics of plasmas using a kinetic approach. In an ideal case, a fully described kinetic approach would be solved using the Fokker-Planck equation that describes the distribution function, $f_{VFP}(r, p, t)$, for each species,

$$\frac{\partial f_{VFP}}{\partial t} + \mathbf{v}\frac{\partial f_{VFP}}{\partial x} + q(\mathbf{E} + \mathbf{v} \times \mathbf{B})\frac{\partial f_{VFP}}{\partial \mathbf{p}} = C(f) \tag{3.4}$$

where $C(f)$ is the collision term. Normally when considering laser plasmas, the ionisation rate is fixed and the plasma is assumed to be collisionless yielding the Vlasov equation. Solving the Vlasov equation in six-dimensions (three space and three momentum) is very difficult. Instead, PIC codes solve this by treating a number of real particles as a weighted macroparticle which approximates the distribution of the real particles. These macroparticles have the same charge to mass ratio as the particles that they represent. The fields in a PIC code are fixed to a grid and the points in between are interpolated whilst the macroparticles are free to move between the grid cells.

The basic algorithm of PIC codes follows 4 principle steps;

1. **Particle Push**; the forces applied to the particles by the fields move the positions and the momenta is updated.
2. **Particles to Grid**; current, charge and particle densities are calculated, these must be interpolated to the grid.
3. **Field Calculations**; Maxwells equations are solved using the values calculated from the previous step.
4. **Fields to Particles**; the newly calculated fields are interpolated back to the particles.

This process is looped until the end of the simulation.

One of the prevalent issues with PIC codes is self-heating. The finite number of macroparticles defined in the simulation leads to errors in the calculation of the current density. These in turn leads to ‘noise’ electro-magnetic fields, which becomes a particle scatterer inside the simulation, leading to an artificial heating of the population of macro-particles. To mitigate this issue, more particles or third-order particle shape can be used; however, both of these are more computationally expensive. Another issue with PIC codes is that they do not simulate all the known physics that are present in laser plasma interactions.

In the case of this thesis the PIC code EPOCH was used [66]. There are other PIC codes available that are used to simulate laser-plasma interactions; EPOCH is purposely different by being released open-source. This allows for modification and developments to be made by the community.

Simulations using EPOCH can be conducted in 1D, 2D or 3D; becoming more computationally expensive as more dimensions are added. It also has the ability to be parallelised across many CPUs which allows for the simulations to be operated on CPU-clusters which will speed up the overall simulation time. For example, a 2D simulation with 6875×3000 cells and 30 particles per cell will take approximately 24 hours to run on 100 cores. In this work, EPOCH is used with sufficient but not excessive computational resources. In each case where simulation is presented in the thesis, the configuration of the simulation will be summarised.

The simulations in this thesis were conducted on the Science and Technology Facilities Councils (STFC) CPU cluster known as SCARF (Scientific Computing Application Resource for Facilities).

The output from EPOCH is very flexible and allows for extensive analysis of the simulation results. The variables that can be output include basics such as the momentum and electric fields, to more complex information such as the absorption of laser energy. A typical file from the output of a simulation at a given time can be many gigabytes; although it is also possible to output each variable separately and at different time steps which can help to reduce the file size. The analysis of the results is conducted in MATLAB which is ideal for handling the large arrays output by the simulation.

3.5 Diagnostic Developments

Diagnostic developments have been made by the author. This includes new diagnostics as well as improving the understanding of other diagnostics that have previously been used on laser-plasma experiments. Only diagnostics relevant to this thesis are included in this section.

3.5.1 Cameras

Cameras are used in a large number of diagnostics on laser-plasma experiments, such as interferometers, shadowgraphy, electron spectrometers, reflectivity monitors etc. Modern digital camera technology is rapidly advancing with EMCCD and deep-cooled CMOS sensors enabling such application as single photon counting. One of the key aspects of a scientific camera is to have a system with a large dynamic range; the difference between the brightest and darkest measurable features. This allows for images to be recorded of the dimmest features whilst not being saturated by others that are often present in high intensity laser interactions.

It is important to know the performance of each camera before deciding which to use. A linearity test was performed using Neutral Density (ND) filters and a uniform light source to determine the dynamic range and operation at low light levels. A number of different cameras available at the CLF were tested, the results are shown in Figure 3.11. The standard deviation of the cameras is determined by calculating the variability over a fixed area of the signal, the same area of the singal that the average is recorded from. The Andor Neo CMOS and Ixon EMCCD have the largest dynamic ranges of the cameras tested which make them ideal for most cases where practical limitation allow.

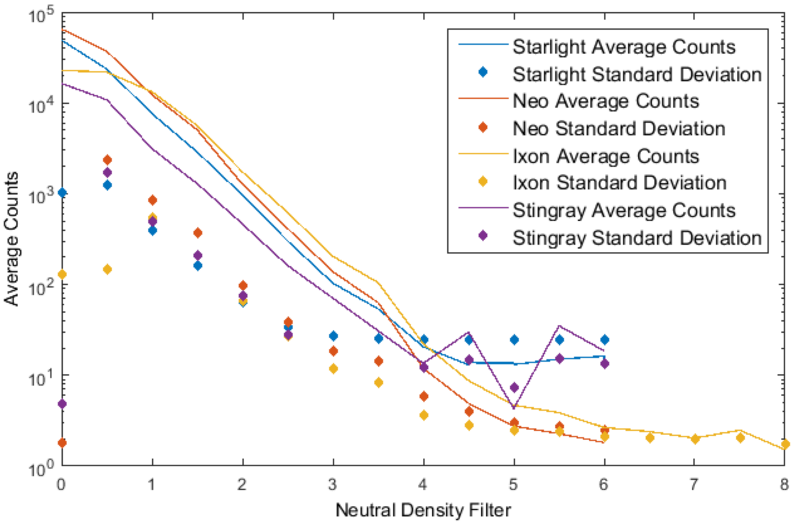

Figure 3.11: Linearity and dynamic ranges of the selection of cameras at the Central Laser Facility. The lines represent the average signal and the diamonds standard deviation of that signal. When the standard deviation is equal to or greater than the signal level, the average counts line flatten off. This indicates that the signal is close to the noise lower level.

3.5.2 Scintillator Based X-ray Spectrometer

One of the simplest and most common techniques for observing the harder thermal spectrum of x-rays is to use an absorption based spectrometer [67, 68] because high density filters will stop x-ray energies up to hundreds of keV which are easily achievable from high-power laser-solid interactions. Another reason such diagnostics are simple to use is because of the ease of calculating the response curves, which will be discussed later. The limitation of current absorption spectrometers is processing time and sensitivity. With new laser systems being developed that promise faster repetition, a spectrometer with lower processing times needs to be developed. From the temperature of the x-ray spectrum, the temperature of the hot electron population can be inferred. There are other x-ray diagnostics that can be used to infer the electron temperature, such as k-alpha emission[69].

A spectrometer that can operate on these new laser systems would require a novel method of detection and x-ray attenuation to provide good spectral resolution.

Scintillators are materials that absorb a high energy photon, which typically produces an electron through the photoelectric effect. This electron collides with many more atoms, exchanging energy with their electrons, exciting them to a higher energy level. The electrons decay to a lower state before finally decaying to the ground state emitting a lower energy photon than initially absorbed. The conversion of high energy photons to lower-energy/optical photons is known as a Stoke Shift. There are two main types of scintillators; organic and in-organic. The internal decay that occurs whilst the electron is in the initial excited state is different for these types of scintillators. Inorganic scintillators have crystal impurities called activators. These activators create sites in which the electron can de-excite before falling back to the valence band. The mechanism in an organic scintillator comes from the internal transition between energy levels in a single molecule. The electron decays from the excited state before transiting to the ground state. The electron can decay via a triplet state which has a longer lifetime.

The decay times of the energy states varies depending on the chosen scintillator; from hundreds of nanoseconds to sub nanosecond. The decay times are currently thousands of times quicker than the repetition rate of current high power laser systems which means this should not factor in the choice of scintillator.

The scintillators can be placed in a 1D array such that they attenuate the incident x-rays as they scintillate. The optical light emitted is imaged and the energy deposited in the scintillators can be measured. A simple schematic of the system is shown in Figure 3.12. Current absorption spectrometers use high density materials to filter the x-rays recorded by the active material. Using an array of scintillator will make the scintillator both the filter and active material. This will allow the diagnostic to utilise more of the x-rays that pass through it. The flexibility of scintillator choice and arrangement means that the spectrometer can be used on a variety of experiments.

Two designs are presented in this section; one for higher energy x-rays from solid

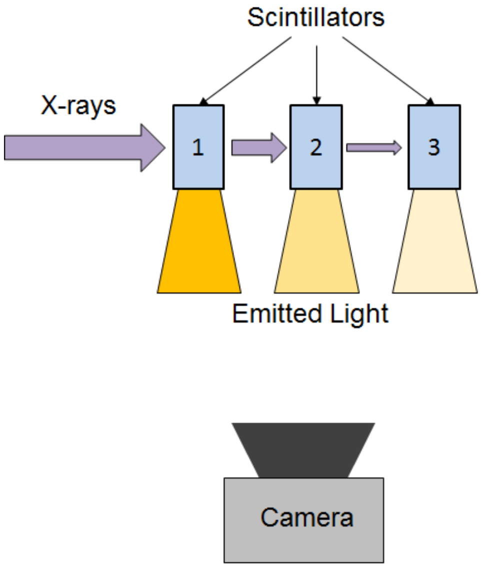

Figure 3.12: A basic schematic of the scintillator based absorption spectrometer. The x-rays pass through the scintillators and lose energy; they reach the next scintillator with less energy than the previously. This will lead to a fall in light from the first to the last scintillator. The light is then imaged using a camera and lens system.

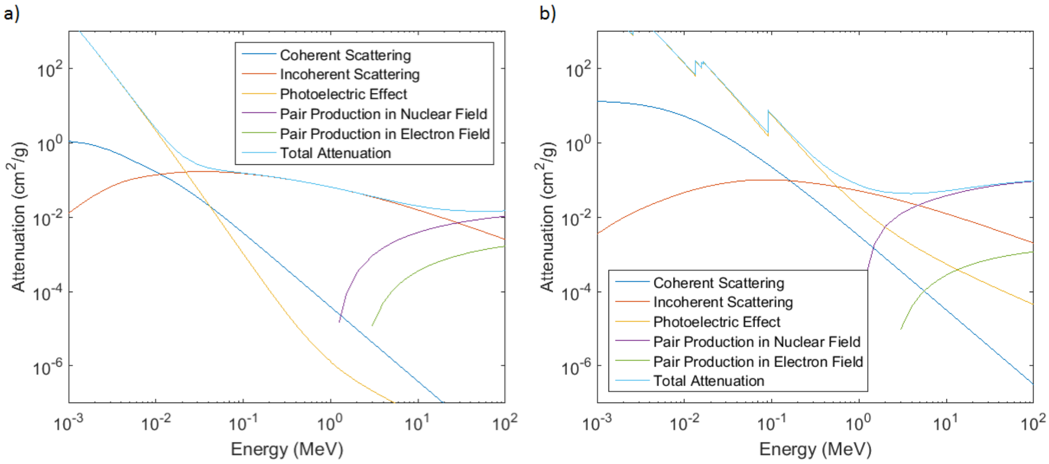

Figure 3.13: Attenuation curves for a) carbon and b) bismuth.

targets and one specifically for betatron x-rays which will have results demonstrating the retrieval of the input spectral shape.

3.5.2.1 High Energy Design

Attenuation curves for a) bismuth and b) carbon are shown in Figure 3.13. These are split into all the effects that sum to the total attenuation. Attenuation from pair production in the presence of an atom and the photoelectric effect are both proportional to the atomic number (Z) of the element, which is clear from the differences of bismuth and carbon in Figure 3.13. Figure 3.14 compares two scintillator materials, BGO and BC422q, that differ in Z and as such possess different X-ray attenuation curves. Bismuth Germinate (BGO) is a high Z and density (7.13 g/cm^3) crystal which has a high attenuation and also a high light output (8000 photons/MeV). BC422q is a plastic scintillator which possesses very good temporal resolution with a density of 1.032 g/cm^3. The chemical composition of BC422q is HC, with ratio of 1.1 between the hydrogen and carbon atoms. The ‘q’ stands for quenching, which refers to a technique used to decrease the temporal response at the same time sacrificeing the light yeild of the scintillator. It is also doped with Benzophenone which reduces rise time and pulse width of the light emitted but also reduces the light yield. For the doping which was used (0.5%) the light yield is ≈3300 photons/MeV. Using a combination of these two scintillators in an array yields the benefits of both of these attenuation curves (which will be demonstrated when calculating the absorption response of a spectrometer in the next section).

To calculate the response of an absorption spectrometer the NIST XCOM [70] attenuation tables can be used, however they only provide the one-dimension attenuation cross-section of a material. Neglecting scattering inside the scintillator which will occur at energies greater than 100 keV will have a major effect on the response of the spectrometer.

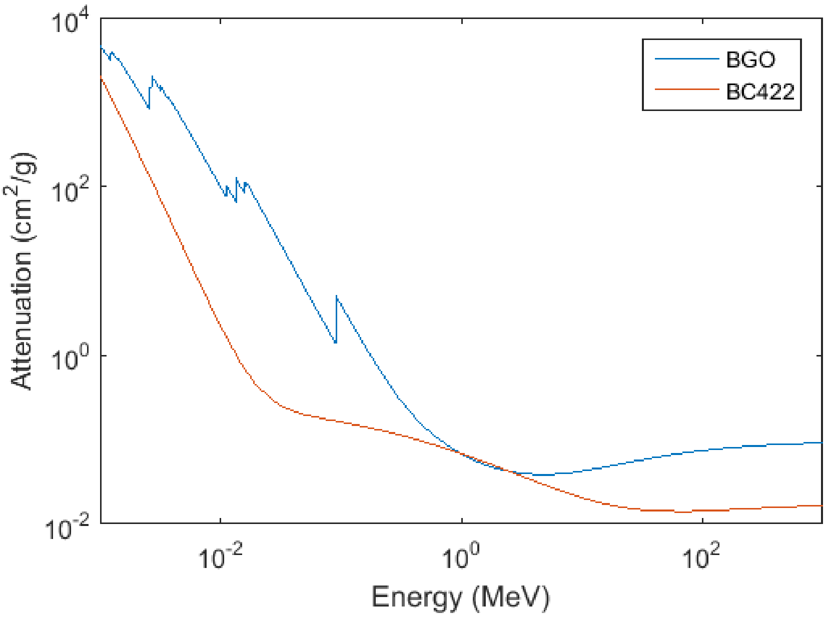

Figure 3.14: Attenuation curves provided by NIST XCOM [70] for two scintillator materials; BGO and BC422q, which are examples of high-Z and low-Z scintiallor materials respectively.

3.5.2.2 High Energy Design - Geant4 Analysis

GEANT4 can be used to calculate the absorption whilst taking into account all scattering effects and secondary particles created by the photoelectric effect, Compton scattering and pair production. A design using an alternating array of BGO and BC422q layers was chosen as the arrangement.

The thicknesses of the two scintillators were chosen such that the mass density for each scintillator was similar so that each scintillator absorbed approximately the same amount of x-rays at 1 MeV. This can be calculated by equating the Beer-Lambert equation for each scintillator,

$$T = e^{-\rho l \sigma(E)} \tag{3.5}$$

$$e^{\left(\rho_{\mathrm{BGO}} l_{\mathrm{BGO}} \sigma_{(BGO,1MeV)}\right)} \approx e^{\left(\rho_{\mathrm{BC422q}} l_{\mathrm{BC422q}} \sigma_{(BC422q,1MeV)}\right)} \tag{3.6}$$

Where $\rho_{\mathrm{B}GO}$ and $\rho_{\mathrm{B}C422q}$ are the densities, $l_{\mathrm{B}GO}$ and $l_{\mathrm{B}C422q}$ are the length and $\sigma_{(BGO,1MeV)}$ and $\sigma_{(BGO,1MeV)}$ are the attenuation of the BGO and BC422q at 1 MeV respectively. The attenuation of both of these materials are very similar at 1 MeV, which can be seen from Figure 3.14 and the mass density of both materials is known, the equation can be simplified to,

$$\frac{\rho_{\mathrm{B}GO}}{\rho_{\mathrm{B}C422q}} = \frac{l_{\mathrm{B}C422q}}{l_{\mathrm{B}GO}} \approx 6 \tag{3.7}$$

This means that the BC422q layer should be 6 times thicker than the BGO layer to ensure the absorption is approximately the same in both types of scintillators. The height and width of the scintillators are 30×12 mm.

The GEANT4 simulations were ran mainly with 10^6 mono energetic x-rays from 1 keV to 100 MeV with a number of different initial energies; the number of particles is mainly limited by the output file size from GEANT4. Additionally, simluations at lower energies were conducted with 10^7 to gain more statistics and as these files are much smaller. From each run the location of the energy deposition was recorded so that the fractional energy absorption could be calculated. The response curves of each of the layers from the simulations are shown in Figure 3.15. The BGO response peaks sharply for the layers 1-4 and then flattens off. The BC422q response, largely unaffected by pair production due to its low Z number, falls in the high energy region. This is helped by the BGO absorbing better in this region. Observing the electron tracks via a visual output, as shown in Figure 3.16, the importance of the scattering effects is demonstrated. Inside the BGO the ionized electrons travel much shorter paths than inside the BC422q; this will lead to energy being lost in the BC422q via scattering.

A significant drop off in the response in the first layers of BC422q is also observed, meaning for certain energies it will be dimmer than the second layer. Scattering effects, such as Compton scattering, through the layers of the array cause the x-rays to down-shift to lower energies which are more likely to be absorbed. The x-rays incident on the first layer of BC422q will not be down-shifted and are

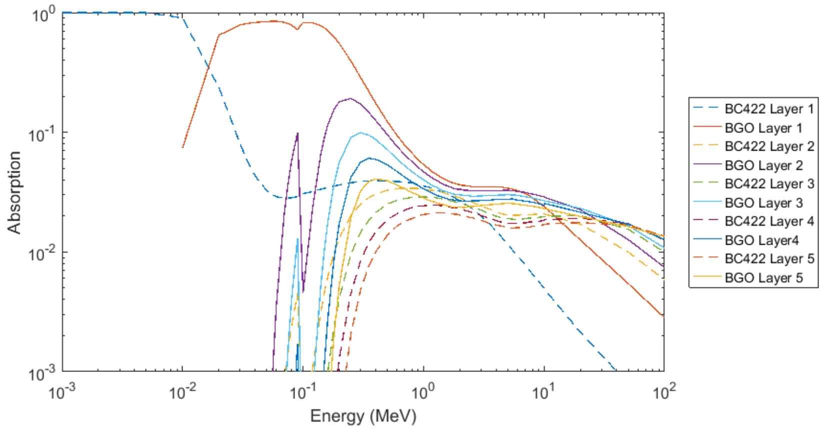

Figure 3.15: Response curve generated from energy deposited in each scintillator layer using GEANT4.

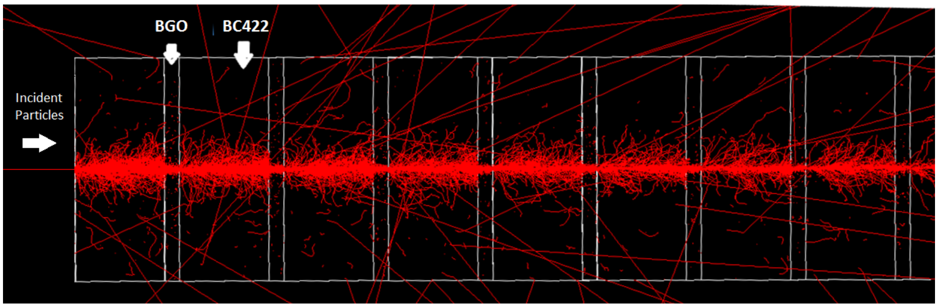

Figure 3.16: Visual output of electrons inside the scintillator layers for 10,000 2 MeV incident photons. The electrons can escape from the BC422q layers as the attenuation outside the propagation direction is much lower than that of BGO.

therefore less likely to be absorbed. The spectra leaving the first layer of BGO and the first layer of BC422q from the same array is shown in Figure 3.17 where this down-shift is apparent.

Initial tests were carried out by deploying the scintillator array as designed above on a high intensity ($\approx 10^{18}$ W/cm^2) solid target experiment in Target Area Petawatt. The beam was diameter was limited (apodised) whilst still at large diameter (reducing from 60 cm to 30 cm), to regulate the energy to ~50 J. The size of the focal spot was changed to perform a focal scan to reduce the temperature of the Bremsstrahlung spectrum by reducing intensity of the incident laser whilst keeping the absorbed energy high. This was conducted on a 100 μm Ta target. The results from the average counts from the first three layers of BC422q and

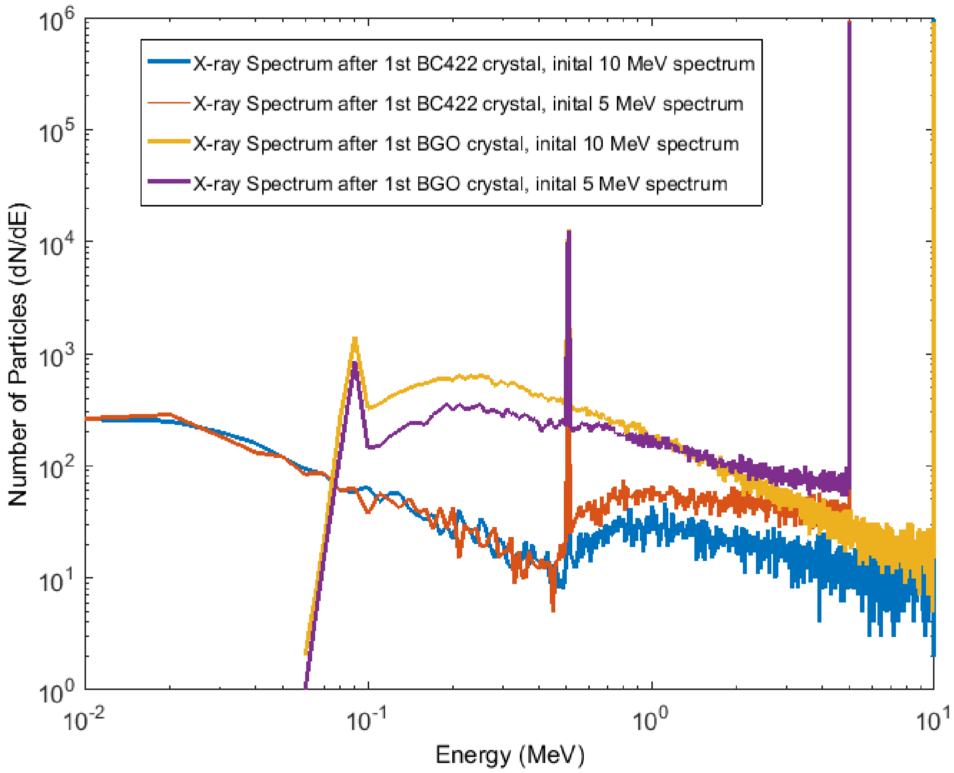

Figure 3.17: Spectra of x-rays entering different layers of scintillators. This highlights the effect that the previous layer has on sequential layers. By down shifting the mono-energetic spectra to lower energies the likelihood of photoelectric absorption increases.

BGO are shown in Figure 3.18. The first two layers of BC422q for the infocus shot appear to have a high flux and do not have similar shapes to the other lower intensity shots. What is also apparent is the BGO data all have very similar shapes for all foci. This could be explained if there was a high flux of lower energy x-rays on the in-focus shot, however this should also be observed in the BGO layer. Also, the output of the BGO layer for this shot is much lower than the 100 μm defocus shot. For this to occur, a secondary source of radiation must be incident onto the array. The main difference between the two scintillators is the chemical composition; BGO contains heavier elements compared to BC422q. Although the attenuation of x-rays, and electrons, is mostly proportional to the atomic-number and density of the material, the attenuation/absorption of neutrons has a very different dependence. Table 3.2 shows the cross section for the

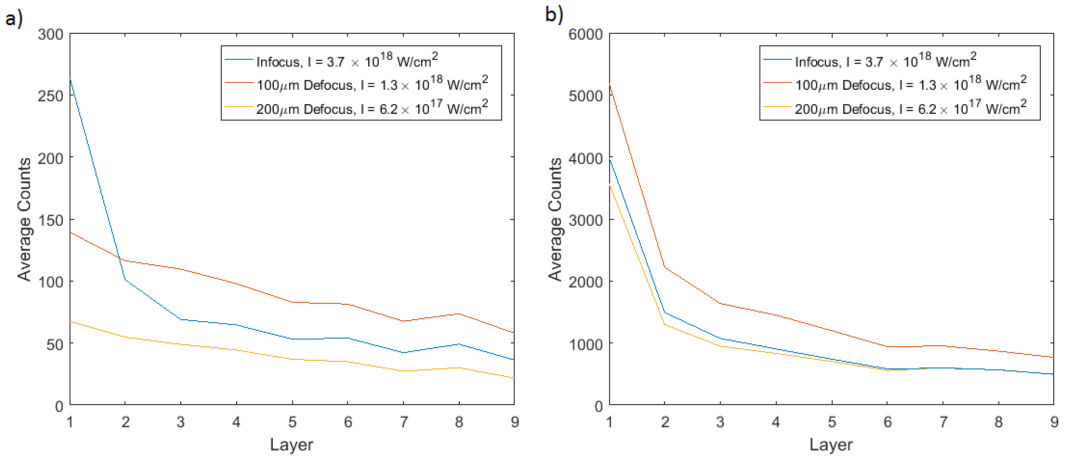

Figure 3.18: The average counts measured on a) the BC422q and b) BGO for three different incident laser intensities. The high flux of the first two layers BC422q for the in-focus, high-intensity shot is not replicated on the BGO layer that is in between. This suggests that BC422q is sensitive to a secondary source that BGO is not.

elements inside the scintillator array. The cross section is highest for hydrogen; this will increase the absorption of neutrons for BC422q as it is ≈50% hydrogen. Using the NIST Centre for Neutron Research calculator, the transmission of each object can be estimated. For BGO the transmission of 1MeV neutrons is 99.9% whereas for BC422q the transmission is very low at 0.87%. This means that any neutrons present from a shot are very likely to be only observed by the BC422 layers and not the BGO layers.

Neutrons are created through nuclear activation on solid target experiments. However, this can be from proton or gamma/x-ray induced reactions, as breifly discussed in Chapter 2. The data from Figure 3.18 a) with the highest flux on the BC422q is also the shot at the highest intensity (3.7×10^{18} W/cm^2). The number of higher energy x-rays capable of inducing photon-nuclear reactions will increase with higher incident laser intensity.

A second test was conducted to eliminate any neutron scintillation; this is described in the following section.

3.5.2.3 Characterisation of Betatron Radiation

A betatron x-ray source was chosen to test the capabilities of the spectrometer as it is highly directional and the interaction is not a direct source of neutrons. Betatron x-rays arise from electron oscillations during laser wakefield acceleration [71, 72] and generally peak at lower energies (< 80 keV) in comparison to Bremsstrahlung x-rays from solid target interaction. It will therefore require a different arrangement of scintillators to properly characterise these x-rays. EJ-208, a plastic scintillator very similar to BC422q, was chosen as it has much higher light yield (9200 photons/1 MeV electrons). Each scintillator is cut to the size of 12×30×5 mm, where 5 mm is the thickness of the scintillator in the attenuation axis. The absorption as a function of energy of the design created from GEANT4 simulations is shown in Figure 3.19.

The intensity of a betatron angular spectrum [72, 73] is,

$$\frac{d^2 I_B}{d\Omega d\theta_B} = \frac{\gamma^2 \xi_B^2}{1+\gamma^2\theta_B^2}\left[K_{2/3}^2\left(\xi_B\right) + \frac{\gamma^2\xi^2}{1+\gamma^2\theta_B^2}K_{1/3}^2(\xi_B)\right] \tag{3.8}$$

where θ_B is the angle away from the axis and $K_{2/3}^2$ and $K_{1/3}^2$ are modified Bessel functions. $\xi_B = (E/E_c)(1+\gamma^2\theta^2)^{3/2}$, where E_c is the critical energy, which is described as the point at which half the energy is above and below and dictates the shape of the spectrum. A prediction for the normalised output can be made

Element	Bound Coherent Scattering (barns)	Bound Incoherent Scattering (barns)	Total Bound Scattering (barns)
H	1.7568	80.26	82.02
C	5.551	0.001	5.551
Bi	9.148	0.0084	9.156
O	4.232	0.0008	4.232
Ge	8.42	0.18	8.6

Table 3.2: Neutron coherent and incoherent scattering cross sections for elements in the scintillator array. The element with the highest total cross section is hydrogen.

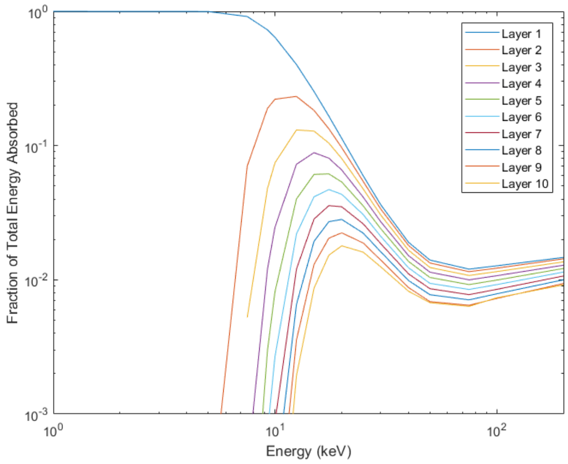

Figure 3.19: Fractional absorption as a function of energy for the scintillator based spectrometer designed for detecting betatrons x-rays using layers EJ208.

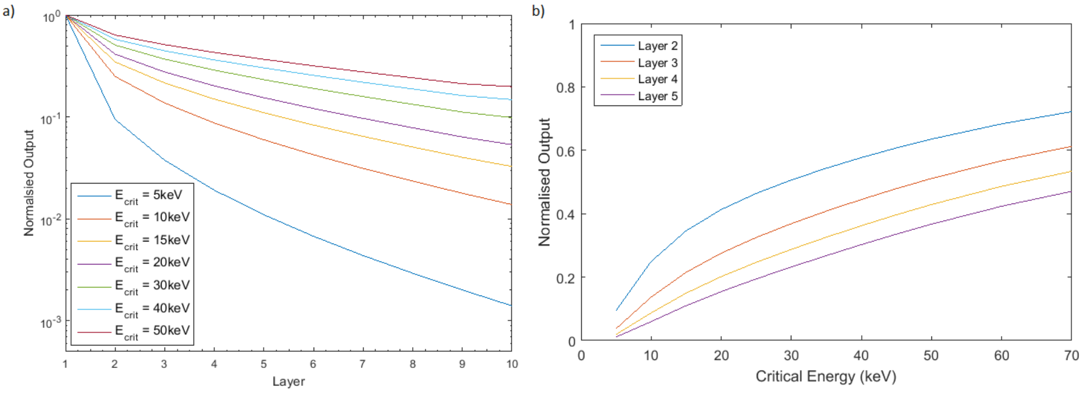

Figure 3.20: a) The simulated normalised output when combining the response curves from GEANT4, Figure 3.19, and the equation for the betatron spectrum. b) The response for each layer as a function of the critical energy.

by multiplying the betatron spectra given by the equation above and the response curve from GEANT4 shown in Figure 3.19. The normalised outputs are shown in Figure 3.20. As the critical energy increases, the curves get closer together/the gradient become shallower and therefore harder to distinguish. To further demonstrate this, the normalised output for layers 2 to 5 against the critical energy is shown in Figure 3.20 b), which again shows that for increasing critical energy the gradients become shallower.

The betatron x-rays were created on an experiment on the Astra-Gemini Laser

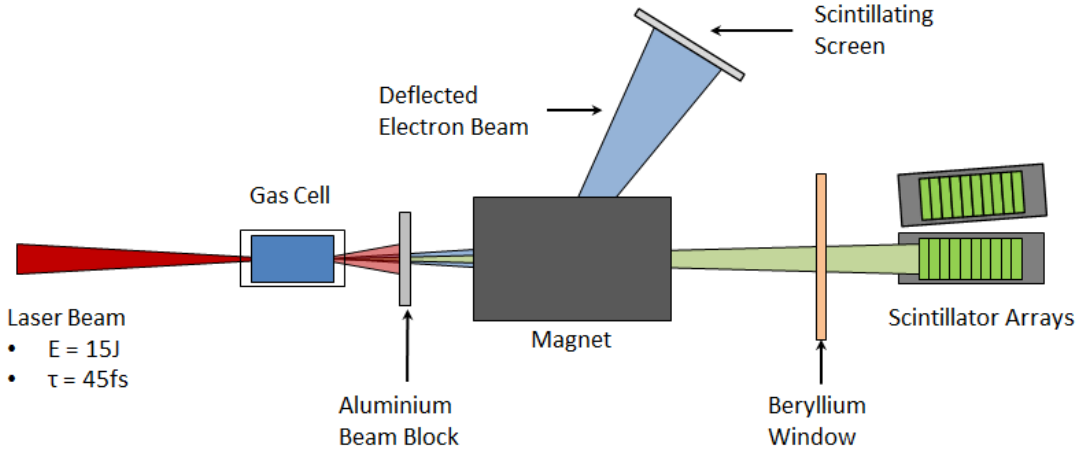

Figure 3.21: The basic experimental layout for creating betatron x-rays. The laser beam is focused into the gas cell where electrons are accelerated and betatron x-rays are produced. The depleted laser beam is blocked by aluminium foil. The electrons are deflected away using a magnet and the spectrum is recorded on a lanex screen above. The x-rays propagate out from the chamber onto the array of scintillators.

which delivered up to 15 J of 800 nm radiation at a pulse length of approximately 45 fs. The beam was focused using an F-40 parabola onto a gas cell with an elliptical focal spot size of (43±9) μm by (39±8) μm. The laser is capable of firing once every 20 seconds. The gas cell is used to control the length and density of the gas used in the interaction.

An experimental layout is shown in Figure 3.21. The betatron x-rays exit the vacuum chamber through a 250 μm thick Kapton window to minimise attenuation. The x-rays are then recorded on the scintillator based spectrometer. A second spectrometer is mounted above to monitor the background/Bremsstrahlung x-rays coming from the target chamber. Each spectrometer is housed inside lead (50 mm in all directions except the rear). Additional scintillators are placed inside the lead to monitor any harder x-rays that penetrate the shielding. The arrays were imaged using Andor Neo CMOS due to its high dynamic range. The gas cell pressure was modified in order to investigate the characteristics of the betatron x-rays.

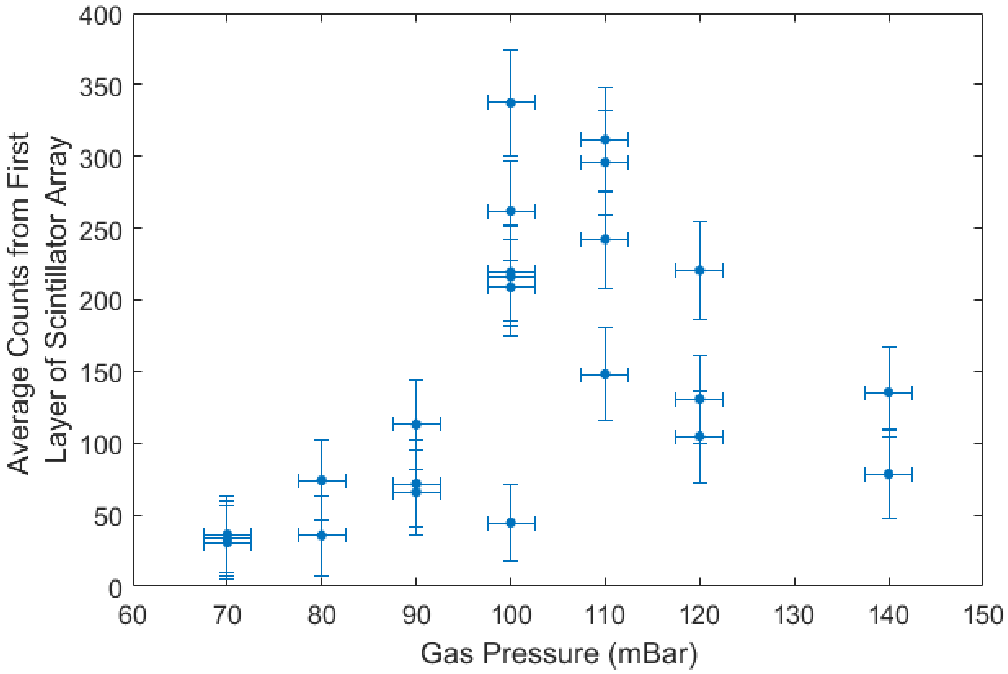

Figure 3.22: The signal recorded on the first layer of EJ208 as a function of gas cell pressure. The flux peaks at a pressure of 100mBar and falls for higher pressure.

The Helium gas pressure inside the gas cell was varied from 60 mBar to 140 mBar, changing the electron density. A background has been measured from scintillators that are placed within the lead shielding that will only see x-rays energetic enough to penetrate 50 mm of lead. A second background was subtracted using the array mounted above which measured the x-ray signal from the chamber. The uncertainty from the measurements comes from the background subtraction and the single pixel error of the cameras. For the data with the highest flux, this uncertainty has the smallest effect. The brightness of the first layer of the scintillator is plotted in Figure 3.22 which peaks between pressures of 100 and 110 mBar. Although one shot at 100 mBar has very low flux, this is likely due to an anomaly observed in the electron beam. As a result, the critical energy is extracted from data from these pressures. The data shown in Figure 3.23 is a shot taken at 100 mBar plotted with error bars from the uncertainties discussed above and the expected outputs of the data from multiplying the spectrum calculated from equation 3.8 by the response curves from GEANT4, as shown in

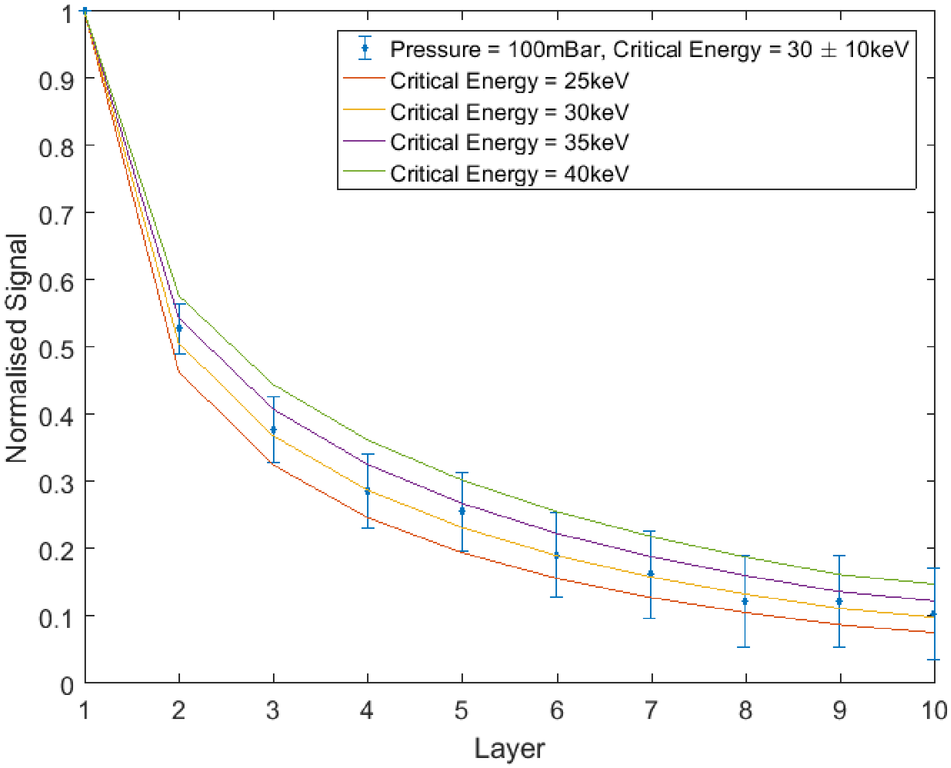

Figure 3.23: The normalised signal from a shot at 100 mBar plotted with the expected output of the scintillator array for many critical energies. The data from this shot was found to have a critical energy of (30±10) keV.

Figure 3.19. The comparison between the data and expected values is obtained by finding the critical energy curves that has the r-squared that is closest to 1. The uncertainties are placed on each measurement assuming a normal distribution and then compared to the expected results; this is done numerous times to calculate the average and uncertainties in the critical energy. For the data shown in Figure 3.23, the critical energy is found to be (30±10) keV.

To improve the uncertainties in this data, further shielding could be used on top of the 50 mm of Pb surrounding the diagnostic. Also, the energies involved in the initial electron beam will indirectly cause the creation of neutrons. Possible neutron shielding to reduce the contamination in the diagnostic, time-of-flight monitors to record the neutron flux or gated camera systems to gate out the neutron flux on the scintillators are all possible methods to improve future betatron spectral measurements.

These initial tests demonstrate the capabilities of the diagnostic as a tool to characterise x-ray spectra. The limitations arises when the signal is low and when background sources of x-rays or a high number of secondary particles that the scintillator is also sensitive to, such as neutrons exist. Although, as shown previously, the initial tests conducted on a solid-target interaction created a bright signal from the scintillators, particularly the BGO, which should allow for better spectral extraction from the diagnostic. The diagnostic has also proven its capability operating on a laser system with a fast repetition rate.

3.5.3 Image Plate Calibrations

Fujifilm image plates (IP) are commonly used in laser-plasma experiments due to high resolution, high dynamic range, re-usability and versatility at detecting different charged particles. Many diagnostics have been designed with IP as the detector; such as electron spectrometers [74, 75], Thomson parabolas [57, 58, 59] or x-ray spectrometers [67, 68, 76]. Numerous papers have also been written on the calibration/sensitivity of IP for each of these uses [77, 78, 79, 80, 81, 82].

There are a number of different types of IP that are designed for specific detection; the most commonly used are BAS-TR, BAS-SR and BAS-MS. The composition of each type of image plate is slightly different; Table 3.3 shows the individual compositions found from [80, 81, 83]. Some of the values from the different sources disagree slightly with one another; in such cases both pieces of information are shown.

IP consists of an active layer of Barium Fluorohalide phosphor crystals doped with Europium (Eu) atoms. When the active layer absorbs incoming energy from an incident beam, the electrons in the Eu are excited to a meta-stable state. These electrons usually stay in their excited state, but they can decay due to defects which leads to a gradual fade [81, 84, 85]. If the IP is exposed to a red laser the meta-stable state is excited to a higher level which rapidly decays producing blue light, a process known as photo-stimulated luminescence (PSL). An IP scanner can extract the position and brightness of the PSL which yields spatial and intensity information about the particle beam incident on the IP.

Inside an IP scanner the blue light produced in the stimulated decay is recorded via a photomultiplier tube (PMT). The PMT can saturate if the incident signal is too strong; therefore the spatial and intensity information from this saturated signal cannot be extracted. The simplest method of recovery of the signal is to conduct more scans. This will lower the number of excited electrons available to decay therefore yielding less light the more times you scan the IP. This can be repeated any number of times until the signal recorded is no longer saturated. However, as the data from the calibrations are given from first scan of the image plate therefore the data must be extrapolated from the unsaturated scan to the signal at scan 1.

At the Central Laser Facility there are two IP scanners (both are the model FLA5100). Each scanner will be slightly different due to the many components

IP Type	Colour		Protective Layer	Sensitive Layer	Undercoat Layer	Base Film	Magnetic Layer	Base Film
BAS-MS	White	Material	C10H8O4 (Mylar)	BaFBr(0.85) I(0.15):Eu	Plastic	C10H8O4 (Mylar)	MnO,ZnO, Fe2O3 +Plastic	C10H8O4 (Mylar)
		Thickness (μm)	9	115/124	12	190	80	25
		Density (g/cm^3)	1.64	3.18	1.4	1.4	3	1.4
BAS-SR	Light Blue	Material	C10H8O4 (Mylar)	BaFBr(0.85) I(0.15):Eu	Plastic	C10H8O4 (Mylar)	MnO,ZnO, Fe2O3 +Plastic	C10H8O4 (Mylar)
		Thickness μ	6-8	112	12	190	80	25
		Density (g/cm^3)	1.64	3.07	1.4	1.4	3	1.4
BAS-TR	Blue	Material	-	BaFBr(0.85) I(0.15):Eu	Plastic	C10H8O4 (Mylar)	MnO,ZnO, Fe2O3 +Plastic	C10H8O4 (Mylar)
		Thickness μ	-	50/60	12	250	80	25
		Density (g/cm^3)	-	2.61	1.4	1.4	3	1.4

Table 3.3: The different types of Image Plate that are commonly used in diagnostic. Information on the compositions of the image plate is found from the following sources [80, 81, 83]. Any discrepancy from the values from the sources have been noted with a slash between the two values.

inside; therefore a calibration of each scanner must be done. In this section we firstly conduct a calibration on each scanner to find any difference in the scanning decay and sensitivity and also a rigid method for data recovery/extrapolation to the first scan. To measure the decay of the IP with each scan and absolute sensitivity of the scanners, the image plate was exposed to a calibrated radiation source. The radioactive source used was iron-55 (Fe-55) which emits 5 keV auger electrons and 6 keV K-capture x-rays with a branching ratio of 60.7 % and 27.8 % respectively.

3.5.3.1 Sensitivity

Image plate scanners come in a variety of models. As discussed before, each scanner is made up of a laser to de-excite the electrons and a PMT to measure the light output. Small differences in optical alignment may lead to different sensitivities or decay curves. Tests were carried out by the author to check whether each of two image plate scanners have similar sensitivities and, later in this section, decay curves. Firstly, two pieces of BAS-TR were 'wiped' of all previously acquired signal using a white light source and then wrapped in Al foil. Additional foil was added to the front to provide different levels of filtering. The two pieces IP were placed approximately 85 mm away from the Fe-55 source and side by side so that the same dose would be received by both IPs. The IPs were exposed for 24 hours. Afterwards, both IPs were removed at the same time and scanned simultaneously on the two previously mentioned scanners. A scanned image from one of the scanners is shown in Figure 3.24 a) where 5 separate areas of different filtering are highlighted. The PSL decay against scan number is shown in Figure 3.24 b). An example of the signal from the two scanners for Area 1 is show in Figure 3.25 a). The ratio between PSL for the two scanners is shown in Figure 3.25 b). The change of ratio between the signal taken in each area between each scanner as a function of scan highlights the differential variation in the decay of the signal on the image plate with each sequential scan for the two different

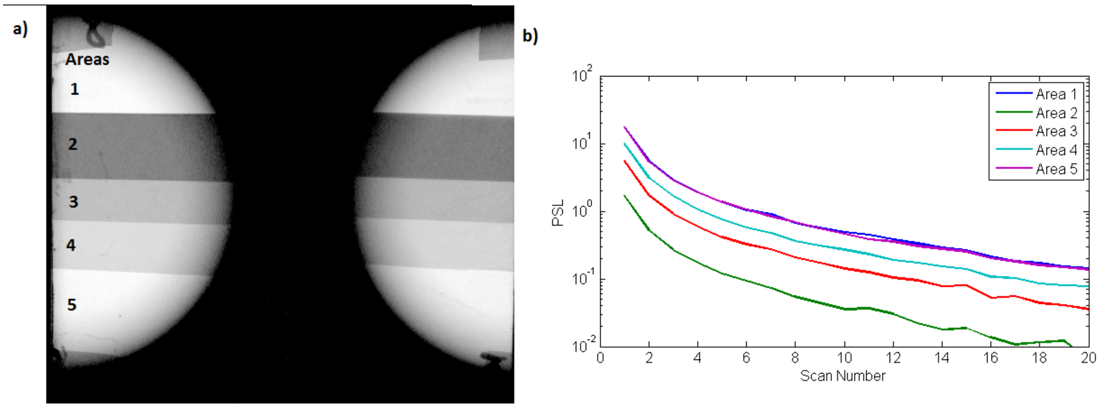

Figure 3.24: a) Separate TR FUJIFILM IP after the first scan from both scanners. Different areas of filtering are labelled 1-5 with b) the decay curves of a IP for 20 scans.

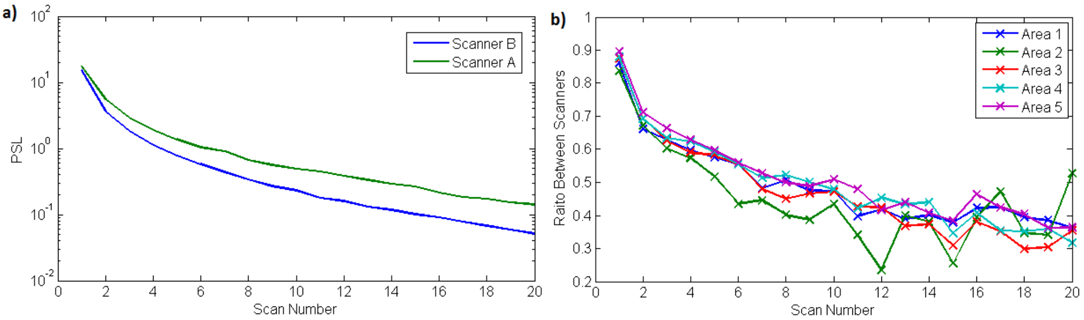

Figure 3.25: a) The difference between the signal of area 1 on two FLA5100 scanners for 20 scans. b) The ratio of the decay curves for all the areas. This ratio is changing suggesting that the decay curves are different for both scanners.

scanners available.

Using this data, an absolute calibration for each scanner can be made. To calculate the absorbed energy on the IPs, the attenuation of the filtering must be calculated. This can be done using the NIST XCOM and ESTAR tables. NIST XCOM is used as scattering effects are unlikely to occur at this low energy. The 5 keV emission of electrons will not penetrate the Al filtering, meaning that the signal on IP is exclusively from the x-rays emitted. The x-rays first have to travel through 85 mm of air; approximately 79% of them will reach the filtering. Using a micrometer caliper, the thicknesses of the Al filters were measured and the transmission through the Al is calculated. Finally, a percentage of the

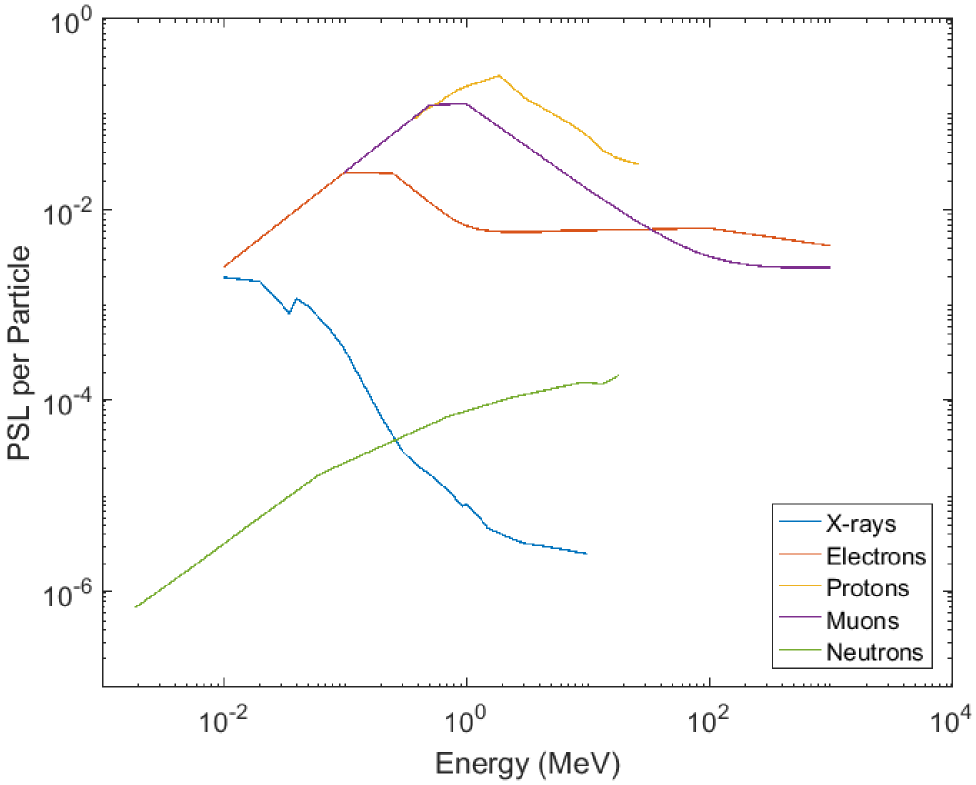

Figure 3.26: The PSL per particle for image plate for a number of different particles. GEANT4 results for the energy deposited per particle were compared to the results in Bonnet *et al*[77] to relate energy to PSL. The curves show that the image plate is less sensitive to x-rays than any other particle shown. The neutron data is found in [82] for BAS-SR.

x-rays will be absorbed into the IP. Using the measured PSL and this fractional absorption, the PSL per photon for scanner A is $(8.9\pm0.9)\times10^{-4}$ and for scanner B $(7.8\pm0.8)\times10^{-4}$. Comparing these with the values given in [77, 80, 81], the difference is small; in fact the literature values differ by similar amounts.

The data shown in Bonnet *et al*[77] shows that the PSL per particle is very dependent on the input energy of the particle. As the results from this section are similar to the results from Bonnet *et al*[77], the full calibration curve in that study shall be used in this thesis.

Additionally, GEANT4 can be used to calculate the amount of energy deposited in the active layer of the image plate. As energy deposited is what an image

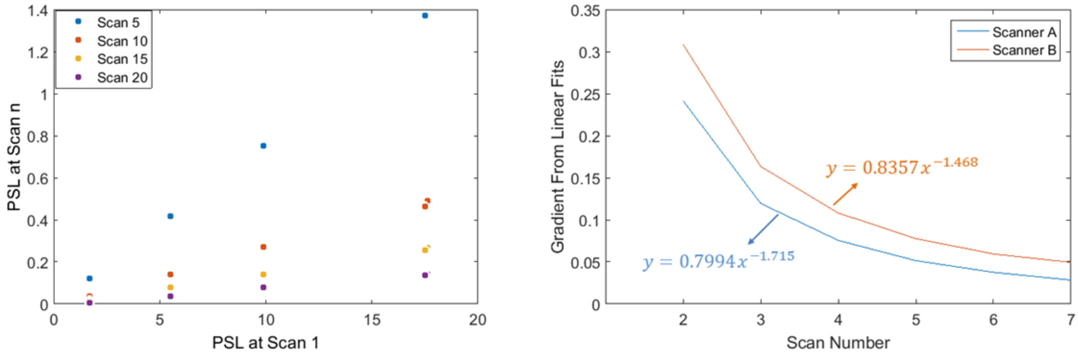

Figure 3.27: a) The signal at scan 1 against signals at scan 5, 10, 15 and 20 that show a linear relationship. b) The gradients from the linear fits plotted against scan number for each scanner. The fits are displayed on the graph next to the corresponding curve. The differences in these curves highlights the deviation emphasized earlier in Figure 3.25.

plate measures but not in the same units, these values must be converted to PSL to a direct comparison. To convert to PSL the difference between the predicted values in GEANT4 and Bonnet *et al* [77] were compared and a conversion factor of 3.2 and 4.3 was found for electrons and x-rays respectively. The sensitivity to a number of particles is shown in Figure 3.26. Protons were added using the data in Bonnet *et al* and muons were added using GEANT4 and the conversion factor for electrons assuming that they deposit energy in a similar manner to electrons due to their similarities in charge. The neutron data was added from Monte Carlo simulations performed by Izumi *et al*[82] for BAS-SR. The image plate is shown to be far more sensitive to electrons than it is to x-rays. For all the particles displayed, the energy deposited and therefore the PSL is dependent on the likelihood of interacting with the active layer.

3.5.3.2 Scan One Recovery/Reconstruction

As stated before, if the signal is saturated it must be extrapolated to the signal at first scan to use the calibrations performed by others. Fitting a decay curve to the data shown in Figure 3.24 would be the simplest method to relate signal to scan number, however no fitting method provides a good fit across all the data.

An alternative method is to plot the PSL at scan one as a function of the signal at an arbitrary scan. This method shows a linear trend between the different signal strengths as shown in Figure 3.27 a). This shows that the signal at the nth scan can be taken back to scan one using this linear relationship. Taking the gradient of each of these and plotting them as a function of scan number yields the graph shown in Figure 3.27 b), which displays the data for both scanners. These can be fitted easily with a decaying power fit. Rearranging the linear equation and substituting the power laws produces the equation;

$$S_1 = \frac{S_x}{ax^{-b}} \tag{3.9}$$

where S_1 is the PSL at scan 1, S_x is the PSL at scan x, x is the scan number and a and b are the constants taken from the power fit in Figure 3.27. This equation will allow for retrieval of the signal from the first scan.

3.5.3.3 Scanning Filters

Although we have discussed how to retrieve data from any scan number in the previous section, scanning a single piece of IP numerous times is time consuming. This issue increases when the user wants to increase the resolution of the scan or the size of the IP. Neutral Density (ND) filters can be placed between the IP and the PMT, reducing the light incident onto the PMT.

A similar exposure as before was conducted on 2 IPs with filtering using the Fe-55 source. An ND 1 filter was placed inside the scanner before the PMT. The data shows that the light was cut down by a factor of 19, this is twice the value expected. As the scanner itself is a closed system, it is very difficult to know the exact optical path the light takes to the PMT. This means that the light cannot be guaranteed to be passing through the ND filter normally which may lead to modifications to the opacity. Although it is not the expected filter value, the introduction of the ND filter will reduce the processing time of the image plate.

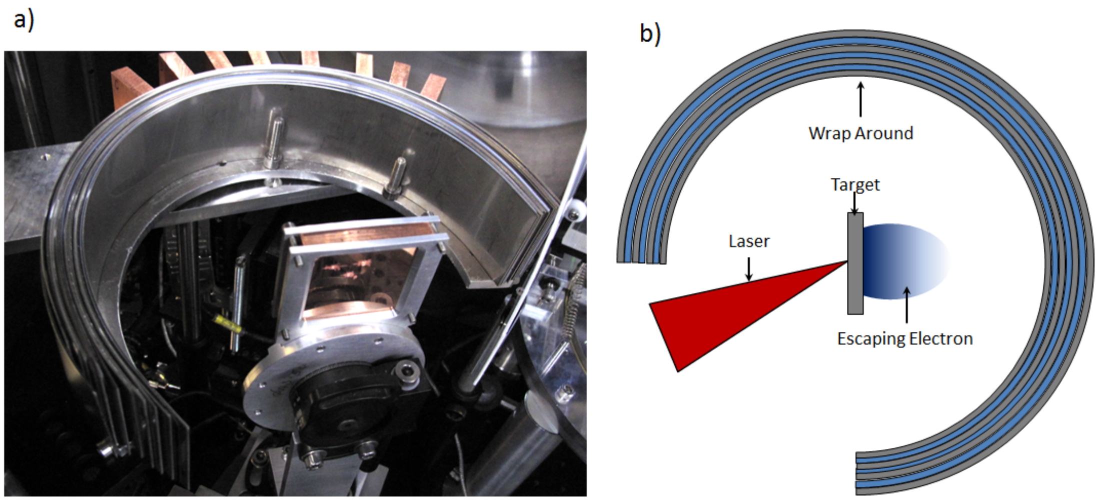

Figure 3.28: a) Image of wraparound diagnostic installed on laser-solid experiment with a copper target in the middle. b) shows a view from the top of the diagnostic.

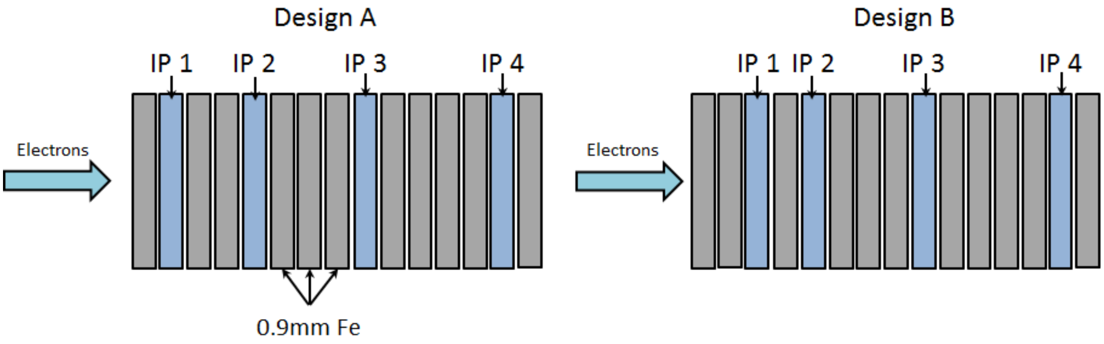

Figure 3.29: Arrangement of Image Plate between Fe filters used in wrap around stack with two variations. design A is the original, designed to give the largest spectral gap between the 1st and 4th image plate providing better spectral measurements. design B is specifically designed to avoid proton contamination onto the first layer of image plate.

Further tests have been conducted using an ND 2 filter that shows a decrease by a factor of 245.

3.5.4 Angular Wrap-Around Stack

Measuring the angular distribution of radiation from a laser-solid interaction has provided validation of theorical models [86, 87] and led to new physical insights into the absorption mechanisms [87, 88, 89]. As well as the angular data, the spectral data of the escaping electrons may provide additional information about the surface charge that they create as they leave the target. The angular wraparound stack [90] can provide both the angular and the spectral data of the escaping electrons simultaneously [91]. The steel and image plate are curved around the target which provides the angular information about the emitted radiation. Figure 3.28 shows a picture of the wraparound stack on an experimental set-up. Multiple layers of image plate can be used in the stack, with differential filtering providing spectral information. Two designs of filtering were developed (designs A and B) which are shown in Figure 3.29, where design B has an additional layer of filtering to reduce/stop proton contamination; this is specifically a worry for thinner targets as these have been shown to create higher energy protons [92]. The difference between the required proton energies to reach the first active layer was simulated using SRIM. For design A the Bragg peak of 21 MeV protons lay within the active layer, whereas for design B it required 31 MeV protons to reach the active layer. These Bragg peaks are shown in Figure 3.30.

These arrangements were tested in GEANT4 to analyse the spectral response of the detector. Each of the layers of Fe was 0.9 mm thick. The image plate type used was BAS-TR with the composition built in GEANT4 the same as that described earlier in this chapter in section 3.5.3.

3.5.4.1 Mono-energetic Electron Absorption Curves

GEANT4 simulations were conducted on these two particular stack designs to find what energies of electrons each layer responded to. The simulations were conducted using 10^6 mono-energetic electrons and repeated multiple times for different input energies. Dividing through by the total amount of input energy will yield the fractional deposited energy in each layer of the image plate, which is shown in Figure 3.31. For design A, the peak response is above 4 MeV, whereas for design B it is 6 MeV. In most cases, the energies required to reach the first layers of both designs will be part of the high energy tail of the electron spectrum

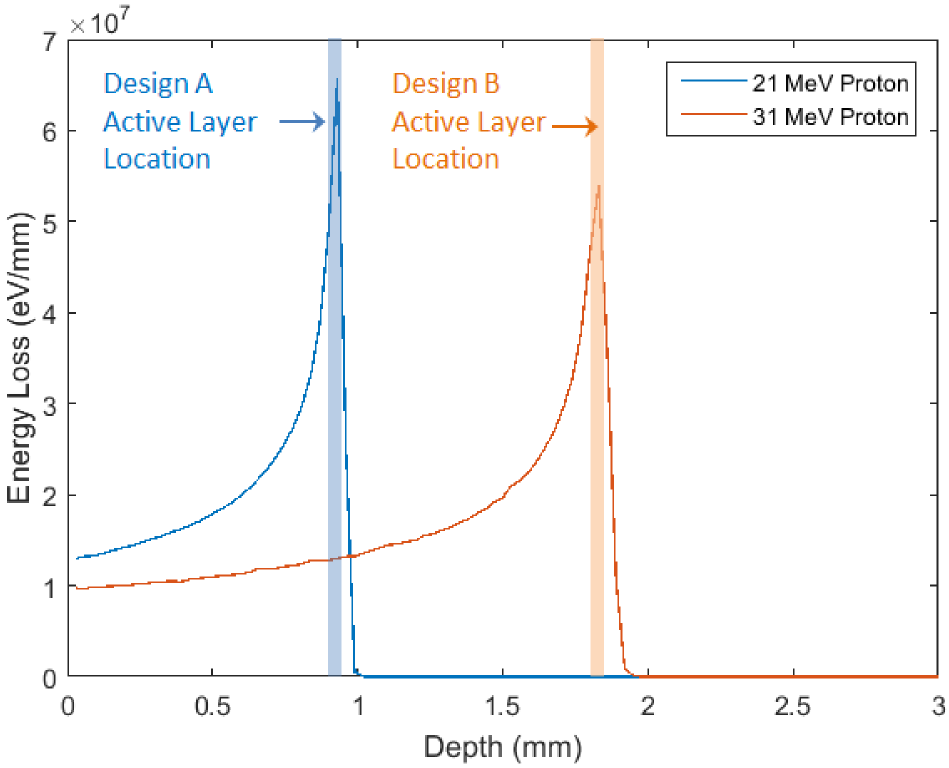

Figure 3.30: SRIM calculations for design A and B to determine the threshold energy of protons required to contribute to the active layer (highlighted by the shaded areas).

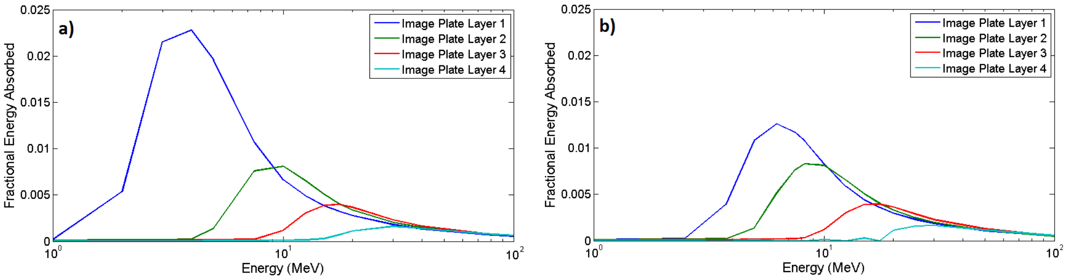

Figure 3.31: Fractional absorption of the image plates at different mono-energetic electron energies for both design A and B, shown in a) and b) respectively, calculated using 10^6 incident particles per energy sample

that rapidly falls off. As design A and B do not vary after the second layer it is clear to see that the subsequent layer have identical absorption.

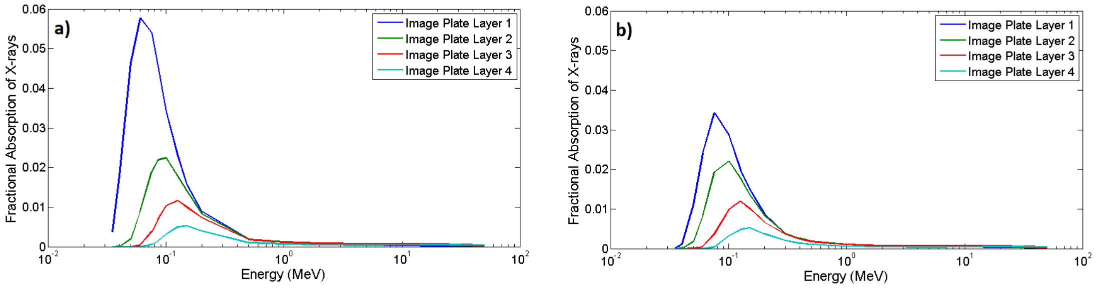

Figure 3.32: Fractional absorbed energy for different mono-energetic x-rays for both designs A and B, shown in a) and b) respectively.

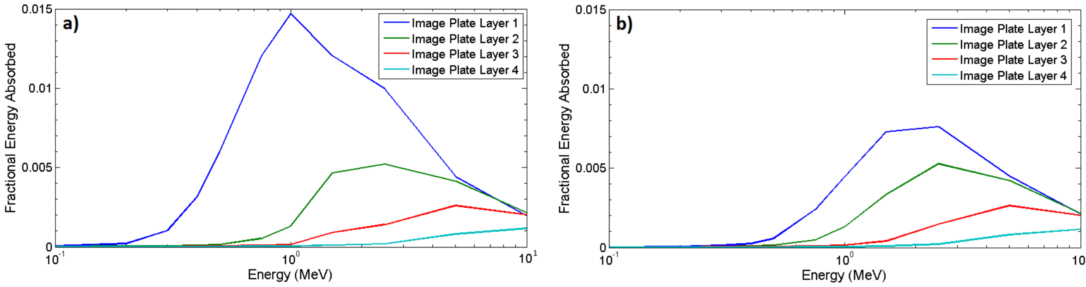

Figure 3.33: Fractional absorbed energy for different electron Maxwellian distributions with temperatures from 100 keV to 10 MeV for both designs A and B, shown in a) and b) respectively.

3.5.4.2 Mono-energetic X-ray Absorption Curves

The response of the image plate layers has also been simulated for many different mono-energetic x-rays. The results for both design A and B is shown in Figure 3.32. Layers 2-4 have very similar response for both designs, but again layer 1 has very different thresholds/peaks. The peaks for x-rays are much sharper than the response of the diagnostic to electrons. This is mainly due to the response of the active layer to x-rays which peaks at ≈35 keV, as shown in Figure 3.26, but the filtering layers cut this energy out. As the energy increases the absorption drops significantly as the cross section for interaction in the active layer is reduced.

3.5.4.3 Maxwellian Electron Distribution Absorption

Modifying the input of GEANT4 allows for the input of spectra rather than single energies. Using a relativistic Maxwellian distribution of electrons, the fractional and total absorption of the layers of IP was measured for an input of 10^5 particles at different temperatures. Due to the method GEANT4 uses to create an input spectrum, the input particles into the system were also recorded enabling the fractional absorbed energy to be calculated. Figure 3.33 shows the fractional absorption for a relativistic Maxwellian spectrum for many temperatures for designs A and B. As we have seen from Figure 3.31, the electrons only start depositing the largest fraction once the energies go above the threshold for each of the two different designs. The difference in the two designs is highlighted again as design A layer 1 responds to lower temperatures than layer 1 in design B. The temperature can be extracted using similar techniques to that shown in the previous section for the scintillator based spectrometer.

3.6 Summary

It is clear from the content of this chapter that executing experiment in laser-solid interactions requires application and knowledge of range of physics. The laser technology has been and is constantly being developed to produce well diagnosed intense laser pulses, the diagnostics deployed on the experiments are becoming faster and better understood and the simulation techniques are growing more extensive. All of these are important in understanding complex laser-plasma interaction physics and thus in reaching the conclusions in this thesis.

Chapter 4

Diagnosing the Internal Electron Temperature using Bremsstrahlung X-rays

The diagnosis of the internal hot-electron distribution produced in high-intensity laser-solid interactions is of utmost importance due to the key role it plays in determining the spectral characteristics of emitted ions [93, 94] and x-rays [95]; both of which are sources for potential applications. The interaction between an intense laser pulse and the plasma on the front of a solid target has led to the development of models that attempt to find the relationship between the intensity and wavelength of the incident laser and the resulting electron temperature distribution. This distribution is often considered to be a Maxwellian [31] in the non-relativistic case. However, as discussed in Chapter 2 the distribution can have other forms, such as a Boltzmann or Maxwell-Jüttner distribution [49]. The high energy component is often simply described using a single temperature whereas in reality there is normally a second lower energy temperature [96]. In this section, for simplicity, the temperature distribution will be described and modelled using the high energy component as this is the most likely source of the high energy (>200 keV) x-rays.

As it stands, there are many models that derive analytically and empirically 'scaling laws' for the relationship between the intensity and temperature. Here, I will only discuss the most commonly used and accepted models.

The scaling model introduce by Beg *et al* [33] was derived from results where the numbers of high energy photons emitted from plastic targets at intensities of ≈2-8×10^{18} W/cm^2 were measured. Assuming a Maxwellian distribution of hot electrons producing the photons inside the target, the temperature in keV was shown to scale as,

$$T_{hot,Beg} = 215 \left[I_{18}\lambda_{\mu}^{2}\right]^{1/3} \tag{4.1}$$

where I_{18} is the intensity of the laser in units of 10^{18} W/cm^2 and λ_μ is the wavelength of the laser in microns. This suggests the hot electron temperature is 215 keV when the laser intensity is at 10^{18} W/cm^2 for a wavelength of 1 μm.

Another scaling law, the ponderomotive scaling, was derived by Wilks *et al* [24] using the ponderomotive potential, see chapter 2. The electron temperature in keV scales as,

$$T_{hot,Wilks} = 511 \left[\sqrt{1 + \left(\frac{I\lambda_{\mu}^{2}}{1.37 I_{18}}\right)} - 1\right] \tag{4.2}$$

A more recent scaling law by Haines *et al* [34] was developed analytically and is given in keV as

$$T_{hot,Haines} = 511 \left[1 + \sqrt{2}\left(\sqrt{\frac{I\lambda_{\mu}^{2}}{1.37 I_{18}}}\right)\right]^{1/2} - 1 \tag{4.3}$$

Many experimental campaigns have measured/inferred the hot electron temperature in a variety of ways, with some directly comparing their results to the previously mentioned scaling laws. A summary of the different measurements made over the last 15 years between the intensities of 10^{17} and 10^{21} W/cm^2 is presented in Figure 4.1.

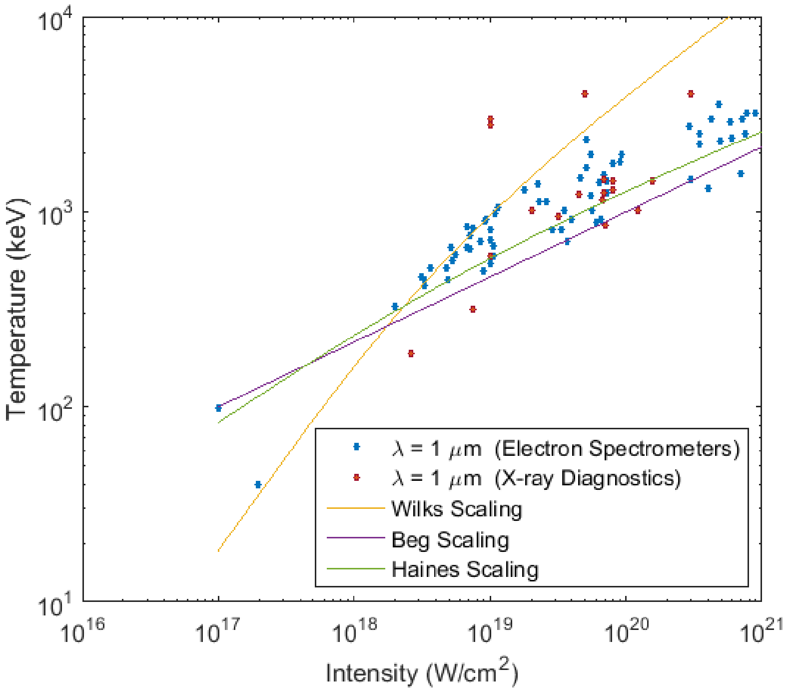

Figure 4.1: A collection of electron temperatures from laser solid experiments for wavelengths of 1 μm, recorded using electron spectrometers [97, 98, 99] and diagnosed using x-rays [68, 89, 100, 101, 102, 103, 104, 105]. The 3 data points at the top/above the Wilks Scaling were recorded using activation techniques which could bias the temperature higher as they are only recording the high energy tail of the emitted x-ray spectrum.

One of the earlier experimental campaigns to compare their results to a scaling law was reported by Malka *et al* [97], using an electron spectrometer to measure the escaping electron distribution from a 30 μm CH target. The laser was incident normally to the target surface and the intensity was varied from 2 to 9×10^{18} W/cm^2. The temperature of the hot electrons at the rear target normal was measured and found to match very closely with the scaling by Wilks *et al* (300-900 keV). More recent experiments by Tanimoto *et al* [98] and H.Chen *et al* [99] also measure the escaping electron temperature from laser-solid interactions with intensities between 10^{17} and 10^{21} W/cm^2 using electron magnetic spectrometers and found that the temperature scales closer to the Beg or Haines scaling (500-2300 keV).

Using an electron spectrometer is possibly the easiest method to measure the hot electron distribution. However, the electrostatic fields set up as the electrons escape the target also act to retard the electrons. This can lead to a cooling of the temperature which was shown both analytically and numerically by Link *et al* [106]. The percentage of this cooling is between 10-30% depending on the laser conditions. Therefore, the internal and escaping electron temperatures are different. Another, and potentially better, method to measure the internal electron temperature is to measure the bremsstrahlung x-rays emitted from the target as they are not influenced directly by the electrostatic fields set up by the escaping electrons. However, in many experimental cases, the majority of hot electrons are trapped and reflux back and forth [69]. This will result in more x-rays being produced, which will be discussed later.

X-ray diagnostics have been deployed on many experiments to measure x-ray spectra to determine the hot electron spectra temperature. These x-ray diagnostics include absorption based spectrometers [95, 107] that are able to monitor/estimate the spectral temperature, or crystal spectrometers[108] that directly observe the spectrum. The hot electron temperature can be infered from inside the target using k-alpha fluorescence imaging using trace layers within the a target [109]. Each of these technique has merits and limitations, such as signal to noise for crystal based spectrometers, as coherent scattering has a low cross-section.

Early experiments by Yu *et al* [110] using a 0.54 μm laser with a pulse length of 400 fs and intensity of 10^{17}-10^{18} W/cm^2 measured a temperature that approximately matched that of the Beg scaling. More recently, C.Chen *et al* [89] Courtois *et al* [101, 102] and MacPhee *et al* [100] have all conducted their experiments on 1 μm laser systems and measured the emitted x-rays. Experiments conducted by MacPhee *et al* and Chen *et al*, using the same absorption based spectrometer, measured a spectrum between 850-1500 keV for intensities of 8-15$\times10^{19}$ W/cm^2. Courtois *et al* used activation diagnostics to measure temperatures up to 3 MeV for 10^{19} W/cm ^{2}.

One of the highest resolution measurements of the high energy x-rays emitted from a solid target was conducted by Zulick *et al* [96] using a high repetition rate laser (0.5 kHz) and a Germanium detector. A dual temperature x-ray spectra was measured, using over 1 million shots, which scaled slower than the Wilks scaling but faster the Beg scaling.

The discussed measurements made with a laser wavelength equal to 1 μm, plus some additional measurements [103, 104, 105], are shown in Figure 4.1. The measurements have been split into data recorded with electron spectrometers and those made using the variety of x-ray diagnostics. For intensities of approximately 5-10×10^{18} W/cm^2 the temperatures appear to fit in-between all three scaling laws. As the intensity increases the number of measurements that match the Wilks scaling is significantly less. At intensities above 10^{20} W/cm^2 the hot electron temperature follows the Haines or Beg scaling more closely than the Wilks scaling. The out-lying data at the top of the graph, measured by Courtois *et al*, was measured using activation of materials. This method would only sample the highest energies of the x-ray distribution (>8 MeV), which might not be representative of the entire spectrum.

Although there is a lot of data from electron spectrometers, there are only 3 data points measured using x-ray spectrometers from C. Chen [105] between the intensities of 10^{18} and 10^{19} W/cm^2; two of these points fall below all three scalings discussed.

In this chapter experimental results from a selection of targets and irradiation conditions that lie within the intensity range of intent (approximately between 10^{18} and 10^{19} W/cm^2) are presented to address this data region.

The x-rays that are produced in solid targets are highly energetic and are typically generated in a small region (<100 μm) which makes them favourable for high resolution imaging for non-destructive testing of materials using x-ray radiography. One of the earliest demonstrations of high-intensity laser-solid x-ray radiography was conducted by Perry *et al* [12] where basic absorption images were recorded through varying thicknesses of lead attenuators using a Kodak film. Since then, work has also been conducted using laser-Wakefield targets to produce x-rays suitable for radiography [103, 111]. More recently, Courtois *et al* [10, 102] conducted experiments characterising the x-ray source for the purpose of radiography. They measure the size of the x-ray source to be 350 μm and 400 μm using penumbral imaging and a resolution test grid respectively; both experiments with $\approx 10^{19}$W/cm^2.

In this chapter, I infer the internal hot-electron temperature from a laser-solid interaction by measuring the emitted x-ray spectra whilst also measuring the scaling of the x-rays flux. Both x-ray measurements are performed using the novel scintillator based absorption spectrometer described in Chapter 3. Once characterised and optimised, x-ray radiography is performed on a number of objects to demonstrate the suitability and applicability of using laser-solid generated x-rays. Additional results from the experiment are reported by Jones *et al* [112] and Brenner *et al* [13].

4.1 Experimental Method

An experiment was conducted using the Vulcan laser system in Target Area West (TAW). A basic schematic of the experimental setup is shown in Figure 4.2. The target was irradiated at 20 degrees by a (10±2) ps laser pulse with a wavelength of 1.054 μm. The focal spot was (7±1) μm FWHM in diameter. The maximum energy on target was (140±15) J leading to a peak intensity of $\approx 1.2\times10^{19}$ W/cm^2.

The flux and spectrum of the x-rays was recorded using the scintillator based spectrometer (see Figure 4.3 a)). The array was positioned at approximately 20 degrees with respect to the laser axis, along the rear target normal, and 2.15 m from the target. The scintillator array was imaged using an Andor CMOS detector due to its high dynamic range, as discussed in Chapter 3. The array

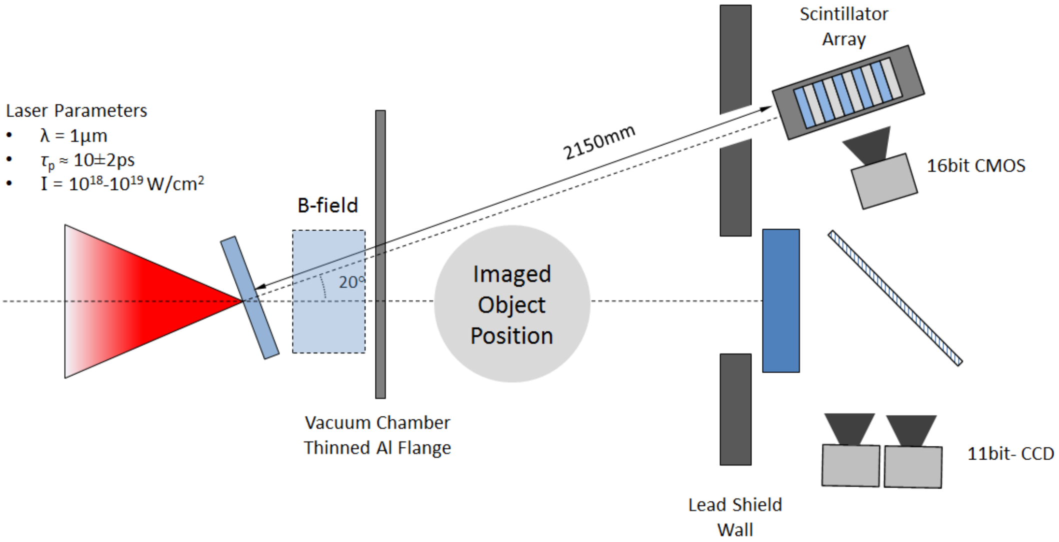

Figure 4.2: Schematic of the experimental setup used to measure the temperature and flux. Radiography was performed on samples placed outside the vacuum chamber as highlighted.

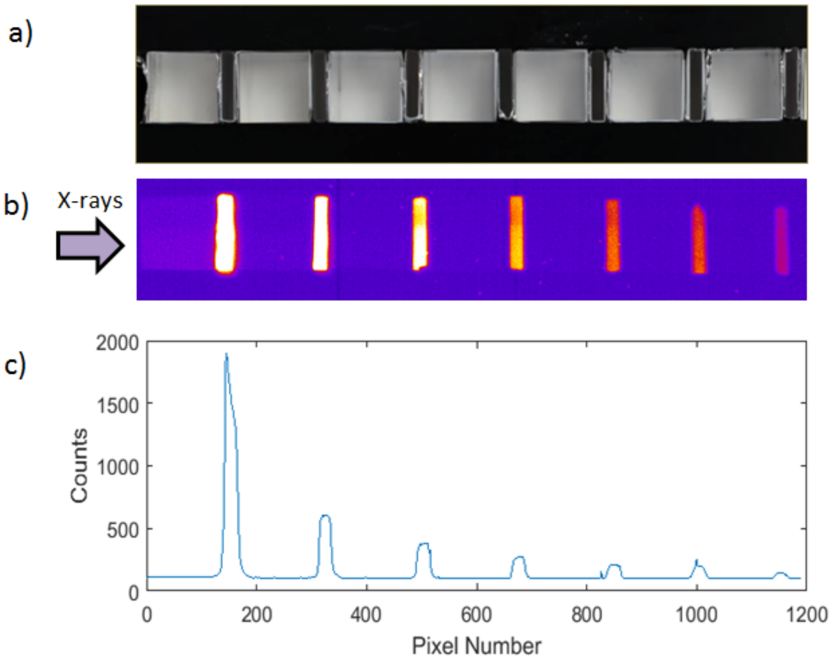

Figure 4.3: a) A picture of the scintillator array. b) An example of a picture of the array during a shot and c) the line-out of the array.

views the interaction through a small aperture in a 50 mm lead shield wall. To reduce the number of indirect scattered hard x-ray hits on the camera chip, the entire camera is also placed behind a lead shield.

The x-rays exit the vacuum chamber by propagating through a thin (5 mm) aluminium port. This is taken into account in the response of the scintillator array by multiplying the response curves shown in Figure 3.15 of Chapter 3 by the attenuation of the steel port and the air between the port and the diagnostic. Before the chamber port there is a magnetic field that is used to deflect any electrons that escape the target.

A typical image from the scintillator array for a full energy shot is shown in Figure 4.3 b). It is clear to see that the smaller scintillator, the BGO, is much brighter than BC422q; this is primarily due the light yield of the two scintillators. Analysis will only be conducted using the BGO layers which are significantly brighter and therefore have better signal-to-noise than the BC422q. Although the camera is placed behind 50 mm of Pb, hard hits are still visible on the recorded image; these are removed using a medium filter; this filter looks at a region of the image finding the out-lying pixels with very high counts and replaces them with the medium value in that region.

In Figure 4.3 the x-rays are incident onto the left of the array. The signal is clearly decreasing as a function of depth which is shown from the lineout in Figure 4.3 c). The average number of counts are extracted from the scintillator over an area that represents the middle 50%; this is done to ensure the light from each layer is not influenced by the neighbouring layer.

The imaging area on the experimental schematic in Figure 4.2 highlights the region where the variety of imaging objects/samples are placed. There are two detectors used to record the x-rays: FujiFilm BAS-SR Image Plate and a Cesium Iodide Thallium-doped (CsI(Tl)) scintillator array. The type of image plate used was SR, which is described in table 3.3. The active layer in the image plate is thin (112 μm) so it is most sensitive to low energy x-rays (<100 keV). The CsI(Tl) is 300×300 mm with 0.5×0.5 mm pixel width with a depth of 10 mm. The thickness of the CsI provides much larger attenuation and therefore it can detect higher energy x-rays ($\approx$100% of energy up to 200 keV); this is shown by

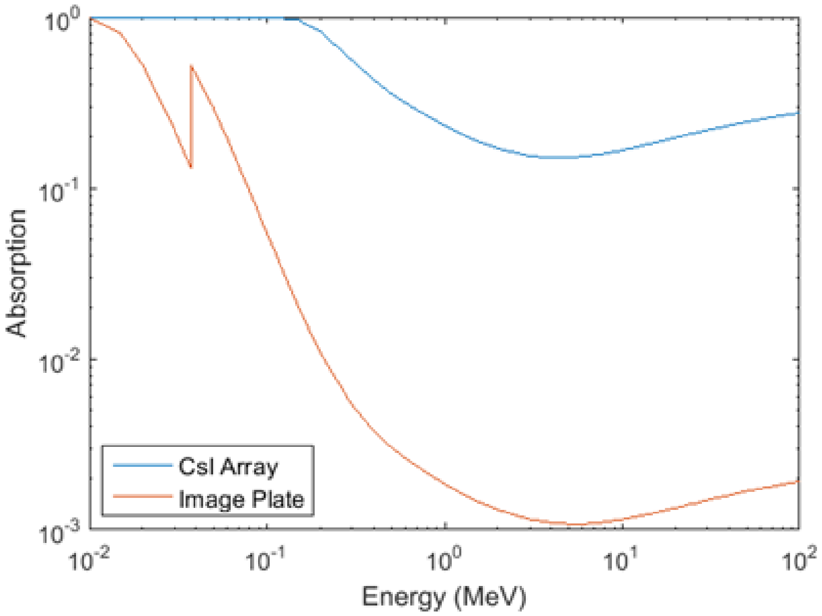

Figure 4.4: Absorption of the CsI(Tl) array and image plate used for radiography calculated using the NIST XCOM attenuation tables [70].

the absorption calculated by the XCOM attenuation tables of each detector in Figure 4.4. To optimise the amount of light captured from the CsI array, two large-area 11 bit-CCDs were used. A major advantage of the CsI array is that it is able to operate at a high repetition rate which is ideal for use on newer high-power laser systems.

Both detectors can be placed close to the sample to perform contact radiography or further away to take advantage of the point-like nature of the source and perform projection imaging. The image plate is scanned at a resolution of 25 μm on the image plate scanner to ensure that the radiography comes out at the highest possible resolution. Although, it has been shown by Fiksel *et al* [113] that an image plate in general has a resolution limit of approximately 100 μm.

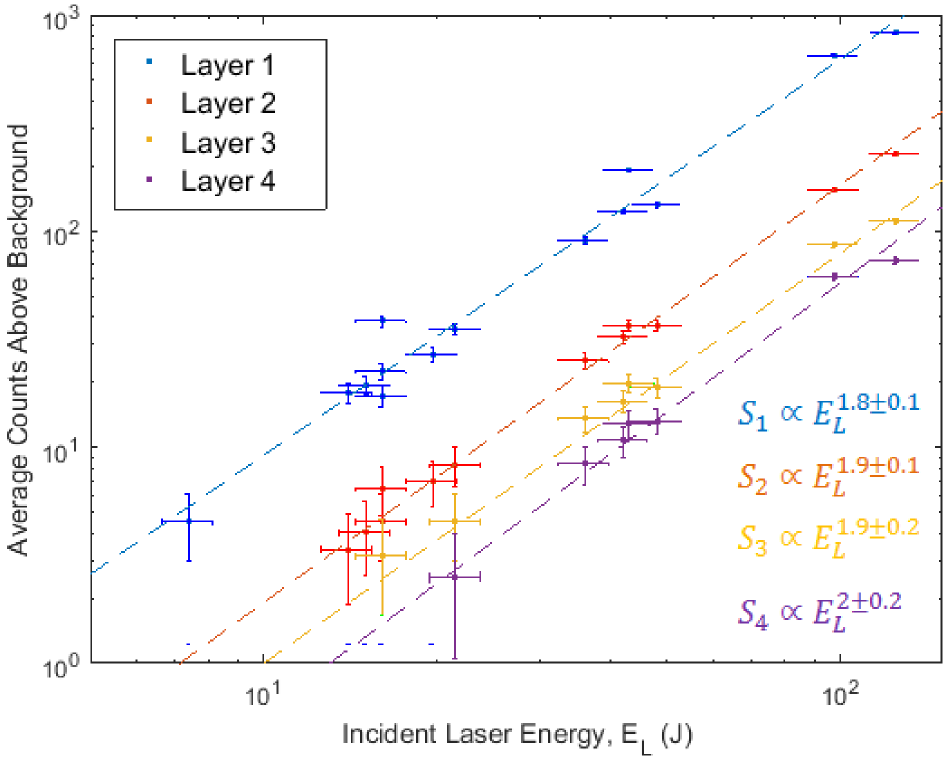

Figure 4.5: The average counts on the layer of scintillator as a function of incident laser energy (J), E_L, onto the target. For each layers a fit power laws with slight different gradients is shown.

4.2 Experimental Results

Firstly, the laser energy (E_L) incident onto a 1 mm thick Al target was varied so that the dependence of the x-ray flux on incident laser energy could be measured. The flux changes were measured by taking the average counts of the first four BGO layers of the scintillator array; this is shown in Figure 4.5. The flux recorded scales as $S_1 \propto E_L^{(1.8\pm0.1)}$, $S_2 \propto E_L^{(1.9\pm0.1)}$, $S_3 \propto E_L^{(1.9\pm0.2)}$ and $S_4 \propto E_L^{(2.0\pm0.2)}$. This clearly shows that the flux is strongly dependent on the incident laser energy. This is similar to scaling of proton flux as a function of incident laser energy measured by Robson *et al* [114] and Brenner *et al* [115].

To model the scaling of the x-ray flux as a function of incident laser energy, GEANT4 was employed. As the electron beam travels through the target, bremss-

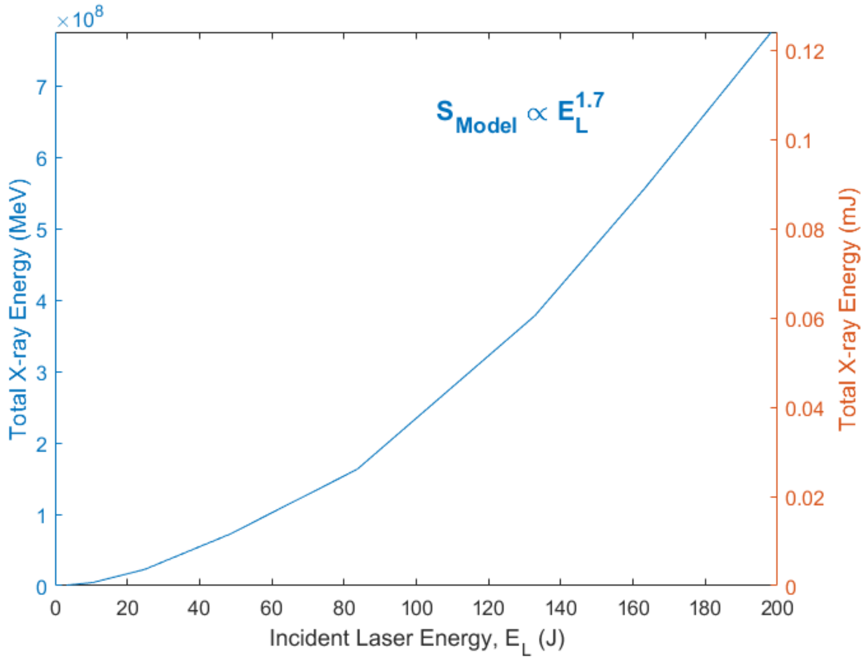

Figure 4.6: The modelled x-ray flux from GEANT4 as a function of the incident laser energy (E_L). The flux scales as the incident laser energy to the power of 1.7.

trahlung is created which can be modelled using GEANT4. It simulates the bremsstrahlung by firstly calculating the mean energy lost by an electron of a given energy in a material as calculated using range and inverse-range tables for that material. The GEANT4 calculations effectively introduce a distribution in the energy loss and x-ray generation depending on the thickness of the material.

Validations of the bremsstrahlung and electromagnetic models for GEANT4 have been undertaken by numerous authors [63, 64, 65, 116, 117]. The typical conclusion regarding the bremsstrahlung models and cross sections/stopping powers is that the additional/optional electromagnetic models are more accurate at lower energies (<1 MeV) than the standard models included in GEANT4. The 'Livermore' electromagnetic model [65, 117] will be used in the following work conducted by the author.

Simulations were conducted using 10^6 initial electrons propagating through 1 mm of aluminium using different relativistic electron temperatures. The emitted x-rays and electrons were recorded at the front and rear of the target so that the forward propagating and backscatter of each particle could be predicted. The x-rays were restricted to a 15 degrees half angle cone to only observe the most forward propagating x-rays as these are the ones recorded using the scintillator array. To take into account the increase in the x-ray flux due to refluxing, the surviving electron fraction was recorded and this fraction of the x-ray energy was added to the x-ray energy from one pass. This was only added every odd pass, as the electrons will be propagating back towards the front of the target on even passes. The backscattered x-rays were also added to the total flux on the even passes. This was repeated until the numbers of electron number dropped below 5% of the original electron number; at this point the amount of x-ray energy added during each pass is negligible compared to the total.

The electron temperature distributions from the simulations were converted to a laser intensity and then incident energy using the Beg scaling and the parameters discussed in the experimental method 4.1. The total energy of the x-rays created by the electrons was then multiplied/normalised to adjust it to the energy estimated in the laser pulse. The x-ray energy as a function of laser energy is shown in Figure 4.6. This model has a scaling to the power of 1.7, which is similar to the experimental data. The difference between the experimental data and the model may arise as GEANT4 does not take into account the collective behaviour of the electrons and the change in resistivity due to heating of the target [118, 119].

A model was developed by Fontaine [120] using numerical (PIC and Monte Carlo) and analytical simulations to calculate the dose per unit incident laser energy as a function of intensity and wavelength. A 2D model using a 6 μm pre-plasma matches closely with the experimental data [50, 101]; fitting this to a power law yields a power of $\approx$0.7. Dividing the values for the x-ray energy by the incident laser energy from the model developed by the author to convert to x-ray flux per unit incident laser energy also yields a value of 0.7. The basic model and experimental data agree well with each other and other models and experimental

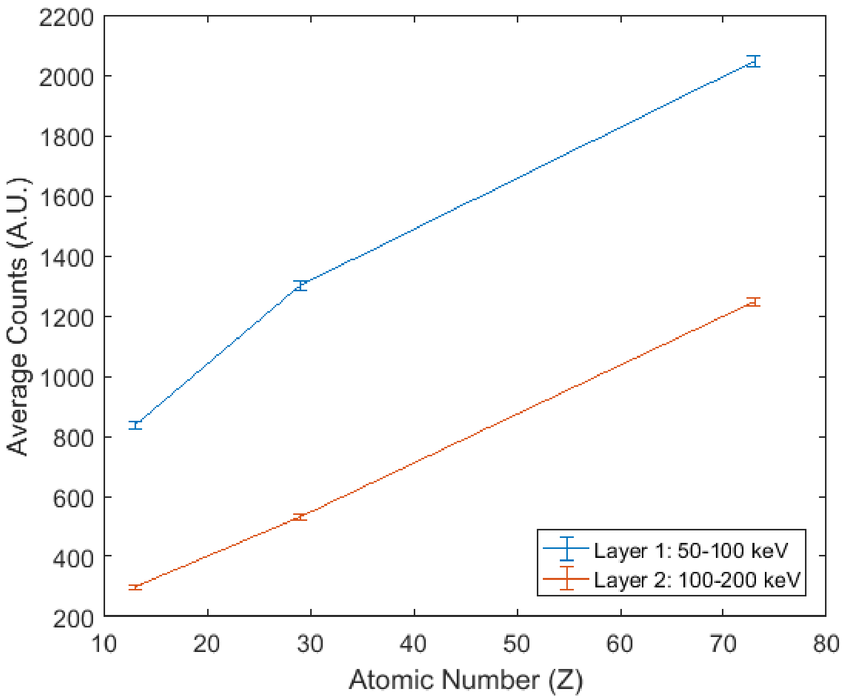

Figure 4.7: The average counts measured from the first two layers of the scintillator array as a function of atomic number of the target on the experimental set up discussed earlier.

data.

To determine the best target material for radiography, three targets were used during this experiment: aluminium, copper and tantalum. Three shots of similar energy (125-130 J) were made on all three targets with a thickness of 3 mm, the results are shown in Figure 4.7. As expected, the output signal of the scintillators increases with the atomic number of the target. The highest flux of x-rays are achieved with Ta, which is ideal for radiography and is the target used for the imaging shots shown later in this chapter in section 4.3.

The process of extracting the electron temperature is similar to that demonstrated for the betatron spectrum in Chapter 3. As the x-ray spectrum from the experimental data is unknown, an example spectrum can be used to calculate the output of the diagnostic and then compared to the experimental results. To create the example spectrum, GEANT4 can simulate a relativistic Maxwellian

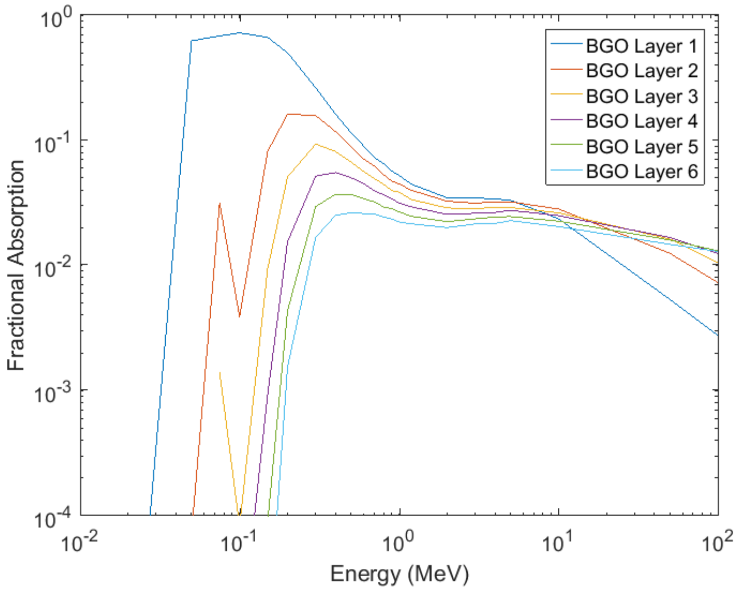

Figure 4.8: Fractional absorption of the BGO layers in the scintillator array with the addition of the Al port.

distribution of electrons travelling through a target; similar to the previous section. The response curves for the diagnostics are already known from previous GEANT4 simulations in Chapter 3. The modifications due to the aluminium port have been added and are shown in Figure 4.8. The port has the most impact on the lowest energy (< 30 keV) x-rays that are unable to propagate through it; the higher energy regions remain largely unaffected.

4.2.1 X-ray Spectra Analysis

The shape of the x-ray spectrum depends on the temperature of the electrons, as shown by equation 2.60 from Chapter 2. However, it is also modified by on the x-ray self-absorption of the target, which depends on both the target material and the target thickness. An example of the effect that different target materials have on the x-ray spectra is shown in Figure 4.9 a) from a GEANT4 simulation using a 1 MeV temperature distribution with an input electron number of 10^6. Aluminium converts less of the electrons into higher energy x-rays when compared to copper and tantalum, this is due to aluminium having a much lower atomic

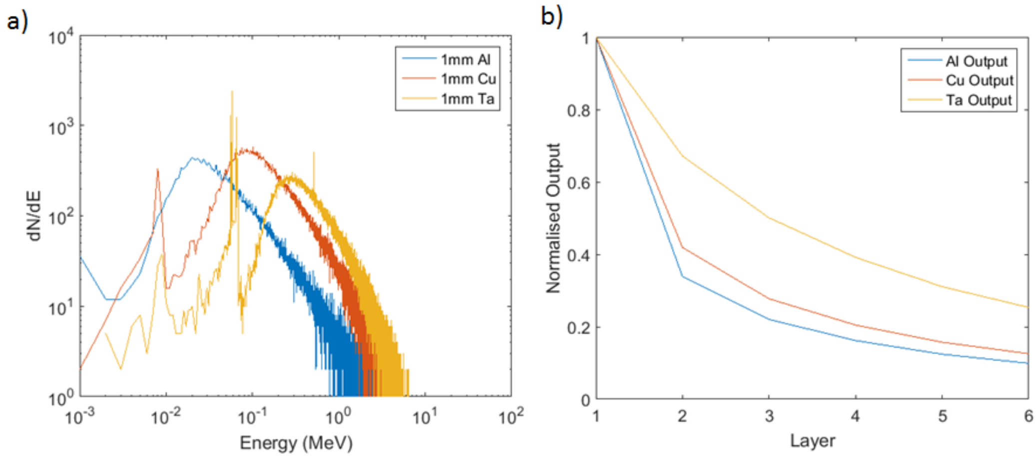

Figure 4.9: a) The x-ray spectra from GEANT4 simulations for a distribution of 1 MeV electrons incident onto three different 1 mm targets. The higher atomic number target produces higher energy spectra. Multiplying the spectra by the response of the diagnostic produces the outputs shown in b). Although the temperature of the electrons is the same for each of the x-ray spectra shown in a), the output of the diagnostic is vastly different.

number and mass density of atoms. The continuous spectral peak for each target differs due to the self-attenuation. For example, the k-edge of tantalum at ≈67 keV attenuated a large amount of x-rays that appear in the copper spectra. Also, each target has unique line emission which will affect the output of the diagnostic.

These differences in the spectra caused by the separate absorption from each material will lead to different outputs from the diagnostic even though the simulation was conducted with the same input distribution of electrons. This can be shown by multiplying these spectra by the response function, which yields the output shown in Figure 4.9 b). The outputs of the diagnostic differ by a significant amount, highlighting why each target needs to be simulated.

For targets in which the electrons do not lose all their energy on the first pass, refluxing must be taken into account. To understand the alteration that refluxing may cause to the x-ray spectra the electrons that reach the back of the target can be recorded and used in a new simulation allowing them to continue to create bremsstrahlung. This was done using the three targets used in the previous simulation (1 mm Al, Cu and Ta). The simulation was conducted three times,

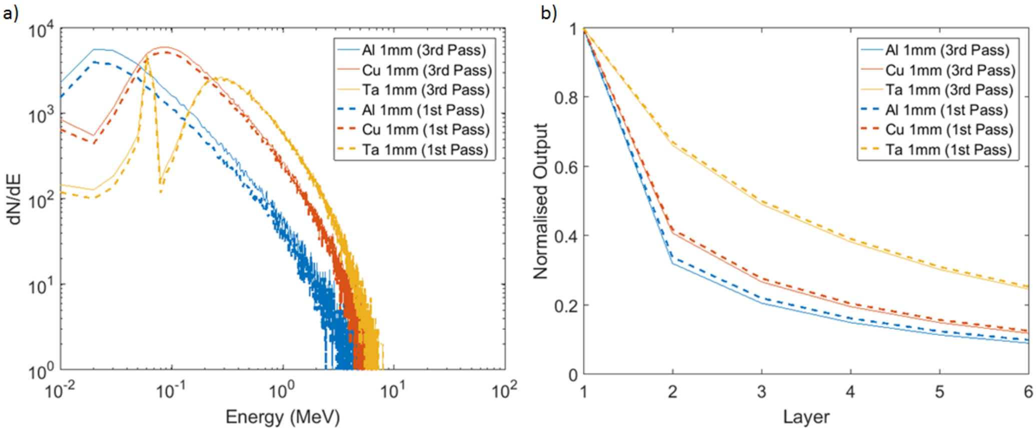

Figure 4.10: The refluxing/recirculation of the electrons inside the target cause a modification to the x-ray spectra as shown in a). The output of the scintillator array is also modified due to the refluxing, as shown in b). This modification is ≈5% for the Al target for a temperature of 1 MeV and ≈2% for 500 keV. Aluminium has the largest error as it has the largest remaining fraction of electrons.

allowing the electrons to complete three passes of the target. On the second pass, the backwards x-ray spectrum is recorded. The recorded x-ray spectra are summed together and are shown in Figure 4.10 a). The dotted lines represent the spectra from a single-pass whereas the solid lines are the spectra as a result of multiple electron passes. The largest effect is observed for the aluminium target as this target has the most electrons refluxing (≈15% remaining after 3 passes). The most notable aspect of the spectra is that the shape is very similar. Multiplying the new spectra by the response matrix yields the output shown in Figure 4.10 b). The maximum difference between these outputs is approximately 5% which is found when simulating the Al target. This measurement was repeated for a 500 keV electron temperature for Al where the difference decreased to ≈2%. This is expected as the temperature is lower; therefore the energy of the electrons are also lower and the electron flux will be more heavily attenuated on the first pass. The creation of the refluxing spectra is computationally time consuming, therefore the difference due to the refluxing will be simply included using these results as the difference is small (maximum of ≈5%).

The majority of laser shots on the experiment were conducted using 1 mm thick Al

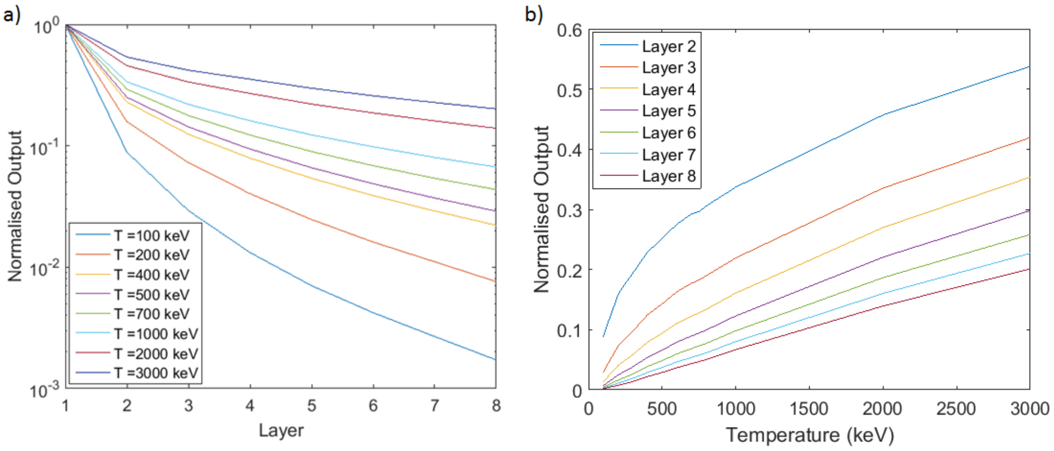

Figure 4.11: output of the diagnostic for a number of different electron temperatures through 1 mm Aluminium target. The output of the diagnostic is smoothly changing as a function of temperature as shown in b). Interpolation is conducted between temperatures that have not been simulated.

or 100 μm thick Ta. Single pass simulations are conducted for each of these targets for many temperatures. The normalised output for 1 mm Al is calculated and shown in Figure 4.11 a) for temperatures ranging from 100 keV to 3 MeV. Figure 4.11 b) shows the normalised output plotted as a function of temperature for the different layers which shows the output on each layer increase smoothly as the temperature increases. This allows for the data to be interpolated in-between the temperatures that have not been simulated; allowing for temperature extraction without running simulations at every input electron temperature.

Each measured shot is compared to the expected detector output for different temperatures; the temperature is varied until the difference is minimised as determined by the least-squares method. To take into account the uncertainties of the comparison, such as the background and the single pixel error present on the camera, the comparison is repeated many times. Each time the comparison is done, the uncertainties are added to the data randomly according to a normal distribution yielding many temperature fits which are then plotted in a histogram; an example of which is shown in Figure 4.12. The average is taken as the resulting temperature of that shot and the standard deviation of the histogram is used as the uncertainty in the temperature extraction.

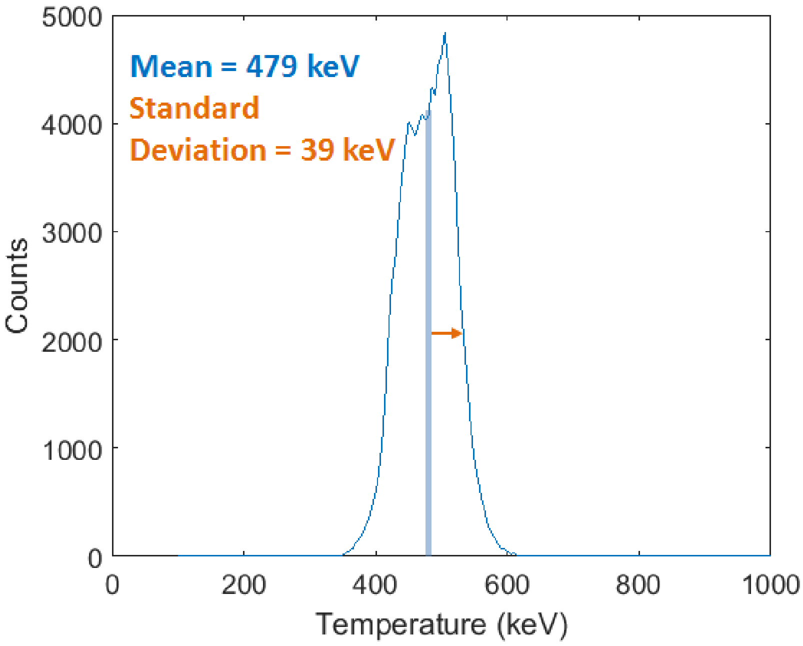

Figure 4.12: A histogram of the extracted temperature of a shot with the uncertainties randomly added to the data taken on a full energy shot onto 100 μm Ta. The mean of the distribution is taken as the temperature with the standard deviation as the uncertainty in that measurement.

The final temperatures, as extracted by the above analysis of the experimental, are plotted in Figure 4.13 with the previous data recorded from the entire field; this shows that the experimental data fits well with previous data in the field. The data fits more closely with the Beg or Haines scaling rather than the Wilkes scaling. This might be as expected as the Wilks scaling [121] is derived from the ponderomotive force, which primarily acts in the laser direction and the diagnostic sampled the distribution along the target normal. Often the angular distribution of the emitted x-rays is due to a combination of all the absorption and scattering mechanisms [87]. In future, a more comprehensive measurement of the x-ray spectra should be performed at many angles to better determine the internal hot electron temperature.

The highest flux of x-rays is achieved when the maximum laser energy is incident and the target is tantalum; this is shown in Figures 4.5 and 4.7 respectively. This is crucial for radiography for which the high photon numbers are required for good

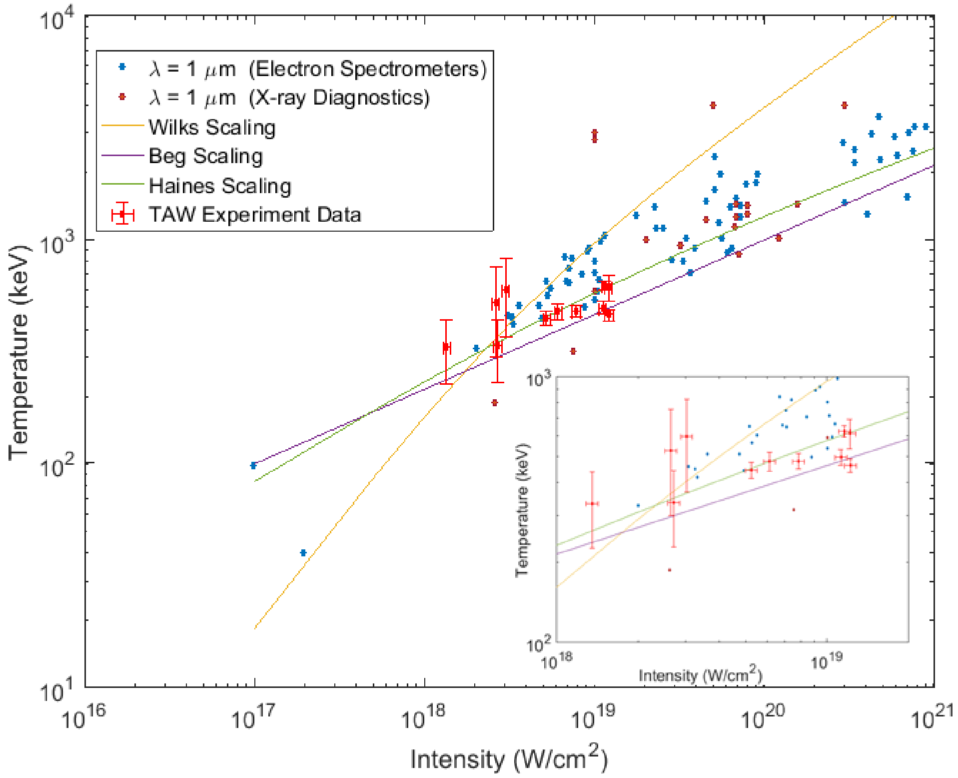

Figure 4.13: The temperatures extracted from the new results presented in this thesis taken with the diagnostic plotted along with the temperatures from the literature.

signal to noise ratio and therefore high image quality. For the highest energy and intensity achievable on this experiment the temperature of the electron/x-ray spectra is close to 700 keV.

4.3 Radiography

Having investigated the optimum conditions for x-ray generation, as a demonstration experiment, the x-ray beam was used to radiograph a variety of samples. The x-rays were recorded using an image plate and the CsI array discussed earlier. The majority of the imaging shots were conducted using a 100 μm Ta target and at maximum laser energy, unless stated otherwise.

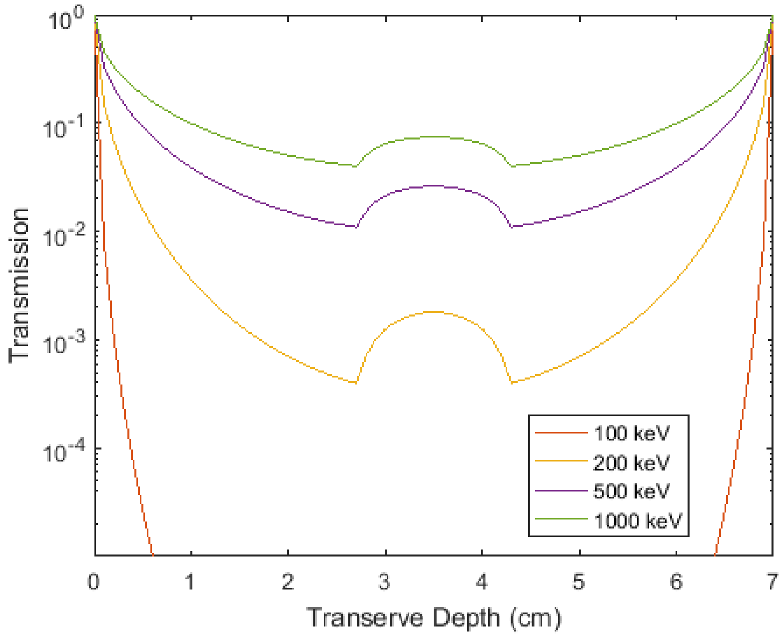

Figure 4.14: The calculated transmission using NIST XCOM attenuation tables of a steel cylinder with an outer diameter of 70 mm and inner diameter of 15 mm for different input x-ray energies.

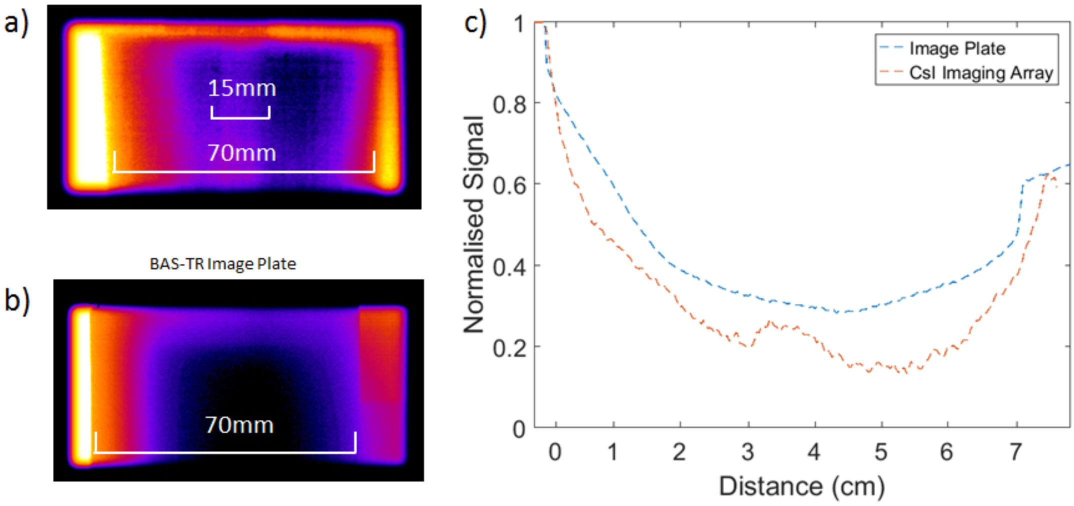

Figure 4.15: Figures a) and b) show the images of the object described taken on the CsI imaging array and an image plate respectively. It is clear that the inner hole is only visible using the CsI array. Taking a lineout of the images clearly shows the visibility of this feature, as shown in c).

To demonstrate the spectral response of each detector, a steel cylinder with an outer diameter of 70 mm and inner hollow region of diameter 15 mm was imaged using both an image plate and the CsI imaging array simultaneously. Figure 4.14

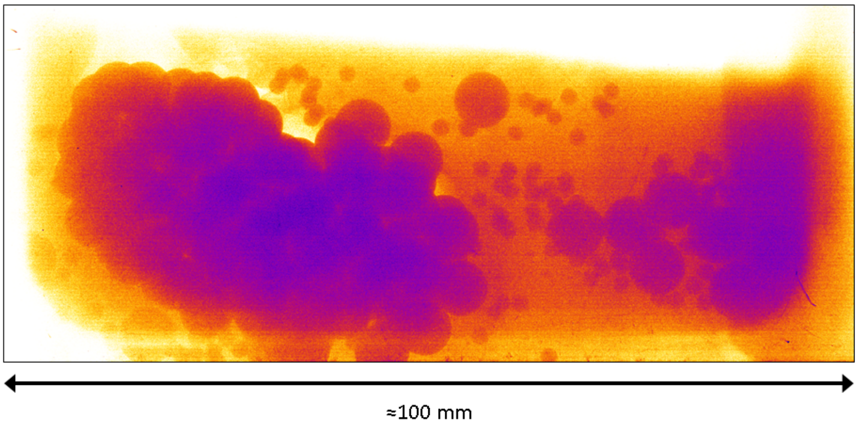

Figure 4.16: Radiograph of steel spheres of varying sizes embedded in concrete recorded on an image plate from a full energy (∼125 J) using a 100 μm Ta target. The smallest steel spheres (sub-millimetre) are still visible through the concrete.

shows the calculated attenuation of the material as a function of depth using the NIST XCOM attenuation tables; the lower energy x-rays are instantly attenuated. The hollow feature is only visible with x-rays with energies greater than 200 keV. As mentioned before, the image plate is primarily sensitive to less than 100 keV x-rays, with a peak sensitivity at ≈50 keV which, as shown in Figure 4.14, do not meaningful transmit through the object. The radiography recorded on the image plate in Figure 4.15 b) shows that the inner hollow region is not visible, as expected. The inner hollow region is visible on the CsI array in Figure 4.15 a) which is only possible if both the x-ray source and detector response to x-rays is greater than 200 keV. This is further highlighted in Figure 4.15 c) which shows lineouts from the two detectors. Note that the signal either side of the object is not the same, this is likely due to the x-ray beam being biased to one side of the image.

Additional radiography was conducted on a on steel spheres randomly embedded in concrete. The spheres vary in size from sub-millimetre to 2 millimetre. An image was recorded on an image plate using a 200 μm Ta target irradiated with ≈129 J which is shown in Figure 4.16. The smallest steel balls are visible in an radiograph. The object was also radiographed on the CsI array with varying

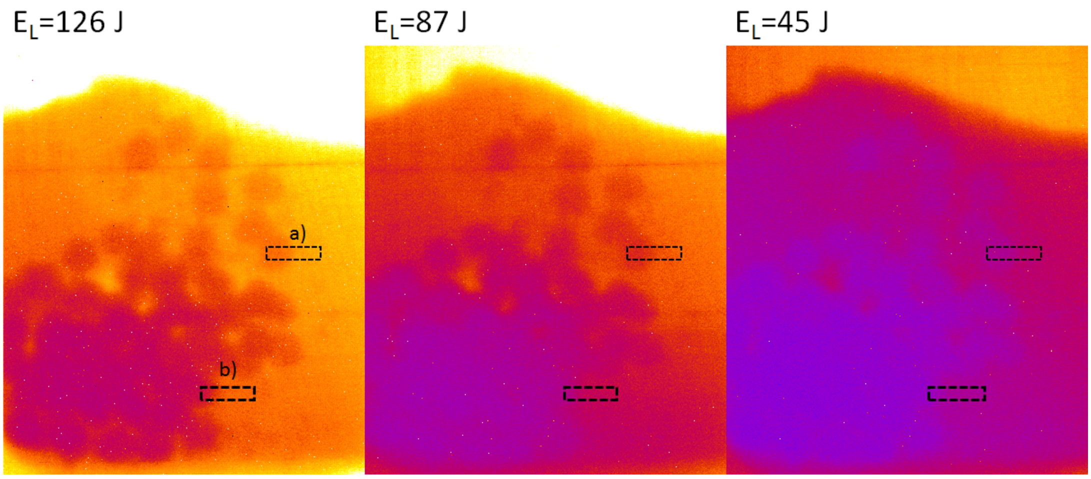

Figure 4.17: Three shots taken on 100 μm thick Ta with varying laser energy to radiograph steel spheres of varying sizes embedded in concrete and recorded on the CsI array. The flux of x-rays is clearly higher at the highest incident laser energies which also increases the visibility, see Figure 4.18 for a the lineout of the dotted areas a) and b).

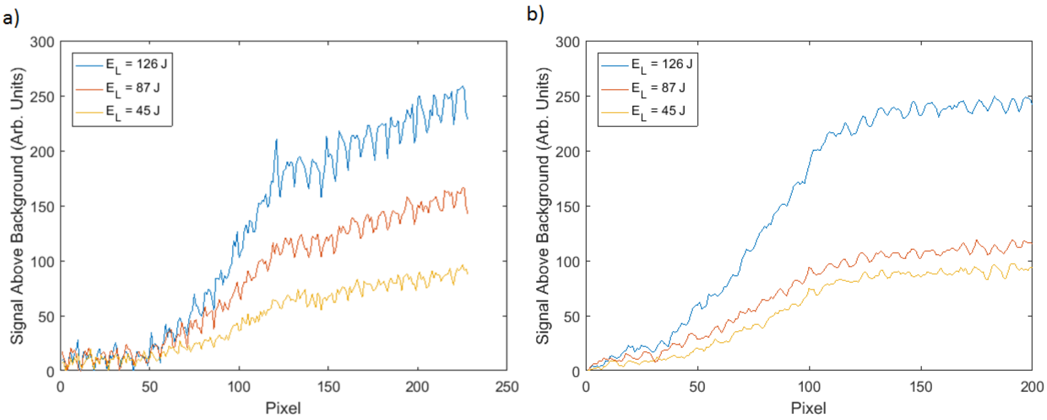

Figure 4.18: The lineouts of the steel sphere highlighted in Figure 4.17 a) and b). The increasing energy improves the contrast of the same features recorded on the CsI array highlighting the need for the highest flux of x-rays.

laser energy as shown in Figure 4.17. The steel balls are more visible when the laser energy is high, as would be expected as the x-ray flux increases, as shown in Figure 4.5. The dotted areas represent the lineouts shown in Figure 4.18 a) and b); the periodic features on the lineout are a result of the pixelation of the CsI array. The largest difference between the brightest and dimmest feature is from the highest energy shot. This highlights the need for high flux to provide the highest possible image-contrast when performing radiography.

4.4 Summary & Conclusions

Initially the scintillator based spectrometer was used to characterise a source of x-rays created as hot electrons travel through a solid target. The flux of the x-rays was shown to scale with the incident laser energy to the power of (1.8±0.1) for the first layer of BGO, as shown in Figure 4.5. The data was only taken on the BGO as the light emitted by the BC422q was too dim. An alternative scintillator with a higher light yield will be paired with BGO to ensure both types of scintillator can be used to characterise the source. The spectrum of the x-rays was shown to scale from 400 keV and 750 keV between the incident laser intensities 8-12$\times10^{18}$ W/cm^2. This is in closer agreement with the Haines and Beg scaling laws rather than the Wilks scaling discussed at the start of this chapter and shown in Figure 4.13. This is consistent with a lot of the data from the literature which suggest that the hot electron temperature does not reach temperatures as high as those predicted by the Wilks scaling.

Radiography was then performed on a number of objects; the two discussed here were the hollow steel cylinder and concrete containing steel spheres. More x-ray radiography images can be found in Jones *et al* [112] and Brenner *et al* [13]. Two detectors were used to perform the radiography: image plate and a 2D-CsI array. The higher energy sensitivity of the CsI was able to detect x-rays that penetrate the steel cylinder allowing for the hollow region to be observed. This was not possible on the image plate as it primarily samples lower energy x-rays. The steel spheres in the concrete were observable on both detectors with the energy scan on the CsI array showing that visibility increases with higher incident laser energy.

To further the understanding of the hot electron population inside the target, multiple scintillator arrays should be deployed at many angles around the target. This method would allow for any angular distribution of the hot electron spectra/temperature to be measured. Using the scintillator spectrometer in conjunction with the wraparound diagnostic discussed in Chapters 3 and 6 would also allow for information to be obtained about the escaping and internal electrons simultaneously. This would provide greater insights into the fields that the electrons experience on the rear surface.

It has been demonstrated that the CsI array can image higher energy features when compared to the image plate; this is due to its attenuation shown in Figure 4.4. To improve the high energy radiography, detectors with higher spatial resolution need to be developed so that they can complete with the ≈100 μm resolution of the image plate. Additionally, the CsI has the capability of operating at a much faster repetition rate than the image plate, which is ideal for newer laser systems.

Chapter 5

Penetrative Imaging using Backscattered X-rays Produced by Wakefield Accelerated Electrons

Backscatter x-ray imaging is the process of directing x-rays at a sample, detecting the resulting backscatter x-rays and spatially resolving an object. This imaging technique has some advantages over the transmissive absorption imaging that is often used. One of the major advantages is that the detector is on the same side as the source; this allows imaging of objects that previously could not be imaged (buried objects or objects a large distance from the source for example). This technique is highly applicable for security imaging [122, 123, 124, 125, 126], archaeology [127] and single-sided structural inspection.

Developments of backscatter imaging techniques in recent years have shown its great potential for a number of applications. Industrial sized demonstrations of the performance of x-ray backscatter imaging on vehicles and containers to create high resolution images of the contents [122, 123] have already been conducted.

Work by Paulus *et al* [125] has shown that is also possible to discriminate between material with different densities and effective atomic numbers. This is highly applicable to the detection of hazardous materials, such as plastic explosives.

The source of these backscatter x-rays is usually through Compton and Rayleigh scattering. Compton scattering is the inelastic process in which the x-ray scatters off an electron. The energy transfer from x-ray to electron is related to the angle by which the x-ray is deflected; lower energy x-rays are more likely to be deflected by larger angles and be backscattered. Rayleigh scattering is an elastic process in which the x-ray loses no energy when scattering. The cross section for Rayleigh scattering is much lower than that of Compton scattering which, as a result, is considered the primary process for creating backscatter x-rays.

The angular cross sections for Compton scatter is given by the Klien-Nishina formula [128],

$$\frac{d\sigma}{d\Omega} = \alpha^2 r_c^2 P(E_\gamma,\theta)^2 \left[P\left(E_\gamma,\theta\right) + P(E_\gamma,0)^{-1} - 1 + \cos^2\left(\theta\right)\right]/2 \tag{5.1}$$

where α is the fine structure constant ($\approx 1/137$), the coulomb radius $r_c = \hbar m_e c$ ($\approx$0.38 pm), E_γ is the incoming x-ray energy and θ is the angle of the emitted x-ray. $P\left(E_\gamma,\theta\right)$ is the ratio of the photon energy before and after the collision with the electron,

$$P\left(E_\gamma,\theta\right) = \frac{1}{1 + \left(E_\gamma/m_e c\right)\left(1 - \cos\left(\theta\right)\right)} \tag{5.2}$$

For x-ray energies from 10-500 keV, Figure 5.1 a) shows the angular distribution of the scattered x-rays. The highest proportion of backscattered x-rays come from the lowest energy x-rays. However, Compton scattering is not the dominant attenuation process until photon energies exceed $\approx$100 keV. Using SiO_2, iron and carbon as examples, the ratios of Compton scattering to each of the other x-ray attenuation processes was calculated and then multiplied by the integrated backscatter cross-section to determine the energy at which Compton

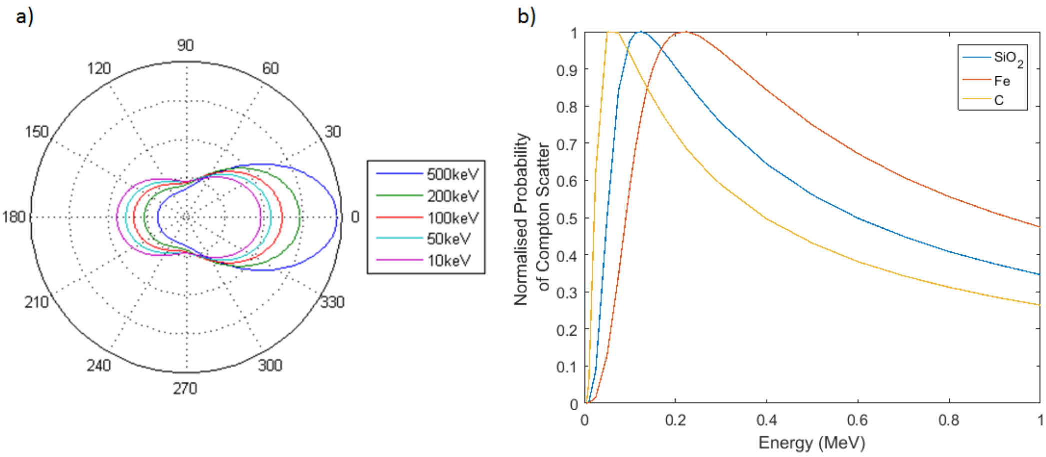

Figure 5.1: a) The angular emission of x-rays for energies ranging from 10-500 keV given by the Klien-Nishina Formula. As the energy increases the x-ray is more likely to be scattered in the forward direction. Although the number of x-rays that are backscattered increases as the energy of the incident x-ray decreases, scattering is not the primary effect. Taking the ratio of Compton scatter to other attenuation process and multiplying by the integrated backscatter cross-section yields results in b). b) shows the normalised probability that the attenuation is caused by Compton scatter for three different materials.

scatter dominates; the result is shown in Figure 5.1 b). For SiO_2, x-rays with ~100 keV are the most likely to undergo backscatter. For materials with higher atomic numbers, such as Fe, this optimum energy increases.

The energy of the backscattered x-rays is limited due to the conservation of momentum. As the incident x-ray energy tends to infinity, the energy of Compton backscatter x-ray tends to 511 keV and 255 keV at 90 and 180 degrees respectively due to the rest mass of the electron.

As discussed in Chapter 2, x-ray attenuation and penetration is dictated by the Beer-Lambert law, as shown in equation 2.62. For a given material and a fixed input energy, the transmission will fall off exponentially, limiting the depth that can be probed.

Secondly, the x-rays that are backscattered through Compton scatter will have less energy than they have initially. This also limits the depth at which the backscattered x-ray can return from, as these will also be exponentially attenuated. This constraint has been shown in Heuvel *et al* [124] when simulating the detection of landmines. The majority of x-rays are unable to penetrate to the relevant distance and return to the surface. Increasing the energy of the input x-rays does increase the penetration depth. However, this reduces the likelihood of the backscatter flux escaping and also decreases the resolution as there will be multiple scattering events.

An alternative approach would be to create the x-rays inside the sample. Electrons can be used to create x-rays via bremsstrahlung deep in the sample material. An electron with the same energy as an x-ray cannot penetrate any deeper. However, through laser-wakefield acceleration it is relatively easy to produce incredibly short bunches of electrons (<100 fs) with energies above 100 MeV. Electrons with this energy would penetrate much deeper than x-rays from sources currently commercially available (<500 keV).

Additionally, for traditional backscatter techniques to achieve high spatial resolution they must be collimated which will typically cause significant reduction to the useful flux. This then requires long integrated acquisitions to be conducted to improve the signal to noise ratio. Electron beams produced from laser-wakefield interactions typically have divergences on the order of milliradians [129]. This means that no further collimation is required and single shot measurements can be conducted.

In this chapter, the basics of a new technique of using electrons as the source of x-ray backscatter within the sample will be discussed. A basic analytical model is created that demonstrates the advantages of using an input source of electrons over x-rays. GEANT4 is then deployed to further demonstrate the advantages of this technique. GEANT4 is used again to test the technique of using short bunches of electrons to temporally resolve distances between objects. This technique is also investigated experimentally; the first time this imaging technique has been demonstrated. Finally, a collection of ideas are presented to further the applicability of the electron/x-ray backscatter techniques.

5.1 Modelling

To begin, a model is created to accurately replicate the energy lost from electrons in a material and conversion of the energy loss into bremsstrahlung x-rays in the forward direction. Information can be obtained from the ESTAR NIST database [130] regarding how much energy electrons will lose per unit distance. Figure 5.2 shows the stopping power of electrons for sand (SiO_2). For electrons below 50 MeV the majority of the electron energy is lost via collisions within the material. The second process, losses due to electrons radiating, is responsible for the production of Bremsstrahlung inside the material. Using these tables, the average energy the electron loses per unit depth and also the amount of that energy that will go into the creation of x-rays can be calculated. The remaining electron energy is calculated in a step-like process; the amount of energy lost per step ($\partial E/\partial x$) is calculated and subtracted from the previous energy. This is given as,

$$E_{e(s)} = E_{e(s-1)} - \frac{\partial E_{e(s-1)}}{\partial x} \tag{5.3}$$

where s is the integer step number, $E_{e(s-1)}$ is the electron energy at the previous step and $\partial E_{e(s-1)}/\partial x$ is the total electron energy lost over the step. The amount of x-ray energy at a given step ($E_{x(s)}$) is calculated in a very similar way except it includes additional attenuation term ($\partial E_{x(s-1)}/\partial x$); and is given as,

$$E_{x(s)} = E_{x(s-1)} + \frac{\partial E_{e\rightarrow x(s-1)}}{\partial x} - \frac{\partial E_{x(s-1)}}{\partial x} \tag{5.4}$$

where $\partial E_{e\rightarrow x(s-1)}/\partial x$ is the amount energy lost by the electrons that goes into radiative losses.

The x-rays that are created in each step, will have a continuous spectra reaching the maximum energy of the electrons at that depth. To simplify the problem, the

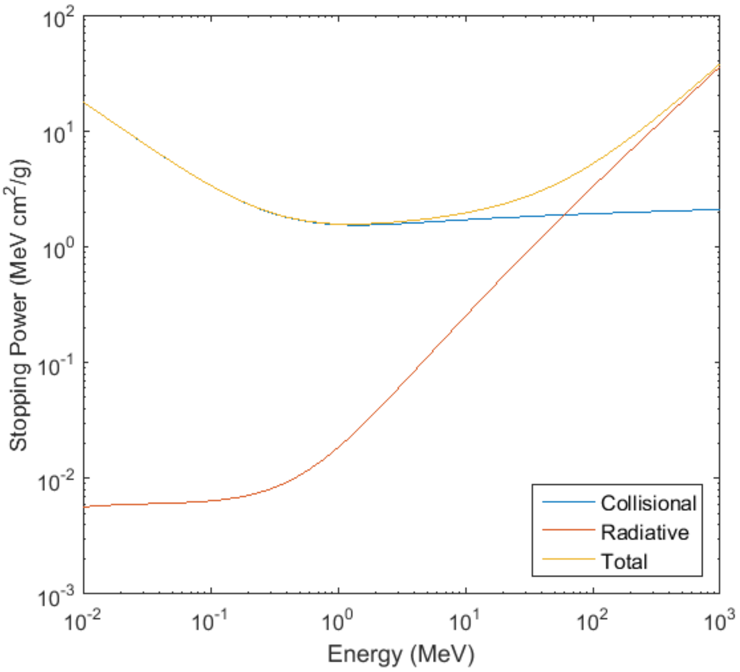

Figure 5.2: The stopping power of electrons in SiO_2 taken from the ESTAR NIST database. The electrons primarily lose energy by two different process, collisional and radiative emission. Radiative emission is the source of bremsstrahlung x-rays and only becomes the dominant process above ≈50 MeV; below this the primary process for energy loss is collisional.

average energy of the x-ray flux is assumed to be the energy that is lost in that step to x-rays taken from the ESTAR tables.

If we now consider an electron population with a singular initial energy, the estimated energy loss of the electrons and production of x-rays and their attenuation inside a target can be calculated. The total energy as a function of depth is shown in Figure 5.3 for 100 MeV electrons in SiO_2. The electrons entirely lose their energy by 200 mm in the target. The total x-ray energy increases as the electron energy decreases. As the electron energy decreases, the amount of the energy that goes into creating x-rays also reduces. This causes the x-ray energy to plateau before the electrons energy is reduced to zero. After the x-ray energy stops increasing, the attenuation of the material begins to reduce the total x-ray energy. This relationship has an exponential decay as expressed the Beer-Lambert law, equation 2.62.

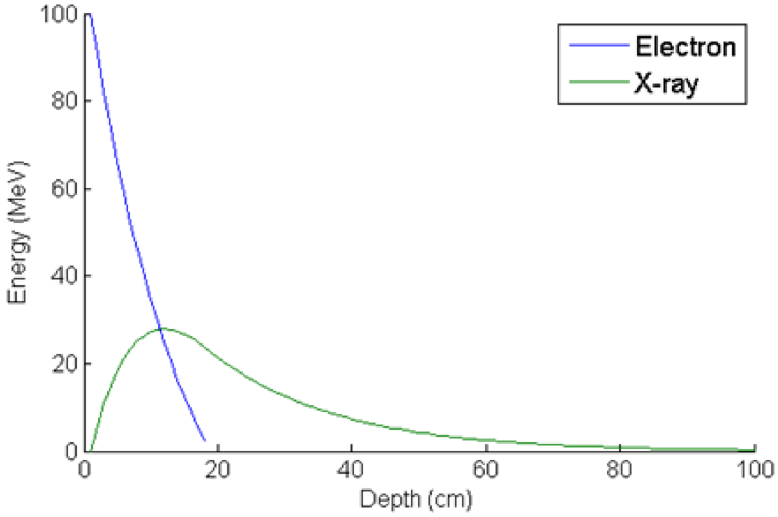

Figure 5.3: The average energy the electrons and the total energy of the resulting emitted x-rays as a function of depth. The electrons, with an initial energy of 100 MeV, lose their energy through the two processes discussed earlier, collisional and radiative. The radiative process creates an x-ray beam that gains energy from the electron beam. The electron energy reaches zero at just below 200 mm. The x-rays stop gaining energy from the electrons as their energy reduces. The x-ray energy starts to be attenuated exponentially from the material, dictated by the Beer-Lambert Law.

The amount of backscattered energy can be calculated using the Klien-Nishima formula, as shown in equation 5.1. First the amount of Compton scatter as a fraction of the overall attenuation is estimated. Then, the fraction of energy backscattered compared to the total energy scatter is calculated. Considering SiO_2 again and x-ray energies of ≈500 keV, Compton scatter makes up ≈97% of the attenuation and ≈25% of those x-rays will be backscattered. The average energy of these backscattered x-rays will be ≈200 keV. Using these values the backscattered x-rays per unit length is shown in Figure 5.4, which has a peak demonstrating that the majority x-rays are coming from deeper inside the material. This peak occurs for two reasons; firstly the total x-ray numbers are initially increasing inside the target as a function of depth, as shown in Figure 5.3. Therefore, the number of backscattered x-rays is also increasing. Secondly, the energy of these backscattered x-rays is limited to ≈250 keV due to the conservation of momentum; this restricts the depths at which they can return from.

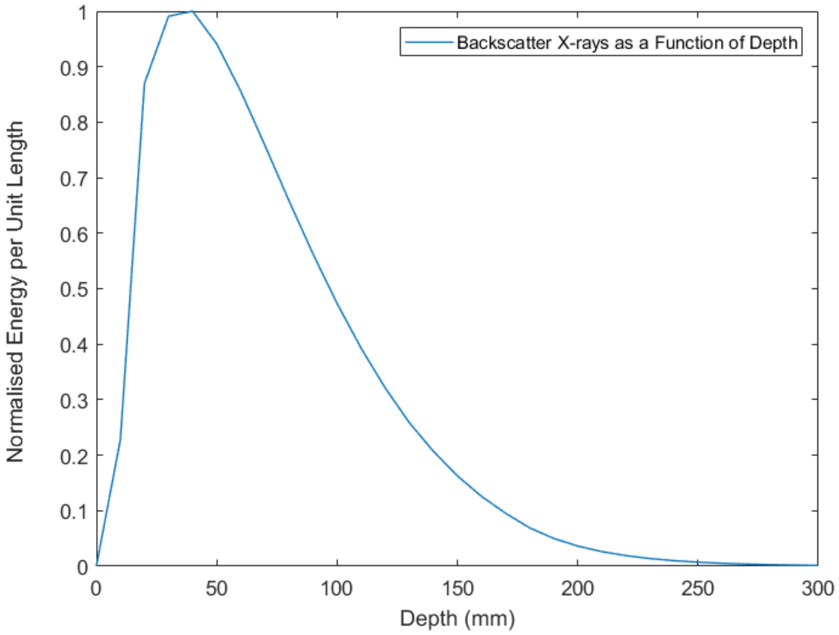

Figure 5.4: The normalised backscatter x-rays as a function of depth in SiO_2. The depth at which these x-rays return from is limited by the energy of the backscattered x-rays, which due to the conservation of momentum is half the rest mass of the electron the x-rays scatter off (≈255 keV). This limit to the return depth and the increase in number of electrons inside the material shown in Figure 5.3 leads to a peak in the number of backscatter x-rays returning from inside the material.

This demonstrates that this method has more x-rays coming back from inside the material than from the surface, which is the main limitation of traditional backscatter techniques.

This model lacks detail in a number of crucial areas. Firstly, although the scattering of the x-rays is taken into account and calculated using the Klien-Nishima formula, a single x-ray can undergo multiple scattering events. This is important as Compton scattering is not angularly or energy symmetric in the forward and backward scatter directions; therefore, multiple scattering events do not average out. Secondly, although the energy loss and creation of electrons and x-rays over an entire distribution can be averaged to a continuous function, in real life some electrons may lose all their energy in one interaction creating an x-ray with all of the electrons immediately preceding energy which is not taken into account in

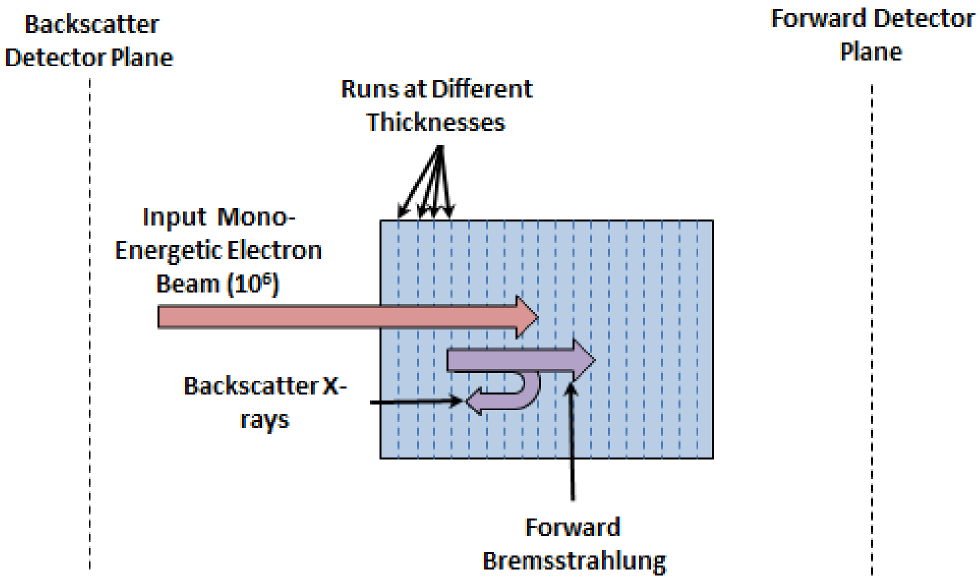

Figure 5.5: Schematic of the GEANT4 setup used to model the forward electron, forward x-rays and the returning backscattered x-rays. The simulations were conducted using 10^6 incident electrons and repeated for different depths of materials. The particles were detected using two large detectors (1×1 m) either side of the probed object.

the model. Finally, with input electron energies above 100 MeV, pair production will become a large source of secondary electrons, positrons and, through annihilation, 511 keV x-rays. Analytically modelling these effects becomes complicated and therefore the best method is to use GEANT4 as this can simulate all of the previously mentioned effects.

5.1.1 GEANT4 Modelling

GEANT4 was setup as shown in Figure 5.5. The simulation was undertkaen multiple times for a single mono-energetic electron energy. The thickness of the target material was increased in steps for each simulation to properly calculate the amount of stopping, x-ray creation and x-ray backscatter per unit depth. To ensure statistical reliability of the simulation, 10^6 input electrons were used each run. Two ideal detectors were placed at the rear and front of the target to detect the forward escaping and backscattered particles; these detectors are large to capture the majority of the particles in both directions.

Firstly, the electron energy remaining at each depth step in the GEANT4 simulation was compared to the electron energy from the model. The results in Figure 5.6 a) for an initial electron energy of 50 MeV, showing that the analytical model closely matches the GEANT4 data till a depth greater than 100 mm. At this point the energy of the model is reduced to zero, whereas GEANT4 has a number of remaining electrons with a total energy in the order of $5{\times}10^{-3}$ of the initial input energy. These electrons are created through the photoelectric effect from x-rays that have penetrated deeper into the material as they appear to have an exponential decay.

To demonstrate that the majority of x-rays that are backscattered come from inside the target, the total number of x-rays as a function of depth was recorded; this is shown in Figure 5.6 c). Initially for shallow depths the number of backscattered x-rays is low; this is because the number of x-rays in the forward direction is also initially low, Figure 5.6 b). As the depth increases, the number of backscatter x-rays increase rapidly. Finally, the backscatter x-ray numbers plateau as the x-rays are not energetic enough to escape the object from the depths at which they are being created. The rapid increase in the middle section of the graph is the depth where the majority of the backscatter x-rays are being created. A curve is fitted to the graph shown in Figure 5.6 c) to smooth out the results then the gradient in calculated. Figure 5.6 d) shows the gradient which represents the number of backscattered x-rays that have escaped per unit depth; a comparison with the analytical results is also shown. The analytical results peak at a lower value ($\approx$35 mm) to the results from GEANT4 ($\approx$80 mm).

The differences arise from the physical processes mentioned earlier that are difficult to analytically model. An example of a typical backscattered x-ray spectrum for SiO_2 is shown in Figure 5.7 which further highlights the number of physical process occurring in these interactions. There is an obvious 511 keV peak that arises from pair production and annihilation. There is also a large discontinuity

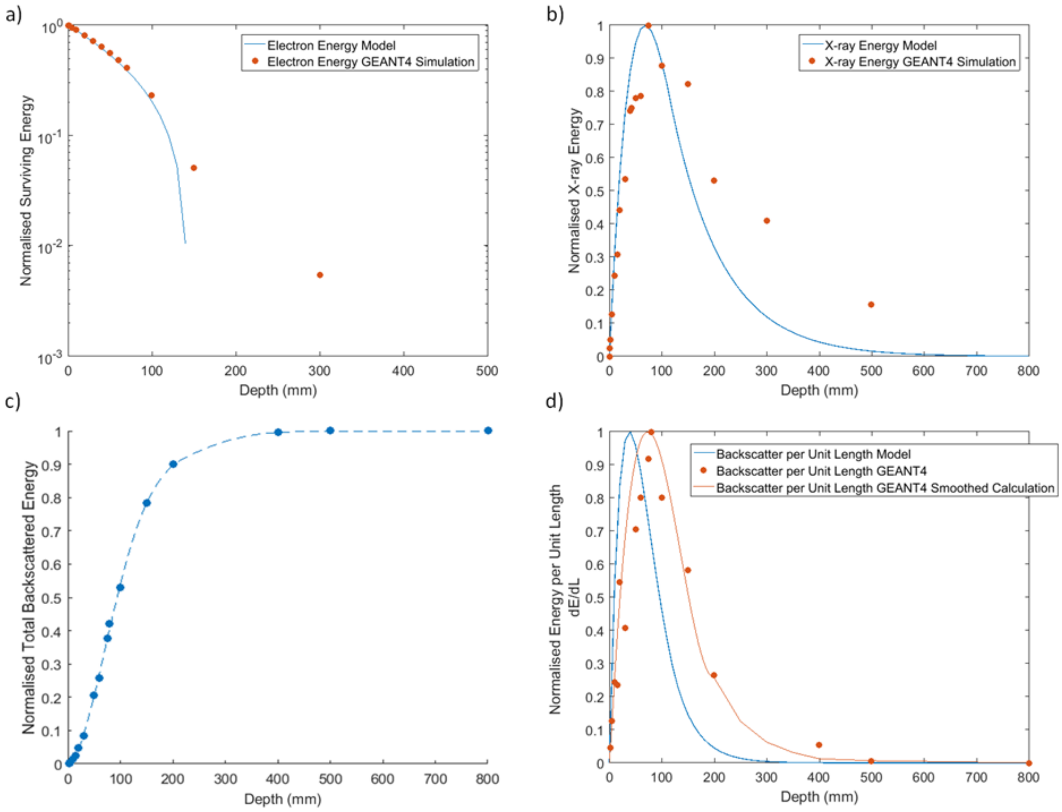

Figure 5.6: a) A comparison between the model and GEANT4 simulation for the electron energy when propagating through a material. The normalised forward x-ray energy for different depths of material, as shown in b), which increases before the energy in the electron beam is depleted and the x-rays begin to be attenuated by the material. c) shows the total normalised energy of x-ray backscatter received as a function of depth whereas d) shows the amount of backscatter per unit depth as a function of depth.

either side of the 511 keV line that occurs due to the 511 keV x-rays scattering and being Compton down-shifted in energy. The peak of the continuous spectrum occurs at ≈100 keV, whilst below the x-rays are self-absorbed by the SiO_2.

The simulation was repeated with different input electron energies, the resulting backscatter per unit depth is shown in Figure 5.8. The peak of the signal does not appear to penetrate much deeper than 100 mm into SiO_2 when changing the energy of the electrons from 100 to 500 MeV. There is however, an increased amount of x-rays coming from deeper in the sample that is located in the tail of the backscatter for increasing energies.

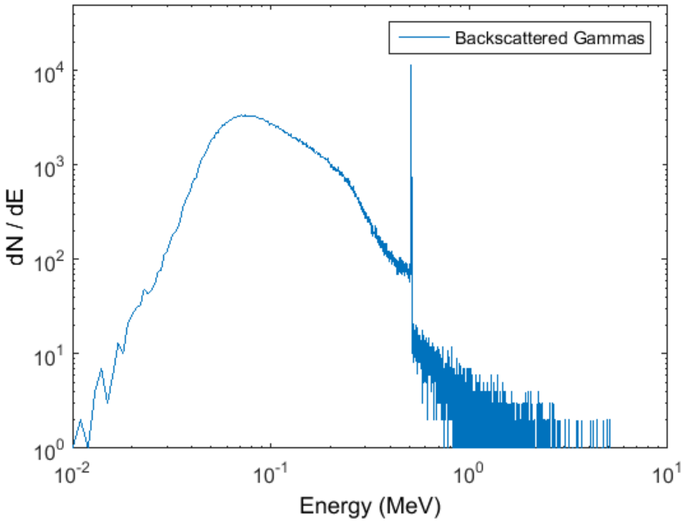

Figure 5.7: Typical backscattered x-ray spectrum from SiO_2 modelled using GEANT4. This spectrum in particular is from a 100 MeV electron beam incident onto a 100 mm thick SiO_2 block.

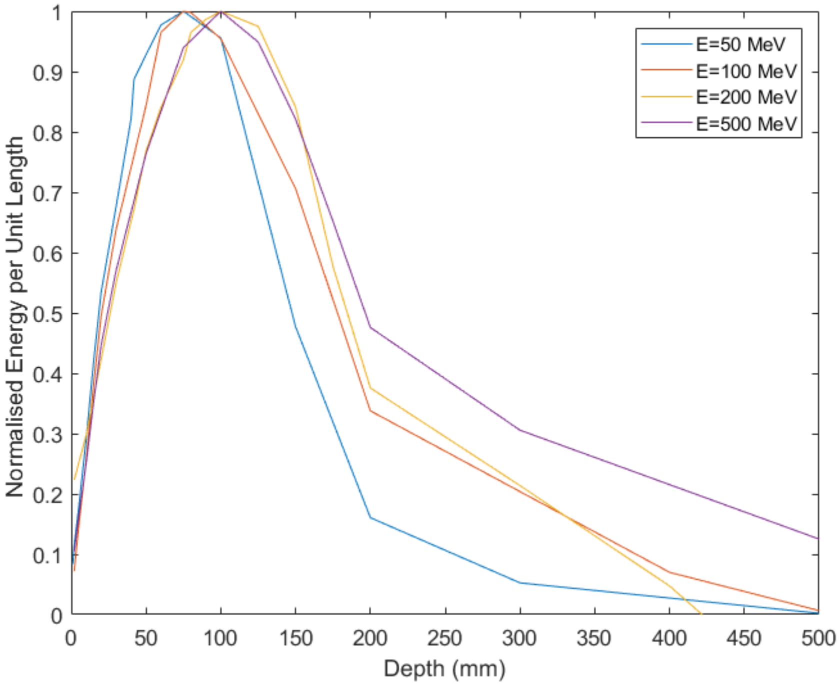

Figure 5.8: Normalised backscatter signal for a number of different incident electron energies. The largest change appears in the tail of the signal where for higher energy electron beams more signal is able to return from deeper depths in the sample.

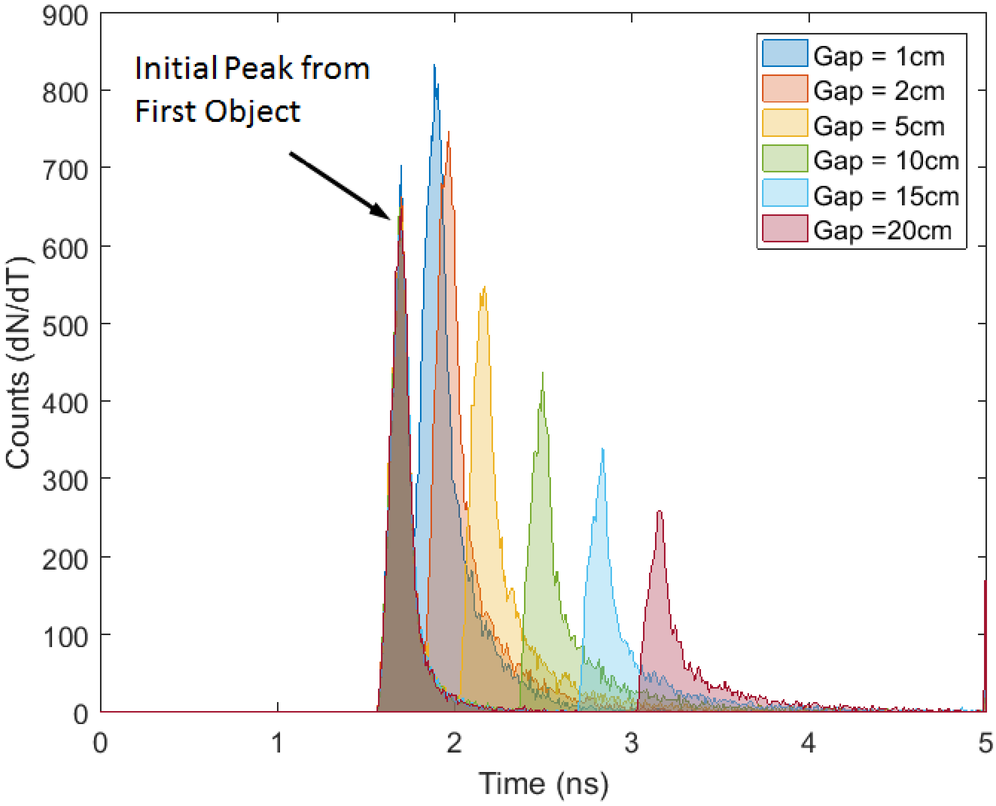

Figure 5.9: Demonstration of temporally resolving distances between objects using a short pulse of electrons. Two Al plates that are 20 mm thick are placed at different distances apart. An electron beam of 250 MeV is sent into the Al plates and the times at which the backscattered x-rays reach a detector 30 mm from the first plate are recorded. The temporal separation of the peaks increases as a function of gap size as expected. This shows that short bunch, such as from laser-Wakefield interaction, can be used to temporally resolve distances between objects (sub-cm).

A property of electrons from laser-wakefield acceleration can be utilised to further enhance the capabilities of this technique. Typically, lasers that are used in laser-wakefield interactions, such as the Astra-Gemini laser discussed in Chapter 3, have pulse durations below 100 fs. The electrons accelerated from this mechanism will therefore have a bunch length of a similar duration. For particles travelling at the speed of light 100 fs is approximately 30 μm, which means the temporal information of the backscattered x-rays will have a spatial resolution of sub millimetre. In reality however, multiple scattering effects will reduce this temporal resolution.

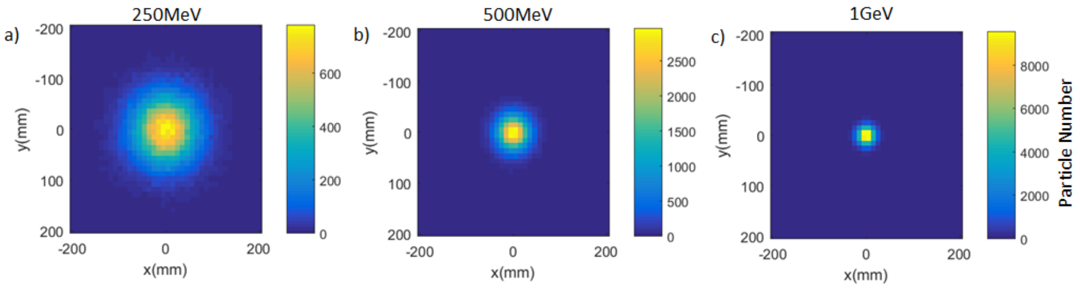

Figure 5.10: Spatial profile of an electron beam propagating 10 m in Air for a) 250 MeV, b) 500 MeV and c) 1 GeV electrons. The spatial profile of the 1 GeV beam is much smaller than the 250 MeV and 500 MeV case.

To demonstrate the temporal resolution technique, two Al plates were set-up in GEANT4 with a gap between them. 10^6 mono-energetic particles are incident onto the objects with zero temporal spread, which is unachievable experimentally but chosen to demonstrate the technique. The backscatter is recorded using a 200×200 mm detector 30 mm from the first object. The size of the detector is large to reduce the number of incident electrons required to achieve good signal to noise. The results from 250 MeV electrons for a number of different gap distances are shown in Figure 5.9. The temporal separation between the peaks increases with the distance as expected. There is sharp rising edge before every peak, this is likely due to the large size of the detector which will allow for small path differences. These results demonstrate that the technique of temporally resolving the backscatter x-rays will yield information about the separation of the objects down to sub-centimetre resolution or the current detector limitations.

The benefits of using electrons as the source of backscatter x-rays has been shown in this section, however the practical limitations must also be considered. The deployment of an electron beam in air must be taken into account due to the transmission and scattering effects. These scattering effects will cause the electron beam to expand affecting the spatial resolution of the backscatter technique. A GEANT4 simulation was conducted using 10^4 electrons travelling through air where detectors were placed at 1, 10, 50 and 100 m; recording spatial position of each electron.

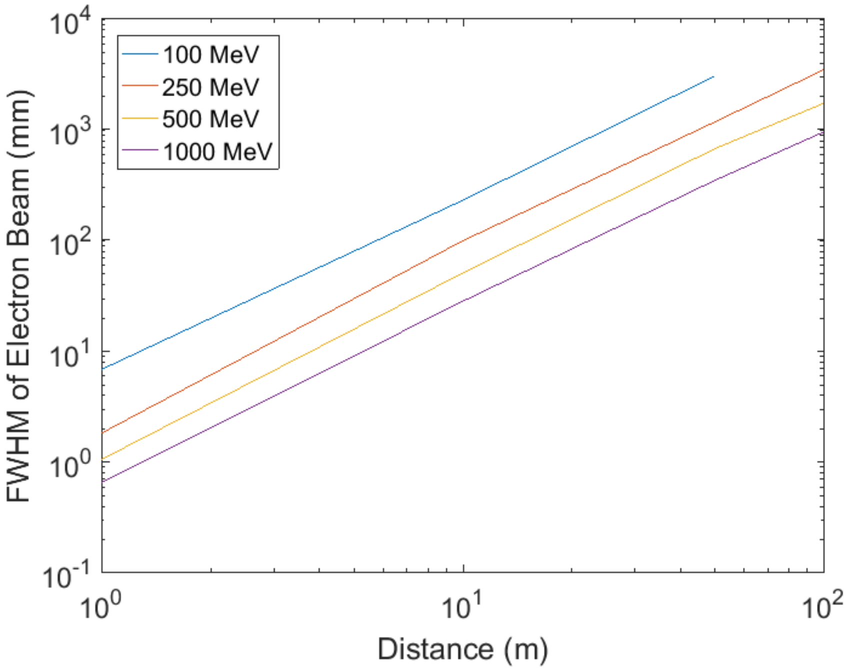

Figure 5.11: The FWHM of the scattered electron beams with energies from 100 MeV to 1 GeV recorded at 1, 10, 50 and 100 m. The smallest beams are recorded for the largest electron energies.

The resulting spatial profile of a 250 MeV, 500 MeV and 1 GeV electron beam at 10 m is shown in Figure 5.10. The 1 GeV electron beam has a much smaller beam width than the 100 MeV beam. The half-width of the electron beam as a function of distance in air is shown in Figure 5.11 for energies ranging from 100 MeV to 1 GeV. As expected, increasing the energy of the initial electron beam reduces the beam half-width.

When the electrons propagate through air, as well as scattering, they lose energy to collisions and bremsstrahlung. The fractional remaining energy of electrons and x-rays is shown in Figure 5.12. Increasing the energy increases the remaining fraction of electrons, however it creates more x-rays. The number of x-rays created could become an issue as they may cause a backscatter spike with the surface of a sample.

The number of remaining electrons is proportional to initial electron energy, although for an initial electron energy of 100 MeV, at 100 m the number of electrons

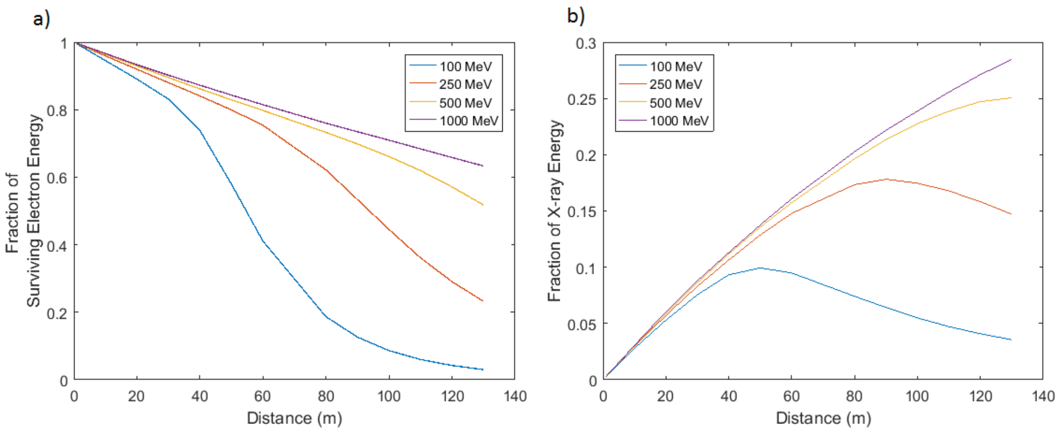

Figure 5.12: The remaining fraction of the a) electrons and b) x-rays for given incident electron energy as a function of distance.

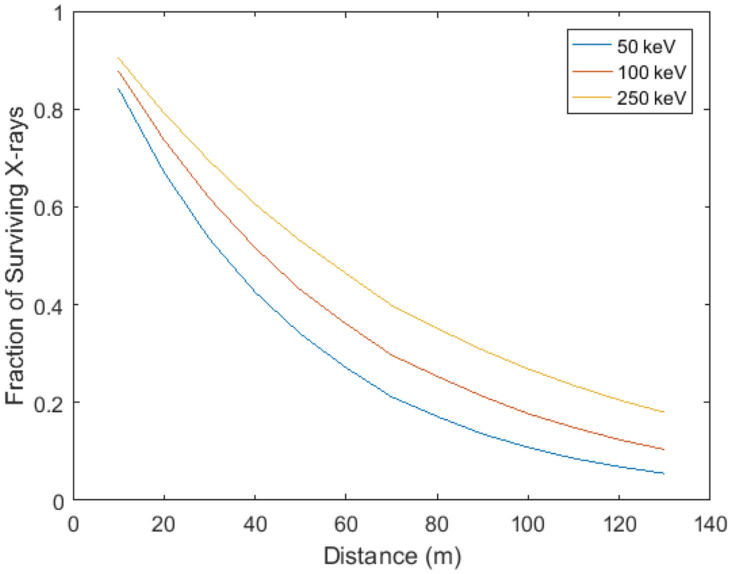

Figure 5.13: The survival fraction of 50, 100 and 250 keV x-rays as energy as a function of distance in air.

drops below 10%; with actually more energy contained in the emitted x-rays at this distance. For greater distances than 40 m ideally the electron energy is kept above 250 MeV where greater than 80% remain. Figure 5.13 shows the remaining fraction of x-rays as a function of distance for input x-ray energies of 50, 100 and 250 keV. This shows that x-rays with energies that are readily available commercially from x-ray tubes will stop much quicker than the available electron energies from laser-wakefield sources.

To test the techniques discussed previously, an experiment was conducted where a high energy electron beam was created. The experimental methods and results are discussed in the following section.

5.2 Experimental Methods

An experiment was conducted using the Astra-Gemini laser system where the laser of 800 nm wavelength delivered ≈10 J in ≈50 fs pulses onto a high-pressure gas jet [131]. The gas used was helium with a mix of 5% nitrogen, with an electron number density of approximately 3.9×10^{18} cm^{-3}. A basic schematic of the setup is shown in Figure 5.14. The laser is focused onto the gas jet using an F/20 parabola down to a focal spot with a FWHM of 25 μm. The resulting peak intensity of the laser is $\approx 1 \times 10^{19}$ W/cm^2. After propagating through the gas jet, the laser is blocked at the rear of the target chamber by a 3 mm steel port, at which the intensity of the laser is below the damage threshold.

The electrons accelerated from the gas jet were initially dispersed using a 100 mm 0.67 T magnet to diagnose the electron spectrum. The photon emission from the dispersed electron interacting with a Lanex screen was imaged using a CCD. A broad spectrum was measured which peaked at (140±10) MeV with a FWHM of 120 MeV. The beam has a integrated charge of approximately 670 pC. When the magnet is removed, the electron beam propagates out of the vacuum chamber as shown in Figure 5.14. The beam is then incident onto test objects inside the imaging area. Behind the imaging area there is a radiation shield/beam dump consisting of 200 mm lead. The backscattered x-rays are detected using a scintillator and a Multi-Channel-Plate Photomultiplier Tube (MCP-PMT) which was ≈2.2 m from the sample and surrounded by lead to ensure shielding from background sources of x-rays, such as the 3 mm steel that the electrons pass through as they exit the vacuum chamber

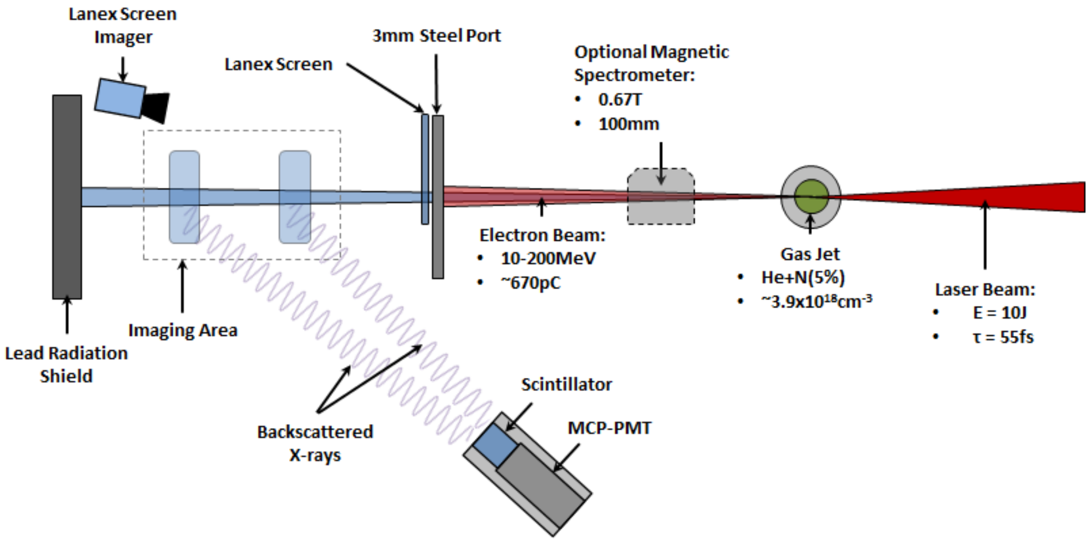

Figure 5.14: The schematic of the experiment that took place on the Astra-Gemini laser system. A 10 J, 55 fs, 800 nm laser irradiates a gas jet that emits a helium and nitrogen mixed gas with a approximate electron number density of 3.9×10^{18} cm^{-3}. The accelerated electrons are initially dispersed using a movable magnet of 0.67 T in order to diagnose the energy spectrum. The electron beam without the magnet is then incident onto objects in the 'imaging area'. Backscattered x-ray created by the objects are recorded using a MCP-PMT. Any penetrating electron or hard x-rays created are block/absorbed by a 200 mm lead wall.

As stated earlier, the temporal resolution of the electron bunch should be below ≈100 ps. However, in this situation the detectors become the main limitation. The scintillator used on the front of the MCP-PMT that achieved the best temporal resolution was a 10×10×10 mm cube of Barium Fluoride (BaF_2). An electron beam incident onto the scintillator yields a temporal resolution of (710±25) ps, which is approximately 200 mm spatially. An arrangement of objects was set up to demonstrate the techniques discussed earlier. The first object was a 140 mm thick foam wall and the second object was a low density organic compound. These two objects are approximately 250 mm apart. The signal recorded on the MCP-PMT was summed over 40 shots to average out the shot to shot variation; the results are shown in Figure 5.15.

The time between the peaks is approximately 1.7 ns. Taking into account the x-rays from the second object having to travel twice the distance between the ob-

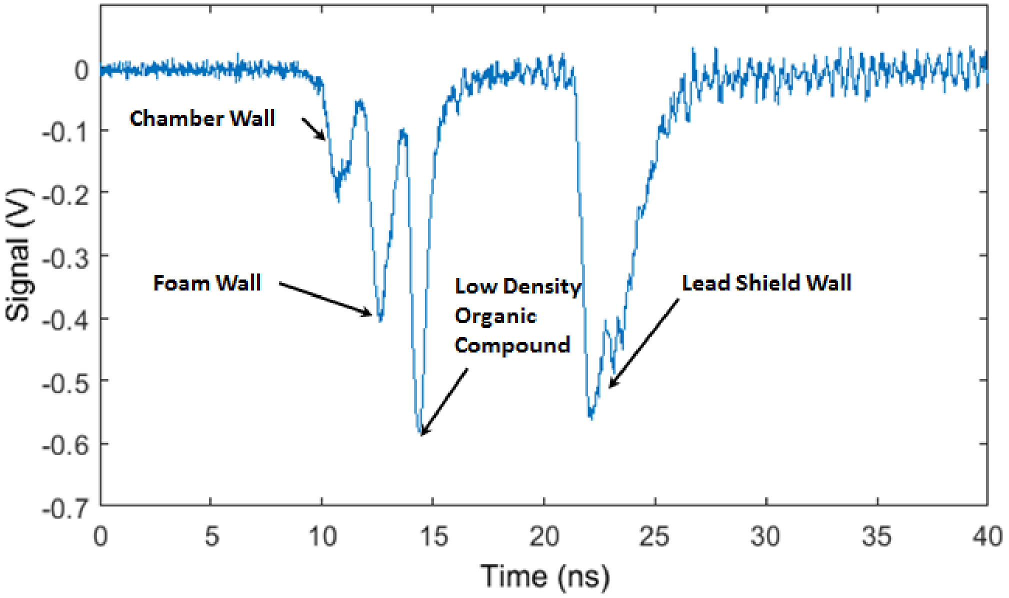

Figure 5.15: The 40 shot average output from the MCP-PMT showing the voltage peaks that correspond to backscattered x-rays returning from different objects.

jects, the calculated distance between the objects is approximately 250 mm. This demonstrates that the penetration and temporal resolution technique performs as expected.

To fully demonstrate the technique, the arrangement of objects was scanned horizontally. The layout of the objects is shown in Figure 5.16 a). The objects are moved by 0.1 m laterally with respect to the electron beam. At each position 40 shots were taken to obtain signals similar to that shown in Figure 5.15. The results of this are shown in Figure 5.16 b) [131]. This 2D image clearly shows the positions of each object, even those hidden behind others.

5.3 Further Work

The method of using electrons to produce backscattered x-rays within the sample has been investigated and demonstrated experimentally for the first time. The

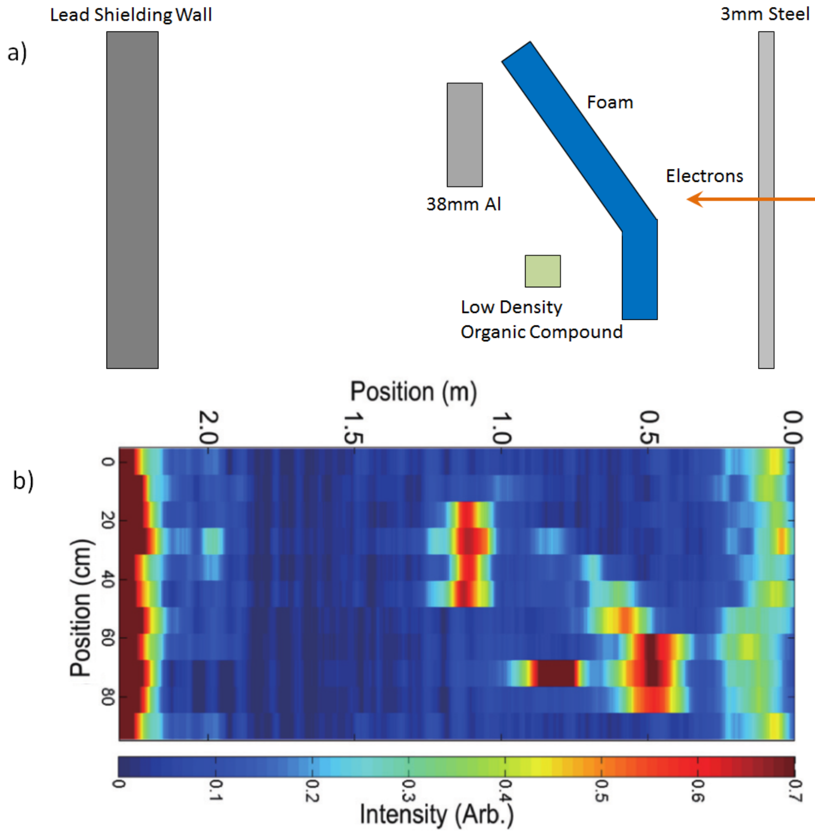

Figure 5.16: a) Arrangement of objects which are laterally scanned over using an electron beam. The detectors, not shown, are positioned below the bottom of the schematic (see Figure 5.14). b) A 2D x-ray backscatter image produced from the electron beam incident onto the objects over 40 shots every 0.1 m laterally.

major benefit of this technique is that the x-rays are mainly coming from inside the sampled object rather than the surface, which allows for deeper penetrative imaging. This section will discuss additional ideas that can be used to further the applicability of this backscatter technique.

Current techniques, as shown in Paulus *et al* [125], are able to identify the atomic number and density of the material using x-ray backscatter. This technique uses multiple collimated spectrometers to identify the attenuation of the material and effective combined atomic number. As the Wakefield electrons are highly energetic, all materials will emit K-alpha signatures as the threshold is the energy of the K-edge, which is <150 keV. Curved-crystal spectrometers [108] would easily be able to identify different materials by monitoring for the K-alpha signature.

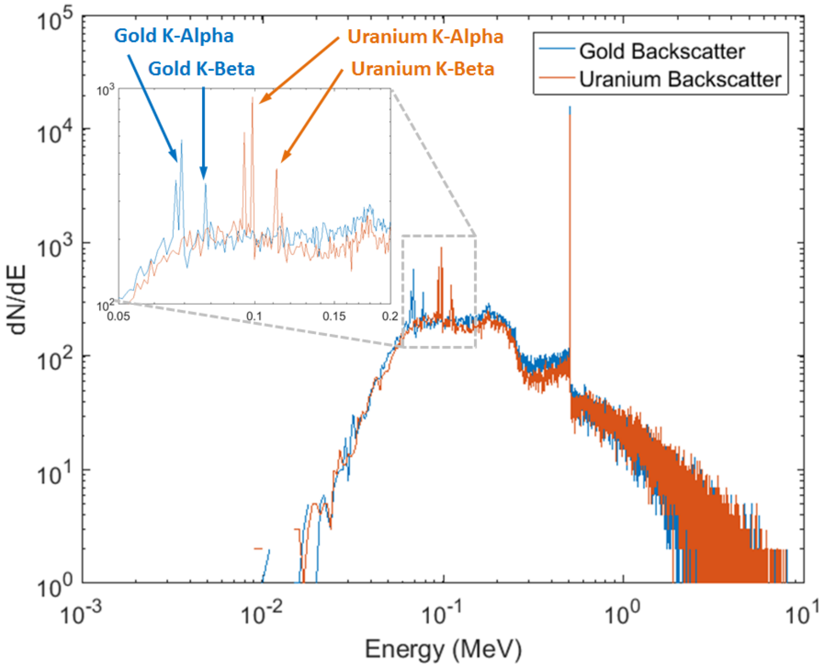

Figure 5.17: Spectral simulation of the backscattered x-rays from an object between two Al plates. The spectrum could be used to identify the material by looking for unique features from each material. In this case gold and uranium have K-alpha/beta between 66-68 keV and 94-98 keV respectively that easily identify each material.

These take advantage of x-ray diffraction and focal circles from Cauchois geometry which allow for increased resolving power at high energy (>50 keV) x-rays. A GEANT4 simulation was conducted using a test object positioned between two aluminium plates. The spectra from a detector plane 300 mm from the first Al plate is plotted for two different sample materials, gold and uranium, in Figure 5.17. The two spectra have distinguishable K-alpha/beta emission between 66-68 keV and 94-98 keV which correspond to gold and uranium respectively. A combination of the technique described in Paulus *et al* to identify materials, temporal resolution measurements using MCP-PMTs and a crystal spectrometer to detect the K-edges would provide a fully encompassing scan of the object, the spatial separation and chemical composition. The obvious limitation of the discussed k-alpha technique is one of depth. The two materials here, gold and uranium, have relatively high energy k-alpha emission, however, from Figure 5.17 it is clear that the self-absorption of the x-rays by the sample below 50 keV would

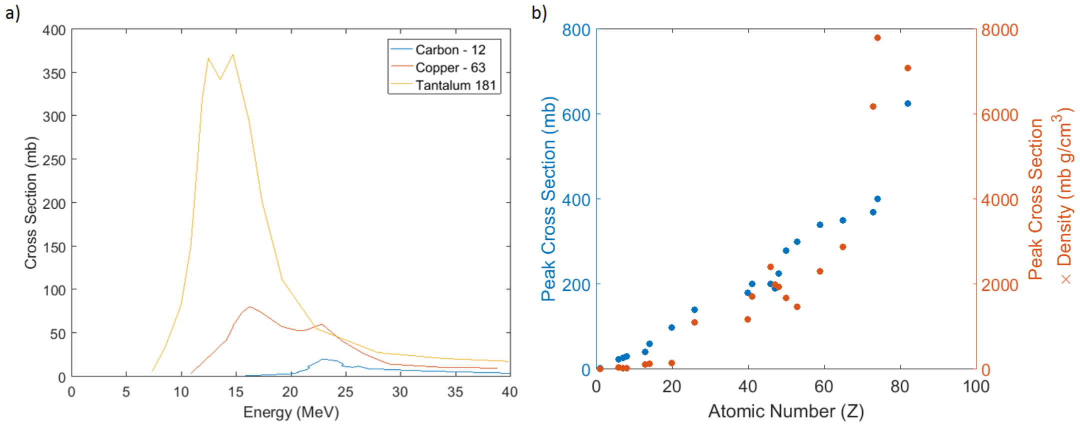

Figure 5.18: a) Cross sections of carbon, copper and tantalum for X-ray/Gamma induced nuclear reactions. b) The relationship between the atomic number and the peak cross section.

restrict the identification of lower atomic number elements using this technique.

The amount of x-ray radiation created by an electron beam of the energies described here is very high, where most of this is forward propagating and irretrievable. One of the consequences of having x-ray energies in excess of 10 MeV is photo-nuclear activation. This can lead to contamination of materials with radioactive isotopes in the imaging process. Whilst this is hazardous to organic materials, the activation of such targets could provide further information about the composition. An example of the photo-nuclear cross-sections (for just (γ,n) reactions) for three materials with varying atomic-number is shown in Figure 5.18 a) [132]; the materials here all peak in the region between 10 and 25 MeV. The cross section for a gamma-neutron nuclear reaction in tantalum is approximately 15 times greater than that of carbon. The relationship between atomic number and peak cross section is shown in Figure 5.18 b) which shows a general increasing trend. The activation of a material also depends on the density; this multiplied by the cross section is also shown in 5.18 b). The density and atomic number of a material does not have a simple relationship, however, there is also a general increasing trend for increasing atomic number.

The most common product of a photo-nuclear reaction is a neutron, as this typically has the highest cross section. It is also possible to cause the release of protons, alpha-particles and multiple neutrons from a excited nucleus; however, these are all less likely than just a single neutron. The neutron that is released from the nucleus is emitted randomly in 4π steradians.

The simulation results in Figure 5.8 have shown that the peak depth from which the backscatter x-rays return from does not increase vastly with energy. However, there is still a substantial amount of x-ray energy that penetrates into the sample, as shown in Figure 5.6 b). If the x-rays penetrate deep into a material where backscatter x-rays are unlikely to return from and interact with a high-Z material, a neutron could be produced. The previously discussed technique of using the emitted K-alpha/beta x-rays to aid in identification, as shown in Figure 5.17, will only work for shallow depths as it is limited by the penetration depth of sub-100 keV x-rays. The stopping range of neutrons in materials is very different than x-rays; they pass through high-Z, high-density materials more easily than materials containing low-Z atoms.

Using neutrons as an inspection method is a well-established technique for a variety of applications. The technique of Pulsed Fast Neutron Analysis (PFNA) uses nanosecond pulses of neutrons and many detectors surrounding the sample to probe the interior [133, 134]. The detectors analyse the arrival time of the gamma-rays from nuclear de-excitations and transmitted and scattered neutrons to determine the contents of the sample. The flash of neutrons created from wakefield accelerated electrons should also be shorter than that used in PFNA as the internal nuclear delay is (at maximum) on the order of picoseconds.

As discussed earlier in this chapter, the high energy x-rays created inside the material will lead to electron-position pair production. The production of these particles, similar to neutron production, is dependent on the atomic number and density of the material. Higher atomic numbers increase the probably of pair production as the process requires the presence of an electric field in order to conserve momentum and larger atomic number elements possess larger electric

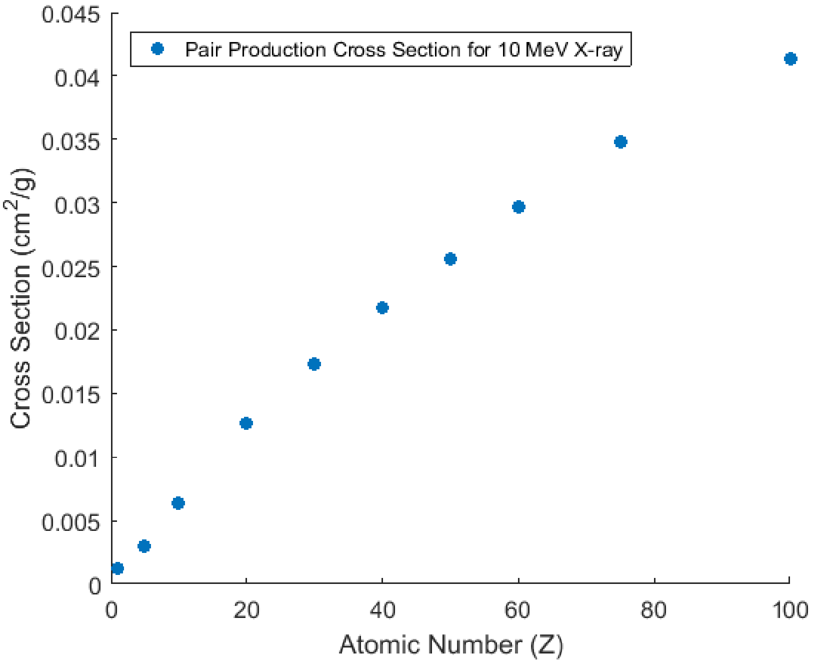

Figure 5.19: Pair production attenuation cross section for 10 MeV x-rays as a function of atomic number.

fields. The cross-section for pair production in the presence of a nucleus for a 10 MeV photon as a function of atomic number is shown in Figure 5.19. The resulting pair of 511 keV x-rays from the annihilation of the positron have higher energy than the majority of the backscatter spectra, allowing them to return from deeper penetration depths. Single shot detection of 511 keV x-rays is possible through the use of high atomic number curved crystal spectrometers [135, 136] or Cadmium-Zinc-Telluride detectors that can spectrally resolve 2D x-ray images [137, 138].

To test the application of using neutrons and 511 keV x-rays to probe further into materials, a GEANT4 simulation was conducted using a concrete block 50 mm thick with 10 mm of material at the rear; the composition of this material was vaired (C,Al,Cu,Fe,Pb,W). The aim of the simulations is to see whether more 511 keV x-rays and neutrons are detectable from deeply buried high Z materials. The simulations were conducted using 10^7 incident 140 MeV electrons. Only the backscattered particles were detected using a detection plane 450 mm from the

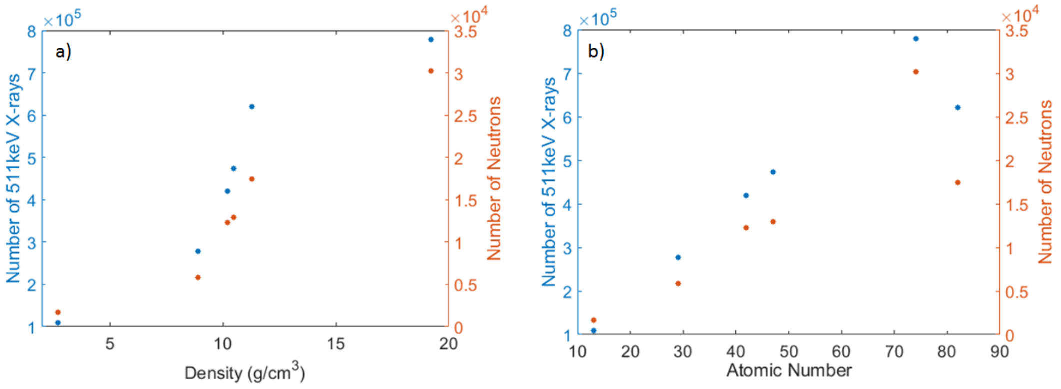

Figure 5.20: The number of 511 keV x-rays and neutrons produced from a 10 mm cube of material behind 50 mm of concrete when irradiated by 10^7 electrons with 140 MeV plotted as a function of a) density and b) atomic number.

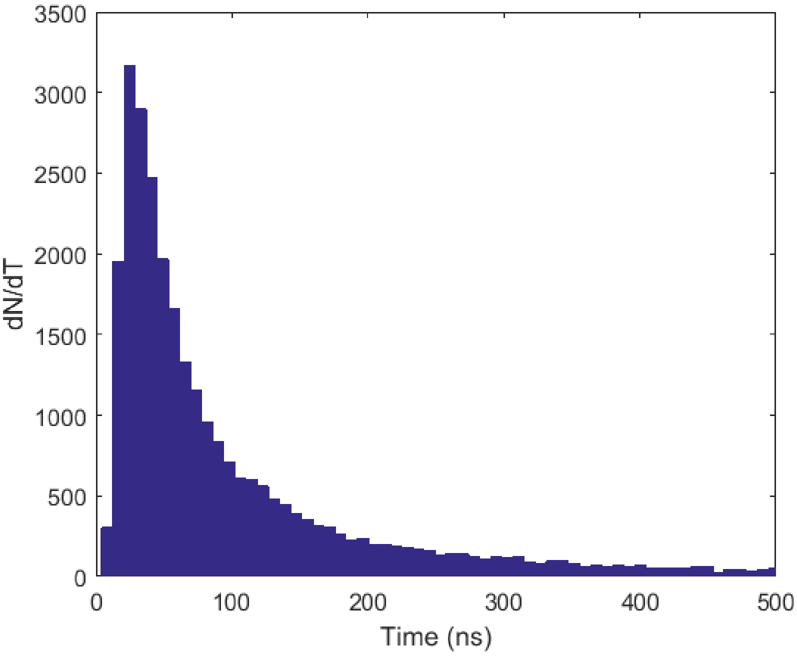

Figure 5.21: The temporal detection of neutrons from a 10 mm tungsten cube behind 50 mm of concrete. The shortest distance between the detector and the tungsten is 450 mm which for 1.5 MeV neutrons would corresponds to the peak that occurs at approximately 30 ns.

surface of the concrete and size of the detector is 2×2 m wide.

The number of neutrons and 511 keV x-rays produced in each simulation is shown in Figure 5.20 as a function of a) density and b) atomic number. The two highest atomic number materials here are lead and tungsten, Z=82 and Z=74 respectively.

The (γ,n) cross section of photo nuclear reactions is higher for lead, however the density of tungsten is ≈8 g/cm^3 greater, resulting in a larger yield of 511 keV x-rays and neutrons for tungsten.

As tungsten generated the most neutrons, it is simulated again to show the temporal output of the backscatter neutrons; this is shown in Figure 5.21. In this example, the flux of neutrons greatly increases at approximately 30 ns. As the neutrons are non-relativistic, they will travel much slower than the electrons and also they will a range of velocities, although 30 ns is the time it takes a 1.5 MeV neutron, which is the average energy of the neutron spectra, to travel the direct distance between the tungsten and the detector of 450 mm. Using this technique, the depth at which the tungsten is situated can be estimated. The accuracy of this technique can be improved by reducing the size of the detector, although, in the case of this simulation, this had to be kept large to increase the detection efficiency and the keep the simulation time manageable.

Here, it has been demonstrated that neutrons and 511 keV x-rays can be used to determine information about materials buried at greater depths than is currently possible to access using traditional backscatter techniques.

5.4 Conclusions

The method of using electrons to produce backscattered x-rays has been investigated. The major benefit of this technique are the x-rays are mainly coming from inside the sampled object rather than the surface, which allows for deeper penetrative imaging. Additionally, the technique of using a short bunch of electrons from a compact short pulse laser-wakefield source to temporally resolve the separation of objects has also been demonstrated. These sources also have a low divergent electron beam which means that they do not need collimating, unlike the traditional x-rays used in x-ray backscatter techniques.

Further developments are being made towards improving the temporal resolution of the scintillators and MCP-PMTs. Increasing the temporal resolution allows for finer detail of the spatial position of the sampled objects.

Additionally, using emitted K-alpha x-rays from materials has been proposed to aid in the identification of material buried at shallow depths. For deeper buried materials, using photo-nuclear produced neutrons and 511 keV created via annihilation of a positron has been proposed; as the number of each of these depends on the density and atomic number of the material.

Chapter 6

Escaping Electron Dynamics as a Function of Laser Pulse Duration and Focal Spot Size

During laser-solid interaction, a population of hot electrons is injected into the target. The internal temperature of these electrons can be investigated as in Chapter 4. When the electrons reach the rear of the target a large proportion of the electrons will reflux [69], however, some electrons will be able to escape the target. These escaping electrons have been investigated in two different conditions; for a varying focal spot size and pulse duration. Each of these were conducted with similar diagnostics; primarily the wraparound diagnostic discussed in Chapter 3. The results from the two experiments are split into separate sections. Initially, an experiment with varying focal spot size is discussed and results are compared with 2D PIC simulations. Secondly an experiment is conducted where the pulse duration is varied and the escaping electrons and protons are diagnosed.

6.1 Escaping Electrons as a Function of Laser Focal Spot Size

The size of the laser focal spot has been shown to have interesting effects on the interaction dynamics in solid target experiments. This has been investigated in the past in regards to the production of protons/ions. Using a 40 fs pulse with 500 mJ of laser energy and peak intensity of 2×10^{19} W/cm^2 incident onto 6-50 μm Al targets, Green *et al* [139] shows an increase in the lower energy proton flux as a function of increasing focal spot size. The beam of protons also appeared to become less divergent as the spot size was increased.

For much thinner targets (50 nm), Xu *et al* [140] demonstrated that under similar laser conditions the maximum energy slightly increased when the laser was defocused, although this is likely due to the contrast of the laser pre-expanding the target at best focus and de-optimising the acceleration conditions. It was also shown that the overall proton flux increased by a significant amount; growing by a factor of 5 when defocused from intensities of 5×10^{19} W/cm^2 to 2×10^{17} W/cm^2.

Using a more intense laser system (a focused intensity of $\approx6\times10^{20}$ W/cm^2), Coury *et al* [141] shows the maximum proton energy decreases as the intensity on target falls. However, the scale at which this decreases is very different depending on how the intensity is reduced. The maximum proton energy falls much more rapidly for decreasing incident laser energy than for increasing focal spot size.

Additional results showing the trend of increasing proton flux as a function of laser focus was shown by Brenner *et al* [115] for similar laser conditions. These results were modelled using the isothermal plasma expansion model introduced by Mora [93], which is often referred to as the 'Mora Model'. An adjustment was made to the model to take into account the effects the laser focus would have on the rear sheath field. This additional term helps the model fit the experimental data well [94].

More recently, an experiment was conducted where the beam was not only defocused but also the use of multiple focal spots with different separation was also investigated [142]. The number of lower energy protons (< 4 MeV) was increased significantly when the incident laser was defocused and also the divergence of the beam was reduced. When using multiple focal spots, an optimum for lower energy protons creation was found for a separation of 9 μ. Additionally, the ellipticity of the proton beam increases as the beams are separated.

The primary diagnosis method during all these experiments has been the measurement of the proton spatial and spectral distributions. An experimental campaign was carried by [143], where a cone target was irradiated with a laser where numerous shots were taken with the focus before and after the inner point of the cone. The hot electron distribution was inferred using k-alpha imaging of a wire attached to the outer point of the cone. They showed that the number of k-alpha x-rays would peak for a focal spot at best focus and also as the defocus was extended far out to +500 μm and -800 μm, dipping between these values. The distance that the electron travelled into the wire reduced as a function of distance away from the focus. The data suggests that the coupling of laser energy into electrons is relatively constant as a function of focus, but the spectrum is lower energy for greater distance from focus. PIC simulations carried out by [144] using the geometry of the experiment described above acheived similar results.

Despite this inferred measurments of the internal electrons from a defocused laser, no direct simultaneous measurements of the escaping electrons have been made even though they play an important role in the proton acceleration mechanism. In this chapter, the escaping electrons have been measured as a function of the defocus/laser spot size using the wraparound diagnostic. 2D PIC simulations have also been conducted to infer the internal electron dynamics as the electrons undergo retardation and refluxing due to the rear surface electric fields.

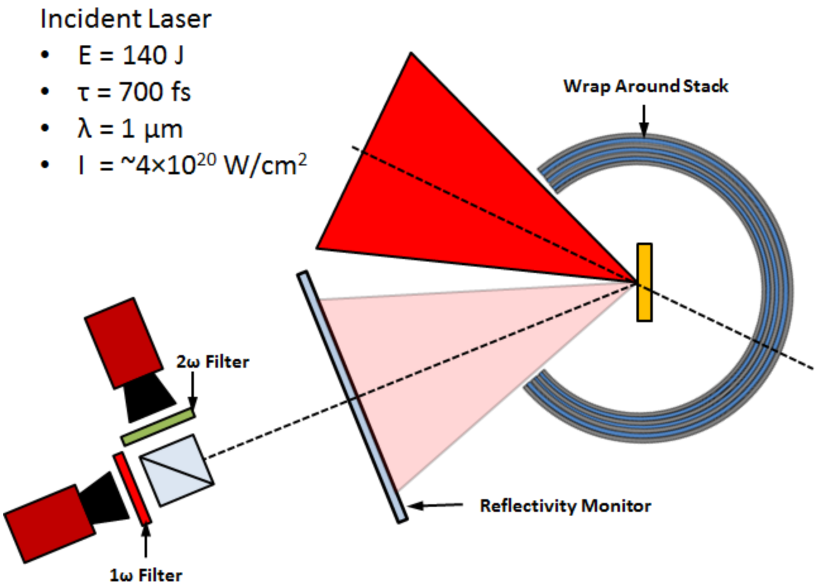

Figure 6.1: Top down schematic of the experimental setup conducted to investigate the escaping electrons. The wraparound diagnostic is place such that the target resides in the middle so that it provides angular information about the emitted electrons. The reflected laser light is recorded using a screen that is imaged using two cameras. Each camera has a filter so that it only observes fundamental or the second harmonic from the laser interaction.

6.1.1 Experimental Method

An experiment was conducted at the PHELIX laser facility at GSI in Darmstadt, which is capable of delivering up to 140 J of 1 μm radiation with a pulse length of $\approx$700 fs. The laser is focused using an F/1.5 parabola to a 4 μm focal spot, achieving peak intensities of $\approx 4 \times 10^{20}$ W/cm^2. The measured contrast of the laser a nanosecond before the main pulse is $\approx 10^{-7}$. The S-polarized laser pulse was focused at 20 degrees onto a 100 μm Cu target. A basic schematic of the experimental setup is shown in Figure 6.1. Reflectivity of the target was measured using two 12 bit CCDs; one to detect the first order reflected light (1ω) and another to detect the second harmonic emission (2ω).

To measure the escaping electron distribution, a curved image plate diagnostic was deployed [90]. The target was placed directly at the centre of the diagnostic where it could measure the angular distribution of the escaping electrons as well

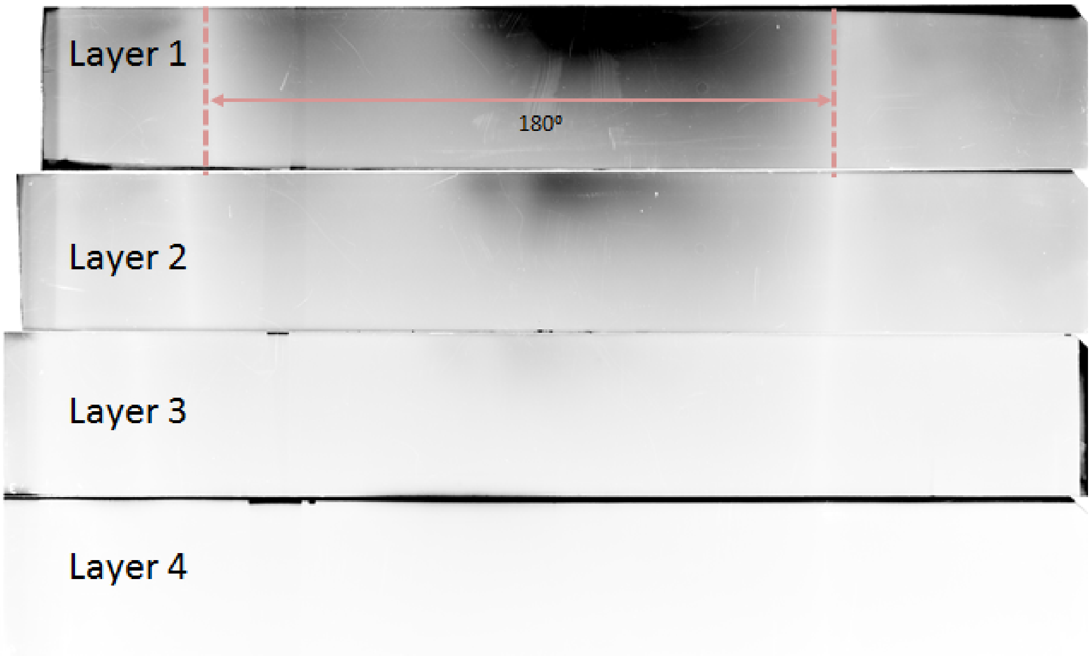

Figure 6.2: Originally scanned image plate from an in-focus shot onto 100 μm thick Cu. The the four layers of the diagnostic are highlighted with the layer number.

as infer information about the flux and spectral distribution from the multiple layers of the image plate.

Due to the proximity of the image plate to the target, the image plate is likely to saturate. The data recovery techniques discussed in Chapter 3 are used to retrieve the original exposure. As each layer of IP subtends a slightly different solid angle, the data was remapped to enable pixel to pixel ratio comparison.

6.1.2 Experimental Results

The raw data taken from a tight focus, full power shot, is shown in Figure 6.2. The edge of the target is represented by the dip in intensity; therefore, the area in-between represents the rear 180 degrees of the target. The top of the image represents the first layer of the diagnostic which has a clear beam-like structure present. After the angular remapping, a Gaussian filter is applied to the image to remove the scratches/blemishes that are present on the image plate as shown

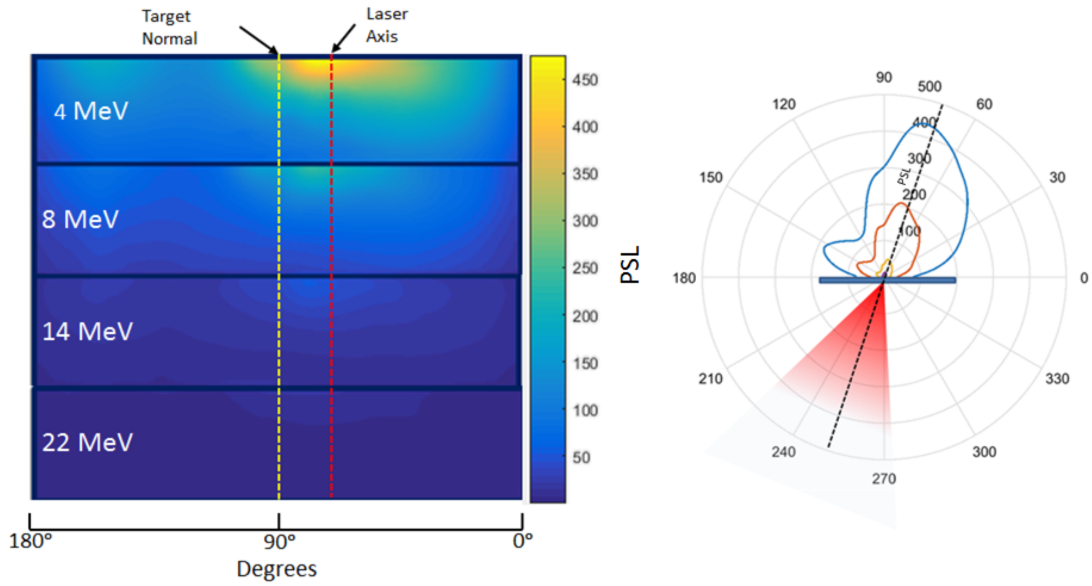

Figure 6.3: The remapped image shown in Figure 6.2 with the target normal and laser axis marked on and with the corresponding polar plot of the data. The laser axis is marked on the polar plot with a dotted line. The peak of the escaping electron distribution is close to the laser axis.

in Figure 6.3 a).

A polar plot of the most intense part of the signal is also shown in Figure 6.3. The laser axis is marked on the polar plot as a dotted line sitting at 20 degrees relative to the target surface. The peak of the escaping electron distribution is close to this line. Polar plots for all the full power shots are shown in Figure 6.4. The escaping electrons from all these shots appear to either primarily propagate along the laser axis or target normal, as previously measured by Norreys *et al* [86] and Santala *et al* [87].

Typically, the escaping electrons are measured using magnetic spectrometers. These normally have millimetre apertures and can be positioned up to a few metres away from the interaction; these spectrometers therefore only subtend very small solid angles ($< 10^{-6}$ steradians). Although all the data shown in Figure 6.4 are similar, differences between shots are apparent; the results from an electron spectrometer would be highly susceptible to these angular fluctuations. This highlights the importance of recording the entire escaping electron distribution.

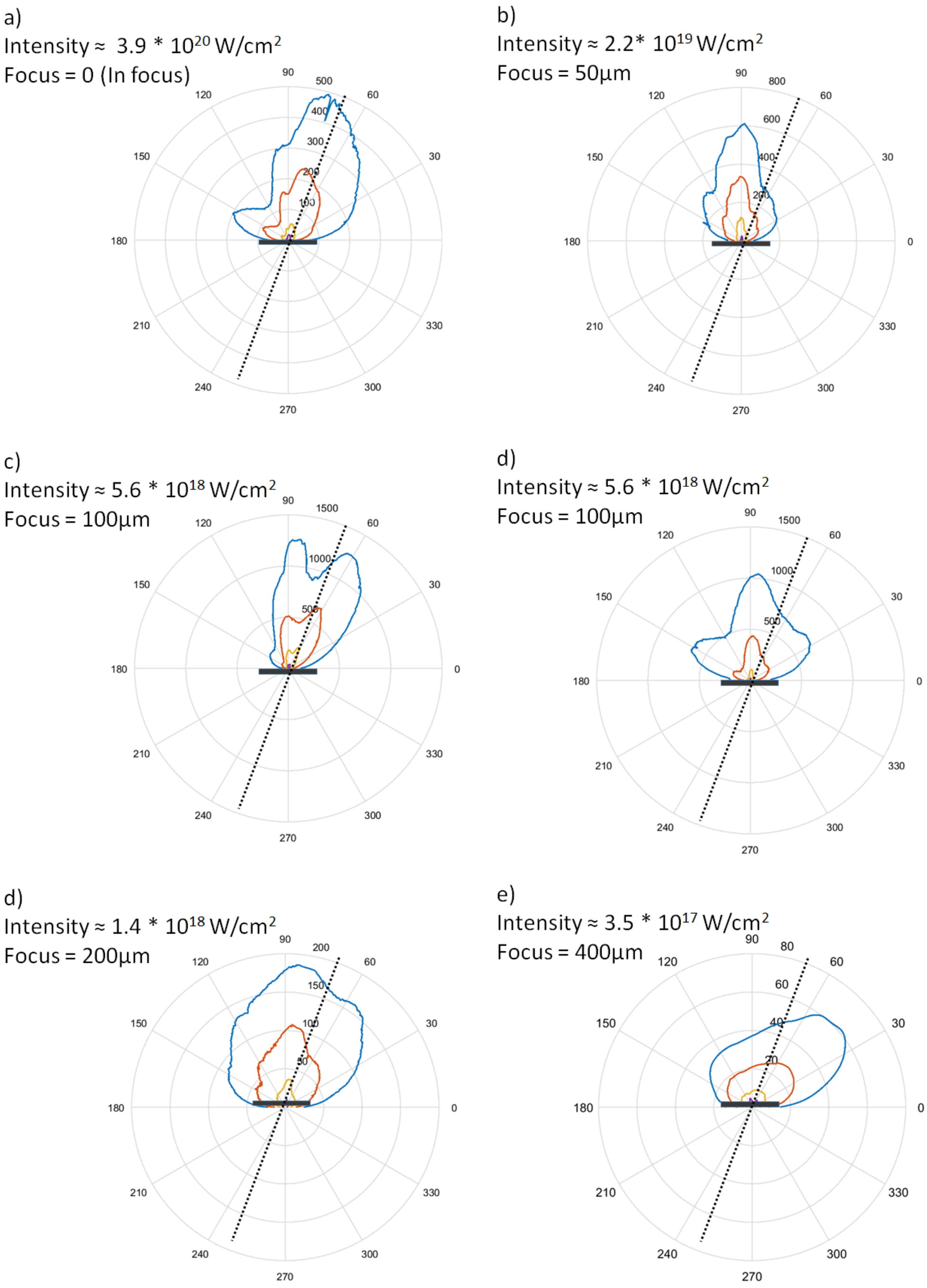

Figure 6.4: Polar plots of the escaping electrons recorded on the wraparound diagnostic for a number of different laser foci. The dotted line marked on the plots represents the incident laser angle and 0 to 180 degrees represent the rear surface of the target.

The integrated and peak PSL of the distribution for the first layer of the wraparound diagnostic are plotted as a function of intensity in Figure 6.5. The mea-

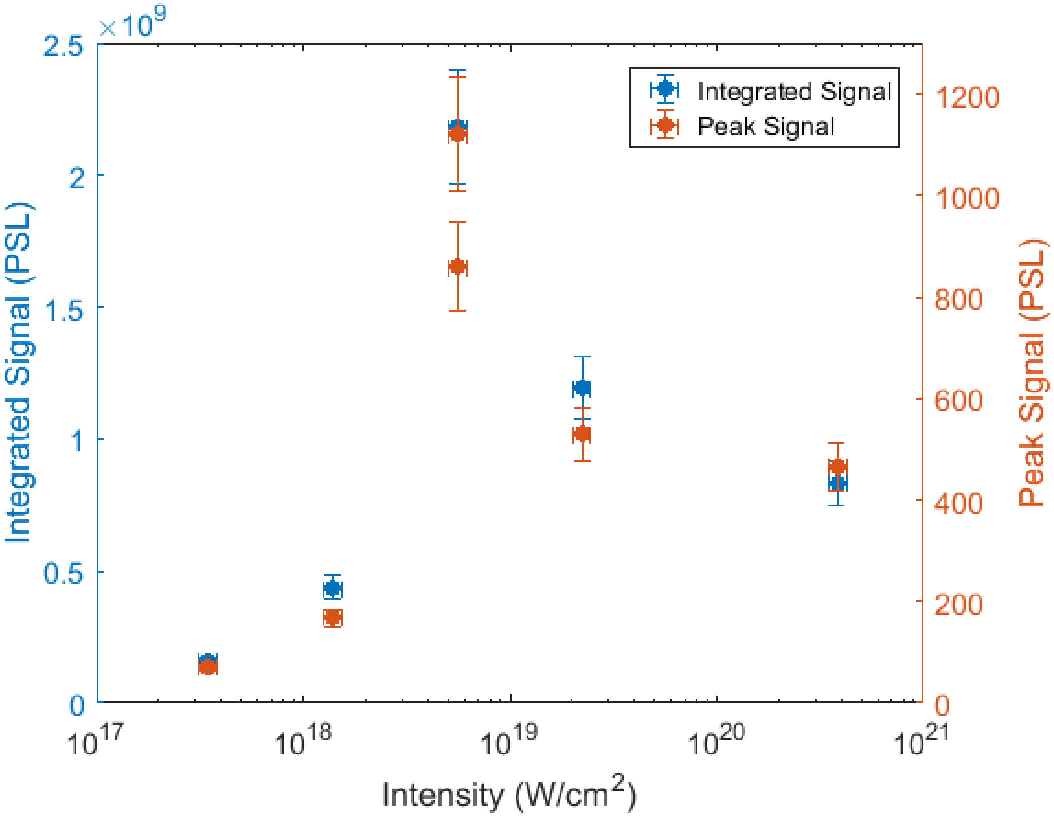

Figure 6.5: Integrated and peaks counts taken from the wraparound diagnostic as a function of incident laser intensity. The full energy shots (diamonds) have a peak in flux when the laser in defocused to 100 μ m.

surement inaccuracy in the counts come from the retrieval of scan 1, as discussed in Chapter 3. The escaping electron flux increases as the laser is defocused and peaks at approximately 5.5×10^{18} W/cm^2, which corresponds to a defocus of 100 μm. The flux then decreases as the laser is defocused further.

Although 1.8 mm of iron was placed in front of the first layer of image plate, there was one shot in which protons appear on the first layer; this is the shot displayed in Figure 6.4 c), a 100 μm defocus shot. As a result, the integrated counts are not included on Figure 6.5 for this shot. The increase in maximum proton energies at intensities of approximately 5.5×10^{18} W/cm^2 is contrary to the literature for thicker targets discussed at the beginning of this chapter.

The results of the specular reflectivity measurements are shown in Figure 6.6. The

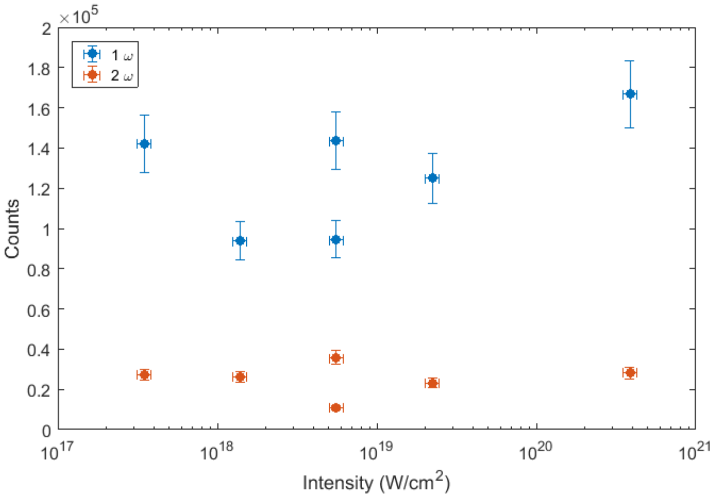

Figure 6.6: The reflectivity measurements at the 1 and 2ω which have been normalised to account for the quantum efficiency of the CCD to the different wavelengths. There is no clear trend in the data which suggests the reflectivity is not varying vastly over the intensities.

1 and 2ω counts have been normalised to take into account the quantum efficiency of the CCD used. The reflected light is fairly constant across all the intensities other than one shot at 5.5×10^{18} W/cm^2 where the 2ω emission decreases. This suggests that the absorption is not changing significantly as a function of intensity. Note that this is not an absolute measure of the absorption from the experiment as no reliable calibration shot was taken.

Experimental and numerical analysis of absorption performed by Ping *et al* [145] shows that there is a strong scaling of absorption with intensity when the incident energy is varied. However, this scaling of absorption is also affected by the incident angle and the pre-plasma present on the front surface. Using a 2D PIC simulation with an incident laser intensity of 3×10^{20} W/cm^2, Ping *et al* measured an absorption of 68% for no pre-plasma and 88% for a large pre-plasma. Reducing the intensity to 1×10^{19} W/cm^2 the absorption drops to 25% for no pre-plasma and 85% for a large pre-plasma. This shows that the absorption will reduce very slowly over an order of magnitude change of intensity in the presence of a large pre-plasma. More recently, using the PHELIX laser, Gray *et al* [146] measured the absorption. The findings from the Gray *et al* study show that absorption changes much more quickly as a function of incident laser energy and is in agreement with Davies [32] and McKenna *et al* [147]. Although this is conducted with higher contrast than the experiment presented in this section, it might be expected that with longer pre-plasma the absorption would change more slowly as with the results shown by Ping *et al.* Gray *et al* [41] also showed that there is a scale length which increases the absorption/hot electron generation that aids the production of protons from the rear surface. As will be discussed later, the ASE on this laser system will create a level of pre-plasma which has been previously measured by Wagner *et al* [148].

6.1.3 Numerical Simulations

The escaping electron temperature can be extracted from the wraparound diagnostic as each layer has a well-defined response curve to electrons as shown in Figure 3.31 of Chapter 3. First, the from of the escaping electron distribution must be understood. The next section describes PIC simulations to study the escaping electron dynamics.

6.1.3.1 PIC - Method

To simulate the effect of a defocused laser, 2D EPOCH PIC simulations were conducted. The simulation box was 200 × 120 μm with 8000×4800 cells giving a spatial resolution of 25 nm. The target thickness, 25 μm, and pulse length 175 fs, have been scaled by the same factor from that used on the experiment, this is to reduce the computational time required to conduct the simulations. An additional 200 nm contaminant layer of protons was added to the rear of the target which represent the protons that are typically accelerated from the rear surface of the target through Target Normal Sheath Acceleration (TNSA).

Due to the measured contrast on the experiment a pre-plasma was added to the simulations. To accurately represent this pre-plasma, which was not measured on this experiment, multiple sources of published data were referred to. Findings published by McKenna and Carroll *et al* [147, 149] show a long, shallow density gradient using an interferometer to measure the electron density on the front surface, up to limit of 1×10^{19} cm^{-3}. They were able to model and confirm the experimental results using the hydrodynamic code POLLUX. What can also be concluded is that there are two scale lengths present, a short scale length and a long scale length. Similar scale lengths are found by La Fontaine *et al* [120] from simulations using the hydrodynamic radiative code CHIVAS.

Wagner *et al* [148] performed measurements of the pre-plasma on the PHELIX laser system at a number of different measured pedestal intensities. Using a transverse probe beam to perform shadowgraphy, the size of the pre-plasma was characterised as a function of time and intensity.

These sources allow for some estimations of the pre-plasma from the experiment conducted by the author. The three data points from Wagner *et al* are between the intensities of 2.5×10^{10} and 5×10^{13} W/cm^2. Fitting the shadow size $S_{(\mu m)}$ measured at these intensities to a log function yields the equation,

$$S_{(\mu m)} = -4\ln\left(I_{LP}\right) + 88 \tag{6.1}$$

where I_{LP} is the intensity of the laser pedestal in W/cm^2. The pre-plasma modelled by McKenna and Carroll *et al* has a steep density scale length of approximately 2 μm which does not change vastly as the intensity is varied. The longer scale length starts at a density of approximately 10^{20} cm^{-3}; this level does not vary much with intensity. The shorter scale length, the one closest to the target, has a scale length of 2 μm. This longer scale length for each incident intensity/-focus is set such that it satisfies the density measured by Wagner and the shadow size, $S_{(\mu m)}$, given by equation 6.1. An example of the estimated scale lengths for a number of different defocuses are shown in Figure 6.7.

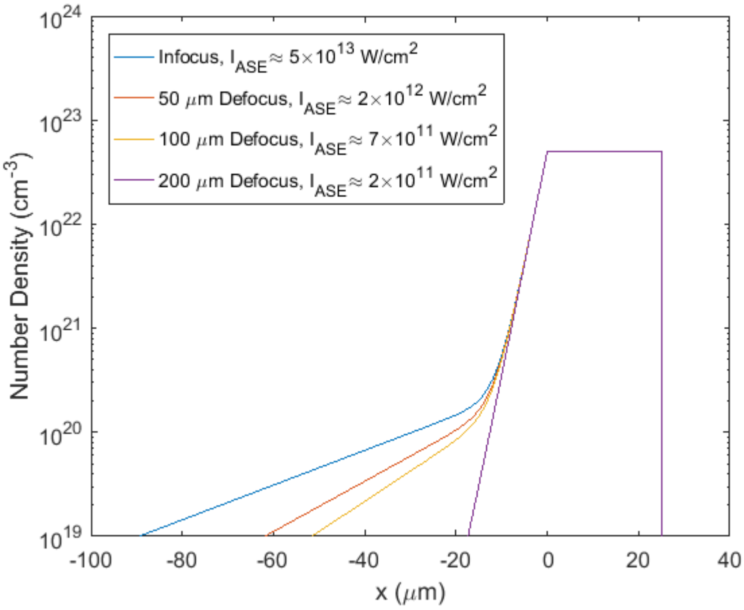

Figure 6.7: Estimated pre-plasma using the measured shadow from Wagner *et al* [148] and the modelling conducted by McKenna and Carroll *et al* [147, 149].

The peak intensity of the laser was chosen to be 5×10^{20} W/cm^2 with a simple Gaussian temporal profile. To ensure that the energy incident onto the target was the same, the laser was focused by modifying the phase front, φ, which is given as,

$$\varphi = -\frac{k_L x - k_L y^2}{2R_c} + \text{atan}\left(\frac{x}{R_r}\right) \tag{6.2}$$

where the $k_L = 2\pi/\lambda$, R_r is the Rayleigh range $R_r = \pi w_0^2/\lambda_L$, R_C is the radius of curvature $R_C = -x\left(1 + (R_r/x)^2\right)$ and w_0 is the diffraction limited width of a Gaussian beam, which for an ideally focused F/1.5 laser with a wavelength of 1 μm is ≈3.7 μm. The beam could then be moved laterally relative to the target to change the area of irradiation on the front surface to simulate the defocus.

To ensure the output files from the simulation were computationally processable the outputs were split into smaller, manageable amounts. Table 6.1 shows the relevant output information from the simulations. Note that the electrons have been split into two outputs; Electron 1 samples less of the electrons but will output down to 250 keV and Electron 2 which samples all the electrons above 5 MeV and output every 10 fs. The latter allows for an approximate spatial resolution of 3 μm. Using such high spatial and temporal resolution on this output allows particle tracking to be an effective tool to diagnose information about the electrons; this will be discussed later in section 6.1.5.

The simulations were conducted for a number of different conditions. Five simulations were undertaken with the longer pre-plasma discussed previously at different defocuses; 0-300 μm using Equation 6.1 to define the scale length. Three additional simulations were conducted at different defocuses with only the shorter 2 μm scale length present.

6.1.3.2 PIC - Results

Firstly, the intensity of the laser incident onto the front surface of the target was examined for different defocuses with the long scale length case. Figure 6.8 shows the intensity maps of 4 different foci at 0.625 ps, approximately when the peak of the laser pulse is incident on the critical surface. Figure 6.8 b) which represents 50 μm defocus shows the laser field penetrating to a higher density than the other intensity plots.

To represent this more clearly, Figure 6.9 a-e) shows the laser intensity envelope and the density of the target for all the intensities/defocuses, from the middle 1 μm of the simulation. For the in-focus simulation, the laser appears to focus at

Output Name	Output Timestep	Output Fraction	Energy Limit
Electron 1	50 fs	0.5	250 keV
Electron 2	10 fs	1	5 MeV
Protons	25 fs	1	2 MeV
Electric Fields	25 fs	N/A	N/A
Magnet Fields	50 fs	N/A	N/A
Density	50 fs	N/A	N/A

Table 6.1: The outputs from EPOCH that have been split into different categories to aid analysis.

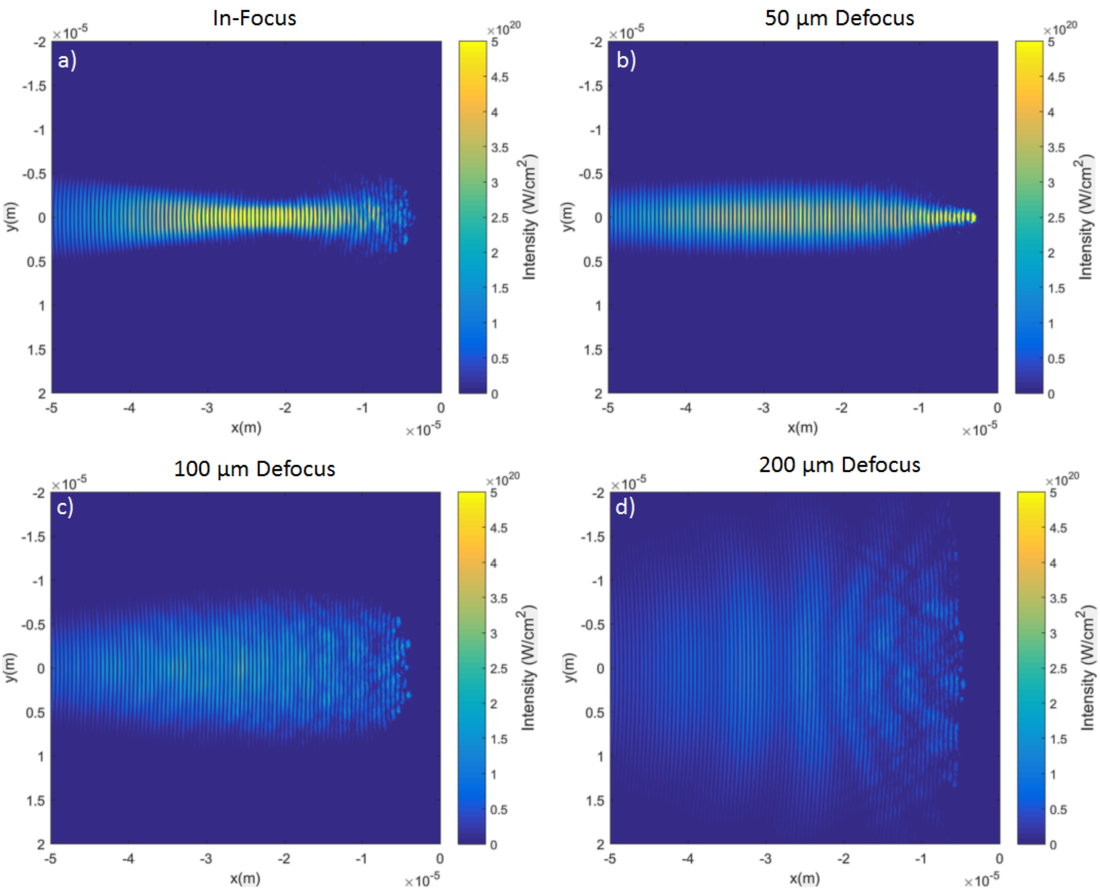

Figure 6.8: Images of the intensity of the laser as it interacts with the target. a-d) represent infocus, 50, 100 and 200 μm defocus relative to the target surface. The target surface begins at 0, in front of this surface is the pre-plasma as described in the previous section and Figure 6.7. For the defocus of 50 μm the laser forms the smallest spot due to the relativistic self-focusing in the plasma.

25 μm before the solid density of the target and approximately 18 μm from the critical surface. This is due to the relativistic self-focusing effect. This makes a channel in the plasma that reduces the electron number density which is shown on the modified density in Figure 6.9 a).

For the 50 μm defocus, the beam does focus 50 μm before the target; however the increase in density keeps the beam from diverging. Once the beam reaches the critical surface it focuses again to a tight spot; this high intensity will increase the critical density by the gamma factor from equation 2.26 from Chapter 2. Figure 6.10 shows the ratio between the modified density as the pulse is incident onto the target and the initial density at time zero. The density near the critical surface

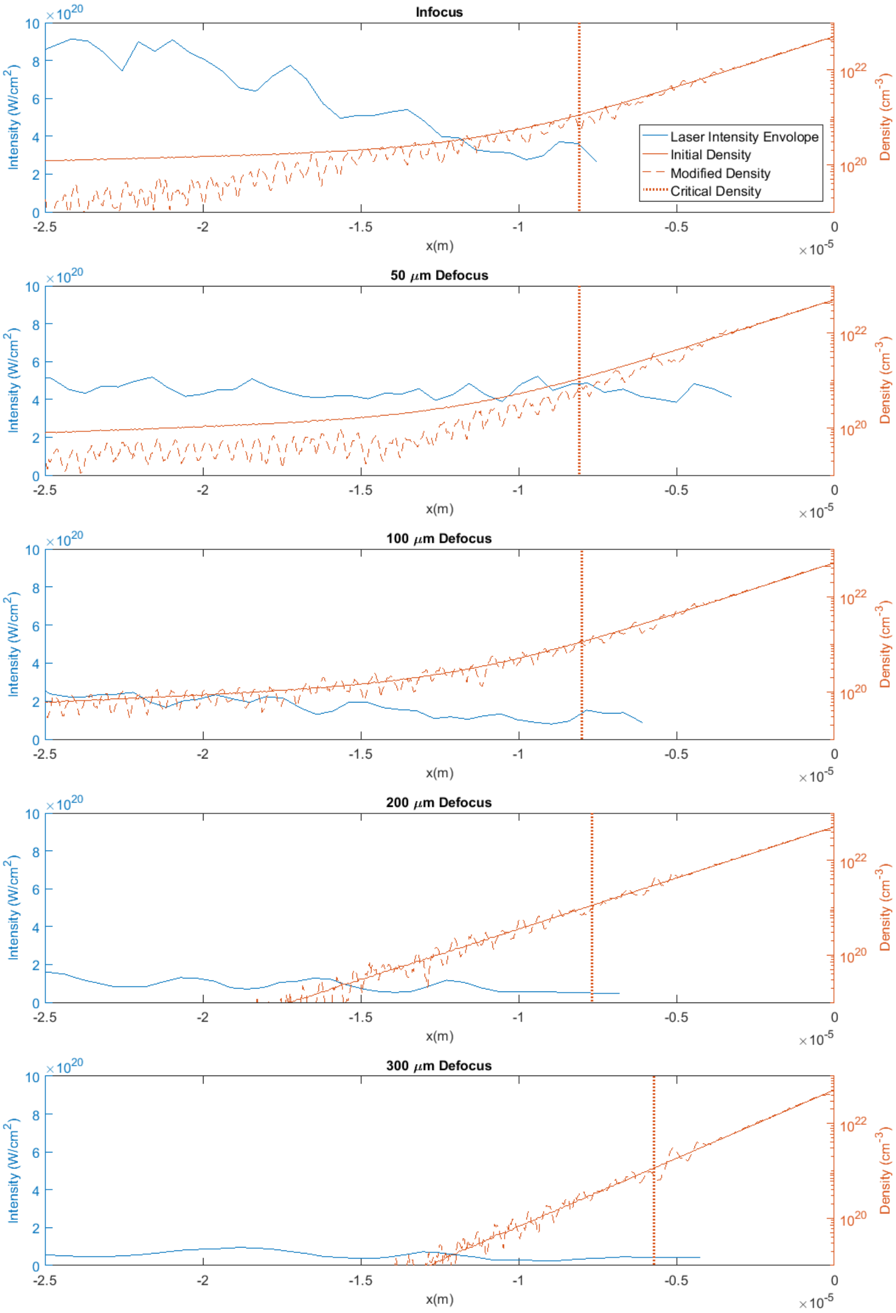

Figure 6.9: Plot of the intensity and density from the simulations conducted for different foci. The non-relativistic critical density of each of the simulations is marked by the vertical dotted line. From Figure 6.8 it is clear that the 50 μm has the highest effective intensity near the critical surface, allowing it to bore further into the expanding plasma compared to the other foci which are also shown here.

is modified the most for the 50 μm defocus condition. As a result, the 50 μm defocused laser beam penetrates further into the critical density region than the

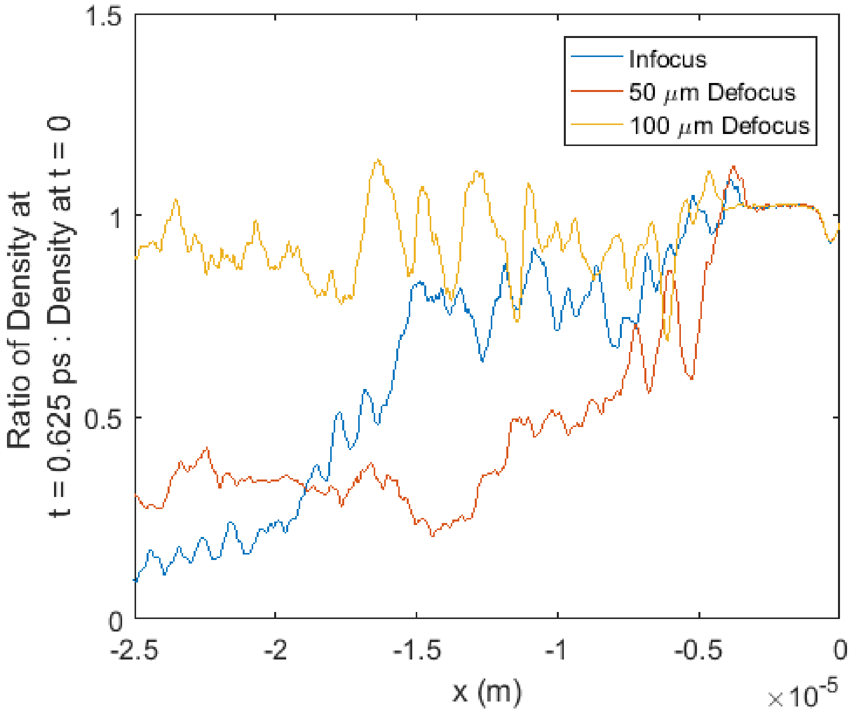

Figure 6.10: The ratio of the modified density to the original density. The densities are modulated and altered by the incident laser. The 50 μm defocus has the largest displacement from the original density.

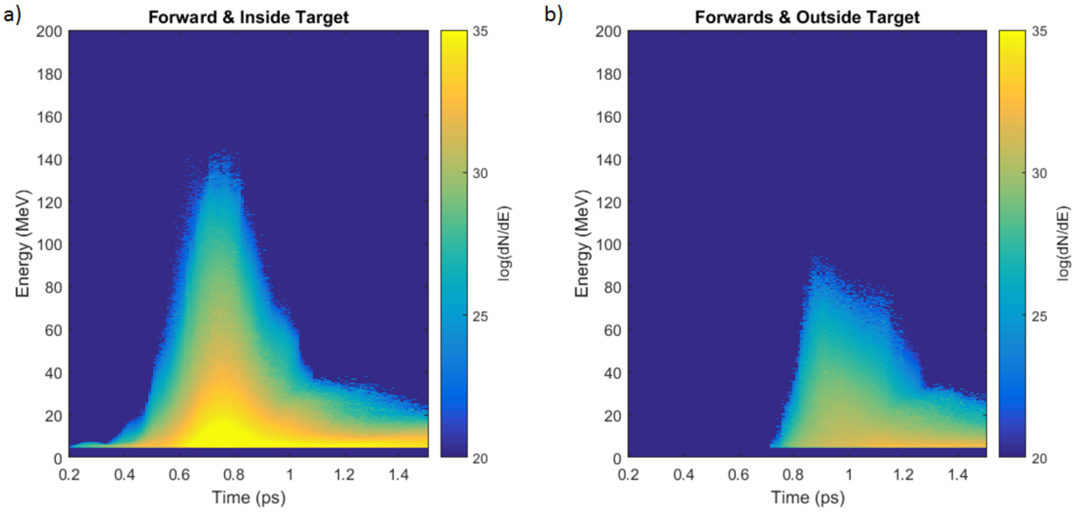

Figure 6.11: Temporal evolution of the forward propagating hot electron population inside the target a) and outside the target b).

other simulations.

The temporal evolution of the accelerated electrons is shown in Figure 6.11; this is split into electrons that are traveling forward through the target and electrons that have left the target and are traveling forward. As the intensity onto the front of the target increases, so does the number and energy of the hot electron distribution, as shown in Figure 6.11 a). The internal hot electron spectrum reaches a maximum in number and energy at approximately 0.75 ps. The thickness of the target is 25 μm; for relativistic electrons it will take approximately 80 fs to transverse the target. After the peak of the laser pulse, the electrons have already reached the rear of the target and started to escape, as shown in Figure 6.11 b). The external electron spectrum peaks at approximately 0.9 ps.

As discussed in Chapter 3, EPOCH describes the particles in the simulation as macro-particles where each macro-particle represents a number of real particles. To plot a spectra of the electrons, the so-called weight of each particle must be added to each energy bin that represents that electron. The spectra of the electrons for the 5 foci at the peak times mentioned previously are shown in Figure 6.12. The highest energy internal and external electrons are produced from the 50 μm defocus interaction, as shown in Figure 6.12 a) and b). The active range of sensitivity for the wraparound diagnostic is mainly below 25 MeV for electrons, as shown in Chapter 3 (Figure 3.31), to highlight this region, Figure 6.12 c) and d) only represents energies 0-25 MeV for the internal and external electrons. The electron distributions from the 0-100 μm defocus all appear to have very similar spectra in this reduced energy region. This temperature is approximately 10 MeV.

The total energy measured by the wraparound diagnostic can be calculated by multiplying the spectra shown in Figure 6.12 d) by the response function in Chapter 3 Figure 3.31. The output is shown in Figure 6.13 where a) shows the normalised output as a function of layer and b) has the normalised output as a function of focal position relative to the target. The in-focus, 50 and 100 μm defocus conditions have similar gradients through the layers. The 50 μm defocus has the highest output on the first and second layers. This is not as high as the

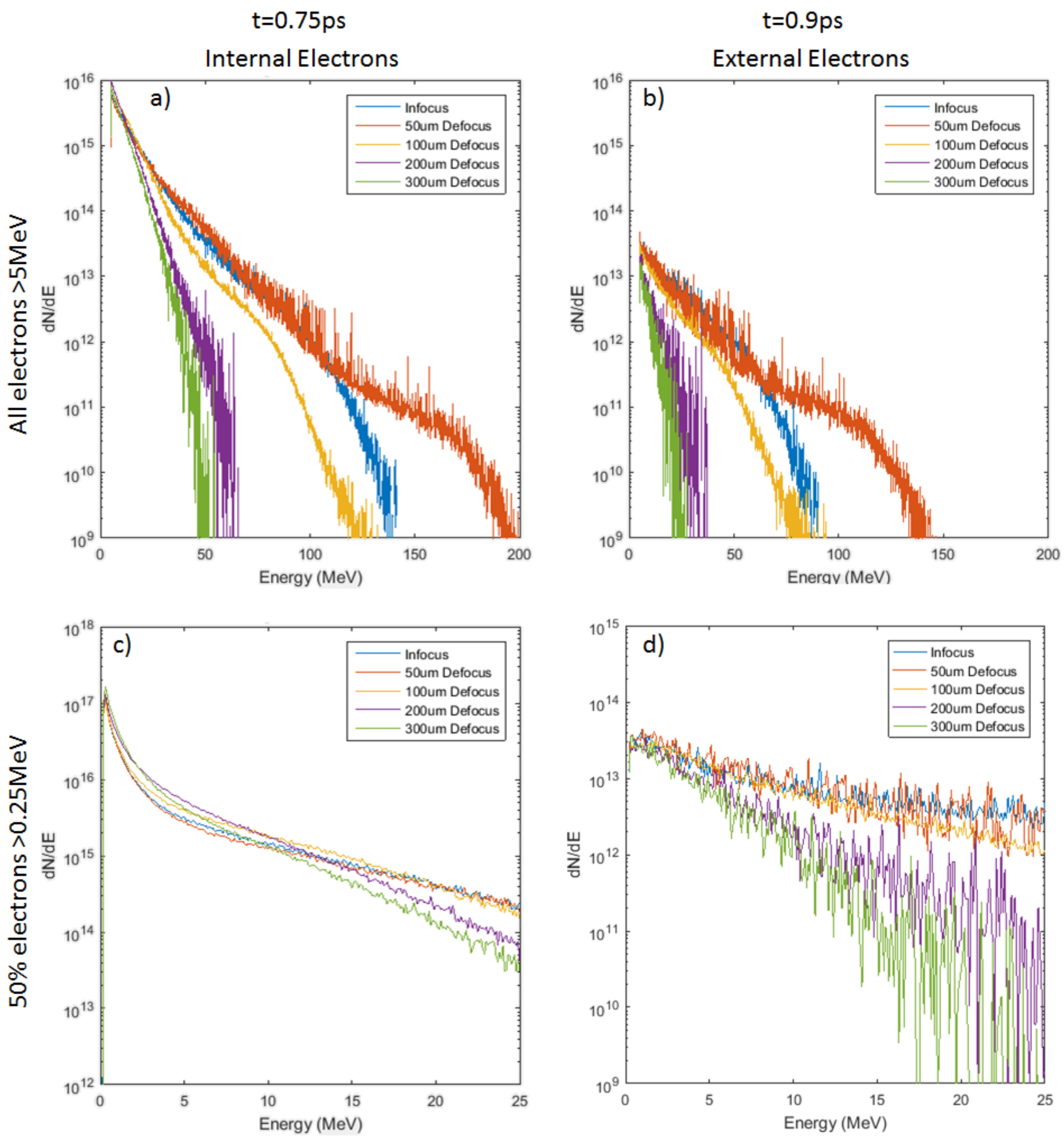

Figure 6.12: The electron spectra from all the simulations at a single time; 0.75 ps for the internal and 0.9 ps for the external electrons. a) and b) represent all the electrons above 5 MeV whereas c) and d) represent half the electrons above 250 keV as dictates by output Electron 1, shown in Table 6.1. Looking at the escaping electrons on d) shows that between the infocus and 100 μm defocus there is not a significant difference between the temperatures, which is approximately 10 MeV.

increase measured in the experiment which was approximately a factor of 2. For the simulations, only an increase of ∼5% is measured.

Three additional simulations were conducted without the longer pre-plasma and

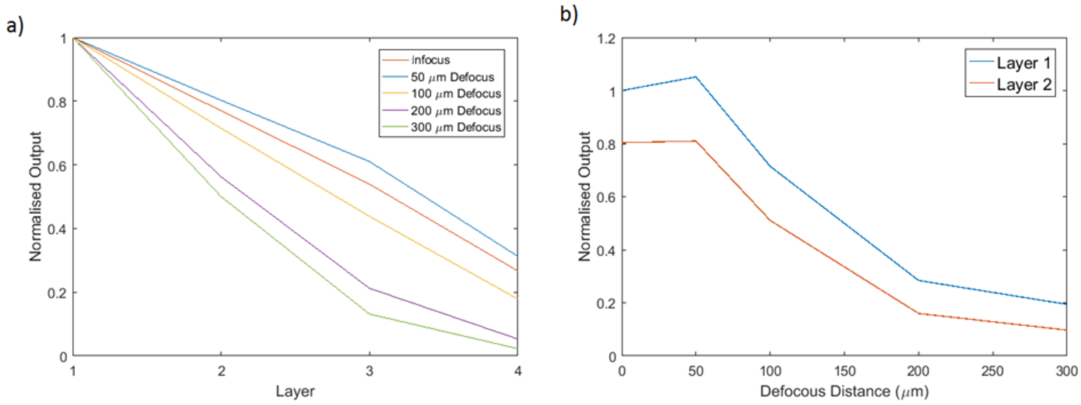

Figure 6.13: a) The simulated output of the wraparound diagnostic calculated using the escaping electron distribution from the EPOCH simulations as a function of layer normalised to the first layer of each. b) The output of the first two layers as a function of defocus distance which shows an increase in flux when the laser is defocused by 50 μm.

just the shorter scale length present. These three simulations were conducted at three different focuses: infocus, 50 μm and 100 μm defocus. As with the previous simulations, an intensity map of the laser incident onto the critical surface is shown in Figure 6.14. What is clear is that the interaction is very different to the one presented in Figure 6.8 when the longer pre-plasma is present and the self-focusing effect causes the 50 μm defocus simulation to have the highest peak intensity. For the short pre-plasma, the highest intensity for these simulations occurs when the beam is focused on the surface of the target.

The resulting internal and external electron spectra is shown in Figure 6.15 for these simulations. The hottest electrons are achieved by the infocus laser, both for the internal and escaping electrons, although the difference between the temperatures predicted in all the simulations is small.

The output from the wraparound diagnostic as a function of layer and focus is calculated again for the escaping electron spectra as shown in Figure 6.15. The highest flux occurs for the tight focus simulations.

A flux increase on the wraparound is only observed for a defocus simulation when there is a large pre-plasma is present, otherwise, when the pre-plasma is shorter,

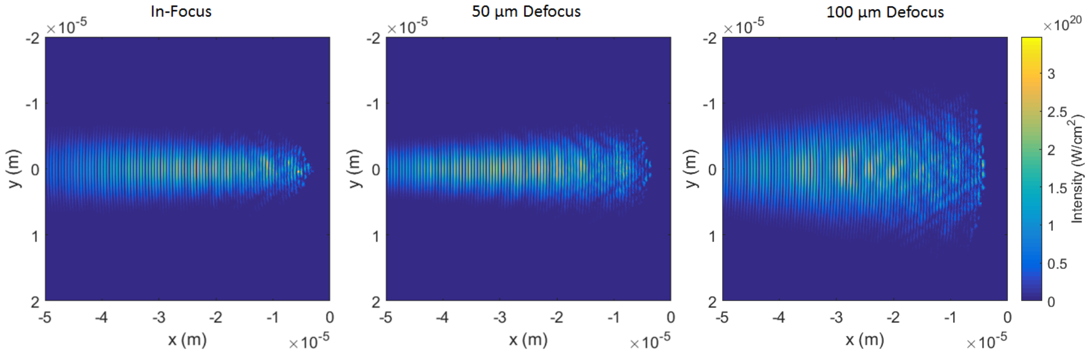

Figure 6.14: Intensity of the laser from 3 simulation with different focus positions incident onto a target without a long pre-plasma. As with Figure 6.8, the target surface is at 0 μm. There is little self-focusing observed in these simulations, unlike the previous simulations where self-focusing was very prominent.

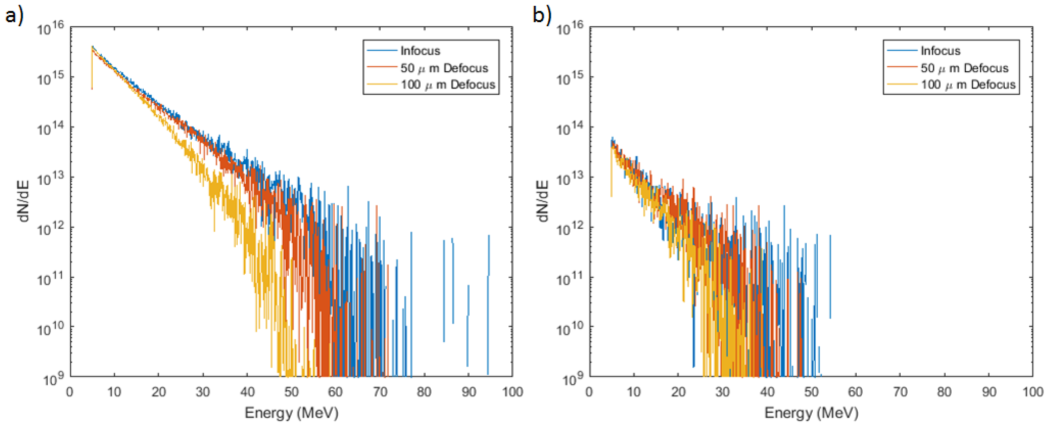

Figure 6.15: The a) internal and b) escaping electron distributions for the shorter pre-plasma simulation. The escaping electrons all appear to have similar temperature distributions.

the flux falls as the laser is defocused. The peak for the experimental data occurs at 100 μm from best focus; this difference is likely to occur due to the estimated pre-plasma conditions and possibly also due to the reduction of the pulse-duration of the laser to save on the computational time.

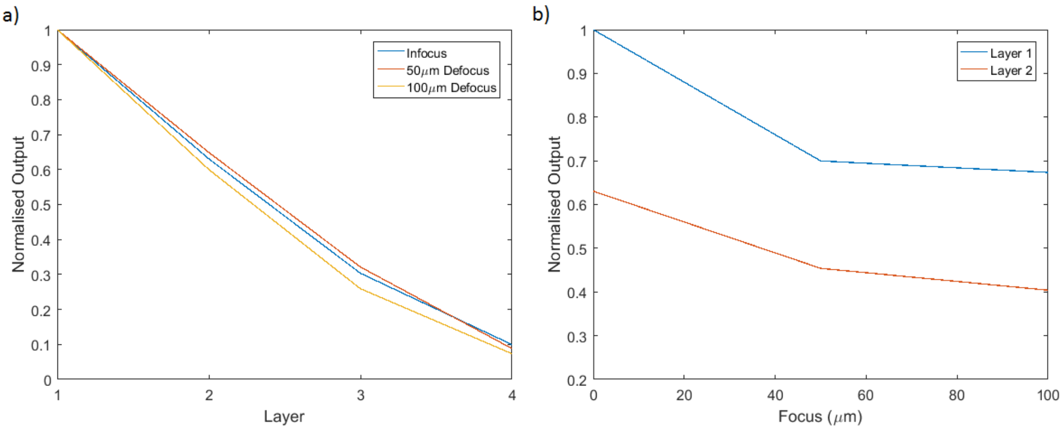

Figure 6.16: The output of the wraparound diagnostic with the input of the spectra shown in Figure 6.15 b). a) The normalised output as a function of layer shows that the temperature remains constant. b) The flux on the first two layers as a function of defocus, this shows the flux peaks at tight focus.

6.1.4 Temperature Extraction

To extract the temperature from the experimental results recorded on the wraparound diagnostic, an estimate of the electron spectra must be compared to the results. There are three distributions described in Chapter 2: Boltzmann, Maxwellian, and Maxwell-Jüttner. The data from the simulations for the electron distributions for infocus and for defocus conditions of 200 μm are shown in Figure 6.17 alongside the three distributions with the relative temperatures listed in the legends. The simulated electron spectrum has been smoothed using a moving average to make the comparison clearer.

It is clear that the best fit to the electron spectra is provided by the Boltzmann distribution as both the Maxwellian and the Maxwell-Jüttner distributions do not fit to the lower energy region (1-10MeV). Multiple temperature distributions could be used to fit to the spectra, however, for simplicity and as the layers of the wraparound diagnostic are sensitive in this region the Boltzmann distribution is the best option to use for simplicity. Using different temperature distributions and multiplying by the response function of the diagnostic yields the normalised outputs shown in Figure 6.18.

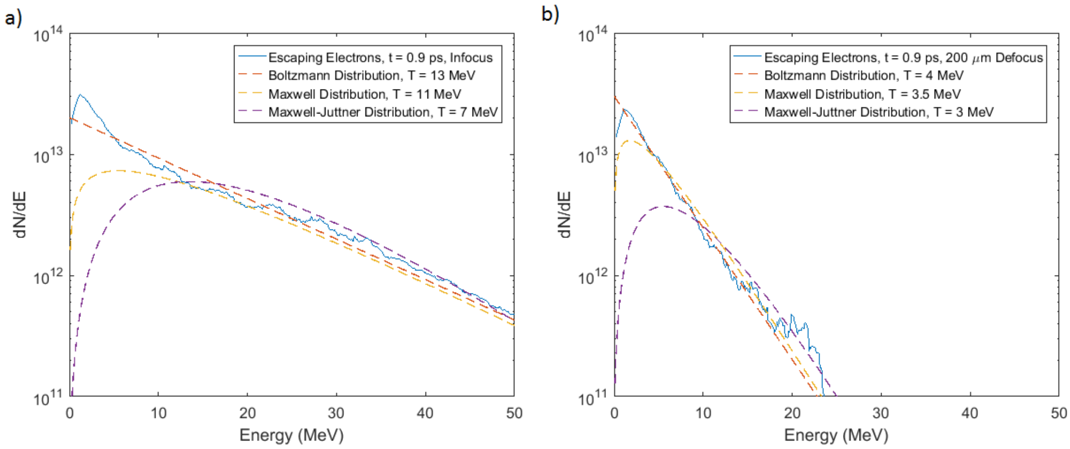

Figure 6.17: The escaping electron distribution from an infocus and 200 μm defocus shot in a) and b) respectively. Also plotted are 3 different forms of electron distribution: Boltzmann, Maxwellian, and Maxwell-Jüttner. The Boltzmann distribution appears to have the best fit to the lower energy electrons (1-10MeV) which is where the layers of the diagnostic begin to become sensitive.

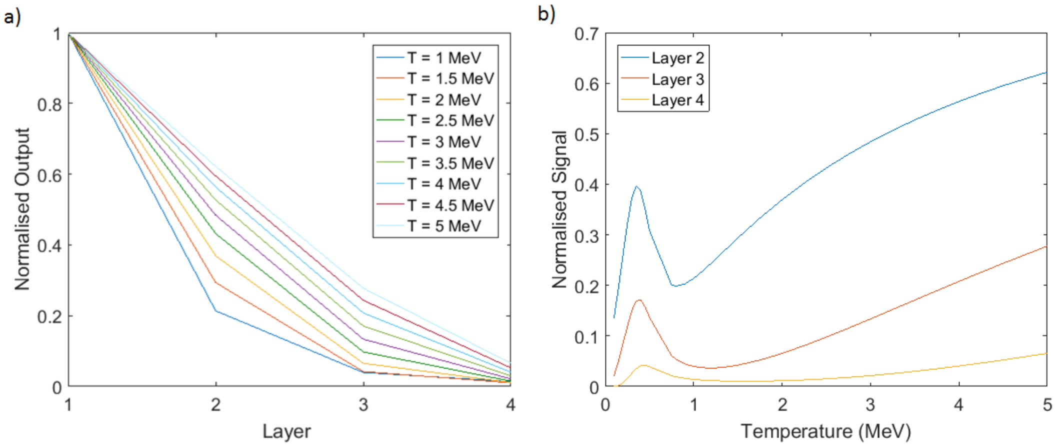

Figure 6.18: a) The normalised output of the wraparound when the response function is multiplied by different Boltzmann electron temperature distribution. b) The normalised output of each layer (relative to layer 1) as a function of temperature. There is an initial peak below 1 MeV which is caused by the x-rays produced in the first filtering layer penetrating to the sensitive layer before the initial electron are able to penetrate to them.

An image plate is sensitive to all ionising radiation, not just electrons. This is not a problem for ions/protons as they should be stopped by the filtering, requiring greater than 30 MeV to reach the first layer, but is particularly an issue when regarding x-rays as they can easily be created with high enough energies to penetrate to all of the image plate layers. To estimate the amount of energy an

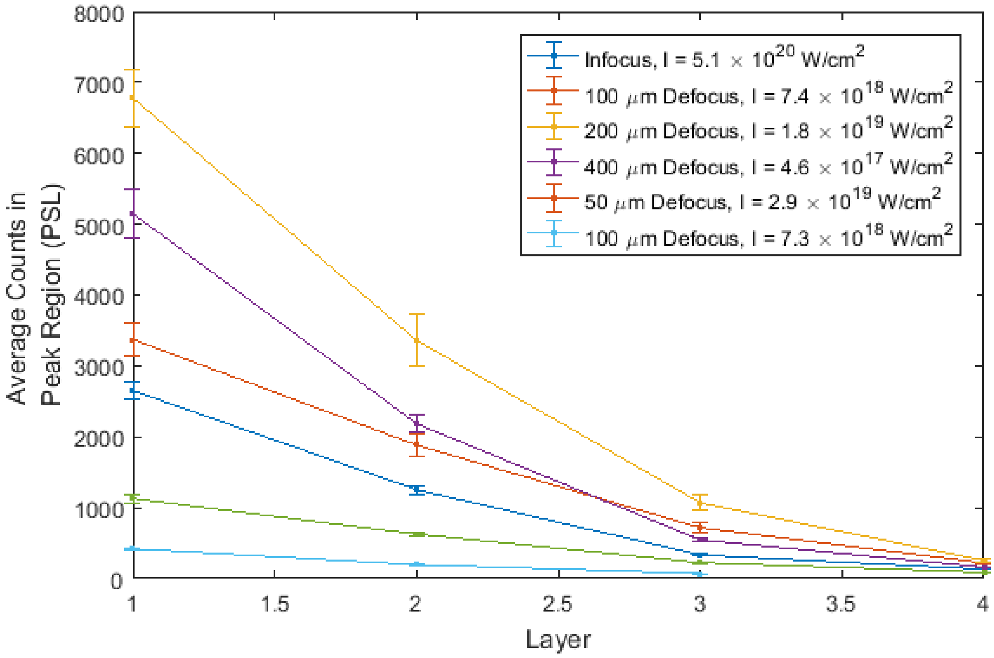

Figure 6.19: The PSL extracted from the peak of the angular distribution for all foci.The uncertainities arise from the standard deviation of measurement of the average.

escaping electron beam has in comparison to the bremsstrahlung x-rays produced by the copper target, GEANT4 was used.

An electron beam was sent into a 100 μm copper target and the number and energy of the electrons and x-rays that reach the rear of the target were recorded. Assuming that the escaping electrons make up 1-10% of the total electron distribution [106] as the majority will reflux, the estimated x-ray flux incident onto the wraparound diagnostic can be calculated. This takes into account the additional bremsstrahlung x-rays which will be produced during the electron-refluxing process, as discussed by Quinn *et al* [69].

The x-rays that are emitted from the target have a typical bremsstrahlung shape spectrum that peaks at 30 keV. Although 30 keV x-rays have similar absorption in the image plate to multi-MeV electrons, see Figure 3.26 from Chapter 3, the first filtering layer cuts out most x-rays below 50 keV.

The experimental data from the wraparound for which temperature is calculated is the average PSL taken at the peak of the signal. Figure 6.19 shows the average counts taken at the peak for all the different shots at all the defocuses. As there was no direct isolated measurement of the x-rays or electrons the percentage of escaping electrons is difficult to obtain. However, the estimated input spectra and experimental results can be compared for a number of different escaping electron percentages (2.5-15%) to see what effect this has on the observable temperature and also the quality of the fit. A comparison between the expected output of the diagnostic for different temperatures and for a number of different escaping electron percentages is done by using the least squares method; the r-squared values for the infocus data is shown in Figure 6.20. From an escaping percentage of 5 to 15%, the best fit temperature lies between 2.4 to 2.8 MeV; this is shown in table 6.2. From this, the temperature is taken as 2.6 ± 0.2 MeV. Changing the escaping electron fraction would have an obvious effect on the flux, however the temperature changes slowly over the different percentages which gives confidence in the method of temperature extraction. This method is repeated for all the data measured across the different foci.

Escaping Electron Percentage	Best Fit Temperature (MeV)
5	2.4
7.5	2.6
10	2.7
12.5	2.75
15	2.8

Table 6.2: A table of the temperatures extracted from the best fits for electron escaping fractions from 5-15% for the infocus data.

The temperatures extracted from the experimental data is shown in Figure 6.21 as a function of laser intensity. This shows that over almost three orders of magnitude in intensity, the escaping electron temperature has not changed by a significant amount. Also on Figure 6.21 are the Beg, Haines and Wilks scaling laws, as discussed in Chapter 4, for internal hot electron temperature scaling as

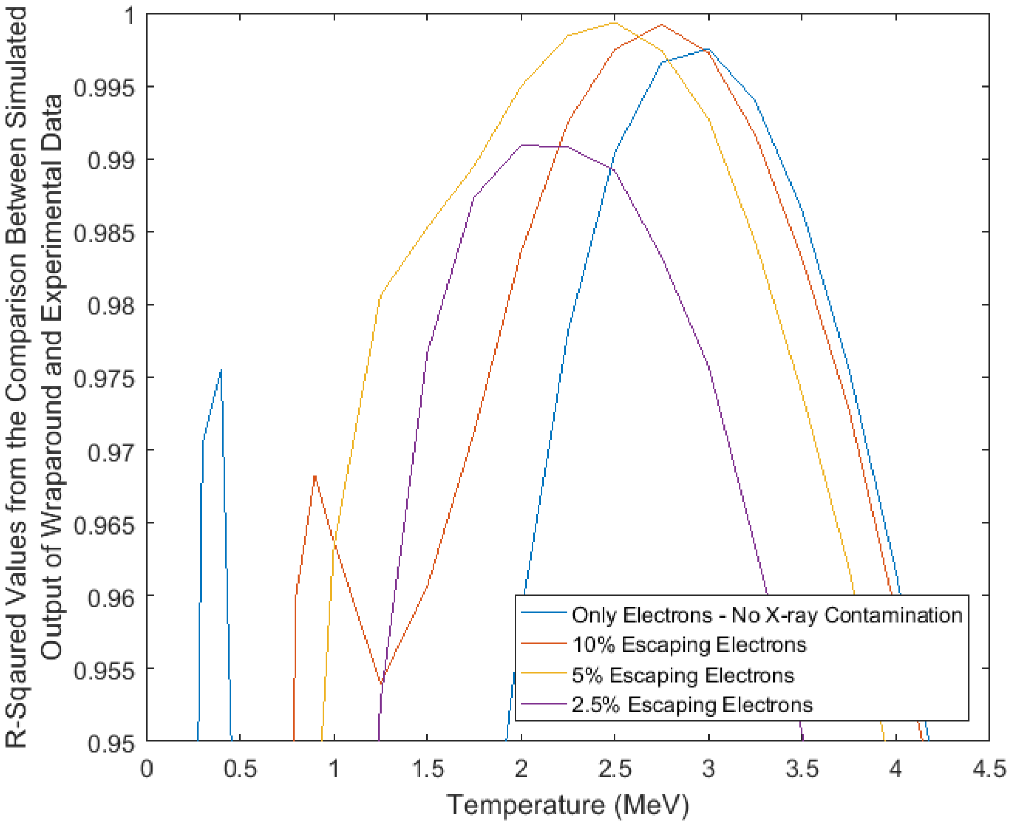

Figure 6.20: The r-squared values calculated from comparison between the experimental data and the different estimations for the percentage of escaping electrons between 2.5 and 10%.

a function of laser intensity. The predicted temperature from these scaling laws, although different, vary from approximately 200 keV to 2 MeV over the intensity range studied during the experimental campaign.

The lack of change in the temperature is only partly observed in the simulations conducted earlier in this chapter. For the long pre-plasma simulations, the output of the diagnostic for the tight focus to 100 μm defocus ($\approx 7 \times 10^{18} < \mathrm{I} < 5 \times 10^{20}\mathrm{W/cm^2}$) shows that the temperature does not change by very much. However, for further defocus ($\approx \mathrm{I} < 7 \times 10^{18}\mathrm{W/cm^2}$), the temperature begin to drop, as shown by the reduced gradient in Figure 6.13. For the case of a short pre-plasma the temperature remains very consistent for the 3 defocuses shown in Figure6.15 b) and 6.16 a). What is clear from the experimental and simulation results is

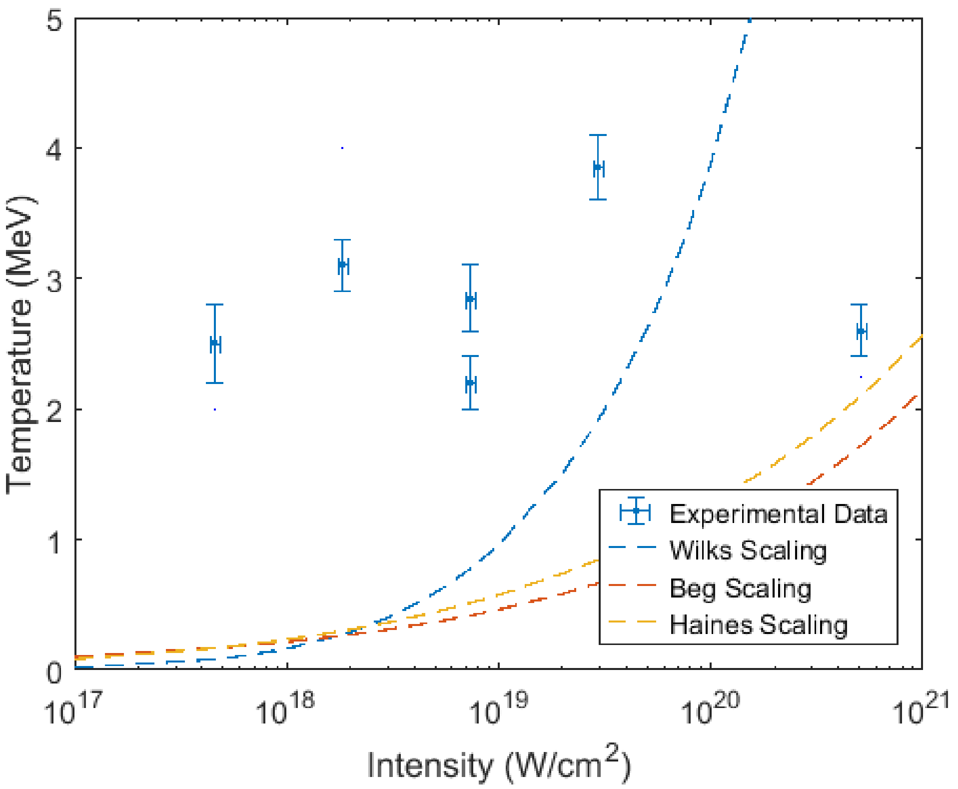

Figure 6.21: The experimentally measured temperatures from the wraparound diagnostic. This is extracted by comparing the experimental results to the expected output of the diagnostic from a Boltzmann electron distribution. The temperatures stay very flat over the intensity range. Also plotted are 3 scaling laws (Wilks [24], Beg[33] and Haines[34]). The experimental data shows much less variation in the temperature than that predicted by the scaling laws.

the importance of measuring the electron density at the front surface prior to the arrival of the main pulse. The formation of the pre-plasma due to ASE and/or pre-pulses is complex as both of these effects are intensity dependent and likely scale differently as a function of focal distance from best focus.

The temperature from both the longer and shorter pre-plasma simulations is higher than that measured from experimental data. There could be a number of reason for this. Firstly, as the simulations are only conducted in 2-dimensions, the electrons may spend longer in the laser field than if they had a third degree of freedom. This could lead to the electrons gaining more energy from the ponderomotive force than they would in reality.

Although the temperature is higher, the relative differences between the outputs is more important. For this we have observed that for certain conditions, a defocused laser will increase the number of escaping electrons and will yield a similar output temperature across a number of foci.

With the peak temperature of the escaping electron distribution diagnosed, an estimate of the total electron energy can be made. To do this we also need the absorption curves shown in Figure 3.31 of Chapter 3, and the calibrations of the image plate for incident high energy electrons, as performed by Nakkanii *et al* [150] and Bonnet *et al* [77]. The total energy escaping as electrons is estimated to be between 10-20% of the total laser across the different foci. Improvements of this measurement can be made if the wraparound diagnostic is accompanied with electron spectrometers (ideally multiple) to aid in angularly resolving the spectra of the escaping electrons.

A number of additional investigations can be conducted from the simulations in this chapter. The next section aims to infer more information about the rear surface fields and the escaping electron dynamics.

6.1.5 Escaping Electron Dynamics

Initially the electrostatic potential is zero; it only increases as the electrons begin to escape/build up on the rear of the target. The temporal evolution of the fields on the rear of the target is shown in Figure 6.22 for the infocus simulation with large pre-plasma. The maximum of this field occurs as the peak of electrons begin to leave the target; this was found to be at $\sim$0.9 ps from Figure 6.22. Figure 6.23 shows a line out of the average electric field value taken across the middle of the simulation box at the peak time. The 50 μm defocus has the highest peak electric field of approximately 5×10^{12} V/m, which is associated with the highest flux of escaping electrons.

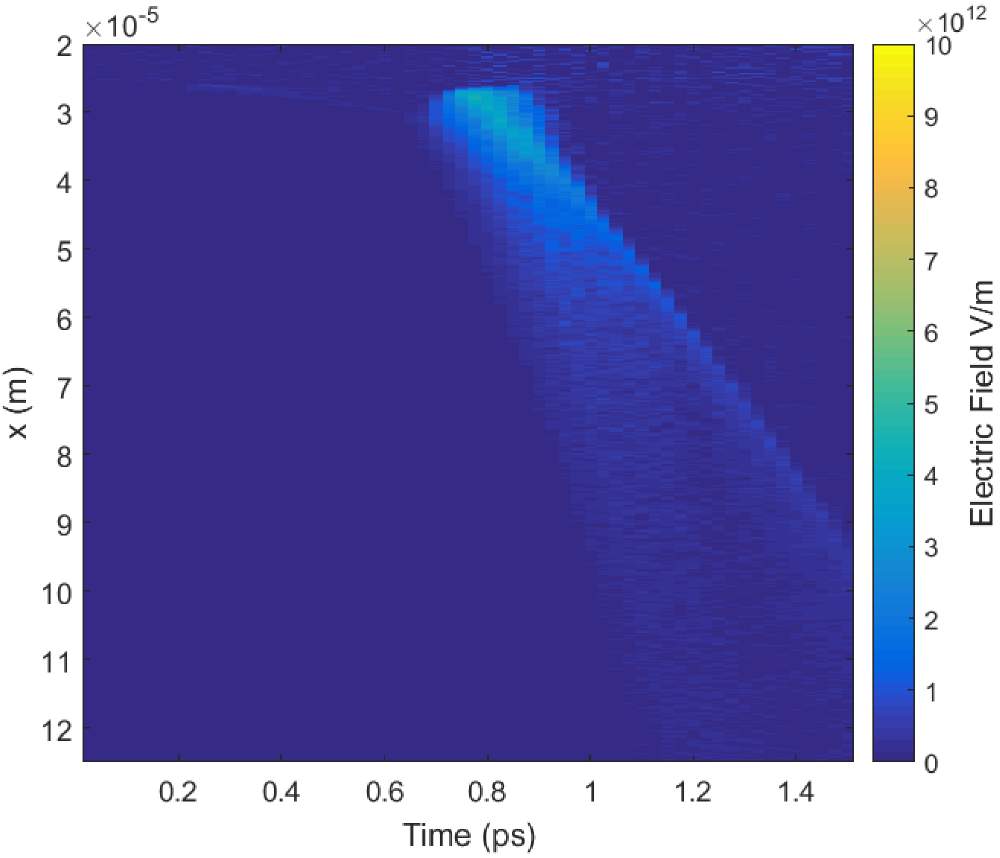

Figure 6.22: The temporal evolution of the electric fields on the rear surface of the target. The target rear surface is at 25 μm which is at the top of the graph. The peak of the field moves away from the target at later times.

As mentioned previously, particle tracking was conducted during the simulation. This involves assigning each particle a unique integer, or ID, that can be used to identify it. The outputs of the simulations are sorted by finding all the unique particle IDs of interest. Information such as the position and momentum can be then extracted at any time step through the simulation. This is very computationally expensive and, as such, a random sample of the output macro-particles has to be taken to reduce the memory requirements. This varies for each focus/simulation as the macroparticle number dictates the memory limit, not the real particle number. As a result, the exact particle numbers from the particle tracking are not directly comparable between simulations.

Using the particle tracking, the energy of the electrons was found at two different

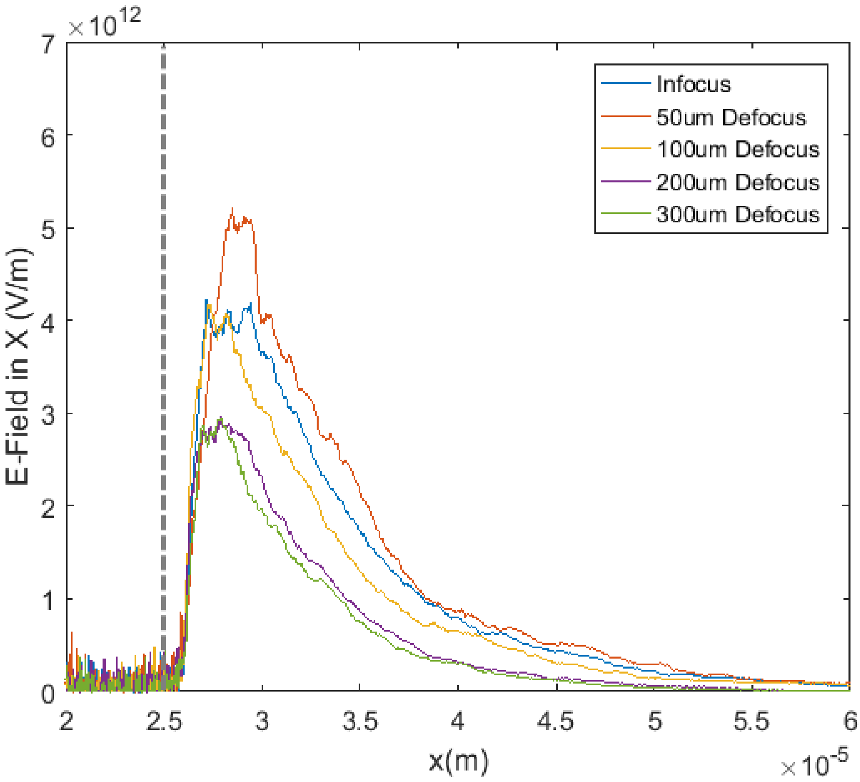

Figure 6.23: A lineout of the electric field in X (the spatial dimension perpendicular to the target surface) on the rear surface of the target at the peak. The dotted line represents the initial position of the target surface. This shows that 50 μm defocus has the highest field strength.

boundaries. These boundaries were 5 μm inside the target from the rear side to monitor the internal electrons and 10 μm from the rear-edge of the simulation box to monitor the escaping electrons. As the simulation was conducted up to 1.5 ps, the escaping electrons measured are those that escape on the first pass of the target. As output Electron 2, as described in Table 6.1, has the smallest time-step between outputs, it provides the highest spatial resolution. Assuming all the electrons are relativistic ($v \approx c$) this output yields a spatial resolution of approximately 3 μm. As the IDs of each particle are known, the escaping electrons can be tracked back to when they cross the boundary inside the target. This allows the energy of the escaping electrons to be found prior to their escape.

The pre-escape energy spectrum is shown in Figure 6.24 for the in-focus simulations of the long and short scale length pre-plasmas, a) and b) respectively. The

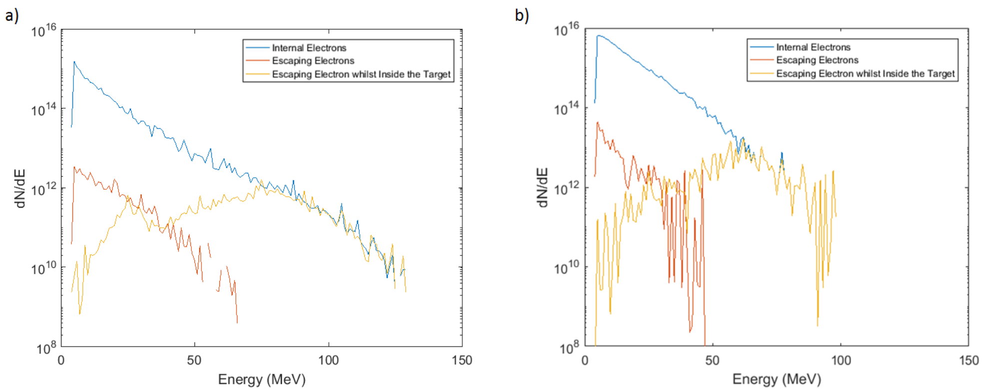

Figure 6.24: Particle tracking spectral results from the infocus simulation of the electrons passing boundaries 5 μm from the rear of the target and 10 μm from the rear of the simulation box for the long and short pre-plasma cases, a) and b) respectively. The spectrum of the escaping electrons inside the target shows that the majority of escaping electrons were previously the highest energy electrons; this is because they have to overcome the electrostatic fields that build up on the rear of the target.

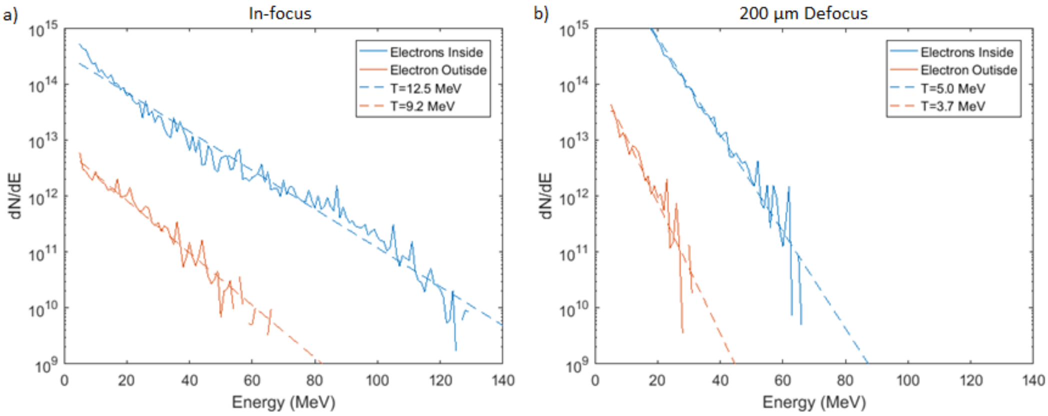

Figure 6.25: Fitted temperatures to the internal and escaping electron distributions for a) tight focus and b) 200 μm defocus simulations. The escaping electron temperature is colder than the internal electron temperature. The percentage of cooling is between 20-25% for each simulation, except for the 50 μm defocus simulations which is approximately 5%. These values are comparable to the 9-31% percentages simulated by Link *et al.*

energy of escaping electrons shown in Figure 6.24 is much lower than the energy of the internal electrons, however these electron previously made up the highest energy electrons inside the target. As was highlighted earlier, there is an electric field that will restrict the energy of electrons able to escape. To overcome this electric field, the electrons require significant amounts of energy.

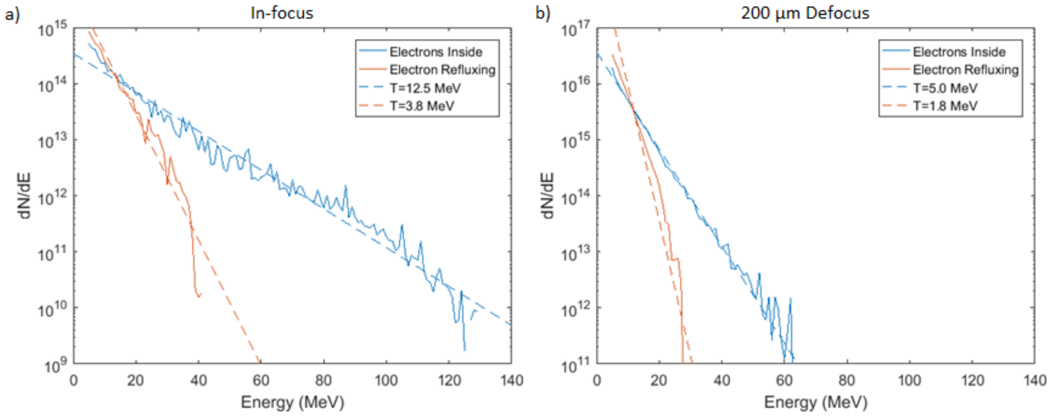

Figure 6.26: Fitted temperature for the internal forward and refluxed electrons. The electrons that are refluxed also experience a cooling which is much greater than the escaping electrons, between 60-80% across all foci. A lot of this cooling is due the highest energy electrons leaving the target.

As mentioned previously, analytical and numerical analysis conducted by Link *et al* [106] found that the escaping electron temperature is slightly lower than the internal electron temperature. This effect is also present in the simulations conducted here. Single temperature Boltzmann fits have been applied to the internal and external electron spectra in Figure 6.25 for the tight focus and 200 μm defocus simulations. The amount of cooling measured is between 20-25% for each simulation, except for the 50 μm defocus which sees a much smaller cooling, approximately 5%. This degree of cooling is comparable to that simulated by Link *et al* which varied from 9-31% depending on target and laser conditions.

As well as the escaping electrons, the dynamics of the refluxing electrons is of interest. The internal forward and backwards electrons are shown in Figure 6.26 for the tight focus and 200 μm defocus simulations. The refluxed electrons appear to have lost a lot of the energy in the process of refluxing. Some of this energy has left the target in the form of the escaping electrons as these are made up of the highest energy electrons. However, the majority of the energy will have been exchanged to the protons and the sheath on the rear surface. The reductions in energy of the refluxing electrons corresponds to a cooling in the region of 60-80% across all foci.

6.2 Escaping Electrons as a Function of Pulse Duration

The use of pulse length to control aspects of laser solid interactions has been investigated in the past. A significant area of interest for these previous investigations was the dynamics and optimisation of proton acceleration. Fuchs *et al* [151] was able to show how the proton conversion efficiency and maximum energy scales with different laser parameters, including pulse length, for intensity between 2×10^{18} and 6×10^{19} W/cm^2 . During the pulse length scan, the intensity was kept constant by varying the laser energy; this resulted in a increase in the proton conversion efficiency and maximum energy as the pulse duration increased. A similar study was conducted by Robson *et al* [114] for a number of different laser parameters with a laser intensity of up to 6×10^{20} W/cm^2. A pulse length scan from 1 to 8 ps was conducted with a constant intensity of approximately 6×10^{19} W/cm^2 which showed the proton energy decreases initially for pulse lengths between 1 and 6 ps before increasing again at 8 ps. In both of these studies the analytical model used for these scaling laws comes from Mora [93], in which a fluid model of the charge separation on the rear surface is studied and a model of the ion dynamics is created. This leads to equations describing the ion spectrum and maximum energy. Robson *et al* describe alterations that they make to the model referred to as the two-phase with 3D effects. They describe this as a more accurate way of incorporating the temporal variation of the hot electrons that drive the plasma expansion and includes a term to take account of the fact that the expansion is 3D. This method agrees more closely with their results although there is still a significant difference. The results shown in Fuchs *et al* match much more closely with the Mora model. Finally, Schreiber *et al* [152] conducted an experiment with 0.7 J incident onto target which remained constant whilst the pulse length was changed from 50 fs to 5 ps. An optimum for the maximum proton energy is found at a pulse length of 250 fs. An analytical model was developed in this paper. It is based solely on a radially confined surface charge set up by the electron reaching the rear surface. This model accurately agrees with the maximum proton energies observed on their experiment as well as the optimum at 250 fs. From the experiment results presented no one has measured the escaping electron distributions as a function of pulse length, which leads to the questions; how are the angular, temperature distribution or flux of electrons affected by such changes to the laser conditions?

To further investigate the escaping electrons, a number of shots were taken on the Vulcan laser in Target Area Petawatt on 100 μm thick Au foil targets where the pulse length was stretched. The energy and focal spot size were fixed so the intensity of interaction was reduced.

6.2.1 Experimental Method

The wraparound diagnostic is employed again to measure the escaping electron distributions. The filtering design used was design B which was 2 pieces of iron before the first layer of TR-image plate. An RCF stack is used to measure the profile and energy of the protons emitted at the rear of the target. The stack is made up of 13 layers of HDV2 and sits 65 mm from the target. The RCF stack is able to sample protons of energies up to 28.8 MeV as calculated using SRIM. The full RCF stack filter design is shown in Figure 6.27 with the Bragg peak energies listed in each RCF layer. The wraparound stack is positioned slightly below the horizontal axis and the RCF sits slightly above; this allows each diagnostic to measure half of the beam for their respective particles.

6.2.2 Experimental Results

Plotted in Figure 6.28 are the signals from the first two layers of the image plate inside the wrap around stack. As discussed in Chapter 3 Section 3.5.3, and similar

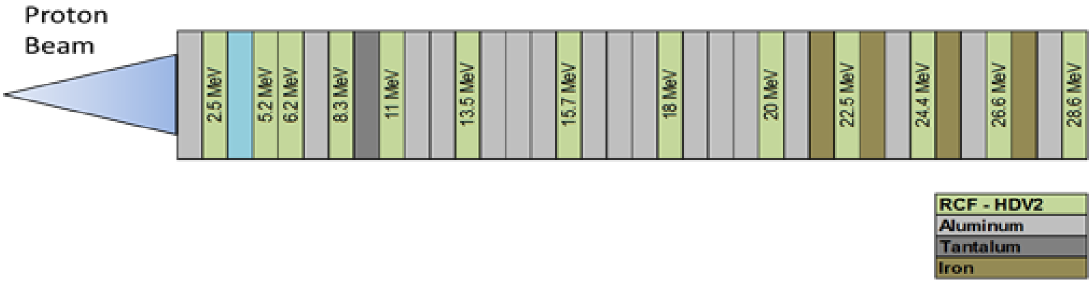

Figure 6.27: Layout of the RCF stack used on the experiment conducted in TAP. The maximum measurable energy is approximately 28.5 MeV.

to the data presented earlier in Chapter 6, the image plate has been interpolated to the initial scan due to saturation of the scanner. Gaussian filters have been applied to remove blemishes, again as shown earlier in Chapter 6.

The polar plots for the shots are plotted next to their corresponding image plate in Figure 6.28. The incoming laser beam axis is drawn on with a dotted line and is extended through the target to show the forward beam direction. From the polar plots it is clear that the escaping electron distribution varies from shot to shot.

The integrated flux per incident joule of laser energy of both the electrons and protons is shown in Figure 6.29. The minimum integrated flux is measured at the longest pulse length/lowest intensity for both the protons and the electrons. The proton signal peaks for the 6 ps shot, whereas the most electrons are observed at the shortest 1 ps pulse length. The peak electron signal in PSL per unit incident laser energy from the wraparound diagnostic is shown in Figure 6.30 which shows a similar trend to the integrated proton data.

The integrated proton dose as a function of RCF layer threshold energy is shown in Figure 6.31. The highest flux at the lowest energies appears for the 6 ps shot. However, the 1 ps shots have higher max energies. The 18 ps shot has the least dose and lowest maximum energy. A simple Maxwellian exponential is fitted to the data in Figure 6.31 with the temperatures listed in the legend. The temperature clearly appears to decrease with increasing pulse length.

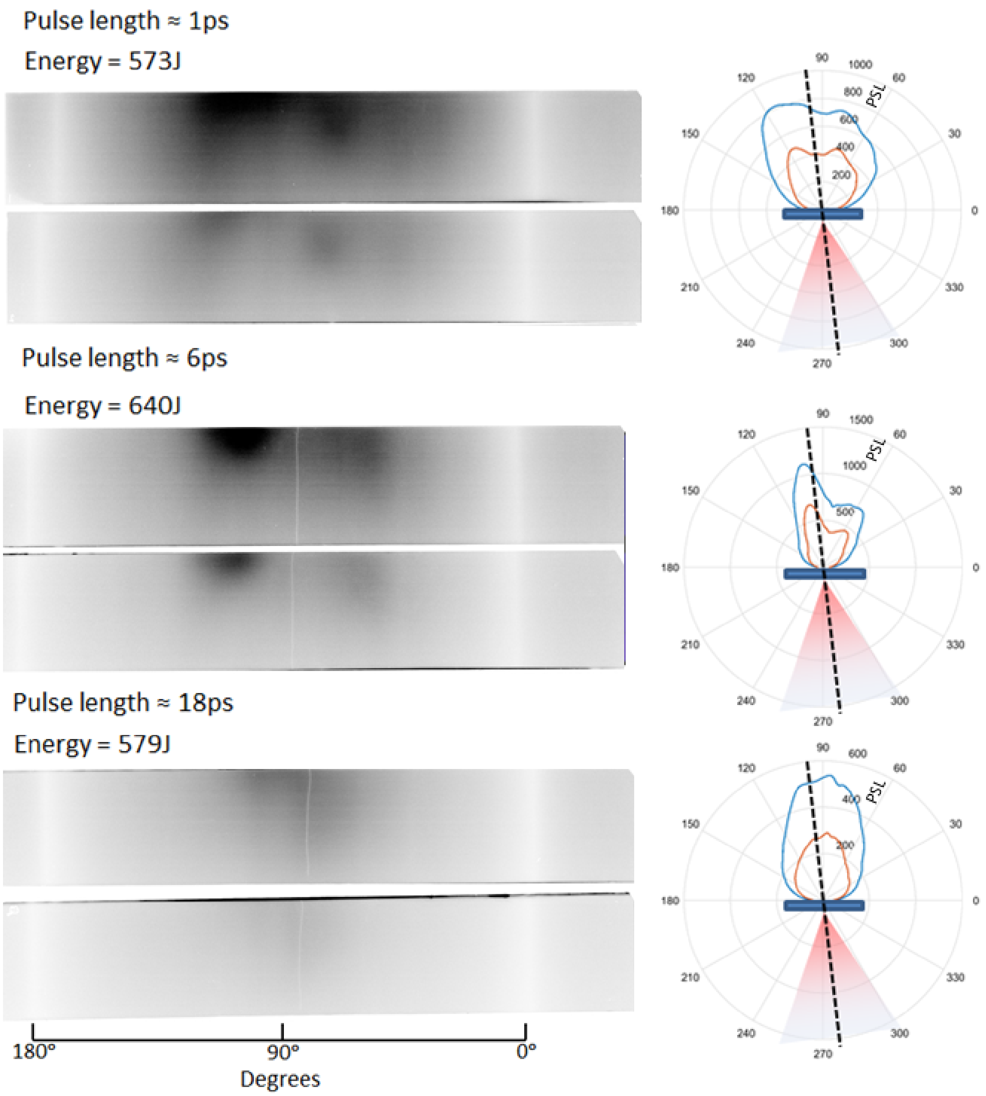

Figure 6.28: The first two layers of the wrap around diagnostic plotted alongside the corresponding polar plots of PSL for a number of pulse durations.

The extracted temperatures from both the wraparound around diagnostic and RCF stack are shown in Figure 6.32. The temperature extraction from the wraparound diagnostic is taken from the peak signal; similar to earlier in this chapter. As stated before, the proton temperature decreases as a function of pulse duration, whereas the escaping electron temperature appears to peak at 6 ps.

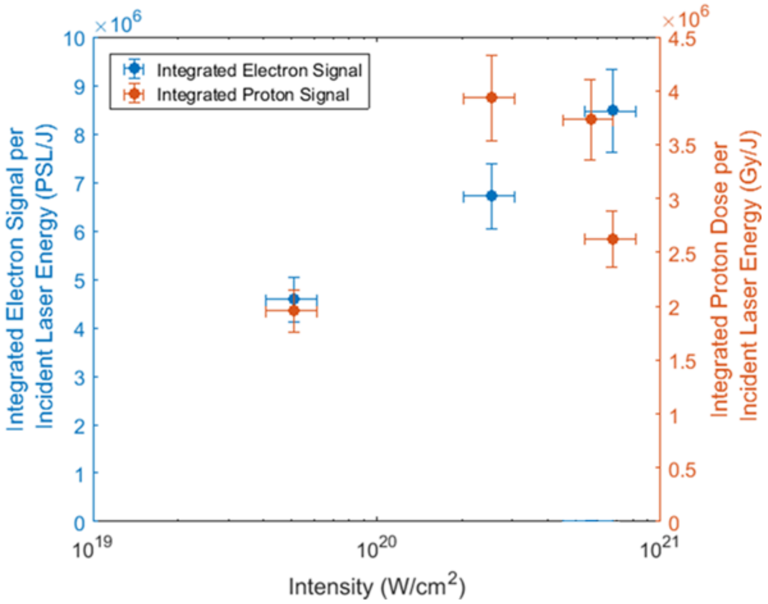

Figure 6.29: The integrated dose of the both the protons from the RCF stack and the PSL due to the electrons from the wraparound diagnostic per unit incident laser energy as a function of intensity. For the electrons, the trend shows the signal is decreasing with longer pulses, whereas for the proton data the signal increases at 6 ps and falls at 18 ps.

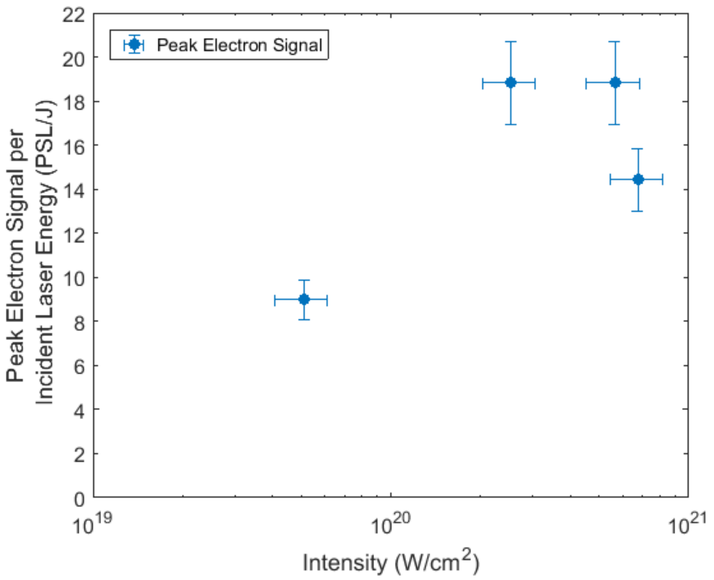

Figure 6.30: The peak electron signal recorded on the wraparound diagnostic as a function of intensity for different pulse durations. The trend is similar to the that of the integrated protons, the electron signal peaks at shorter (1-6 ps) pulse durations and then there is a minimum at the longest.

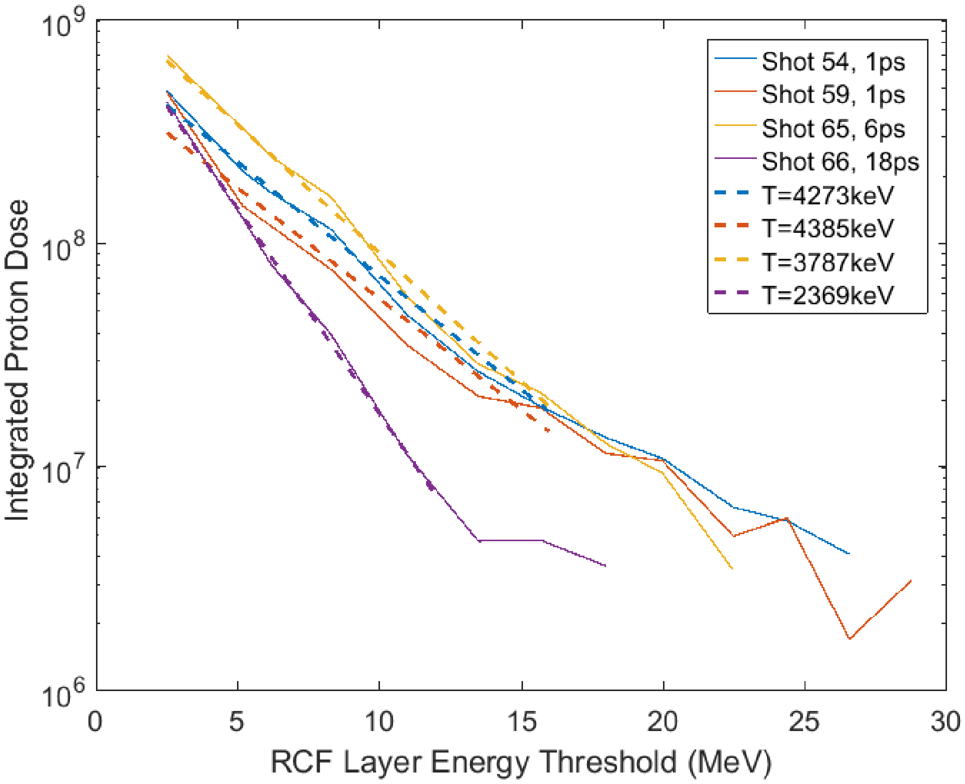

Figure 6.31: The integrated dose from the RCF layers plotted as a function of the RCF layer energy threshold. A simple Boltzmann distribution has been fitted to each data set. The highest temperature occurs for the shortest pulse duration, however the highest flux, particularly for the energies up to 15 MeV, occurs at 6 ps.

6.2.3 Modelling

Both the escaping electrons and protons can be separately analytically modelled. The maximum proton energy as a function pulse duration can be modelled using methods from previous studies which will be discussed first.

6.2.3.1 TNSA Modelling

A model to analytically describe the proton acceleration developed by Scheiber *et al* [152] can be used to calculate the maximum proton energy. This equation

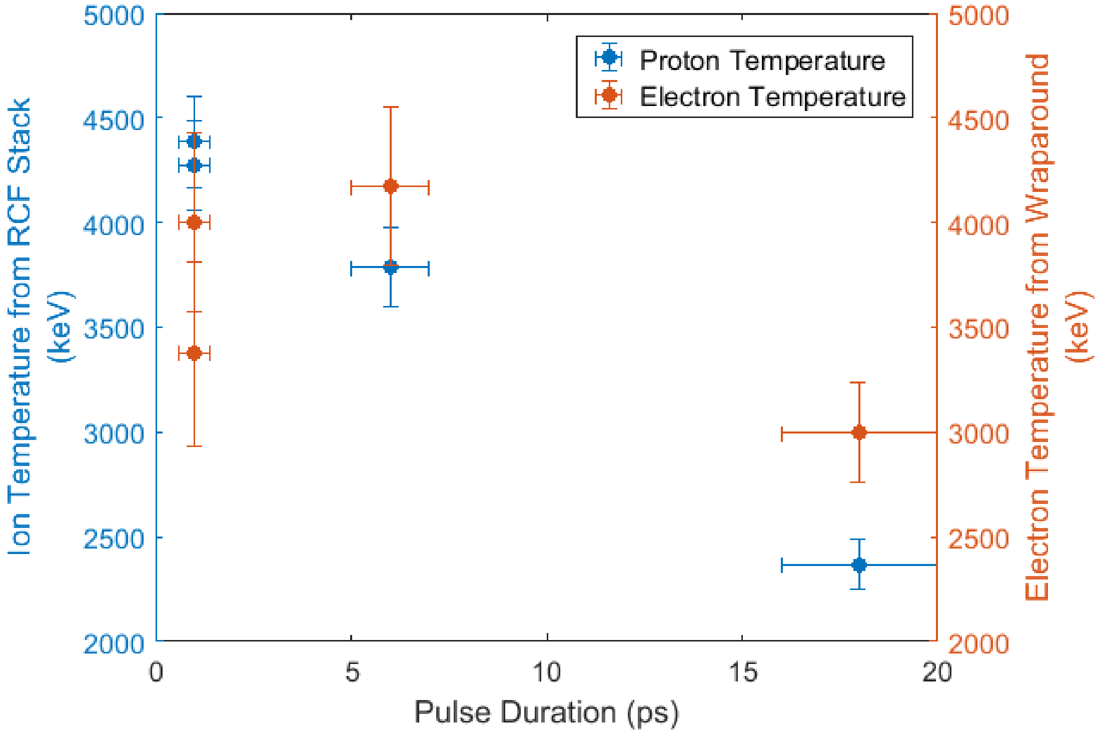

Figure 6.32: The temperature extracted from the wraparound diagnostic and RCF stack for the electrons and proton respectively. The temperature of the protons is falling as a function of pulse duration whereas the electron temperature peaks at 6ps.

given by Scheiber is,

$$\frac{\tau_L}{\tau_0} = \left(1 + \frac{1}{2}\frac{1}{1-x^2}\right) + \frac{1}{4}ln\left(\frac{1+x}{1-x}\right) \tag{6.3}$$

where $\tau_0 = B/v\left(\infty\right)$, τ_L is the pulse duration and $x = \left(E_m/E_{i,\infty}\right)^{12}$; where B is the size of the sheath on the rear, $v(\infty)$ is the velocity of the fast ions, E_m is the maximum proton energy and $E_{(i,\infty)}$ is the energy of a given ion species if accelerated for an infinite amount of time. $E_{(i,\infty)}$ is given as,

$$E_{i,\infty} = q_i 2mc^2\left(\frac{f_{abs}P_L}{P_R}\right)^{1/2} \tag{6.4}$$

where P_L is the power of the laser, q_i is the charge of the ion, $P_R = mc^3/r_e = 8.7$ GW and f_{abs} is the conversion of laser light into hot electrons. There are two main advantages for the model presented by Schreiber. Firstly, it does not explicitly depend on the internal electron temperature. As there are a number of different scaling laws for the hot electron temperature, each can be argued in the case where the internal temperature is not measured experimentally, such as this experiment. As a result this eliminates one parameter of uncertainity. Secondly, as the pulse length increases the maximum proton energy, E_{max}, tends towards $E_{(i,\infty)}$ which is a quickly falling function that depends on the power of the laser. This results in falling maximum proton energies as the intensity is decreased with a rising pulse length. Finally, as stated previously, short laser pulses have a reduced acceleration time which will yield an optimum pulse duration to achieve the highest achievable proton energy for a particular incident energy and focal spot.

The Mora model [93] for the maximum proton energy, based on a self-similar 1D expansion model, is given by,

$$E_{max} = 2T_{hot}\Big[ln\left(t_p + \left(t_p^2 + 1\right)^{1/2}\right)\Big]^2 \tag{6.5}$$

where $t_p = \omega_{pi}\tau_{acc}/(2exp(1))^{1/2}$ is the normalised acceleration time and ω_{pi} is the ion plasma frequency. The important factor here is τ_{acc}, which Fuchs *et al* fixed at 1.3 times the laser pulse length. Brenner *et al* [94] argues that this quantity should depend on 3 parameters: the laser pulse duration (τ_L), the expansion time ($\tau_{expansion}$) and the average time for electrons to transversely escape the acceleration volume. They combine in the following form,

$$\tau_{acc} \approx \sqrt{\tau_L^2 + \tau_{expansion}^2 + \left(\frac{D_L}{2u_e}\right)^2} \tag{6.6}$$

where D_L is the size of the focal spot, u_e is the average velocity of the electrons. The expansion time is given as $\tau_{expansion} \sim 6\omega_{pi}^{-1}$ from Buffechoux *et al* [153].

The energy of the laser onto target depends on the throughput of the compressor and the energy contained in the focal spot. The throughput of the compressor was measured by comparing calorimetry data from before and after; this yields a throughput of approximately 62%. The FWHM of the focal spot contains 30±5% of the beam energy (this is only true for tight focus).

The size of the rear surface sheath depends on the focal spot size, which was measured to have a diameter of 7 μm. It also depends on the angular divergence of the beam of accelerated electrons. Green *et al* [154] collates a number of angular divergences from various experiments at different intensities. This data can be fitted using a logarithmic function. The uncertainty in the data is taken into account by using a fit of the upper and lower bounds of the error-bars. These equations are,

$$\theta_{upper} = 6.3 \ln (I_{18}) + 7.5, \tag{6.7}$$

$$\theta_{lower} = 5.2 \ln (I_{18}) - 0.3 \tag{6.8}$$

where I_{18} is the intensity of the laser as a factor of 10^{18} W/cm^2. This data ranges from 2×10^{19} W/cm^2 to 1.2×10^{21} W/cm^2 which covers the full range of the experimental data here. The absorption is also a variable that is not fixed. Schreiber and Fuchs use a scaling of absorption as a function of intensity proposed by Yu *et al* [110] and Key *et al* [5] and an upper limit of 0.5 observed by Hatchett *et al* [104]. Since then many studies of absorption have taken place. Davies [32] collates many of these studies which therefore encompasses many different laser parameters; see equation 2.52.

Although the temperature of the hot electrons is not required for the Schreiber model it is for the Mora model. Two models were used, the ponderomotive/Wilks [24] and the Beg scaling [33], as discussed in Chapter 4.

Using the estimates for the energy, absorption, temperature of the hot electrons and the electron divergence angle, with the upper and lower bounds of our errors, the maximum proton energies can be estimated. The models of maximum proton energies as a function of pulse length are plotted in Figure 6.33 represented by the shaded region. The errors in the models arise from the uncertainty in the

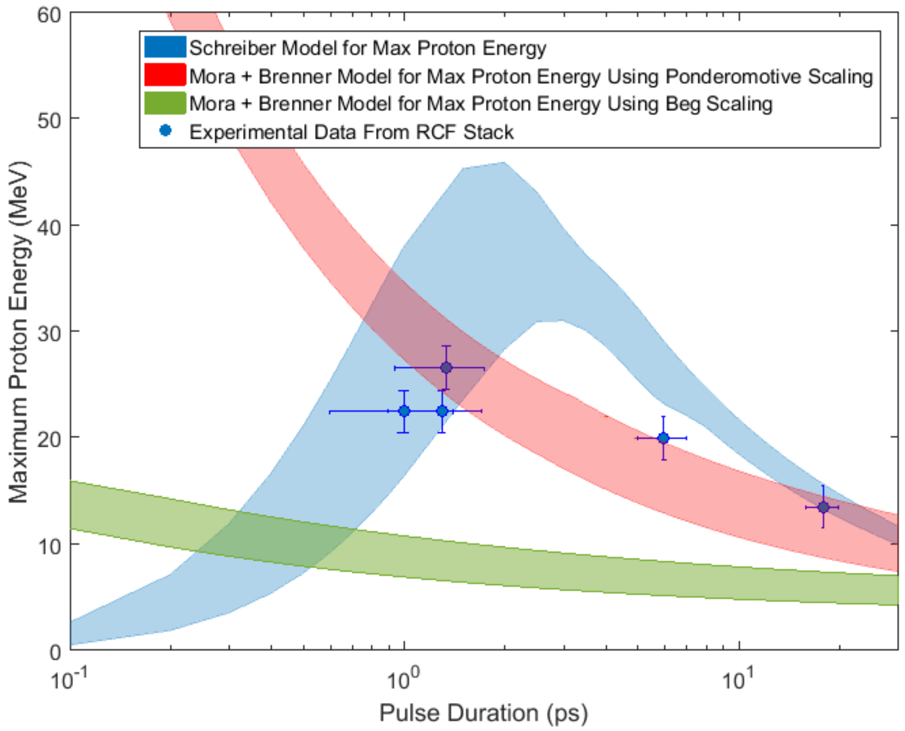

Figure 6.33: The maximum proton energy models plotted as a function of pulse length with the experimental data. The model described in Schreiber *et al* [152] and Mora [93] plus Brenner [94, 155] for maximum proton energy as a function of pulse length for two different temperature models. The shaded regions represent the errors in the models that arise from the error in the energy in the focal spot and the electron divergence angle from Green et al [154]. The experimental data for the maximum proton energy from the RCF stack is also plotted.

divergence angle and the energy contained in the laser spot. The experimental data for the maximum proton energy is also plotted in Figure 6.33. The error quoted in the pulse length is calculated from the standard deviation of the measured pulses throughout the experimental campaign; for 1 ps this is over 50 shots, for the other shots this is 5 shots each. The errors determined in the maximum proton energy come from the resolution of the RCF stack. It is clear that the data at 1 ps and 18 ps fit the Schreiber (blue) and the Mora and Brenner using ponderomotive scaling (red) regions well. The Mora and Brenner model using the Beg scaling (green), underestimates the proton energies significantly across all pulse lengths. The data at 6 ps appears to fit much more closely to the Mora and

Brenner model using the ponderomotive/Wilks scaling (red) than the Schreiber model.

6.2.3.2 Modelling of the Escaping Electrons

Unlike the previous modelling of the escaping electrons conducted with the PIC code EPOCH, the long pulse lengths used in this experiment make it very difficult to model numerically. To model the electrons analytically, a simple 1D capacitor model [106] can be created to investigate the relative number of total escaping electrons as a function of pulse duration.

To begin, the model needs to have a temporally evolving electron distribution that is related to the intensity of the laser pulse incident onto the target. Assuming a Gaussian temporal intensity for the laser pulse, a matching temperature can be found. The intensity of the laser is calculated using the incident laser energy, focal spot size and the pulse duration. The temperature of the distribution and incident laser energy also relate to the total number of electrons, which is also calculated assuming a constant absorption. Figure 6.34 a) shows the temporal variation in the intensity and temperature of the laser and electrons respectively, and Figure 6.34 b) shows the temporal evolution of the electron spectrum for a pulse duration of 1 ps FWHM. The electrons appear to heat up before the laser, however, the laser at this point is already at 1×10^{18} W/cm^2 which is intense enough to create temperatures up to hundreds of keV.

The potential on the rear of the target is set as $V = q_{esc\ e^-}/C$; as the initial number of escaping electrons, $q_{esc\ e^-}$, is zero, the initial voltage on the rear surface is also zero. Each energy at each time-step is tested to see whether the electrons are sufficiently energetic to overcome the electrostatic barrier. This is calculated as $E_{final} = E_{initial} - eV$; if E_{final} is greater than zero the electron escapes with a new energy, if E_{final} is less than zero the electron does not escape and the next energy/time-step is tested.

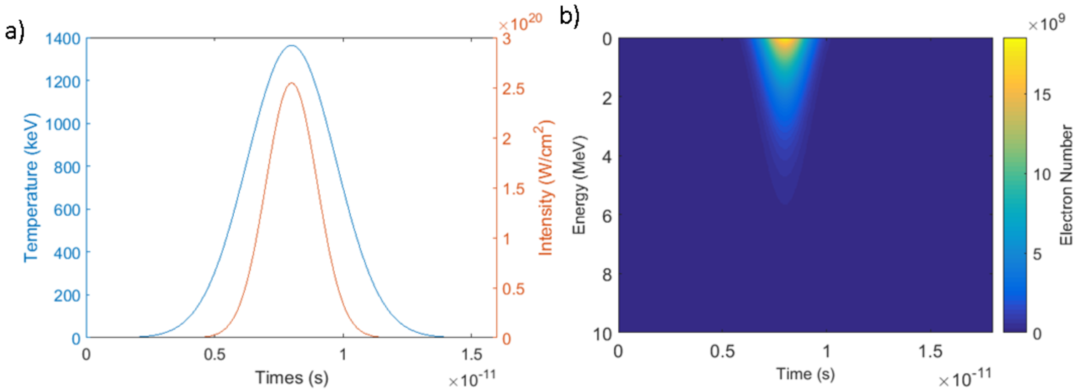

Figure 6.34: Temporal plot of a the laser created in the capacitor model. a) shows the intensity and temperature temporal profiles for a 1 ps laser using the same energy incident onto target and the same focal spot size as present in the experiment. The number of electrons as a function of time and energy is shown in b).

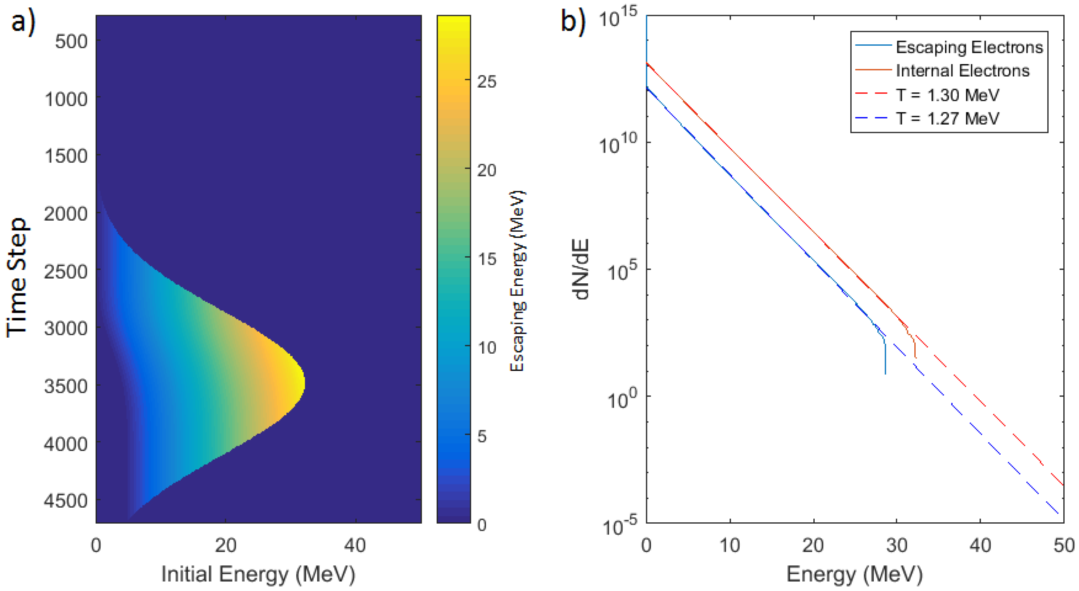

Figure 6.35: The output electron energies from the capacitor model for a 1ps pulse. The temporal evolution of the electron energies, as shown in a), shows that the electrons escaping at later times are reduced in energy. This causes the temperature of the electrons to cool, as shown in b).

As described in Link *et al* [106], there are two limits for the capacitance C. If the capacitance is large, the voltage on the rear will grow very slowly which enables almost all the electrons to escape. From the simulation conducted earlier in this chapter, the fields grow quickly and to large values. This suggests that the

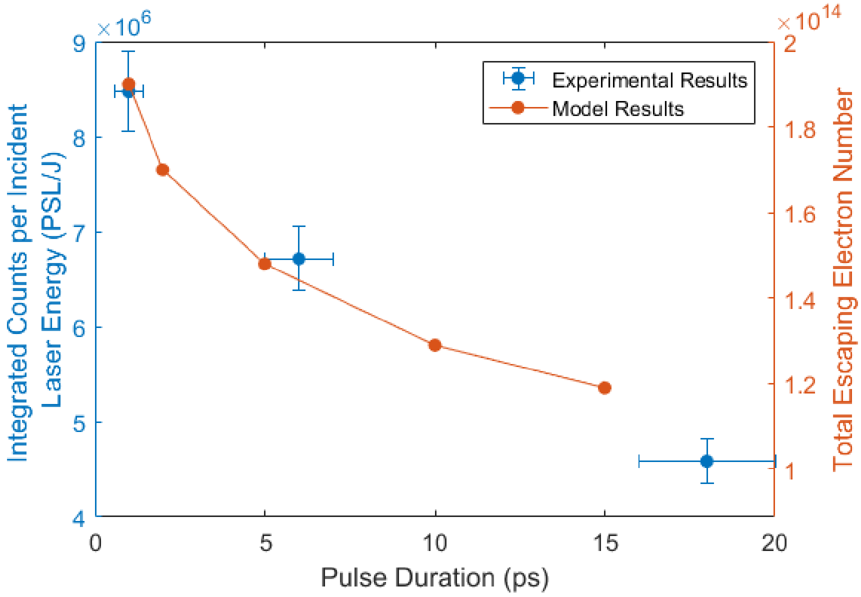

Figure 6.36: The modelled total escaping electron numbers compared to the integrated PSL per unit incident laser energy from the experiment as a function of pulse duration.

capacitance is very small; in our case the capcitance is set to 10^{-18} which is similar to that suggested by [156] using a disc/sphere with a radius of approximately 1 μm. In this case, as the voltage increases, the final energy of an electron that does escape will be reduced significantly. This will lead to the temperature cooling observed in Figure 6.25. The model has temporal resolution of 2.5 fs and energy resolution of 10 keV.

The model was ran for a number of pulse lengths to calculate the escaping electron number and compare it to the experimental data; the results of these simulations are shown in Figure 6.36. These show that for the same laser conditions, the total number of escaping electrons is expected to fall as a function of pulse length. Surprisingly, this simple 1D capacitor model matches the experimental results closely. In the model, as the pulse length increases, the temperature decreases which means that a greater number of electrons are accelerated. Less electrons are able to escape because of the reduction of the temperature/energy. This means the escaping electron percentage, shown in Figure 6.37, also decreases as a function of pulse length.

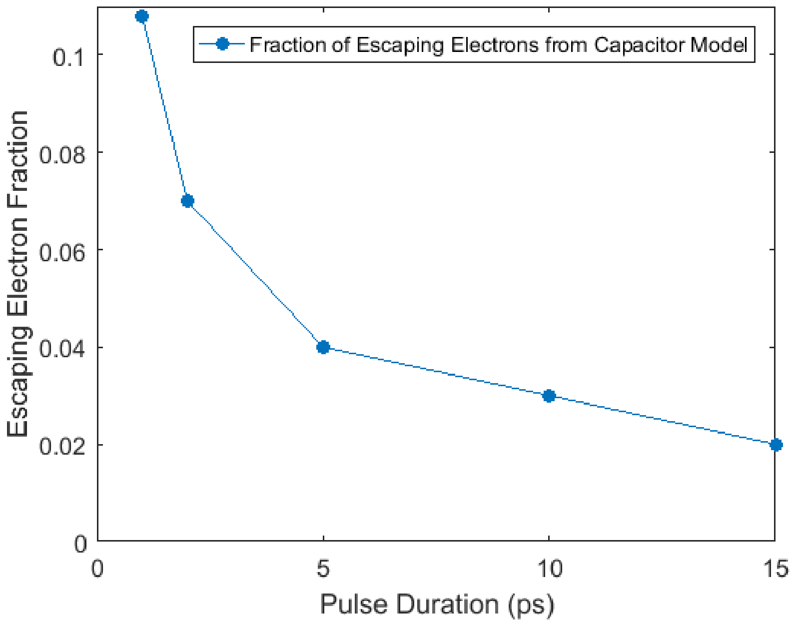

Figure 6.37: The fraction of escaping electrons from the capacitor model as a function of pulse duration. This shows that the fraction of escaping electrons is decreasing with increasing pulse length.

6.3 Conclusions and Future Work

Measurements of the escaping electrons were made using the wrap-around diagnostic for varying laser focal conditions. The results showed a significant increase in flux as the laser is defocused and the incident laser intensity was reduced from 4×10^{20} to 5.5×10^{18} W/cm^2 as shown in Figure 6.5. The escaping electron temperature was found to remain mostly constant as a function of intensity as shown in Figure 6.21.

2D PIC simulations were conducted to investigate the escaping electron dynamics and to understand the experimental results. Two sets of simulations were conducted; one set with a short pre-plasma and another with a longer pre-plasma. For the shorter pre-plasma, there is no increase in flux across the different foci and the temperatures from all the simulations (0-100 μm foci) remains very constant. However, for the longer pre-plasma simulations, the high electron number density present prior in front of the target caused the laser to self-focused; the 50 μm defocus simulation focused to the highest intensity incident onto the critical surface. This generates the hottest internal and external electrons as shown in Figure 6.12. The temperature for the 0-100 μm foci remain constant and there is a flux increase for the 50 μm defocus. Although these simulations thoroughly investigate the effect of defocus on a solid target, more extensive simulations could be conducted in 3D if sufficient computational resources became available.

The scale length of the previously mentioned simulations were not measured during the experimental campaign but rather estimated using studies conducted at similar intensities and on the same laser system. The scale length is shown to play a large role in the accelerated electrons and subsequently in the escaping electron flux and spectral distribution. The effect of the pre-plasma has been shown before on the accelerated protons [41, 147], with further investigation, the accelerated electrons could be optimised using the focal spot and pre-plasma for proton acceleration or fast-ignition schemes. As the growth of the pre-plasma is complex and depends on numerous parameters, a study needs to be conducted into its formation as a function of laser focus for a constant intensity, as per the experimental condition in this study.

Improvements to the temperature extraction process of the experimental data could be achieved by measuring the x-rays alongside the escaping electrons as the x-rays produced from the target cause a unwanted and unpreventable background signal to the layers of image plate. The extent of this was investigated using GEANT4 simulations. However, a more accurate method would be to use x-ray spectrometers positioned at many different angles around the target, such as the scintillator spectrometer demonstrated in Chapter 4, to measure angular temperature of the internal electrons. This would help with the deconvolution of the data measured using the wraparound diagnostic and also provide information about the difference between the internal and external electron distributions.

PIC simulations were also used to investigate the escaping electrons and their dynamics using particle tracking. The majority of escaping electrons appear to be made up of the highest energy internal electrons; this is inferred by identifying the electrons that escape and tracking them back to inside the target. These results are shown in Figure 6.24.

The cooling of the escaping and refluxing electrons are also calculated and shown in Figures 6.25 and 6.26 respectively. The cooling of the escaping electrons is comparable to that determined by Link *et al* also using PIC simulation. A large cooling is observed in the refluxing electrons, between 60-80% across all focuses. This is likely due to the fact the escaping electrons are made up of the highest energy particles and also because of the energy exchange to the protons that are accelerated on the rear surface. Experimentally, the cooling of the refluxing electrons could be measured by comparing the output of x-ray diagnostics monitoring the forward and backward propagating directions relative to the incident laser. Measuring this whilst monitoring the rear surface and accelerated proton simultaneously would provide insight into the mechanisms that cause the electrons to lose energy when they reflux.

A second experimental campaign was conducted measuring the protons using an RCF stack in conjunction with the wraparound diagnostic as a function of laser pulse durations. The data of the electrons and protons show similar trends. As the pulse duration is increased, the peak electron and integrated proton signal increases. At even longer pulse durations the flux of both electrons and protons decreases. This simultaneous measurement and correlation between the electrons and protons is helpful when diagnosing the processes that occur at the rear surface. As mentioned previously, conducting a similar measurement with additional x-ray diagnostics would allow for more information to be inferred about the internal electron distribution.

Modelling of the proton maximum energy is done using the Mora model [93], which is modified using the parameters suggested by Brenner *et al* [94], and the model examined by Schreiber *et al* [152]. The experimental data best fits the

Mora and Brenner model using the Wilks scaling for the electron temperature.

The escaping electron flux is modelled using a simple capacitor model, as described by Link *et al* [106]. The experimental measurement of the escaping electron flux, which decreases as a function of pulse duration, fits well with the simplistic analytical model. More complexity could be added to the model, such as adding a radial component to take into account the sheath expansion laterally on the rear surface or a time decay of the effective capacitance.

Further investigations into the escaping electrons and the effects they have on many other aspects that are present from laser-solid interactions would be beneficial. One such area would be in the investigation of electro-magnetic pulse (EMP) that is generated during the shot. It is believed that this EMP pulse is partly created due to the electrons as they leave the target; this has been investigated by Poyé and Dubois *et al* [51]. Another area that links with the escaping electrons is terahertz generation on the rear surface [157, 158].

Chapter 7

Summary & Conclusions

The work reported in this thesis demonstrates some of the fundamental electron dynamics from laser-solid interactions and the applicability of exciting novel applications. This final chapter will briefly summarise the results and conclusions and discuss future work that could build upon the findings.

7.1 Diagnosing the Internal Electron Temperature using Bremsstrahlung X-rays

Many measurements of the escaping electron distribution from laser-solid interactions have been conducted before, as shown in Figure 4.13. Most of these measurements have been conducted using electron spectrometers, which can suffer as the electrons measured have been strongly influenced by the fields present on the rear surface. Fewer measurements have been conducted using x-ray spectrometers, which benefit as x-rays do not experience the potential retardation as they leave the target. Also, the majority of these are conducted with passive detectors, such as an image plate. With the technology for higher repetition rate high-power laser systems becoming available, the use of a scintillator based spectrometer is ideal.

The temperature of the spectra was measured between the intensities of 8 and 12×10^{18} W/cm^2 using the scintillator spectrometer. This temperature scales from 400 keV to 750 keV. This matches closely to the Beg and Haines scaling law.

For the application of x-ray radiography, characterisation of the spectra and also the flux of the x-rays is important. The scaling of the x-ray flux as a function of incident laser energy was measured and shown to scale as laser energy to the power of (1.8 ± 0.1) for the first layer of the scintillator diagnostic (50-200 keV).

X-ray radiography was performed on a host of samples/objects, shown in Figures 4.16 4.17 4.15 and reported in Jones *et al* [112] and Brenner *et al* [13]. The results of the radiography show that the x-rays are highly penetrative and bright which are suitable for imaging purposes.

7.2 Penetrative Imaging using Backscattered X-rays Produced by Wakefield Accelerated Electrons

Backscattered x-ray scanning is already used as a security imaging technique which is used on large containers and vehicles [122]. A novel application of using a laser-wakefield interaction to accelerate a bunch of highly energetic electrons to create backscatter x-rays inside a material has been investigated. This technique has the advantage that it is able to penetrate to much greater depths than traditional backscatter methods. The main reason for this is that the x-rays are being created inside the material rather than on the surface. The bunch of electrons is also very short which also enables the temporal evolution of the backscattered x-rays to be measured. This allows for an x-ray ‘radar’ image to be reconstructed, as reported in Deas *et al* [131]. Both techniques were comprehensively modelled using the Monte Carlo code GEANT4 prior to experiment.

Temporal measurements of the penetrative technique were performed at the Astra-Gemini Laser system using an electron beam with energy of highest brightness at (140±10) MeV with a FWHM of 120 MeV. The resulting temporal measurement is shown in Figure 5.15. A collection of temporal measurements taken across a series of objects results in a 2D image as shown in Figure 5.16 which demonstrates the capabilities of the technique.

Further Monte Carlo work was conducted to investigate the future developments of these methods. The emitted K-alpha x-rays from materials can aid in the identification of material buried at shallow depths as shown in 5.17. Detecting the neutrons and 511 keV x-rays also allows for deeper penetrative detection and possible identification of materials as the number of the neutrons and x-rays created scales as a function of density and atomic number.

7.3 Escaping Electron Dynamics as a Function of Laser Pulse Duration and Focal Spot Size

The angular emission, flux and temperature of the escaping electron distribution has been measured using the wraparound diagnostic described in Chapter 3. The focus of the laser was varied such that the intensity ranged from approximately 4×10^{17} W/cm^2 to 4×10^{20} W/cm^2. Experimentally, the flux of the electrons increases when the laser is defocused to 100 μm giving an incident intensity of $\sim 10^{19}$ W/cm^2; as the defocus is increased further the flux decreases considerably.

The temperature of the escaping electrons was extracted by assuming a Boltzmann distribution. The temperature of the escaping electrons remains relatively constant as a function of intensity/focus. The estimated escaping electron energy is 10-20% [91] of the incident laser energy. Improvements to both these measurements can be achieved if the wraparound diagnostic is deployed simultaneously with a magnetic electron spectrometer.

In order to numerically investigate this, PIC simulations were conducted that showed that a flux increase at a particular focus and relatively constant temperature across a range of focuses can occur for particular pre-plasma conditions. The pre-plasma for the PIC simulations were estimated from a number of sources [147, 148, 149] as it was not measured on the experiment. The extent of the effects that the pre-plasma has on the incident laser was shown in these simulations. Previously, experiments have been conducted that have purposely introduced a pre-plasma to investigate the consequences. Gray *et al* [41] observed an optimum pre-plasma for laser coupling into electrons and sequentially the accelerated ions from the rear surface. This is similar to the experimental campaign discussed here.

Additional numerical analysis of the escaping electrons was conducted to determine some of the important aspects of their production. Using particle tracking, the hot electrons that escape were shown to be the electrons that possess the highest energy inside the target. Upon exiting the target, the escaping electrons lose a vast amount of energy due to the electrostatic fields. The external electron temperature has also been shown to be up to 25% cooler than the internal electron temperature. This is comparable to the cooling percentage found by Link *et al* [106] using analytical and numerical modelling. Interestingly, the refluxing electrons have also been shown to cool by up to 80%; this has yet to be measured experimentally.

Measurements of the escaping electrons, and also the accelerated protons, were also conducted on the TAP laser for varying pulse length. The maximum proton energy decreases as a function of pulse duration. Modelling using the Mora model [93] with additional considerations for the size of the expansion on the rear surface developed by Brenner *et al* [94] and the hot electron scaling from Wilks *et al* [24] provides the best fit to the experimental data.

A simple 1D capacitor model was created to analytically model the total number of escaping electrons as simulating long pulse durations (>10 ps) is infeasible It is shown that the total number of escaping electron reduces as a function of pulse duration. This closely matches the integrated electron signal from the wraparound as a function of pulse duration measured experimentally.

7.4 Further Work

The work conducted in Chapters 4 and 6 provide insight into the physics occurring inside the target. Combining the x-ray measurements of the internal electron temperature and the escaping electron angular and temperature distributions would provide many important insights into the physics of the hot electrons. One area of interest would be the prediction that the electrons, as they escape the target, experience a time evolving electric field which reduces the temperature of those that are able to escape. Both of the electron populations could be measured using the diagnostics mentioned above. A method to probe the rear surface fields was demonstrated by Borghesi *et al* [159] and Romagnani *et al* [160], using protons accelerated from a separate laser interaction. This would give insights into the evolution of this field and how it effects escaping electrons.

The two applications of x-rays from laser-plasma interactions shown in this thesis, radiography in Chapter 4 and the temporal penetrative backscattered technique in Chapter 5, have lots of potential. The limitations of the x-ray radar in terms of depth and material identification, as discussed in Chapter 5 section 5.3, has yet to be investigated. Regarding radiography, the spectrum and flux has been measured as a function of incident laser energy, but as is clear from Chapter 6, the pulse duration and focal spot size can enhance the electron flux. Also, investigating the function as well as optimising the pre-plasma, as conducted by [101], and also defocusing may further enhance hot electron flux. Further investigation into the x-ray characteristics with these laser and target parameters could yield brighter and more energetic x-rays that would be ideal for probing even denser materials.

The ability to measure the full angular escaping electron distribution could also provide useful insight to the transport of the electrons through the target. An electron beam with high current passing through a material can cause a ‘pinching’ effect due to its own magnetic field and the resistivity of the material, as shown by equation **??**. Studies of the effect of the change of resistivity due to heating of the target on the electron transport and the resulting ion beams has been investigated in the past [118, 119, 161]; more recently, the effect of a forced resistivity change has been investigated. This works by introducing a material of much higher conductivity into a material with high resistivity, such as a copper wire through plastic [162, 163]. The electrons injected into the copper will be guided through the wire if the radius of the wire, divergence and temperature of the the electron are properly matched. The measurement of the escaping electrons using the wraparound diagnostic on an experiment to investigate these effects would provide evidence of guiding. Secondly, as the electrons are guided through the higher density material, they will produce x-rays. These x-rays have the potential to have a much smaller source size than those produced from simple planar targets as used in Chapter 4. The proposed size of these wires is approximately 5 μm. Current measurements of the resolution from simple solid targets [10, 11] indicate a source size of ≈ 100 μm. Therefore, the wires have the potential of improving the resolution of the x-rays considerably.

Appendix A

Appendix

A.1 Gaussian Filter

A Gaussian filter is used to remove any blemishes or scratches that are present that can occur during the scanning process or handling the image plate. This is an important step that ensures that when making comparisons between the layers that the blemishes do not significantly change the desired result. The removal of these blemishes is achieved by taking a fast Fourier transform of the image then multiplying it by a 2D Gaussian profile, removing any of the higher frequency features on the image. A ratio of the image before and after the filter to ensure that no significant alternations to the original underlying signal were made. An example of this filter is shown in Figure A.1.

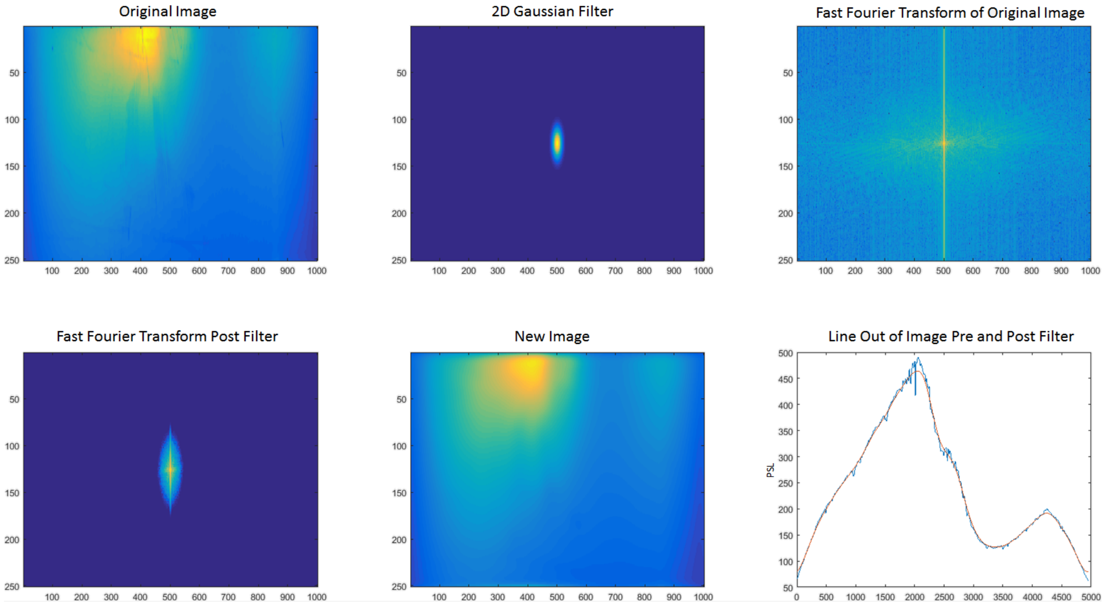

Figure A.1: Example of the Gaussian filter applied to each layer of IP to removed blemishes and scratches. A fast Fourier transform of the original image has been taken and been multiplied by a 2D Gaussian profile. As the low and high frequency components of the images are in the centre and edge of the image respectively, multiplying by the Gaussian filter will remove the high frequency. The new image shows the effectiveness of this method, with the line out ensuring that no major alterations to the image have occurred.

References

[1] TH Maiman. Stimulated optical radiation in ruby. *Nature*, 187(4736), 1960.

[2] John Nuckolls, Lowell Wood, Albert Thiessen, and George Zimmerman. Laser Compression of Matter to Super-High Densities: Thermonuclear (CTR) Applications. *Nature*, 239(5368):139–142, 1972.

[3] George H Miller and Craig R Wuest. The National Ignition Facility. *Instrumentation*, 43:2841–2853, 2004.

[4] A. Pukhov and J. Meyer-ter Vehn. Laser Hole Boring into Overdense Plasma and Relativistic Electron Currents for Fast Ignition of ICF Targets. *Physical Review Letters*, 79(14):2686–2689, 1997.

[5] M.H. Key, M.D. Cable, T.E. Cowan, K.G. Estabrook, B.a. Hammel, S.P. Hatchett, E.a. Henry, D.E. Hinkel, J.D. Kilkenny, J.a. Koch, W.L. Kruer, a.B. Langdon, B.F. Lasinski, R.W. Lee, B.J. Macgowan, a.J. MacKinnon, J.D. Moody, M.J. Moran, a.a. Offenberger, D.M. Pennington, M.D. Perry, T.J. Phillips, T.C. Sangster, M.S. Singh, M.a. Stoyer, M. Tabak, G.L. Tietbohl, M. Tsukamoto, K.B. Wharton, and S.C. Wilks. Hot electron production and heating by hot electrons in fast ignitor research. *Physics of Plasmas*, 5(5):1966–1972, 1998.

[6] M. Roth, T. E. Cowan, M. H. Key, S. P. Hatchett, C. Brown, W. Fountain, J. Johnson, D. M. Pennington, R. A. Snavely, S. C. Wilks, K. Yasuike, H. Ruhl, F. Pegoraro, S. V. Bulanov, E. M. Campbell, M. D. Perry, and

H. Powell. Fast ignition by intense laser-accelerated proton beams. *Physical Review Letters*, 86(3):436–439, 2001.

[7] Félicie Albert and Alec G R Thomas. Applications of laser wakefield accelerator-based light sources. *Plasma Physics and Controlled Fusion*, 58(10):103001, 2016.

[8] J M Cole, J Wood, N Lopes, K Poder, J Bryant, S Alatabi, D R Symes, R Abel, S Kneip, S P D Mangles, and Z Najmudin. Microtomography of human trabecular bone with a laser-wakefield driven x-ray source. *Plasma Physics and Controlled Fusion*, 014008:1–6, 2014.

[9] S. Kneip, C. McGuffey, F. Dollar, M. S. Bloom, V. Chvykov, G. Kalintchenko, K. Krushelnick, A. Maksimchuk, S. P D Mangles, T. Matsuoka, Z. Najmudin, C. A J Palmer, J. Schreiber, W. Schumaker, A. G R Thomas, and V. Yanovsky. X-ray phase contrast imaging of biological specimens with femtosecond pulses of betatron radiation from a compact laser plasma wakefield accelerator. *Applied Physics Letters*, 99(9):1–4, 2011.

[10] C. Courtois, R. Edwards, A. Compant La Fontaine, C. Aedy, S. Bazzoli, J. L. Bourgade, J. Gazave, J. M. Lagrange, O. Landoas, L. Le Dain, D. Mastrosimone, N. Pichoff, G. Pien, and C. Stoeckl. Characterisation of a MeV Bremsstrahlung x-ray source produced from a high intensity laser for high areal density object radiography. *Physics of Plasmas*, 20(2013):083114, 2013.

[11] D. R. Rusby, C. M. Brenner, C. Armstrong, L. A. Wilson, R. Clarke, A. Alejo, H. Ahmed, N. M. H. Butler, D. Haddock, A. Higginson, A. McClymont, S. R. Mirfayzi, C. Murphy, M. Notley, P. Oliver, R. Allott, C. Hernandez-Gomez, S. Kar, P. McKenna, and D. Neely. Pulsed x-ray imaging of high-density objects using a ten picosecond high-intensity laser driver. In *SPIE Security+ Defence*, pages 99920E–99920E. International Society for Optics and Photonics, 2016.

[12] M. D. Perry, J. A. Sefcik, T. Cowan, S. Hatchett, A. Hunt, M. Moran, D. Pennington, R. Snavely, and S. C. Wilks. Hard x-ray production from high intensity laser solid interactions (invited). *Review of Scientific Instruments*, 70(1):265, 1999.

[13] C M Brenner, S R Mirfayzi, D R Rusby, C Armstrong, A Alejo, L A Wilson, R Clarke, H Ahmed, N M H Butler, D Haddock, A Higginson, A McClymont, C Murphy, M Notley, P Oliver, R Allott, C Hernandez-Gomez, S Kar, P McKenna, and D Neely. Laser-driven x-ray and neutron source development for industrial applications of plasma accelerators. *Plasma Physics and Controlled Fusion*, 58(1):014039, 2016.

[14] Saumyabrata Banerjee, Paul D. Mason, Klaus Ertel, P. Jonathan Phillips, Mariastefania de Vido, Oleg Chekhlov, Martin Divoky, Jan Pilar, Jodie Smith, Thomas Butcher, Andrew Lintern, Steph Tomlinson, Waseem Shaikh, Chris Hooker, Antonio Lucianetti, Cristina Hernandez-Gomez, Tomas Mocek, Chris Edwards, and John L. Collier. 100 J-level nanosecond pulsed diode pumped solid state laser. *Optics Letters*, 41(9):2089–2092, 2016.

[15] Georg Korn, John L Collier, and Patrizio Antici. Science and Technology with Ultra-Intense Lasers. Technical report, 2011.

[16] Paul D. Mason, Saumyabrata Banerjee, Klaus Ertel, P. Jonathan Phillips, Thomas Butcher, Jodie Smith, Mariastefania De Vido, Oleg Chekhlov, Cristina Hernandez-Gomez, Chris Edwards, and John Collier. High energy diode-pumped solid-state laser development at the central laser facility. In *SPIE Photonics Europe*, pages 989309–989309. International Society for Optics and Photonics, 2016.

[17] Albert Gold and H. Barry Bebb. Theory of multiphoton ionization. *Physical Review Letters*, 14(3):60–63, 1965.

[18] P. Agostini, F. Fabre, G. Mainfray, G. Petite, and N. K. Rahman. Free-free

transitions following six-photon ionization of xenon atoms. *Physical Review Letters*, 42(17):1127–1130, 1979.

[19] Y Gontier and M Trahin. Energetic electron generation by multiphoton absorption. *Journal of Physics B: Atomic and Molecular Physics*, 13(22):4383–4390, 1980.

[20] LV Keldysh. Ionization in the field of a strong electromagnetic wave. *Zh. Eksperim. i Teor. Fiz.*, 47, 1964.

[21] H. W. Powell, M. King, R. J. Gray, D. A. MacLellan, B. Gonzalez-Izquierdo, L. C. Stockhausen, G. Hicks, N. P. Dover, D. R. Rusby, D. C. Carroll, H. Padda, R. Torres, S. Kar, R. J. Clarke, I. O. Musgrave, Z. Najmudin, M. Borghesi, D. Neely, and P. McKenna. Proton acceleration enhanced by a plasma jet in expanding foils undergoing relativistic transparency. *New Journal of Physics*, 17(10):103033, 2015.

[22] DC Barnes, T Kurki-Suonio, and T Tajima. Laser self-trapping for the plasma fiber accelerator. *IEEE transactions on plasma science*, 15:154–160, 1987.

[23] Paul Gibbon. *Short pulse laser interactions with matter.* World Scientific Publishing Company, 2004.

[24] Scott C Wilks and William L Kruer. Absorption of ultrashort, ultra-intense laser light by solids and overdense plasmas. *IEEE Journal of Quantum Electronics*, 33(11):1954–1968, 1997.

[25] N. G. Denisov. On a Singularity of the Field of an Electromagnetic Wove. *Jetp*, 4(4):544–553, 1957.

[26] F. Brunel. Not-So-Resonant, Resonant Absorption. *Physical Review Letters*, 59, 1987.

[27] Paul Gibbon and A. R. Bell. Collisionless absorption in sharp-edged plasmas. *Physical Review Letters*, 68(10):1535–1538, 1992.

[28] WLl Kruer and Kent Estabrook. J× b heating by very intense laser light. *Physics of Fluids (1958-1988)*, 28(1):430–432, 1985.

[29] J.R. Davies. The Alfvén limit revisited and its relevance to laser-plasma interactions. *Laser and Particle Beams*, 24(02):299–310, 2006.

[30] Hannes Alfvén. On the motion of cosmic rays in interstellar space. *Physical Review*, 55(5):425, 1939.

[31] B Bezzerides, S J Gitomer, and D W Forslund. Randomness, Maxwellian Distributions, and Resonance Absorption. *Physical Review Letters*, 44(10):651–654, 1980.

[32] J R Davies. Laser absorption by overdense plasmas in the relativistic regime. *Plasma Physics and Controlled Fusion*, 51(1):014006, 2009.

[33] F. N. Beg, A. R. Bell, A. E. Dangor, C. N. Danson, A. P. Fews, M. E. Glinsky, B. A. Hammel, P. Lee, P. A. Norreys, and M. Tatarakis. A study of picosecond lasersolid interactions up to 10^{19} W cm^2. *Physics of Plasmas*, 4(2):447–457, 1997.

[34] M. G. Haines, M. S. Wei, F. N. Beg, and R. B. Stephens. Hot-electron temperature and laser-light absorption in fast ignition. *Physical Review Letters*, 102(4):1–4, 2009.

[35] Danilo Giulietti, Leonida A Gizzi, Dipartimento Fisica, and Università Pisa. X-Ray Emission from Laser Produced Plasmas. 1, 1998.

[36] G. Nelson and D. Reilly. Gamma-ray interactions with matter. *Passive Nondestructive Analysis of Nuclear Materials*, (I):27–42, 1991.

[37] Donna Strickland and Gerard Mourou. Compression of Amplified Chirped Optical Pulses *. *Optics Communications*, 56(3):219–221, 1985.

[38] Ross J Gray. *On Mechanisms of Laser-Coupling to Fast Electrons in Ultraintense Laser-Solid Interactions by.* PhD thesis, 2013.

[39] Chris Hooker, Yunxin Tang, Oleg Chekhlov, John Collier, Edwin Divall, Klaus Ertel, Steve Hawkes, Bryn Parry, and P P Rajeev. Improving coherent contrast of petawatt laser pulses. *Optics express*, 19(3):2193–2203, 2011.

[40] F. Wagner, C. P. João, J. Fils, T. Gottschall, J. Hein, J. Körner, J. Limpert, M. Roth, T. Stöhlker, and V. Bagnoud. Temporal contrast control at the PHELIX petawatt laser facility by means of tunable sub-picosecond optical parametric amplification. *Applied Physics B: Lasers and Optics*, 116(2):429–435, 2014.

[41] R. J. Gray, D. C. Carroll, X. H. Yuan, C. M. Brenner, M. Burza, M. Coury, K. L. Lancaster, X. X. Lin, Y. T. Li, D. Neely, M. N. Quinn, O. Tresca, C. G. Wahlström, and P. McKenna. Laser pulse propagation and enhanced energy coupling to fast electrons in dense plasma gradients. *New Journal of Physics*, 16, 2014.

[42] F. Pérez, A. Kemp, L. Divol, C. Chen, and P. Patel. Deflection of MeV Electrons by Self-Generated Magnetic Fields in Intense Laser-Solid Interactions. *Physical Review Letters*, 111(24):245001, 2013.

[43] J Ebrardt and J M Chaput. LMJ project status. *Journal of Physics: Conference Series*, 112(3):032005, 2008.

[44] N. Miyanaga, H. Azechi, K. A. Tanaka, T. Kanabe, T. Jitsuno, J. Kawanaka, Y. Fujimoto, R. Kodama, H. Shiraga, K. Knodo, K. Tsubakimoto, H. Habara, J. Lu, G. Xu, N. Morio, S. Matsuo, E. Miyaji, Y. Kawakami, Y. Izawa, and K. Mima. 10-kJ PW laser for the FIREX-I program. *Journal de Physique IV (Proceedings)*, 133:81–87, 2006.

[45] T.R Boehly, D.L Brown, R.S Craxton, R.L Keck, J.P Knauer, J.H Kelly, T.J Kessler, S.A Kumpan, S.J Loucks, S.A Letzring, F.J Marshall, R.L McCrory, S.F.B Morse, W Seka, J.M Soures, and C.P Verdon. Initial per-

formance results of the OMEGA laser system. *Optics Communications*, 133(1-6):495–506, 1997.

[46] C L S Lewis, G Nersisyan, M Borghesi, D Doria, B Dromey, T Dzelzainis, M Makita, K McKeever, D Riley, S White, D Marlow, G Williams, and M Zepf. The TARANIS laser : A multi-terawatt system for laser plasma physics. *Journal of Physics: Conference Series*, 388(15):152036, 2012.

[47] S. M. Wiggins, M. P. Anania, G. H. Welsh, E. Brunetti, S. Cipiccia, P. A. Grant, D. Reboredo, G. Manahan, D. W. Grant, and D. A. Jaroszynski. Undulator radiation driven by laser-wakefield accelerator electron beams. In *SPIE Optics+ Optoelectronics*, pages 95090K–95090K. International Society for Optics and Photonics, 2015.

[48] Siddharth Patankar. *High-power laser systems for driving and probing high energy density physics experiments.* PhD thesis, Imperial College London, 2013.

[49] Paul McKenna, David Neely, Robert Bingham, and Dino Jaroszynski. *Laser-plasma interactions and applications.* Springer, 2013.

[50] R J Clarke, D Neely, R D Edwards, P N M Wright, K W D Ledingham, R Heathcote, P McKenna, C N Danson, P A Brummitt, J L Collier, P E Hatton, S J Hawkes, C Hernandez-Gomez, P Holligan, M H R Hutchinson, a K Kidd, W J Lester, D R Neville, P A Norreys, D A Pepler, T B Winstone, R W W Wyatt, and B E Wyborn. Radiological characterisation of photon radiation from ultra-high-intensity laser-plasma and nuclear interactions. *Journal of radiological protection*, 26(3):277–286, 2006.

[51] J. L. Dubois, F. Lubrano-Lavaderci, D. Raffestin, J. Ribolzi, J. Gazave, A. Compant La Fontaine, E. D'Humières, S. Hulin, Ph Nicolaï, A. Poyé, and V. T. Tikhonchuk. Target charging in short-pulse-laser-plasma experiments. *Physical Review E - Statistical, Nonlinear, and Soft Matter Physics*, 89(1), 2014.

[52] M. J. Mead, D. Neely, J. Gauoin, R. Heathcote, and P. Patel. Electromagnetic pulse generation within a petawatt laser target chamber. *Review of Scientific Instruments*, 75(10 II):4225–4227, 2004.

[53] C N Danson, P A Brummitt, R J Clarke, J L Collier, B Fell, a J Frackiewicz, S Hawkes, C Hernandez-Gomez, P Holligan, M H R Hutchinson, A Kidd, W J Lester, I O Musgrave, D Neely, D R Neville, P A Norreys, D A Pepler, C J Reason, W Shaikh, T B Winstone, R W W Wyatt, and B E Wyborn. Vulcan petawatt: Design, operation and interactions at 5×10^{20} W cm^{-2}. *Laser and Particle Beams*, 23(May 2016):87–93, 2005.

[54] C Hernandez-Gomez, S P Blake, C Burton, R J Clarke, J L Collier, B Costello, V Dubrosky, A J Frackiewicz, M Galimberti, S Hancock, S J Hawkes, R Heathcote, A K Kidd, I O Musgrave, D Neely, M M Notley, B T Parry, D A Pepler, W Shaikh, T B Winstone, and B E Wyborn. An overview of the Target Area West short pulse upgrade. *CLF Annual Report (2007)*, pages 260–261, 2007.

[55] V. Bagnoud, B. Aurand, A. Blazevic, S. Borneis, C. Bruske, B. Ecker, U. Eisenbarth, J. Fils, A. Frank, E. Gaul, S. Goette, C. Haefner, T. Hahn, K. Harres, H. M. Heuck, D. Hochhaus, D. H H Hoffmann, D. Javorková, H. J. Kluge, T. Kuehl, S. Kunzer, M. Kreutz, T. Merz-Mantwill, P. Neumayer, E. Onkels, D. Reemts, O. Rosmej, M. Roth, T. Stoehlker, A. Tauschwitz, B. Zielbauer, D. Zimmer, and K. Witte. Commissioning and early experiments of the PHELIX facility. *Applied Physics B: Lasers and Optics*, 100(1):137–150, 2010.

[56] C. J. Hooker, S. Blake, O. Chekhlov, R. J. Clarke, J. L. Collier, E. J. Divall, K. Ertel, P. S. Foster, S. J. Hawkes, P. Holligan, B. Landowski, W. J. Lester, D. Neely, B. Parry, R. Pattathil, M. Streeter, and B. E. Wyborn. Commissioning the Astra Gemini petawatt Ti:sapphire laser system. In *2008 Conference on Quantum Electronics and Laser Science Conference on Lasers and Electro-Optics, CLEO/QELS*, pages 2–3, 2008.

[57] D. Gwynne, S. Kar, D. Doria, H. Ahmed, M. Cerchez, J. Fernandez, R. J. Gray, J. S. Green, F. Hanton, D. A. Maclellan, P. McKenna, Z. Najmudin, D. Neely, J. A. Ruiz, A. Schiavi, M. Streeter, M. Swantusch, O. Willi, M. Zepf, and M. Borghesi. Modified Thomson spectrometer design for high energy, multi-species ion sources. *Review of Scientific Instruments*, 85(3), 2014.

[58] EL Clark. *Measurements of Energetic Particles from Ultraintense Laser Plasma Interactions*. PhD thesis, 2002.

[59] D C Carroll, K Jones, L Robson, P Mckenna, S Bandyopadhyay, P Brummitt, D Neely, Central Laser Facility, F Lindau, and O Lundh. The design, development and use of a novel Thomson spectrometer for high resolution ion detection. *Central Laser Facility Annual Report*, pages 16–20, 2006.

[60] F Nürnberg, M Schollmeier, E Brambrink, A Blazević, D C Carroll, K Flippo, D C Gautier, M Geissel, K Harres, B M Hegelich, O Lundh, K Markey, P McKenna, D Neely, J Schreiber, and M Roth. Radiochromic film imaging spectroscopy of laser-accelerated proton beams. *The Review of scientific instruments*, 80(3):033301, 2009.

[61] James F. Ziegler, M.D. Ziegler, and J.P. Biersack. SRIM The stopping and range of ions in matter (2010). *Nuclear Instruments and Methods in Physics Research Section B: Beam Interactions with Materials and Atoms*, 268(11-12):1818–1823, 2010.

[62] S. Agostinelli, J. Allison, and K. Amako. GEANT4 - a simulation toolkit. *Nuclear Instruments and Methods in Physics Research A*, 506(506):250–303, 2003.

[63] Katsuya Amako, Susanna Guatelli, Vladimir N Ivanchenko, Michel Maire, Barbara Mascialino, Koichi Murakami, Petteri Nieminen, Luciano Pandola, Sandra Parlati, Maria Grazia Pia, Michela Piergentili, Takashi Sasaki, and Laszlo Urban. Comparison of Geant4 electromagnetic physics models

against the NIST reference data. *IEEE Transactions on Nuclear Science*, 52(4):910–918, 2005.

[64] S Chauvie, S Guatelli, V Ivanchenko, F Longo, A Mantero, B Mascialino, P Nieminen, L Pandola, S Parlati, L Peralta, M.G. Pia, M Piergentili, P Rodrigues, S Saliceti, and A Trindade. Geant4 low energy electromagnetic physics. In *IEEE Symposium Conference Record Nuclear Science 2004.*, volume 3, pages 1881–1885, 2004.

[65] G.A.P. Cirrone, G. Cuttone, F. Di Rosa, L. Pandola, F. Romano, and Q. Zhang. Validation of the Geant4 electromagnetic photon cross-sections for elements and compounds. *Nuclear Instruments and Methods in Physics Research Section A: Accelerators, Spectrometers, Detectors and Associated Equipment*, 618(1-3):315–322, 2010.

[66] T. D. Arber, K. Bennett, C. S. Brady, A Lawrence-Douglas, M. G. Ramsay, N. J. Sircombe, P. Gillies, R. G. Evans, H. Schmitz, A. R. Bell, and C. P. Ridgers. Contemporary particle-in-cell approach to laser-plasma modelling. *Plasma Physics and Controlled Fusion*, 57(11):113001, 2015.

[67] R H H Scott, F Pérez, M J V Streeter, E L Clark, J R Davies, H-P Schlenvoigt, J J Santos, S Hulin, K L Lancaster, F Dorchies, C Fourment, B Vauzour, A A Soloviev, S D Baton, S J Rose, and P A Norreys. Fast electron beam measurements from relativistically intense, frequency-doubled laser-solid interactions. *New Journal of Physics*, 15(9):093021, 2013.

[68] C D Chen, J A King, M H Key, K U Akli, F N Beg, H Chen, R R Freeman, A Link, A J Mackinnon, A G MacPhee, P K Patel, M Porkolab, R B Stephens, and L D Van Woerkom. A Bremsstrahlung spectrometer using k-edge and differential filters with image plate dosimeters. *The Review of scientific instruments*, 79(10):10E305, 2008.

[69] M N Quinn, X H Yuan, X X Lin, D C Carroll, O Tresca, R J Gray, M Coury, C Li, Y T Li, C M Brenner, a P L Robinson, D Neely, B Zielbauer, B Au-

rand, J Fils, T Kuehl, and P McKenna. Refluxing of fast electrons in solid targets irradiated by intense, picosecond laser pulses. *Plasma Physics and Controlled Fusion*, 53(2):025007, 2011.

[70] Martin J Berger, JH Hubbell, SM Seltzer, J Chang, JS Coursey, Ry Sukumar, DS Zucker, and K Olsen. Xcom: photon cross sections database. *NIST Standard reference database*, 8(1):3587–3597, 1998.

[71] S. Kneip, C. McGuffey, J. L. Martins, S. F. Martins, C. Bellei, V. Chvykov, F. Dollar, R. Fonseca, C. Huntington, G. Kalintchenko, A. Maksimchuk, S. P. D. Mangles, T. Matsuoka, S. R. Nagel, C. A. J. Palmer, J. Schreiber, K. Ta Phuoc, A. G. R. Thomas, V. Yanovsky, L. O. Silva, K. Krushelnick, and Z. Najmudin. Bright spatially coherent synchrotron X-rays from a table-top source. *Nature Physics*, 6(12):980–983, 2010.

[72] F. Albert, B. B. Pollock, J. L. Shaw, K. A. Marsh, J. E. Ralph, Y. H. Chen, D. Alessi, A. Pak, C. E. Clayton, S. H. Glenzer, and C. Joshi. Angular dependence of betatron X-ray spectra from a laser-wakefield accelerator. *Physical Review Letters*, 111(23), 2013.

[73] E. Esarey, B. A. Shadwick, P. Catravas, and W. P. Leemans. Synchrotron radiation from electron beams in plasma-focusing channels. *Physical Review E - Statistical, Nonlinear, and Soft Matter Physics*, 65(5):1–15, 2002.

[74] Hui Chen, Anthony J Link, Roger van Maren, Pravesh K Patel, Ronnie Shepherd, Scott C Wilks, and Peter Beiersdorfer. High performance compact magnetic spectrometers for energetic ion and electron measurement in ultraintense short pulse laser solid interactions. *The Review of scientific instruments*, 79(10):10E533, 2008.

[75] Kazuo A. Tanaka, Toshinori Yabuuchi, Takashi Sato, Ryosuke Kodama, Yoneyoshi Kitagawa, Teruyoshi Takahashi, Toshiji Ikeda, Yoshihide Honda, and Shuuichi Okuda. Calibration of imaging plate for high energy electron spectrometer. *Review of Scientific Instruments*, 76(1):013507, 2005.

[76] Sadaoki Kojima, Takahito Ikenouchi, Yasunobu Arikawa, Shohei Sakata, Zhe Zhang, Yuki Abe, Mitsuo Nakai, Hiroaki Nishimura, Hiroyuki Shiraga, Tetsuo Ozaki, Shuji Miyamoto, Masashi Yamaguchi, Akinori Takemoto, Shinsuke Fujioka, and Hiroshi Azechi. Development of Compton X-ray spectrometer for high energy resolution single-shot high-flux hard X-ray spectroscopy. *Review of Scientific Instruments*, 87(4):0–10, 2016.

[77] T. Bonnet, M. Comet, D. Denis-Petit, F. Gobet, F. Hannachi, M. Tarisien, M. Versteegen, and M. M. Aleonard. Response functions of imaging plates to photons, electrons and 4He particles. *Review of Scientific Instruments*, 84(10):103510, 2013.

[78] G. Jackson Williams, Brian R. Maddox, Hui Chen, Sadaoki Kojima, and Matthew Millecchia. Calibration and equivalency analysis of image plate scanners. *Review of Scientific Instruments*, 85(11):130–133, 2014.

[79] S. G. Gales and C. D. Bentley. Image plates as x-ray detectors in plasma physics experiments. *Review of Scientific Instruments*, 75(10):4001–4003, 2004.

[80] B. R. Maddox, H. S. Park, B. A. Remington, N. Izumi, S. Chen, C. Chen, G. Kimminau, Z. Ali, M. J. Haugh, and Q. Ma. High-energy x-ray backlighter spectrum measurements using calibrated image plates. *Review of Scientific Instruments*, 82(2), 2011.

[81] A. L. Meadowcroft, C. D. Bentley, and E. N. Stott. Evaluation of the sensitivity and fading characteristics of an image plate system for x-ray diagnostics. *Review of Scientific Instruments*, 79(11):4–8, 2008.

[82] N. Izumi, J. Lee, E. Romano, G. Stone, B. Maddox, T. Ma, V. Rekow, D. K. Bradley, and P. Bell. X-ray and neutron sensitivity of imaging plates. *SPIE Proceedings*, 8850(August):885006, 2013.

[83] B. Hidding, G. Pretzler, M. Clever, F. Brandl, F. Zamponi, A. Lübcke, T. Kämpfer, I. Uschmann, E. Förster, U. Schramm, R. Sauerbrey,

E. Kroupp, L. Veisz, K. Schmid, S. Benavides, and S. Karsch. Novel method for characterizing relativistic electron beams in a harsh laser-plasma environment. *Review of Scientific Instruments*, 78(8), 2007.

[84] I J Paterson, R J Clarke, N C Woolsey, and G Gregori. Image plate response for conditions relevant to laserplasma interaction experiments. *Measurement Science and Technology*, 19(9):095301, 2008.

[85] K Zeil, S D Kraft, A Jochmann, F Kroll, W Jahr, U Schramm, L Karsch, J Pawelke, B Hidding, and G Pretzler. Absolute response of Fuji imaging plate detectors to picosecond-electron bunches. *Review of Scientific Instruments*, 81(1):1–6, 2010.

[86] P. A. Norreys, M. Santala, E. Clark, M. Zepf, I. Watts, F. N. Beg, K. Krushelnick, M. Tatarakis, A. E. Dangor, X. Fang, P. Graham, T. McCanny, R. P. Singhal, K. W. D. Ledingham, A. Creswell, D. C. W. Sanderson, J. Magill, A. Machacek, J. S. Wark, R. Allott, B. Kennedy, and D. Neely. Observation of a highly directional γ-ray beam from ultrashort, ultraintense laser pulse interactions with solids. *Physics of Plasmas*, 6(5):2150, 1999.

[87] M. I. K. Santala, M. Zepf, I. Watts, F. N. Beg, E. Clark, M. Tatarakis, K. Krushelnick, A. E. Dangor, S. C. Wilks, A. C. Machacek, J. S. Wark, R. Allott, R. J. Clarke, and P. A. Norreys. Effect of the Plasma Density Scale Length on the Direction of Fast Electrons in Relativistic Laser-Solid Interactions. *Physical Review Letters*, 84(7):1459–1462, 2000.

[88] F. Pérez, G. E. Kemp, S. P. Regan, M. A. Barrios, J. Pino, H. Scott, S. Ayers, H. Chen, J. Emig, J. D. Colvin, M. Bedzyk, M. J. Shoup, A. Agliata, B. Yaakobi, F. J. Marshall, R. A. Hamilton, J. Jaquez, M. Farrell, A. Nikroo, and K. B. Fournier. The NIF x-ray spectrometer calibration campaign at Omega. *Review of Scientific Instruments*, 85(11):11D613, 2014.

[89] C. D. Chen, A. J. Kemp, F. Perez, A. Link, F. N. Beg, S. Chawla, M. H.

Key, H. McLean, A. Morace, Y. Ping, A. Sorokovikova, R. B. Stephens, M. Streeter, B. Westover, and P. K. Patel. Comparisons of angularly and spectrally resolved Bremsstrahlung measurements to two-dimensional multi-stage simulations of short-pulse laser-plasma interactions. *Physics of Plasmas*, 20(5):052703, 2013.

[90] R. J. Gray, X. H. Yuan, D. C. Carroll, C. M. Brenner, M. Coury, M. N. Quinn, O. Tresca, B. Zielbauer, B. Aurand, V. Bagnoud, J. Fils, T. Kühl, X. X. Lin, C. Li, Y. T. Li, M. Roth, D. Neely, and P. McKenna. Surface transport of energetic electrons in intense picosecond laser-foil interactions. *Applied Physics Letters*, 99(17):171502, 2011.

[91] D. R. Rusby, L. A. Wilson, R. J. Gray, R. J. Dance, N. M. H. Butler, D. A. MacLellan, G. G. Scott, V. Bagnoud, B. Zielbauer, P. McKenna, and D. Neely. Measurement of the angle, temperature and flux of fast electrons emitted from intense lasersolid interactions. *Journal of Plasma Physics*, 81(05):475810505, 2015.

[92] D. Neely, P. Foster, A. Robinson, F. Lindau, O. Lundh, A. Persson, C.-G. Wahlstrom, and P. McKenna. Enhanced proton beams from ultra-thin targets driven by high contrast laser pulses. *Applied Physics Letters*, 89(2):021502, 2006.

[93] Patrick Mora. Plasma expansion into a vacuum. *Physical Review Letters*, 90(18):185002, 2003.

[94] C M Brenner, P McKenna, and D Neely. Modelling the effect of laser focal spot size on sheath- accelerated protons in intense laserfoil interactions. *Plasma Physics and Controlled Fusion*, 56(8):084003, 2014.

[95] C. D. Chen, J. A. King, M. H. Key, K. U. Akli, F. N. Beg, H. Chen, R. R. Freeman, A. Link, A. J. MacKinnon, A. G. MacPhee, P. K. Patel, M. Porkolab, R. B. Stephens, and L. D. Van Woerkom. A Bremsstrahlung

spectrometer using k-edge and differential filters with image plate dosimeters. *Review of Scientific Instruments*, 79(10):2006–2009, 2008.

[96] C Zulick, B Hou, F Dollar, A Maksimchuk, J Nees, A G R Thomas, Z Zhao, and K Krushelnick. High resolution bremsstrahlung and fast electron characterization in ultrafast intense lasersolid interactions. *New Journal of Physics*, 15(12):123038, 2013.

[97] G. Malka and J. Miquel. Experimental Confirmation of Ponderomotive-Force Electrons Produced by an Ultrarelativistic Laser Pulse on a Solid Target. *Physical Review Letters*, 77(1):75–78, 1996.

[98] Tsuyoshi Tanimoto, H. Habara, R. Kodama, M. Nakatsutsumi, Kazuo A. Tanaka, K. L. Lancaster, J. S. Green, R. H H Scott, M. Sherlock, Peter A. Norreys, R. G. Evans, M. G. Haines, S. Kar, M. Zepf, J. King, T. Ma, M. S. Wei, T. Yabuuchi, F. N. Beg, M. H. Key, P. Nilson, R. B. Stephens, H. Azechi, K. Nagai, T. Norimatsu, K. Takeda, J. Valente, and J. R. Davies. Measurements of fast electron scaling generated by petawatt laser systems. *Physics of Plasmas*, 16(6), 2009.

[99] Hui Chen, S. C. Wilks, W. L. Kruer, P. K. Patel, and R. Shepherd. Hot electron energy distributions from ultraintense laser solid interactions. *Physics of Plasmas*, 16(2):8–12, 2009.

[100] A. G. MacPhee, K. U. Akli, F. N. Beg, C. D. Chen, H. Chen, R. Clarke, D. S. Hey, R. R. Freeman, A. J. Kemp, M. H. Key, J. A. King, S. Le Pape, A. Link, T. Y. Ma, H. Nakamura, D. T. Offermann, V. M. Ovchinnikov, P. K. Patel, T. W. Phillips, R. B. Stephens, R. Town, Y. Y. Tsui, M. S. Wei, L. D. Van Woerkom, and A. J. MacKinnon. Diagnostics for fast ignition science. *Review of Scientific Instruments*, 79(10), 2008.

[101] C. Courtois, A. Compant La Fontaine, O. Landoas, G. Lidove, V. Meot, P. Morel, R. Nuter, E. Lefebvre, A. Boscheron, J. Grenier, M. M. Aleonard, M. Gerbaux, F. Gobet, F. Hannachi, G. Malka, J. N. Scheurer, and

M. Tarisien. Effect of plasma density scale length on the properties of bremsstrahlung x-ray sources created by picosecond laser pulses. *Physics of Plasmas*, 16(1):013105, 2009.

[102] C. Courtois, R. Edwards, A. Compant La Fontaine, C. Aedy, M. Barbotin, S. Bazzoli, L. Biddle, D. Brebion, J. L. Bourgade, D. Drew, M. Fox, M. Gardner, J. Gazave, J. M. Lagrange, O. Landoas, L. Le Dain, E. Lefebvre, D. Mastrosimone, N. Pichoff, G. Pien, M. Ramsay, A. Simons, N. Sircombe, C. Stoeckl, and K. Thorp. High-resolution multi-MeV x-ray radiography using relativistic laser-solid interaction. *Physics of Plasmas*, 18(2):023101, 2011.

[103] R. D. Edwards, M. A. Sinclair, T. J. Goldsack, K. Krushelnick, F. N. Beg, E. L. Clark, A. E. Dangor, Z. Najmudin, M. Tatarakis, B. Walton, M. Zepf, K. W. D. Ledingham, I. Spencer, P. A. Norreys, R. J. Clarke, R. Kodama, Y. Toyama, and M. Tampo. Characterization of a gamma-ray source based on a laser-plasma accelerator with applications to radiography. *Applied Physics Letters*, 80(12):2129, 2002.

[104] Stephen P. Hatchett, Curtis G. Brown, Thomas E. Cowan, Eugene A. Henry, Joy S. Johnson, Michael H. Key, Jeffrey A. Koch, A. Bruce Langdon, Barbara F. Lasinski, Richard W. Lee, Andrew J. Mackinnon, Deanna M. Pennington, Michael D. Perry, Thomas W. Phillips, Markus Roth, T. Craig Sangster, Mike S. Singh, Richard A. Snavely, Mark A. Stoyer, Scott C. Wilks, and Kazuhito Yasuike. Electron, photon, and ion beams from the relativistic interaction of Petawatt laser pulses with solid targets. *Physics of Plasmas*, 7(5):2076, 2000.

[105] Cliff D Chen. *Spectrum and Conversion Efficiency Measurements of Suprathermal Electrons from Relativistic Laser Plasma Interactions.* PhD thesis, 2009.

[106] A. Link, R. R. Freeman, D. W. Schumacher, and L. D. Van Woerkom. Ef-

fects of target charging and ion emission on the energy spectrum of emitted electrons. *Physics of Plasmas*, 18(5), 2011.

[107] R. H H Scott, E. L. Clark, F. Pérez, M. J V Streeter, J. R. Davies, H. P. Schlenvoigt, J. J. Santos, S. Hulin, K. L. Lancaster, S. D. Baton, S. J. Rose, and P. A. Norreys. Measuring fast electron spectra and laser absorption in relativistic laser-solid interactions using differential bremsstrahlung photon detectors. *Review of Scientific Instruments*, 84(8), 2013.

[108] John F Seely, Lawrence T Hudson, Glenn E Holland, and Albert Henins. Enhanced x-ray resolving power achieved behind the focal circles of Cauchois spectrometers. *Applied optics*, 47(15):2767–2778, 2008.

[109] Mark N Quinn. Investigations of Fast Electron Transport in Intense Laser-Solid Interactions by Declaration of Authorship. 2011.

[110] J Yu, Z Jiang, J C Kieffer, and a Krol. Hard x-ray emission in high intensity femtosecond laser-target interaction. *Physics of Plasmas*, 6(4):1318–1322, 1999.

[111] Y. Glinec, J. Faure, L. Dain, S. Darbon, T. Hosokai, J. Santos, E. Lefebvre, J. Rousseau, F. Burgy, B. Mercier, and V. Malka. High-Resolution γ-Ray Radiography Produced by a Laser-Plasma Driven Electron Source. *Physical Review Letters*, 94(2):025003, 2005.

[112] Christopher P Jones, Ceri M Brenner, Camilla A Stitt, Chris Armstrong, Dean R. Rusby, Seyed R. Mirfayzi, Lucy A. Wilson, Aarón Alejo, Hamad Ahmed, Ric Allott, Nicholas M.H. Butler, Robert J. Clarke, David Haddock, Cristina Hernandez-Gomez, Adam Higginson, Christopher Murphy, Margaret Notley, Charilaos Paraskevoulakos, John Jowsey, Paul McKenna, David Neely, Satya Kar, and Thomas B. Scott. Evaluating laser-driven Bremsstrahlung radiation sources for imaging and analysis of nuclear waste packages. *Journal of Hazardous Materials*, 318:694–701, 2016.

[113] G. Fiksel, F. J. Marshall, C. Mileham, and C. Stoeckl. Note: Spatial resolution of Fuji BAS-TR and BAS-SR imaging plates. *Review of Scientific Instruments*, 83(8):10–13, 2012.

[114] L. Robson, P. McKenna, D. Neely, M. Zepf, R.J. Clarke, K.W.D. Ledingham, T. McCanny, P.T. Simpson, F. Lindau, O. Lundh, P. Mora, and C. Wahlstrom. Scaling of proton acceleration driven by petawatt-laser-plasma interactions. *Nature Physics*, 3(1):58–62, 2007.

[115] C.M. Brenner, J.S. Green, A.P.L. Robinson, D.C. Carroll, B. Dromey, P.S. Foster, S. Kar, Y.T. Li, K. Markey, C. Spindloe, M.J.V. Streeter, M. Tolley, C.-G. Wahlström, M.H. Xu, M. Zepf, P. McKenna, and D. Neely. Dependence of laser accelerated protons on laser energy following the interaction of defocused, intense laser pulses with ultra-thin targets. *Laser and Particle Beams*, 29(03):345–351, 2011.

[116] J Allison, J Apostolakis, A Bagulya, C Champion, S Elles, F Garay, V Grichine, A Howard, S Incerti, V Ivanchenko, J Jacquemier, M Maire, A Mantero, P Nieminen, L Pandola, G Santin, D Sawkey, A Schälicke, and L Urban. Geant4 electromagnetic physics for high statistic simulation of LHC experiments. *Journal of Physics: Conference Series*, 396(2):022013, 2012.

[117] L. Pandola, C. Andenna, and B. Caccia. Validation of the Geant4 simulation of bremsstrahlung from thick targets below 3 MeV. *Nuclear Instruments and Methods in Physics Research, Section B: Beam Interactions with Materials and Atoms*, 350:41–48, 2015.

[118] D. A. Maclellan, D. C. Carroll, R. J. Gray, N. Booth, M. Burza, M. P. Desjarlais, F. Du, B. Gonzalez-Izquierdo, D. Neely, H. W. Powell, A. P L Robinson, D. R. Rusby, G. G. Scott, X. H. Yuan, C. G. Wahlströ̈m, and P. McKenna. Annular fast electron transport in silicon arising from low-temperature resistivity. *Physical Review Letters*, 111(9), 2013.

[119] R J Dance, N M H Butler, R J Gray, D A MacLellan, D R Rusby, G G

Scott, B Zielbauer, V Bagnoud, H Xu, A P L Robinson, M P Desjarlais, D Neely, and P McKenna. Role of lattice structure and low temperature resistivity in fast-electron-beam filamentation in carbon. *Plasma Physics and Controlled Fusion*, 58(1):014027, 2015.

[120] A Compant La Fontaine. Photon dose produced by a high-intensity laser on a solid target. *Journal of Physics D: Applied Physics*, 47(32):325201, 2014.

[121] Scott C Wilks and William L Kruer. Absorption of Ultrashort, Ultra-Intense Laser Light by Solids and Overdense Plasmas. 33(11):1954–1968, 1997.

[122] Alex Chalmers. Rapid Inspection of Cargos at Portals using Drive-through Transmission and Backscatter X-ray Imaging. *Proceedings of SPIE*, 5403:644–648, 2004.

[123] Alex Chalmers. Three applications of backscatter x-ray imaging technology to Homeland Defense. *Proceedings of SPIE*, 5778:989–993, 2005.

[124] Johan Van Den Heuvel and Franco Fiore. Simulation study of x-ray backscatter imaging of pressure-plate improvised explosive devices. *Detection and Sensing of Mines, Explosive Objects, and Obscured Targets XVII*, 8357:835716–835716, 2012.

[125] C. Paulus, J. Tabary, N. Billion Pierron, J .M. Dinten, E. Fabiani, F. Mathy, F. Mougel, J. Rinkel, and L. Verger. A multi-energy X-ray backscatter system for explosives detection. *Journal of Instrumentation*, 8(04):P04003–P04003, 2013.

[126] Roderick D. Swift. Mobile x-ray backscatter imaging system for inspection of vehicles. *Proceedings of SPIE*, 2936:124–132, 1997.

[127] G Harding and E Harding. Compton scatter imaging: A tool for historical exploration. *Applied Radiation and Isotopes*, 68(6):993–1005, 2010.

[128] Oskar Klein and Yoshio Nishina. Über die streuung von strahlung durch freie elektronen nach der neuen relativistischen quantendynamik von dirac. *Zeitschrift für Physik*, 52(11-12):853–868, 1929.

[129] S. Kneip, C. McGuffey, J. L. Martins, M. S. Bloom, V. Chvykov, F. Dollar, R. Fonseca, S. Jolly, G. Kalintchenko, K. Krushelnick, A. Maksimchuk, S. P D Mangles, Z. Najmudin, C. A J Palmer, K. Ta Phuoc, W. Schumaker, L. O. Silva, J. Vieira, V. Yanovsky, and A. G R Thomas. Characterization of transverse beam emittance of electrons from a laser-plasma wakefield accelerator in the bubble regime using betatron x-ray radiation. *Physical Review Special Topics - Accelerators and Beams*, 15(2):2–6, 2012.

[130] Martin J Berger. Estar, pstar, and astar: Computer programs for calculating stopping-power and range tables for electrons, protons, and helium ions. *Unknown*, 1992.

[131] R. M. Deas, L. A. Wilson, D. Rusby, A. Alejo, R. Allott, P. P. Black, S. E. Black, M. Borghesi, C. M. Brenner, J. Bryant, R. J. Clarke, J. C. Collier, B. Edwards, P. Foster, J. Greenhalgh, C. Hernandez-Gomez, S. Kar, D. Lockley, R. M. Moss, Z. Najmudin, R. Pattathil, D. Symes, M. D. Whittle, J. C. Wood, P. Mckenna, and D. Neely. A laser driven pulsed X-ray backscatter technique for enhanced penetrative imaging. *Journal of X-Ray Science and Technology*, 23(6):791–797, 2015.

[132] N Otuka, Eea Dupont, V Semkova, B Pritychenko, AI Blokhin, M Aikawa, S Babykina, M Bossant, G Chen, S Dunaeva, et al. Towards a more complete and accurate experimental nuclear reaction data library (EXFOR): international collaboration between nuclear reaction data centres (nrdc). *Nuclear Data Sheets*, 120:272–276, 2014.

[133] D.R. Brown and T. Gozani. Cargo inspection system based on pulsed fast neutron analysis. *Radiation Protection Dosimetry*, 116(1-4):753–756, 1995.

[134] J. Rynes, J. Bendahan, T. Gozani, R. Loveman, J. Stevenson, and C. Bell.

Gamma-ray and neutron radiography as part of a pulsed fast neutron analysis inspection system. *Nuclear Instruments and Methods in Physics Research, Section A: Accelerators, Spectrometers, Detectors and Associated Equipment*, 422(1-3):895–899, 1999.

[135] Hui Chen, R. Tommasini, J. Seely, C. I. Szabo, U. Feldman, N. Pereira, G. Gregori, K. Falk, J. Mithen, and C. D. Murphy. Measuring electron-positron annihilation radiation from laser plasma interactions. *Review of Scientific Instruments*, 83(10):1–4, 2012.

[136] J. F. Seely, C. I. Szabo, Uri Feldman, Hui Chen, L. T. Hudson, and A. Henins. Gamma ray spectra from targets irradiated by picosecond lasers. *High Energy Density Physics*, 7(3):150–154, 2011.

[137] TE Schlesinger, JE Toney, H Yoon, EY Lee, BA Brunett, L Franks, and RB James. Cadmium zinc telluride and its use as a nuclear radiation detector material. *Materials Science and Engineering: R: Reports*, 32(4):103–189, 2001.

[138] S Cipiccia, S M Wiggins, D Maneuski, E Brunetti, G Vieux, X Yang, R C Issac, G H Welsh, M Anania, M R Islam, B Ersfeld, R Montgomery, G Smith, M Hoek, D J Hamilton, N R C Lemos, D R Symes, P P Rajeev, V O Shea, J M Dias, and D A Jaroszynski. Compton scattering for spectroscopic detection of ultra-fast, high flux, broad energy range X-rays. *Review of Scientific Instruments*, 84(11):113302, 2013.

[139] J. S. Green, D. C. Carroll, C. Brenner, B. Dromey, P. S. Foster, S. Kar, Y. T. Li, K. Markey, P. McKenna, D. Neely, A. P L Robinson, M. J V Streeter, M. Tolley, C. G. Wahlström, M. H. Xu, and M. Zepf. Enhanced proton flux in the MeV range by defocused laser irradiation. *New Journal of Physics*, 12, 2010.

[140] M. H. Xu, Y. T. Li, D. C. Carroll, P. S. Foster, S. Hawkes, S. Kar, F. Liu, K. Markey, P. McKenna, M. J V Streeter, C. Spindloe, Z. M. Sheng, C. G.

Wahlström, M. Zepf, J. Zheng, J. Zhang, and D. Neely. Enhancement of ion generation in femtosecond ultraintense laser-foil interactions by defocusing. *Applied Physics Letters*, 100(8):1–5, 2012.

[141] M. Coury, D. C. Carroll, A. P. L. Robinson, X. H. Yuan, C. M. Brenner, M. Burza, R. J. Gray, M. N. Quinn, K. L. Lancaster, Y. T. Li, X. X. Lin, O. Tresca, C. G. Wahlström, D. Neely, and P. McKenna. Influence of laser irradiated spot size on energetic electron injection and proton acceleration in foil targets. *Applied Physics Letters*, 100(7):074105, 2012.

[142] B. Aurand, L. Senje, K. Svensson, M. Hansson, A. Higginson, A. Gonoskov, M. Marklund, A. Persson, O. Lundh, D. Neely, P. McKenna, and C. G. Wahlström. Manipulation of the spatial distribution of laser-accelerated proton beams by varying the laser intensity distribution. *Physics of Plasmas*, 23(2), 2016.

[143] I. A. Bush, A. G R Thomas, L. Gartside, S. Sarfraz, E. Wagenaars, J. S. Green, M. Notley, H. Lowe, C. Spindloe, T. Winstone, A. P L Robinson, R. Clarke, T. Ma, T. Yabuuchi, M. Wei, F. N. Beg, R. B. Stephens, A. MacPhee, A. J. MacKinnon, M. H. Key, W. Nazarov, M. Sherlock, and J. Pasley. Effect of defocusing on picosecond laser-coupling into gold cones. *Physics of Plasmas*, 21(1), 2014.

[144] Lei Yang and John Pasley. Particle-in-cell simulations of hot electron generation using defocused laser light in cone targets. *Physics of Plasmas*, 23(8), 2016.

[145] Y. Ping, R. Shepherd, B. F. Lasinski, M. Tabak, H. Chen, H. K. Chung, K. B. Fournier, S. B. Hansen, A. Kemp, D. A. Liedahl, K. Widmann, S. C. Wilks, W. Rozmus, and M. Sherlock. Absorption of short laser pulses on solid targets in the ultrarelativistic regime. *Physical Review Letters*, 100(8):6–9, 2008.

[146] R.J. Gray, R. Wilson, S.D.R Williamson, M. King, R.J. Dance, C. Armstrong, C. Brabetz, F Wagner, B Zielbauer, V Bagnoud, D Neely, and P Mckenna. Influence of critical surface curvature on energy absorption in intense laser-solid interactions. *Under Review*, 2017.

[147] P. McKenna, D. C. Carroll, O. Lundh, F. Nürnberg, K. Markey, S. Bandyopadhyay, D. Batani, R. G. Evans, R. Jafer, S. Kar, D. Neely, D. Pepler, M. N. Quinn, R. Redaelli, M. Roth, C. G. Wahlström, X. H. Yuan, and M. Zepf. Effects of front surface plasma expansion on proton acceleration in ultraintense laser irradiation of foil targets. *Laser and Particle Beams*, (26):591–596, 2008.

[148] Florian Wagner, Stefan Bedacht, Alex Ortner, Markus Roth, Anna Tauschwitz, Bernhard Zielbauer, and Vincent Bagnoud. Pre-plasma formation in experiments using petawatt lasers. *Optics Express*, 22(24):29505, 2014.

[149] DC Carroll, MN Quinn, XH Yuan, and Paul McKenna. Effects of front surface plasma expansion on proton acceleration driven by the Vulcan Petawatt laser. *clf.rl.ac.uk*, pages 19–22, 2008.

[150] N Nakanii, K Kondo, T Yabuuchi, K Tsuji, K a Tanaka, S Suzuki, T Asaka, K Yanagida, H Hanaki, T Kobayashi, K Makino, T Yamane, S Miyamoto, and K Horikawa. Absolute calibration of imaging plate for gev electrons. *Review of Scientific Instruments*, 79(6):066102, 2008.

[151] J. Fuchs, P. Antici, E. D'Humières, E. Lefebvre, M. Borghesi, E. Brambrink, C. A. Cecchetti, M. Kaluza, V. Malka, M. Manclossi, S. Meyroneinc, P. Mora, J. Schreiber, T. Toncian, H. Pépin, and P. Audebert. Laser-driven proton scaling laws and new paths towards energy increase. *Nature Physics*, 2(1):48–54, 2006.

[152] J. Schreiber, F. Bell, F. Gr$\ddot{i}$ner, U. Schramm, M. Geissler, M. Schn$\ddot{u}$rer, S. Ter-Avetisyan, B. M. Hegelich, J. Cobble, E. Brambrink, J. Fuchs, P. Au-

debert, and D. Habs. Analytical model for ion acceleration by high-intensity laser pulses. *Physical Review Letters*, 97(4):1–4, 2006.

[153] S. Buffechoux, J. Psikal, M. Nakatsutsumi, L. Romagnani, A. Andreev, K. Zeil, M. Amin, P. Antici, T. Burris-Mog, A. Compant-La-Fontaine, E. D'Humières, S. Fourmaux, S. Gaillard, F. Gobet, F. Hannachi, S. Kraft, A. Mancic, C. Plaisir, G. Sarri, M. Tarisien, T. Toncian, U. Schramm, M. Tampo, P. Audebert, O. Willi, T. E. Cowan, H. Pépin, V. Tikhonchuk, M. Borghesi, and J. Fuchs. Hot electrons transverse refluxing in ultraintense laser-solid interactions. *Physical Review Letters*, 105(1):1–5, 2010.

[154] J. Green, V. Ovchinnikov, R. Evans, K. Akli, H. Azechi, F. Beg, C. Bellei, R. Freeman, H. Habara, R. Heathcote, M. Key, J. King, K. Lancaster, N. Lopes, T. Ma, A. MacKinnon, K. Markey, A. McPhee, Z. Najmudin, P. Nilson, R. Onofrei, R. Stephens, K. Takeda, K. Tanaka, W. Theobald, T. Tanimoto, J. Waugh, L. Van Woerkom, N. Woolsey, M. Zepf, J. Davies, and P. Norreys. Effect of Laser Intensity on Fast-Electron-Beam Divergence in Solid-Density Plasmas. *Physical Review Letters*, 100(1):015003, 2008.

[155] Ceri M Brenner. *Laser-Driven Proton Beams: Mechanisms for spectral control and efficiency enhancement*. PhD thesis, 2012.

[156] J. Myatt, W. Theobald, J. A. Delettrez, C. Stoeckl, M. Storm, T. C. Sangster, A. V. Maximov, and R. W. Short. High-intensity laser interactions with mass-limited solid targets and implications for fast-ignition experiments on OMEGA EP. *Physics of Plasmas*, 14(5):056301, 2007.

[157] Guo Qian Liao, Yu Tong Li, Yi Hang Zhang, Hao Liu, Xu Lei Ge, Su Yang, Wen Qing Wei, Xiao Hui Yuan, Yan Qing Deng, Bao Jun Zhu, Zhe Zhang, Wei Min Wang, Zheng Ming Sheng, Li Ming Chen, Xin Lu, Jing Long Ma, Xuan Wang, and Jie Zhang. Demonstration of Coherent Terahertz Transition Radiation from Relativistic Laser-Solid Interactions. *Physical Review Letters*, 116(20):1–6, 2016.

[158] W P Leemans, C G R Geddes, J Faure, Cs Tóth, J van Tilborg, C B Schroeder, E Esarey, G Fubiani, D Auerbach, B Marcelis, M a Carnahan, R a Kaindl, J Byrd, and M C Martin. Observation of terahertz emission from a laser-plasma accelerated electron bunch crossing a plasma-vacuum boundary. *Physical review letters*, 91(August):074802, 2003.

[159] M. Borghesi, A. Schiavi, D. H. Campbell, M. G. Haines, O. Willi, A. J. MacKinnon, P. Patel, M. Galimberti, and L. A. Gizzi. Proton imaging detection of translent electromagnetic fields in laser-plasma interactions (invited). *Review of Scientific Instruments*, 74(3 II):1688–1693, 2003.

[160] L. Romagnani, J. Fuchs, M. Borghesi, P. Antici, P. Audebert, F. Ceccherini, T. Cowan, T. Grismayer, S. Kar, A. MacChi, P. Mora, G. Pretzler, A. Schiavi, T. Toncian, and O. Willi. Dynamics of electric fields driving the laser acceleration of multi-MeV protons. *Physical Review Letters*, 95(19):4–7, 2005.

[161] P. McKenna, A. P. L. Robinson, D. Neely, M. P. Desjarlais, D. C. Carroll, M. N. Quinn, X. H. Yuan, C. M. Brenner, M. Burza, M. Coury, P. Gallegos, R. J. Gray, K. L. Lancaster, Y. T. Li, X. X. Lin, O. Tresca, and C.-G. Wahlström. Effect of Lattice Structure on Energetic Electron Transport in Solids Irradiated by Ultraintense Laser Pulses. *Physical Review Letters*, 106(18):185004, 2011.

[162] A. P L Robinson, H. Schmitz, J. S. Green, C. P. Ridgers, N. Booth, and J. Pasley. Control of wire heating with resistively guided fast electrons through an inverse conical taper. *Physics of Plasmas*, 22(4), 2015.

[163] R. A B Alraddadi, A. P L Robinson, N. C. Woolsey, and J. Pasley. The effect of grading the atomic number at resistive guide element interface on magnetic collimation. *Physics of Plasmas*, 23(7), 2016.